

PhD 1998

*Structural Investigation of Layered
Compounds Based on the
Perovskite SrTiO₃*

Mark Bowden
Clare College
Cambridge, UK



*A Dissertation submitted to the University of Cambridge,
for the degree of Doctor of Philosophy*



November, 1994

Abstract

Declaration

The work described in this dissertation was carried out in the Department of Chemistry, University of Cambridge, between October 1991 and November 1994. It represents the author's original work, except wherein references are acknowledged, and has not been submitted for a degree at any other university



Mark Bowden
November 1994

Abstract

Changes of stoichiometry in the perovskite SrTiO_3 have been investigated in the $\text{SrO-La}_2\text{O}_3\text{-TiO}_2$ system, which result in the formation of layered structures within the perovskite matrix. When present in low concentrations, the layers are distributed in a disordered fashion and therefore cannot be detected by diffraction techniques. They may, however, be observed using high-resolution electron microscopy (HREM), which revealed a tendency for the layers to group together at low concentrations. As the frequency of layers increased, they were observed to form ordered arrays, and led to three different layered families of stoichiometric compounds which may be defined by the layer structure and the interlayer spacing. These are summarised in the following table, where the layer orientation given refers to planes in perovskite:

Composition change	Layer orientation	Compositional series	Ordered members
Addition of SrO	{100}	$\text{Sr}_{n+1}\text{Ti}_n\text{O}_{3n+1}$	$n=1, 2$ and 3
Addition of O	{110}	$\text{Sr}_{n-4}\text{La}_4\text{Ti}_n\text{O}_{3n+2}$	$n=4, 4.5$ and 5
Removal of Ti	{111}	$\text{Sr}_{n-3}\text{La}_4\text{Ti}_n\text{O}_{3n+3}$	$n=3, 4$ and 5

Previous studies have not agreed regarding the stability of the $n=3$ {100} layered compound. In this report, the well-ordered nature of this material has been verified using HREM, and the structures of all of the {100} and {111} layered phases refined by the Rietveld method. The $n=4.5$ and $n=5$ {110} layered materials have not been reported previously, although isostructural compounds are known.

A new compound with the composition $\text{Sr}_3\text{La}_2\text{Ti}_2\text{O}_{10}$ has been identified, and its structure determined using a combination of HREM and Rietveld analysis. It contains slabs of the $n=1$ {100} layered structure, resulting in ribbons of TiO_6 octahedra running parallel to the b axis. In the electron microscope, the surfaces of crystals were found to be covered by a rim of disordered material. This was observed to crystallise into the perovskite structure under the influence of the electron beam.

For many of the compounds described above, HREM revealed defects in the layer stacking and layer structure. The nature of these defects has been investigated using computer-based models and, where appropriate, simulation of HREM images.

Discussion

Much of the behaviour of the layered compounds has been discussed in terms of elastic strain. The layer structures of all of the compounds had a different size than the corresponding perovskite dimension, and so the cell parameters converged toward the perovskite value as the thickness of the perovskite lamellae increased. Consideration of elastic strain can explain this behaviour, as well as the stability ranges of the layered families.

Experiments designed to synthesise an $n=3$ {100} layered compound containing copper were not successful. However, three solid solution ranges were found, including complete solid solution between Sr_2TiO_4 and La_2CuO_4 .

Table of Contents

Declaration	i
Abstract	ii
Acknowledgements	vi
Chapter 1. Introduction	1
1.1 Overview	1
1.2 Crystallographic Shear in ReO_3 Structures	4
1.3 Reduced Titanium Oxides	7
1.4 The Perovskite Structure	9
1.4.1 Crystallographic Shear in Perovskites	12
1.4.2 Oxygen-deficient Perovskites	14
1.5 Aurivillius Compounds	17
Chapter 2. Experimental Methods	19
2.1 Introduction	19
2.2 The Rietveld Method.....	21
2.2.1 Basis of the Refinement	22
2.2.2 Criteria of Fit.....	27
2.2.3 Data Collection	28
2.3 High-Resolution Electron Microscopy.....	30
2.3.1 Electron-Specimen Interactions	33
2.3.1.1 The Phase Object Approximation.....	33
2.3.1.2 The Multi-Slice Method	34
2.3.2 Lens Aberrations and the Transfer Function	36
2.3.3 Chromatic Aberration and Beam Divergence	39
2.4 Experimental Procedures.....	43
2.4.1 Sample Preparation	43
2.4.2 X-ray Diffraction.....	44
2.4.3 Electron Microscopy and Image Simulation.....	45
Chapter 3. Compounds in the SrO-TiO_2 system	50
3.1 Introduction	50
3.2 Ordered Compounds.....	54
3.2.1 Phase Stability	54
3.2.2 Structure Refinement	57
3.3 Disorder and Defects.....	64
3.3.1 Layer Stacking	64
3.3.2 Changes in Layer Direction	67
3.3.3 Termination of the Layer Structure.....	71
3.4 Summary and Conclusions	73
Chapter 4. Investigation of Reported Compounds in the Sr-La-Ti-O System	74
4.1 Introduction	74

4.1.1 Solid Solutions in SrTiO ₃	75
4.1.2 Fixed Composition Phases	77
4.2 La-Substituted SrTiO ₃	79
4.2.1 Structural Determination.....	79
4.2.2 The Accommodation of Extra Oxygen	84
4.2.3 Characterisation of New Compounds	87
4.3 Other Reported Sr-La-Ti-O Compounds.....	90
4.3.1 SrLa ₂ Ti _n O _{2n+4} Compounds	90
4.3.2 Sr _{n-3} La ₄ Ti _n O _{3n+3} Compounds	90
4.4 Summary and Conclusions	95
Chapter 5. Sr₃La₂Ti₂O₁₀, a New Compound in the SrO-La₂O₃-TiO₂ System	97
5.1 Introduction	97
5.2 Formulation of a Draft Structure	98
5.3 Confirmation by Rietveld and HREM.....	100
5.4 Defects and Intergrowths	104
5.5 Surface Modification Under the Electron Beam.....	108
5.6 Summary and Conclusions	113
Chapter 6. The Importance of Elastic Strain	114
6.1 Introduction	114
6.2 Brief Literature Review.....	116
6.2.1 Continuum Elasticity Models.....	116
6.2.2 Atomistic Simulation	118
6.2.3 Layer Mismatch	119
6.3 Application to the Present Materials.....	121
6.3.1 Description in Terms of Elastic Strain.....	121
6.3.2 Quantitative Models	125
6.4 Similarities to Other Systems.....	129
6.5 Summary and Conclusions	132
Chapter 7. Ruddlesden-Popper Compounds Containing Copper	134
7.1 Introduction	134
7.1.1 Mixed Cuprates-Titanates	134
7.1.2 Ruddlesden-Popper Cuprates.....	137
7.2 Solid Solutions Between Copper and Titanium	142
7.3 Three-layered Cuprates	146
7.4 Summary and Conclusions	153
Chapter 8. Summary and Concluding Remarks	154
8.1 Layers in Perovskite Compounds.....	154
8.2 The Nature of the Intergrowth Phases.....	156
8.3 Layered Perovskites Containing Copper.....	158
8.4 New Structures and Future Possibilities	160
Appendix. X-ray Diffraction Data	164
References	167

4.1.1 Solid Solutions in SrTiO ₃	75
4.1.2 Fixed Composition Phases	77
4.2 La-Substituted SrTiO ₃	79
4.2.1 Structural Determination.....	79
4.2.2 The Accommodation of Extra Oxygen	84
4.2.3 Characterisation of New Compounds	87
4.3 Other Reported Sr-La-Ti-O Compounds.....	90
4.3.1 SrLa ₂ Ti _n O _{2n+4} Compounds	90
4.3.2 Sr _{n-3} La ₄ Ti _n O _{3n+3} Compounds	90
4.4 Summary and Conclusions.....	95
Chapter 5. Sr₃La₂Ti₂O₁₀, a New Compound in the SrO-La₂O₃-TiO₂ System	97
5.1 Introduction	97
5.2 Formulation of a Draft Structure.....	98
5.3 Confirmation by Rietveld and HREM.....	100
5.4 Defects and Intergrowths	104
5.5 Surface Modification Under the Electron Beam.....	108
5.6 Summary and Conclusions	113
Chapter 6. The Importance of Elastic Strain	114
6.1 Introduction	114
6.2 Brief Literature Review.....	116
6.2.1 Continuum Elasticity Models.....	116
6.2.2 Atomistic Simulation	118
6.2.3 Layer Mismatch	119
6.3 Application to the Present Materials.....	121
6.3.1 Description in Terms of Elastic Strain.....	121
6.3.2 Quantitative Models.....	125
6.4 Similarities to Other Systems.....	129
6.5 Summary and Conclusions	132
Chapter 7. Ruddlesden-Popper Compounds Containing Copper	134
7.1 Introduction	134
7.1.1 Mixed Cuprates-Titanates	134
7.1.2 Ruddlesden-Popper Cuprates.....	137
7.2 Solid Solutions Between Copper and Titanium.....	142
7.3 Three-layered Cuprates	146
7.4 Summary and Conclusions	153
Chapter 8. Summary and Concluding Remarks	154
8.1 Layers in Perovskite Compounds.....	154
8.2 The Nature of the Intergrowth Phases.....	156
8.3 Layered Perovskites Containing Copper.....	158
8.4 New Structures and Future Possibilities	160
Appendix. X-ray Diffraction Data	164
References	167

Acknowledgements

Undertaking a project as involved as this inevitably requires the assistance of many people, and I have been fortunate to receive help from many sources, most of whom I hope I have acknowledged here. I would like to begin by thanking my supervisor, Dr D.A. Jefferson, for his ready and effectual assistance at key points throughout this work, and for the excellent training given in teaching the art of high-resolution electron microscopy. I have been particularly impressed by his direct and constructive comments made during the preparation of this manuscript.

Thanks are also due to Brian Challis, who has helped keep the microscopes and other laboratory equipment running as smoothly as possible, and to Drs W.H. Zhou and A.I. Kirkland for discussions and assistance with HREM image simulations. I am also grateful to Mr M. J. Ryan (New Zealand Institute for Industrial Research and Development) for running several of the XRD patterns for Rietveld refinement.

Funding for this work was generously given by the New Zealand Institute for Industrial Research and Development, and I would like to thank all those involved who have given me their support; particularly Drs I.W.M. Brown, D. Smith, G.J. Gainsford, D.M. Bibby and G.J. Leary. I would also like to acknowledge the financial support provided by the Overseas Research Students awards scheme.

Finally, I would like to sincerely thank those who have provided the environment and opportunity to carry out this work. Liz, for her patience and understanding, as well as her kindly-given motivation. And two colleagues who have been instrumental in allowing my career to develop this far: Dr K.J.D. MacKenzie and Dr I.W.M. Brown. Without their long-standing support, I would not have been in a position to undertake this work.

Acknowledgements

Undertaking a project as involved as this inevitably requires the assistance of many people, and I have been fortunate to receive help from many sources, most of whom I hope I have acknowledged here. I would like to begin by thanking my supervisor, Dr D.A. Jefferson, for his ready and effectual assistance at key points throughout this work, and for the excellent training given in teaching the art of high-resolution electron microscopy. I have been particularly impressed by his direct and constructive comments made during the preparation of this manuscript.

Thanks are also due to Brian Challis, who has helped keep the microscopes and other laboratory equipment running as smoothly as possible, and to Drs W.H. Zhou and A.I. Kirkland for discussions and assistance with HREM image simulations. I am also grateful to Mr M. J. Ryan (New Zealand Institute for Industrial Research and Development) for running several of the XRD patterns for Rietveld refinement.

Funding for this work was generously given by the New Zealand Institute for Industrial Research and Development, and I would like to thank all those involved who have given me their support; particularly Drs I.W.M. Brown, D. Smith, G.J. Gainsford, D.M. Bibby and G.J. Leary. I would also like to acknowledge the financial support provided by the Overseas Research Students awards scheme.

Finally, I would like to sincerely thank those who have provided the environment and opportunity to carry out this work. Liz, for her patience and understanding, as well as her kindly-given motivation. And two colleagues who have been instrumental in allowing my career to develop this far: Dr K.J.D. MacKenzie and Dr I.W.M. Brown. Without their long-standing support, I would not have been in a position to undertake this work.

Chapter 1

Introduction

- 1.1 Overview
 - 1.2 Crystallographic Shear in ReO_3 Structures
 - 1.3 Reduced Titanium Oxides
 - 1.4 The Perovskite Structure
 - 1.5 Aurivillius Compounds
-

1.1 Overview

When describing a chemical compound, we frequently refer to it by its chemical formula. Representation in this fashion implies an invariant ratio between the various elements which comprise the compound, although it is recognised that there is some tolerance in this ratio at the atomic level. Most materials accommodate a small change in stoichiometry through the formation of point defects, perhaps a lattice vacancy or interstitial atom. Such defects are usually energetically less stable than the perfect lattice, and are therefore only present in small concentrations according to the configurational entropy. This means that the composition range of most materials is extremely limited, and efforts to prepare compounds outside this range result in mixtures of at least two separate phases.

Some materials do not conform to this picture, however, and appear to exist over a wide composition range. Such materials are often termed “non-stoichiometric compounds”. We must draw a distinction here between non-stoichiometric compounds and substitutional solid solutions. In the latter case, an atom is directly replaced by another similar atom, and occupies the same lattice site. An example is the substitution of sodium with potassium in common salt to give the solid solution

range $\text{Na}_{1-x}\text{K}_x\text{Cl}$. In non-stoichiometric compounds, the ratio between atoms on the various lattice sites is perturbed, for example removal of iron from the mineral wüstite Fe_{1-x}O .

In some non-stoichiometric compounds, the compositional variation can be attributed to point defects, or to clusters of point defects. There is a class of materials, however, in which the defects aggregate along planes to provide a new crystallographic feature with a locally different stoichiometry. A classic example is the formation of crystallographic shear planes in reduced WO_3 , described later in this chapter. Compounds can also be prepared where the defect planes are regularly distributed with a constant spacing between them. If several differently spaced arrangements can be made, then a *homologous series* (Magnéli, 1953) of compounds arises in which the stoichiometry of each is defined by the spacing between adjacent planes. Hence the same mechanism which accounts for non-stoichiometry can also lead to a series of new stoichiometric compounds.

In this thesis, the structural chemistry of planar features in one particular compound, SrTiO_3 , is examined. Several layer types with different orientations can be formed in this material, and each gives rise to a series of stoichiometric compounds, as well as accounting for non-stoichiometry near the SrTiO_3 composition. One of the aims of this study was to determine and characterise the types of stoichiometric compounds which can be prepared. Disordered compounds have also been synthesised, including some with defects in the layer structure. Computer modelling has been used to show how the structure might adapt to accommodate these defects.

We begin in this chapter by describing the structures of a number of layered compounds, although the particular materials prepared during the investigation are discussed more fully later in those chapters which deal with specific structure types. The introductory descriptions are intended to give some idea of the broader family of layered materials, as well as providing information which will become relevant in later discussions. The SrTiO_3 structure is also detailed, which forms the basis for all of the subsequent materials prepared.

The following chapter describes the experimental methods used during sample preparation and analysis. Two principle methods have been used to elucidate structural information: X-ray powder diffraction and high-resolution electron microscopy. Because of the importance of these two techniques, much of the experimental chapter is devoted to a discussion of their theory and practical application.

Chapter 3 examines the first group of layered materials - the so-called Ruddlesden-Popper compounds $\text{Sr}_{n+1}\text{Ti}_n\text{O}_{3n+1}$. The principle aim was to determine the number of ordered compounds in this series and provide a better understanding of their structures. Compositions where the Ruddlesden-Popper layers are present in disordered arrangements have also been studied.

In the subsequent chapter, the range of compositions is broadened by including lanthanum in addition to strontium and titanium. The increased valence of La^{3+} compared with Sr^{2+} provides the opportunity to vary the oxygen stoichiometry as well as that between metals. An attempt is made to clarify the stability of reported phases in the $\text{SrO-La}_2\text{O}_3\text{-TiO}_2$ system, and to investigate the structure of La-substituted SrTiO_3 . High-resolution electron microscopy proves to be an invaluable tool for discovering how the extra oxygen is accommodated in these materials. Two further layered families of compounds are found, and the relationship between these and the first series described in Chapter 3 is demonstrated.

During the study of the $\text{SrO-La}_2\text{O}_3\text{-TiO}_2$ system, a new compound was discovered which does not appear to have been described before. Chapter 5 is concerned with characterising this compound, and a structure is derived from high-resolution microscope images which is also consistent with X-ray diffraction studies. The surface of this material was found to be coated by a layer of amorphous material, which gradually crystallised under the electron beam. This process is followed with a series of images taken from the same crystal fragment, and an account is given of how the structure at the surface differs from that of the bulk phase.

Chapter 6 attempts to draw together many of the common threads to provide a more unified picture of the layered compounds. It is shown how the elastic strain arising from the presence of the layer structure may also be responsible for determining the range and stability of ordered sequences. Some of the published work dealing with elastic strain is reviewed, and similarities between the compounds prepared in this investigation and those in other systems are highlighted.

The next chapter describes the results of studies involving copper-containing compounds which are layered parallel to perovskite {100} planes. There are two principle objectives. The first is to determine the extent to which solid solution between copper and titanium can be realised within these structures. Following this, efforts to prepare layered materials with triple copper-oxygen layers are described. Finally, the results are summarised and general conclusions drawn in Chapter 8.

1.2 Crystallographic Shear in ReO_3 Structures

The ReO_3 structure provides the simplest system for demonstrating the principles of crystallographic shear. ReO_3 possesses a cubic structure in which ReO_6 octahedra share corners in a regular, three-dimensional network (Figure 1-1).

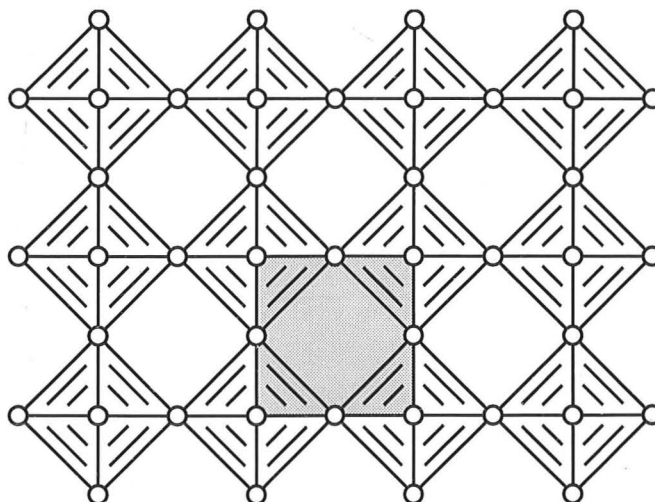


Figure 1-1

View down any of the principle axes of the ReO_3 structure. Re atoms lie at the centres of the octahedra formed by the oxygen atoms (shown as small circles). A unit cell is shaded.

Tungsten oxide (WO_3) has essentially the same structure, but is slightly distorted with W atoms displaced from the centres of the octahedra, which are tilted slightly. This latter compound loses oxygen readily, causing the octahedra to become more regular and allowing structures to be depicted in the ideal, ReO_3 -style form. Rather than distributing oxygen vacancies randomly throughout the structure, it is possible to accommodate the change in oxygen content by forming a new layer structure which has a locally different stoichiometry. This is illustrated in Figure 1-2. The oxygen vacancies are initially aligned across a crystallographic plane, in this case parallel to $\{100\}$. Then the vacancies may be eliminated by moving the portions either side of this plane relative to one another so that the previous metal atom coordination is restored in place of the lattice vacancies. The geometrical operation is termed "crystallographic shear" (abbreviated as CS) and the new region of structure called the crystallographic shear plane. Wadsley (1955) first described how this geometric transformation could be used to account for the observed structures in reduced WO_3 .

In fact, the CS planes found in reduced WO_3 are not oriented along $\{100\}$ planes as Figure 1-2 indicates, but along $\{102\}$ and $\{103\}$ planes. The same principles of CS can be applied in many different directions, and the resulting structures for $\{102\}$ and $\{103\}$ planes are shown in Figure 1-3. Upon initial reduction, CS planes form in the $\{102\}$ orientation (Tilley, 1970), and show considerable disorder, both in the regularity of their spacing as well as the appearance of small twin domains (Tilley, 1978-9). The $\{102\}$ CS plane orientation appears to persist down to a degree of

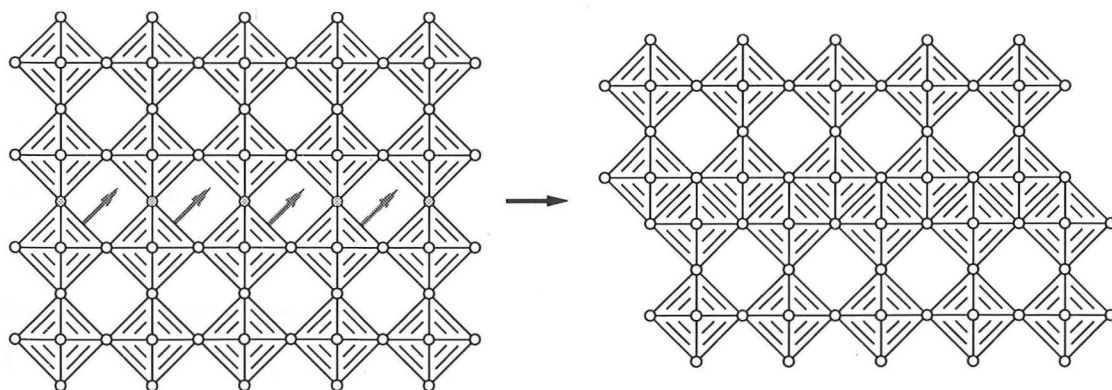


Figure 1-2

Crystallographic shear along a $\{100\}$ plane in reduced WO_3 . The oxygen vacancies (shaded in the left-hand structure) are eliminated by translating the lower half of the structure in the direction of the arrows. The final structure (right) has two rows of edge-sharing octahedra along the shear plane.

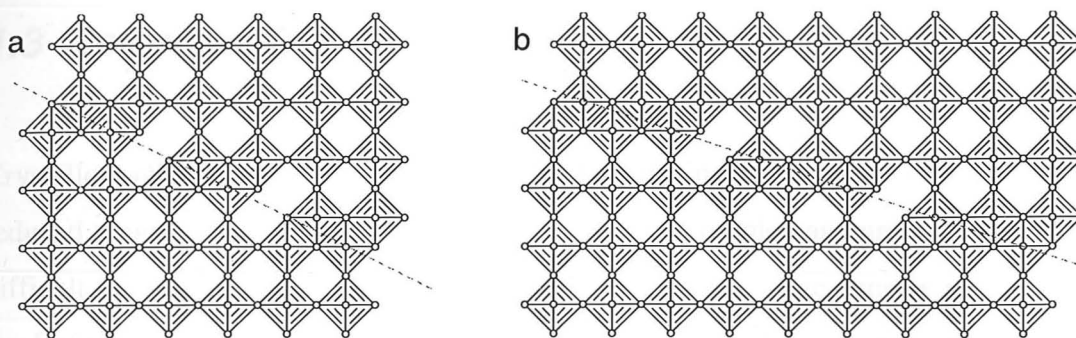


Figure 1-3 Crystallographic shear structures in reduced WO_3 along a) $\{102\}$ and b) $\{103\}$ planes.

reduction corresponding to about $\text{WO}_{2.94}$, when the average separation between planes is about 18 octahedra.

Below this level, $\{103\}$ CS planes have the preferred orientation. Because the layer planes become closer as the degree of reduction increases, ordered arrays of $\{103\}$ planes are found more frequently than for $\{102\}$ planes. This leads to a homologous series of oxides where the composition is directly related to the shear plane separation. For the $\{103\}$ family of tungsten oxides, the series is given by the formula $\text{W}_n\text{O}_{3n-2}$ where n represents the number of WO_6 octahedra between neighbouring CS planes along a diagonal (*i.e.* not the shortest) direction. Magnéli (1953) reported the $n=20$ member of this series and determined its structure before the principles of crystallographic shear had been established. Other reported $\{103\}$ compounds include the $n=40$ (Gado and Magnéli, 1965) and $n=25$ (Sundberg, 1976) members. Booth *et al.* (1982) observed reasonably well-ordered $\{103\}$ planes in fragments of samples with values of n ranging from 15 to 25, but noted that even after reaction for 5 months at 1100°C the samples could not be considered single-phase.

The structural chemistry of tungsten-based oxides is complex, and only the basic elements have been discussed here. When other metals are included, further structural features are observed, including shear planes in the $\{001\}$ and $\{104\}$ orientations. Examples of the resulting microstructures can be seen in the review by Ekström and Tilley (1980).

1.3 Reduced Titanium Oxides

Crystallographic shear in reduced rutile (TiO_{2-x}) is similar in many ways to that in reduced tungsten trioxide, but the structures are more complex and are therefore more difficult to visualise. This is because the rutile structure is more densely packed than the ReO_3 -type structures, comprising a more complicated arrangement of octahedra. In rutile, chains of TiO_6 octahedra are present which extend along the c direction by sharing edges. The oxygen atoms in this edge-sharing region also form the apices of the adjoining chain, which is consequently rotated by 90° about the chain direction with respect to its neighbours. These elements of the rutile structure are shown in Figure 1-4.

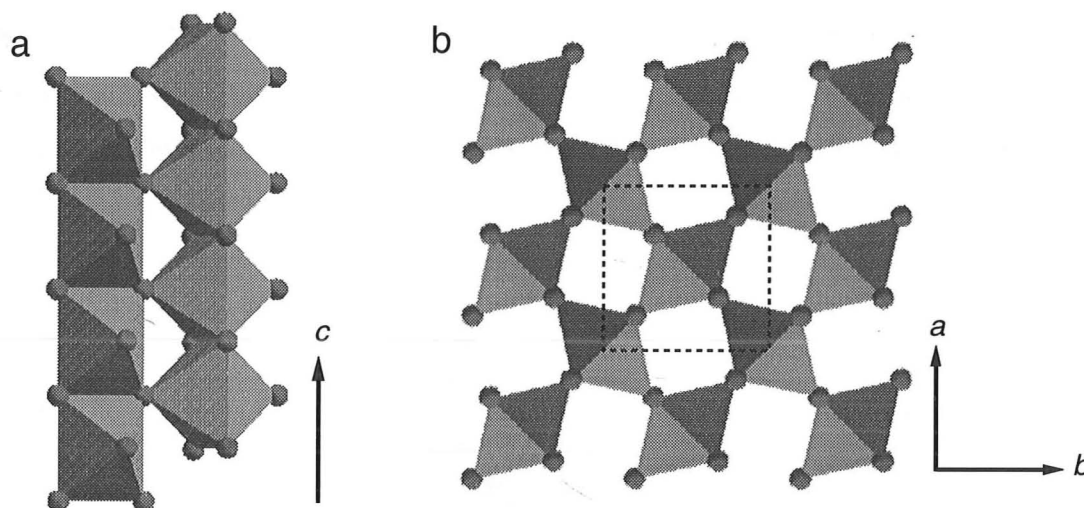


Figure 1-4 a) View showing how two of the edge-sharing TiO_6 chains in rutile are linked. b) The rutile structure viewed along c , *i.e.* along the chain direction. The dotted box outlines a unit cell.

Initial reduction results in the formation of CS planes parallel to rutile $\{132\}$ planes (Eikam and Smallman, 1964). At low concentrations, these are often found in clusters (Bursill and Hyde, 1972) where the spacing between successive planes increases further from the centre of the group. Maze-like networks of small twin domains are also frequently observed. The structure of the CS plane was outlined by Anderson and Hyde (1967), and arises in a similar manner to the reduced tungsten oxides. Oxygen atoms along the CS plane are removed and the resulting structure collapses to

eliminate the lattice vacancies, in this case producing a face-sharing arrangement of octahedra along the *CS* plane.

Bursill and Hyde (1971) proposed that the $\{132\}$ *CS* planes may order to produce a homologous series of oxides Ti_nO_{2n-1} . These oxides could not be prepared as single-phase powders, but were identified in crystal fragments by electron diffraction and showed a wide variation in order and extent of twinning. Electron diffraction patterns for structures corresponding to values of n between 16 and 24 were obtained and, interestingly, were confined to even-numbered members of the series. The reason for this has not been made clear.

A further series of compounds, confusingly with the same general formula Ti_nO_{2n-1} , also exists where the *CS* plane is aligned with $\{121\}$ planes in rutile. Materials with n between 4 and 9 were identified by Andersson *et al.* (1957). Compounds in this series are considerably more ordered, to the extent that single-crystal X-ray studies have confirmed the structures of all members ($n=4$, Marezio *et al.*, 1973; $n=5$, Marezio *et*

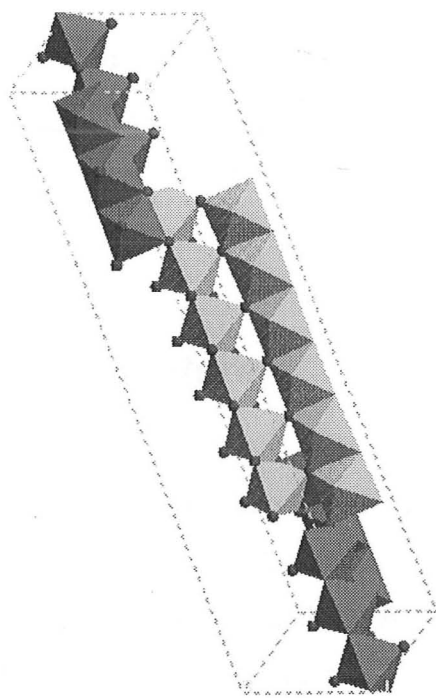


Figure 1-5

Oblique view of a single unit cell of the Ti_6O_{11} structure. Elements of the rutile structure can be seen in the chains of edge-sharing octahedra, 6 octahedra long. There are two *CS* planes, $\frac{1}{4}$ and $\frac{3}{4}$ along the c axis, and neighbouring rutile slabs have been shaded differently for emphasis.

al., 1977; $6 \leq n \leq 9$, Le Page and Strobel, 1982b). A view of the $n=6$ structure is shown in Figure 1-5, which consists of slabs of the rutile structure 6 octahedra wide joined at the shear plane by face-sharing octahedra. $\{121\}$ CS phases are not observed as isolated features, but only in samples where the degree of reduction leads to an oxygen content of less than $\text{TiO}_{1.90}$.

CS planes in the $\{132\}$ orientation are found in samples reduced down to about $\text{TiO}_{1.93}$, leaving the question as to what structures exist in the intervening region. Bursill *et al.* (1971) have shown that in this region the CS plane orientation gradually changes ('swings') from $\{132\}$ to $\{121\}$, offering the possibility that all oxygen stoichiometries can be achieved by an ordered array of planes which have different orientations. The occurrence of swinging CS planes is particularly prevalent in systems where another metal is included in addition to titanium. Perhaps the most spectacular example is the observation of an extensive ordered array of sinusoidal CS planes in $(\text{Ti,Fe})\text{O}_{1.90}$ where the orientation of each plane oscillated between (041) and $(04\bar{1})$ with a wavelength of about 335\AA (Bursill *et al.*, 1978).

Compounds reduced further than the $n=4$ $\{121\}$ CS compound can no longer be described in terms of crystallographic shear planes. The materials Ti_3O_5 , Ti_2O_3 , and TiO are three-dimensional structures in their own right.

1.4 The Perovskite Structure

The ideal perovskite structure is a close relative of the ReO_3 structure (Section 1.2), possessing the same array of corner-sharing metal oxide octahedra. Perovskite compounds have the general formula ABO_3 , and the A cation is located in the void present between 8 of the BO_6 octahedra (Figure 1-6). The resulting oxygen coordination for the A cation is 12-fold, and so perovskite compounds are formed from combinations of fairly large A cations with comparatively small B cations.

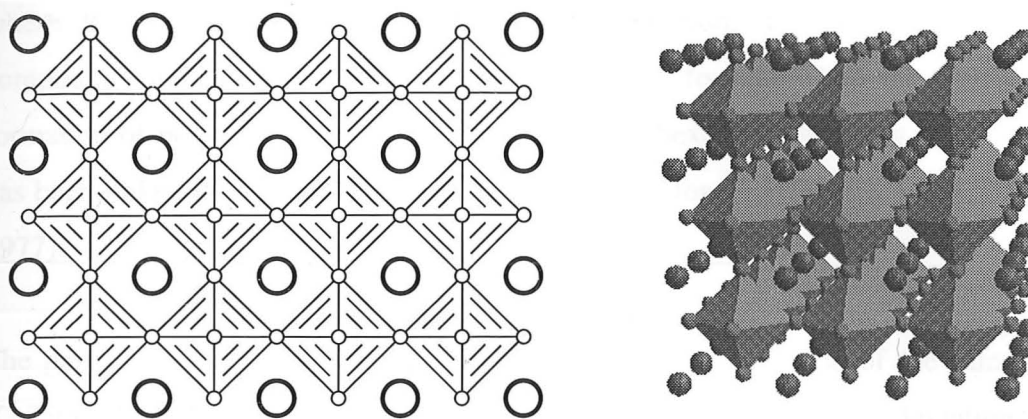


Figure 1-6 The cubic perovskite, ABO_3 , structure. The diagram on the left shows the BO_6 octahedra in lighter ruling, while the A cations are heavily ruled to emphasise the difference in height along the direction of projection. This difference, as well as the three-dimensional corner-sharing of octahedra, can also be seen in the perspective view on the right.

As well as considering an array of BO_6 octahedra surrounding A cations, it is also possible to describe the perovskite structure in terms of close-packed AO_3 layers with B cations in the octahedral interstices (see, *e.g.*, Katz and Ward, 1964). These layers can be envisaged in a similar manner to those used to describe metals as a packing of hard spheres. Each AO_3 layer comprises a hexagonal arrangement of A and O atoms where every A atom has 6 O atoms for nearest neighbours. Close-packing of AO_3 layers leads to an octahedron of oxygens for each A atom, suitable for occupation by the B cation. If the stacking is cubic close-packed, the octahedra all share corners and the perovskite structure described above results. The layers may also be stacked in a hexagonal close-packed arrangement, in which case the octahedra share faces. This structure is found for $BaNiO_3$ (Lander, 1951). Mixed cubic and hexagonal stacking is also possible, and is found for a number of compounds, including some prepared in this study (Chapter 4).

The stability of perovskites has been related to the ionic radii of the constituent atoms. From geometric considerations, Goldschmidt (1926) defined a tolerance factor t given by:

$$t = \frac{R_A + R_O}{\sqrt{2}(R_B + R_O)} \quad (1.1)$$

where R_X is the ionic radius of the subscripted atom X . A survey of known compounds indicated that stable perovskites were formed when $0.8 < t < 1.0$. The formation of perovskite-related materials based on hexagonal stacking of AO_3 layers has been linked with tolerance factors slightly larger than 1 (Hutchison and Jacobson, 1977).

The perovskite structure was originally proposed for the mineral of the same name ($CaTiO_3$), but it was soon realised that this compound possesses small deviations from the ideal structure, resulting in orthorhombic symmetry (Megaw, 1946). Few materials exhibit the perfect structure at room temperature; among these is the parent for compounds prepared in this study, $SrTiO_3$.

Deviations from the ideal structure may arise through cation displacements which account for the physical properties of some materials, for example ferroelectricity in $BaTiO_3$, but the distortions which produce the greatest structural changes are due to rotation of the octahedra. If the octahedra are to remain reasonably regular, then it is impossible to rotate one without also applying cooperative tilts to its neighbours. Glazer (1972) has considered the permutations of possible tilting schemes when the octahedra are rotated about each of their three tetrad axes, and derived 23 possible systems and their symmetries. Many known perovskites were classified according to this scheme, but only 9 of the possible systems were encountered, with two in particular found for a large number of compounds. No reasons were given as to why these particular combinations of rotations were apparently widespread. O'Keefe and Hyde (1977) have also examined octahedral rotations in perovskite, and described 6 systems where the octahedra remain regular and the B-O-B angles are, as far as possible, kept to a uniform value. The main reason for the octahedral rotations, of whatever combination, is to accommodate A cations which are normally found with coordination numbers less than 12.

The number of potential combinations of A and B atoms which could give rise to perovskites is large, since the range of possible oxidation states encompasses much of the periodic table. The requirement for a combined valence of 6+, coupled with ionic

radii considerations, means that 'simple' perovskites are found in the $A^+B^{5+}O_3$, $A^{2+}B^{4+}O_3$, and $A^{3+}B^{3+}O_3$ systems. The range is further extended when 'complex' perovskites are considered in which the A and B positions are occupied by a mixture of elements. In addition, structures can be formed where there are vacancies on either the cation or the anion sites. Many reported compositions, as well as a discussion of the physical properties of perovskites, can be found in the text by Galasso (1969).

1.4.1 Crystallographic Shear in Perovskites

A large number of non-stoichiometric compounds based on perovskite are known, some of which may be described in terms of crystallographic shear. Further details of the structures are given in later chapters, but an account is given here of several different layered defects in perovskite arising through crystallographic shear. The first is one in which the CS plane is parallel to the perovskite (001) plane, and a layer of Ti and O atoms is removed (Figure 1-7a). If the remaining portions of the structure are displaced by half a unit cell in each of the a and b directions, as well as brought closer together in the c direction, then the resulting structure (Figure 1-7b) contains a double row of Sr and O atoms representing elements of the rocksalt structure. Further discussion of the compounds based on this layer type is given in Chapter 3.

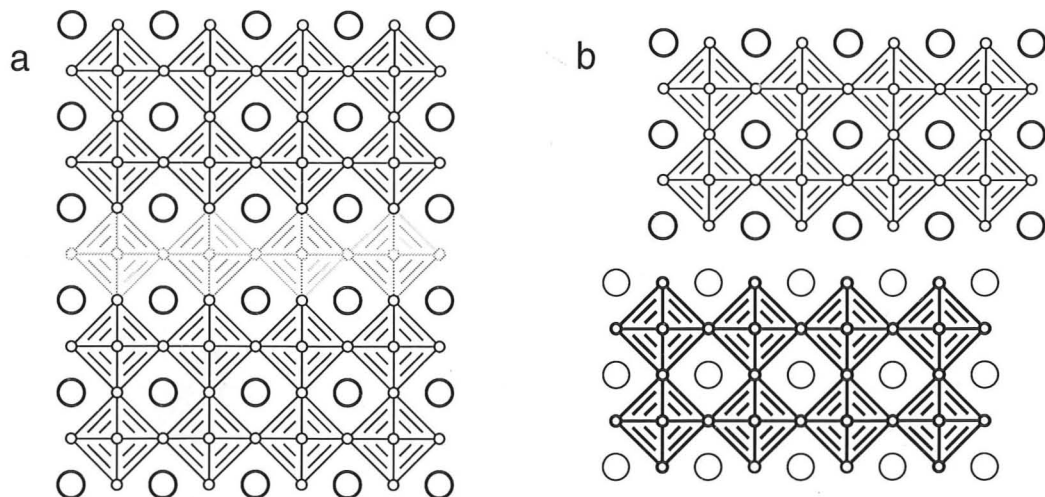


Figure 1-7

Crystallographic shear along $\{100\}$ in perovskite. The Ti and O atoms shaded lightly in (a) are removed and remaining perovskite units displaced to give the layered structure (b). Light and heavy ruling indicate a difference in height perpendicular to the plane of projection.

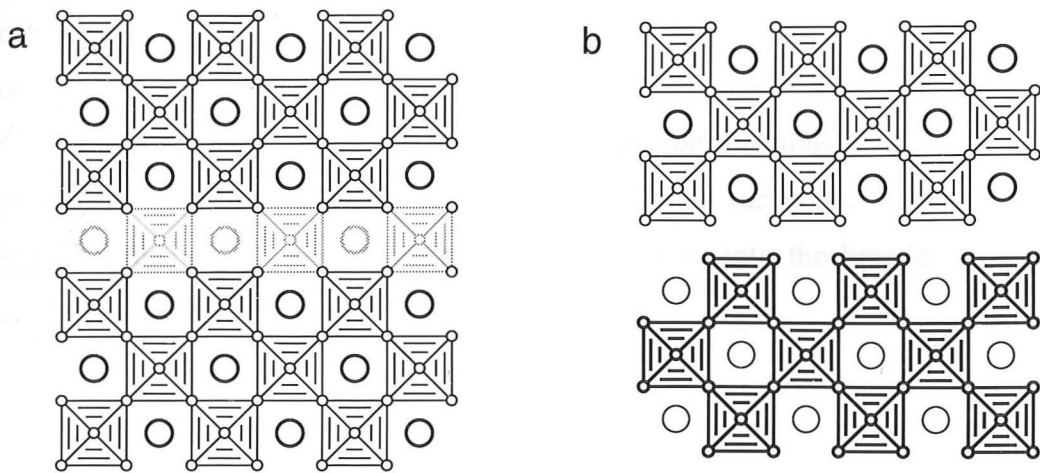


Figure 1-8 Formation of a $\{110\}$ CS plane in perovskite. Symbols are the same as in the previous diagram.

If the CS plane is parallel to (110) and again the atoms lying on a plane running through the centres of the octahedra are removed, then the structure illustrated in Figure 1-8 results. Similar displacements of the perovskite units either side of the CS plane have been applied. The change in stoichiometry equates to an addition of a plane of oxygen atoms, and structures possessing this planar feature are described in Chapter 4.

Also discussed in Chapter 4 are structures where the CS plane is aligned parallel to a $\{111\}$ plane, shown in Figure 1-9. In this case, only Ti atoms are removed and, in contrast to the previous examples, the ideal displacement is purely along the CS plane.

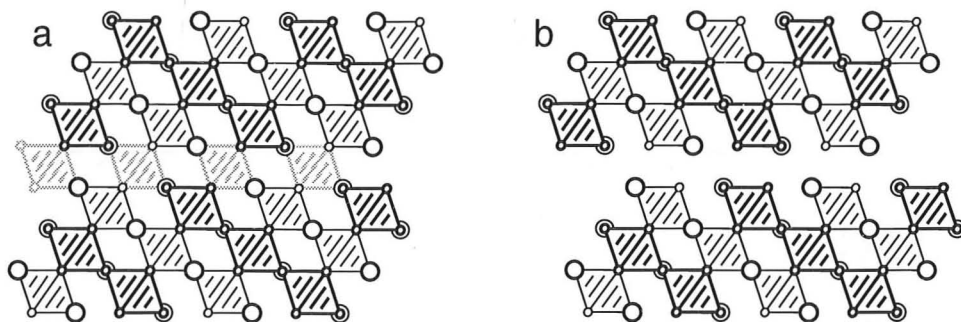


Figure 1-9 Generation of $\{111\}$ layered planes in perovskite. As in the previous two diagrams, the lightly shaded atoms in (a) are removed to produce the structure in (b) through crystallographic shear.

The description of these structures in terms of crystallographic shear is not entirely the same as those in the WO_{3-x} and TiO_{2-x} systems. In particular, the CS operation does not restore all of the metal atoms to their previous coordinations, and the structure does not 'close up' in quite the same way to eliminate the vacancies. Nevertheless, it does highlight how the layered perovskite structures fit into the broader family of layered compounds.

1.4.2 Oxygen-deficient Perovskites

In Sections 1.2 and 1.3, the elimination of oxygen vacancies was seen as the driving force for the formation of CS planes in ReO_3 -type and TiO_2 structures. Perovskite-based materials also display a considerable degree of oxygen deficiency, although the same operations of CS are no longer feasible due to the intervening A cations. The particular structure adopted by oxygen-deficient perovskites depends largely on the nature of the B cation, and the type of coordination it may accept.

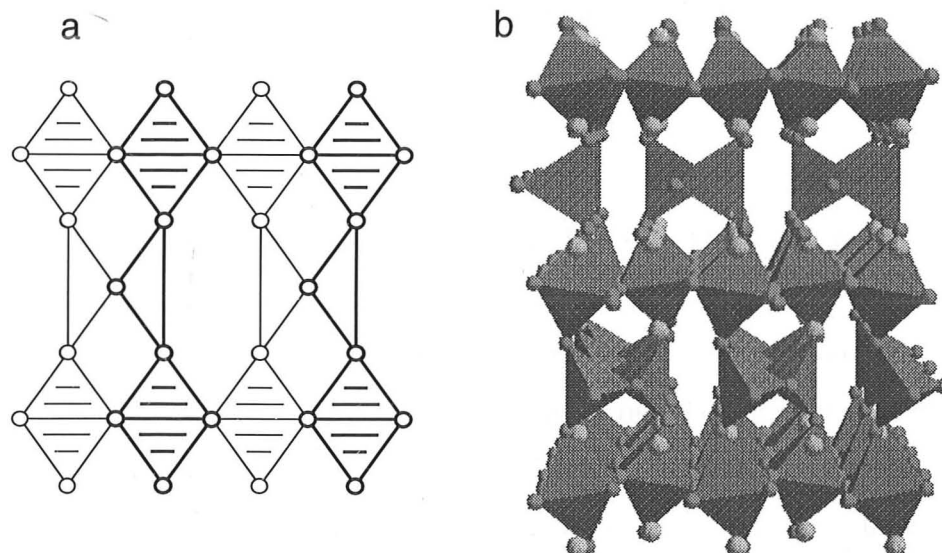


Figure 1-10

a) View along $\{110\}$ in perovskite where rows of oxygen atoms have been removed to leave 4-coordinate polyhedra. The A cations have been omitted for clarity. This forms the basis of the brownmillerite structure, shown in perspective in b). The large spheres are the A cations, smaller spheres O atoms, and Ca and Fe lie in the octahedra and tetrahedra respectively.

Materials with layered structures are found in compounds based on the brownmillerite ($\text{Ca}_2\text{Fe}_2\text{O}_5$) structure. This structure has been refined by Berggren (1971) and may be derived from perovskite by removing rows of oxygen atoms along lines parallel to the (110) direction (Figure 1-10a). This leaves 4-coordinate Fe-O polyhedra, and the structure relaxes to allow these to approach more regular FeO_4 tetrahedra. The brownmillerite structure (Figure 1-10b) contains alternate layers of FeO_4 tetrahedra and FeO_6 octahedra, the latter arranged as in perovskite.

Oxygen-deficient perovskites in the CaTiO_3 - $\text{Ca}_2\text{Fe}_2\text{O}_5$ system have been studied by Grenier *et al.* (1977,1978). This system allows the oxygen content of the perovskite to be varied according to the formula $\text{Ca}(\text{Ti,Fe})\text{O}_{3-x}$ where $0 \leq x \leq 0.5$. For small levels of oxygen deficiency ($x < \sim 0.25$), the structure retains the pseudo-cubic symmetry of perovskite, indicating disorder of the oxygen vacancies. At more oxygen-deficient compositions, however, several new ordered phases were identified with structures related to brownmillerite, but with larger perovskite lamellae. Specimens were prepared with perovskite layers two and three octahedra thick, and an ordered intergrowth of perovskite lamellae one and two octahedra thick was also observed. Disordered intergrowths were also found in some samples. Similar structures have been observed in other systems by, for example, Alario-Franco *et al.* (1983) and Bando *et al.* (1981).

In other materials, the B cation is not normally associated with tetrahedral coordination, and so different structures arise. In the CaMnO_{3-x} system, Reller *et al.* (1984) have identified a number of ordered compounds containing MnO_5 square pyramids as well as MnO_6 octahedra. No disordered compounds were observed, and all the high-resolution electron microscope images could be interpreted as domains of the stoichiometric compounds $\text{CaMnO}_{2.8}$, $\text{CaMnO}_{2.75}$, $\text{CaMnO}_{2.667}$, $\text{CaMnO}_{2.556}$, and $\text{CaMnO}_{2.5}$. In the last of these compounds, Mn is entirely present in square pyramidal coordination. For the oxygen-deficient nickelates, square planar coordination seems to be the preferred geometry. Vidyasagar *et al.* (1985) have described the structure of $\text{LaNiO}_{2.5}$ which contains alternating layers of NiO_6 octahedra and NiO_4 square planes.

The present study is largely concerned with structures based on SrTiO_3 , and this material is also known to accept oxygen vacancies down to the composition $\text{SrTiO}_{2.5}$, where all of the titanium is trivalent. There has been no clear agreement in the literature as to how the oxygen vacancies are arranged. Both Kestigan *et al.* (1957) and M^cCarthy *et al.* (1969) reported that the structure remained cubic over the entire composition range, and that the unit cell parameter did not vary significantly.

Alario-Franco and Vallet-Regi (1977) observed a 6-fold superlattice along [111] in electron diffraction patterns taken from a sample with the nominal composition $\text{SrTiO}_{2.5}$. The corresponding high-resolution images showed similarly spaced lattice fringes, but a structural model to account for these observations was not given. Tofield (1978) highlighted the experimental difficulties in preparing reduced strontium titanates. Although a sample of nominal composition $\text{SrTiO}_{2.5}$ held in a tantalum crucible was sealed in an evacuated quartz tube before being heated in an evacuated mullite furnace tube, the final sample was found to be oxidised to $\text{SrTiO}_{2.81}$. This was thought to be due to reaction with the quartz tube, which had devitrified. No superlattice spots were detected in the electron diffraction patterns recorded from this sample.

In a more recent study of oxygen-deficient SrTiO_3 , Gong *et al.* (1991a) prepared single crystals with the composition $\text{SrTiO}_{2.72}$. Long-range order could not be found by X-ray or electron diffraction, but the symmetry had changed to tetragonal ($a=3.9177(3)\text{\AA}$, $c=3.8879(5)\text{\AA}$), and one of the two crystallographically distinct oxygen atoms was found to have a lower occupancy than the other.

The descriptions of oxygen-deficient perovskites have been included here primarily for completeness in describing stoichiometry changes in perovskite compounds. The examination of these materials did not form an objective of the present study.

1.5 Aurivillius Compounds

In a series of papers, Aurivillius (1949a, 1949b, 1950) described a new family of bismuth-containing compounds based on perovskite. Their structures can be illustrated by reference to one of these compounds, $\text{Bi}_4\text{Ti}_3\text{O}_{12}$, which is shown in Figure 1-11. There are two primary layered components. The larger of these are layers of the perovskite structure 3 octahedra high, bounded by planes parallel to $\{100\}$ perovskite planes. Division of the structure and assigning which atoms belong to the perovskite unit is somewhat arbitrary, but it is customary to portray the perovskite layers as comprising 3 TiO_6 octahedra enclosing 2 Bi atoms in the A positions, to give a charged layer composition $(\text{Bi}_2\text{Ti}_3\text{O}_{10})^{2-}$. Interleaved between the perovskite lamellae are layers with the composition $(\text{Bi}_2\text{O}_2)^{2+}$ in which Bi atoms occupy sites displaced out of the square plane formed by 4 oxygen atoms. These oxygen square planes share edges, and adjacent Bi atoms are positioned alternately above and below the oxygen plane (see Figure 1-11b).

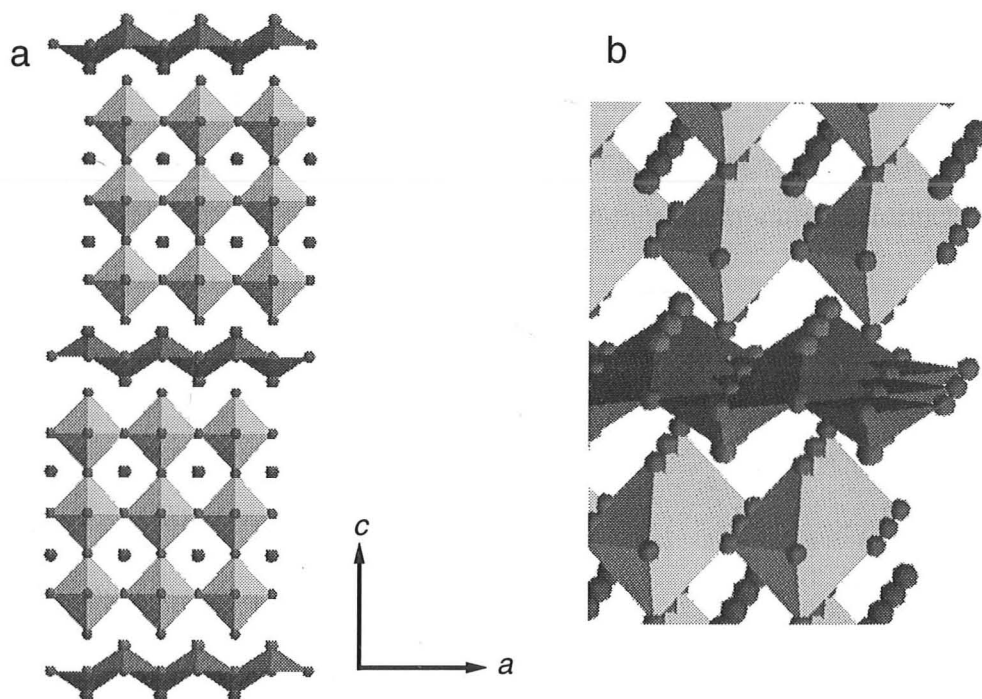


Figure 1-11 a) View along $[010]$ (pseudotetragonal cell) of $\text{Bi}_4\text{Ti}_3\text{O}_{12}$. The perovskite layers are separated by Bi_2O_2 layers, shown here in darker shading. b) Enlarged, off-axis view highlighting the Bi coordination, which is out of the plane of the square formed by the four nearest oxygen neighbours.

Aurivillius also determined the structures of compounds where the perovskite unit is 2 octahedra high (typified by $\text{CaNb}_2\text{Bi}_2\text{O}_9$; Aurivillius, 1949a) and 4 octahedra high ($\text{BaBi}_4\text{Ti}_4\text{O}_{15}$; Aurivillius, 1950), providing the basis for a series of compounds $\text{Bi}_2\text{O}_2\text{A}_{n-1}\text{B}_n\text{O}_{3n+1}$ where A and B represent combinations of cations suitable for the formation of perovskite. The value of n in this formula indicates the number of octahedra in the perovskite lamellae, and materials with n ranging from 1 to 5 have been prepared (Hutchison *et al.*, 1977). Aurivillius phases inherit much of the compositional flexibility of perovskites, and numerous combinations of elements can be accommodated; Subbarao (1962), for example, reported 19 different compounds with this structure type.

Another notable feature of Aurivillius compounds is their ability to form intergrowth structures, which comprise a regularly alternating sequence of perovskite units of two different thicknesses. Hence compounds have been prepared with perovskite layers 1 and 2 octahedra thick (Kikuchi *et al.*, 1977), 2 and 3 octahedra (Kikuchi, 1976), and 3 and 4 octahedra across (Kikuchi, 1977). Intergrowths are only found when the perovskite lamellae differ in thickness by one octahedron; the attempt by Kikuchi (1977) to synthesise alternating $n=1$ and $n=3$ layers instead resulted in a new $n=2$ material. High-resolution electron microscopy has played an important role in determining the structures and extent of ordering in these compounds (Horiuchi *et al.*, 1977; Jefferson *et al.*, 1984).

Chapter 2

Experimental Methods

- 2.1 Introduction
 - 2.2 The Rietveld Method
 - 2.3 High-Resolution Electron Microscopy
 - 2.4 Experimental Procedures
-

2.1 Introduction

During the examination of the specimens prepared in the present investigation, two principal questions frequently arose. These were : *what chemical compounds are present ?*; and *what is the structure of each of these compounds ?* By the term structure, we refer to the arrangement in space of the atoms which make up each compound. To answer these questions, two main experimental methods were used - X-ray powder diffraction (XRD), from which structural information is deduced indirectly, and high-resolution electron microscopy (HREM), which gives a direct picture of the atomic structure. In many ways these two techniques complement each other, providing structural information ranging from localised defects on the scale of a few angstrom units through to an average structure covering many hundreds of crystallites. Because of the importance of XRD and HREM to the present study this chapter begins, after some general introduction, by describing theoretical aspects of obtaining structural information by diffraction and imaging. In later sections, the experimental details pertaining to sample preparation and analysis are documented.

Identification of chemical compounds was carried out primarily by XRD. The wavelength of X-rays is of roughly the same order as interatomic spacings, and gives rise to diffraction from a crystalline specimen at a series of discrete angles to an

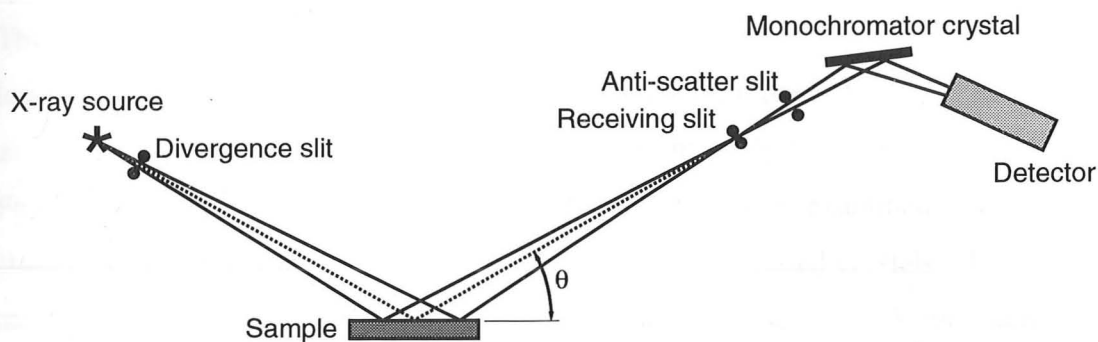


Figure 2-1 Schematic diagram indicating the basic geometry for the collection of powder diffraction patterns.

incident X-ray beam. The precise positions and intensities of the diffraction peaks are dependent on the type and arrangement of atoms within the crystal. Hence every crystalline compound produces its own unique X-ray diffraction pattern which may be identified by comparison with patterns stored in a reference database. This is a well established method for phase identification, and the database maintained by the International Centre for Diffraction Data (ICDD) now contains in excess of 59,000 patterns. The measurement of diffraction patterns was accomplished in the present study using the basic geometry outlined in Figure 2-1.

X-ray diffraction was also used in this investigation to refine the crystal structures of a number of compounds, using the Rietveld method described in Section 2.2. This was carried out for materials whose structures were previously known in outline but not in detail, and also for new compounds with as yet unreported structures. Since the sample size used for XRD was relatively large - in the order of 0.1-1g - the information obtained represents an average structure over many crystallites.

By contrast, the structural information obtained using HREM pertained to small, localised regions. The resolution of currently available electron microscopes is such that features corresponding to individual columns of metal atoms may be discerned, making this tool ideal for examining structure, and especially structural defects, on an atomic scale. However, the images observed cannot be interpreted directly as a simple atomic representation, but must be compared to simulated images before any conclusions are drawn. The methods for achieving this are outlined in Section 2.3.

The unparalleled ability of HREM to observe such small regions of structure also leads to a criticism that the images recorded may not be representative of the sample as a whole. Two methods were used in the present study to combat this problem. Firstly, a number of different crystals from each sample were examined to reduce the chances of images being recorded from contaminant or unusual crystals. The second method was to ensure that any information obtained from HREM was consistent with the bulk structural information provided by XRD. In this way, the complementary nature of the two techniques was used to build a more complete structural model than either method alone could provide.

2.2 The Rietveld Method

Although the XRD pattern of a compound may be readily calculated from its crystal structure, the reverse calculation cannot be performed as only diffracted intensities, rather than the complex amplitudes, are measured. In order to establish a compound's crystal structure, the usual method is to compare the diffraction peaks calculated from a trial structure to the observed peaks, and adjust the trial structure in a least-squares minimisation procedure until the closest agreement is obtained. Most structures determined in this way have used diffraction patterns recorded from single crystals, where the diffraction peaks may be measured individually with their geometrical relationships known. Powder patterns, however, are unsuitable for exactly the same treatment because the three-dimensional intensity data are compressed into a single dimension, and overlap of peaks frequently occurs. To overcome this difficulty, Rietveld (1969) showed that the least-squares refinement could be carried out to obtain the best agreement between observed and calculated *step intensities* in a powder diffraction pattern, eliminating the need to determine the intensities of overlapping peaks. The crystal structure is refined simultaneously with the instrumental factors and diffraction-optical effects required to calculate the entire pattern.

It should be emphasised that this is a method of structure *refinement* and its success depends on establishing a suitable trial structure to begin with. In addition, the deficiencies of most common laboratory diffraction equipment limits the precision to which structures can be refined. The major source of error is found in the function used to describe the peak shape, which may be considerably different from the observed shape, particularly at low angles. There is little point in refining the crystal structure further when the discrepancy between the observed and calculated pattern is primarily due to an irreconcilable deficiency in the instrumental parameters. Another common problem arises when refining the structural parameters of light elements, for example oxygen. The power of an atom to scatter X-rays is proportional to the number of electrons it contains, and so the intensities of diffraction peaks from a metal oxide are principally due to the heavier metal atoms. These problems are not so significant if a neutron diffractometer is used, since the peak shapes are close to a Gaussian distribution, and the scattering power varies irregularly with atomic number. However, access to neutron diffraction equipment is not always easily obtainable and many workers resort to X-radiation. Compared to single crystal refinements, powder methods suffer from peak overlap and weak reflections at high angles, thereby limiting the number of useful data measurements. Despite the drawbacks, Rietveld refinement of X-ray powder diffraction data has been successfully applied to many structures, particularly those where large enough single crystals are difficult or impossible to prepare.

2.2.1 Basis of the Refinement

The possibility of carrying out Rietveld refinement became apparent as the availability and sophistication of computers arose, enabling diffraction patterns to be stored in numerical form representing the intensities at a series of closely spaced angles across the range of the experiment. The aim of the refinement is to minimise the difference between these observed intensities (y_i) and those calculated (y_{ic}) from the crystal structure and instrumental model. The parameters defining the structure and instrument are adjusted to give the smallest difference S_y defined by the equation :

$$S_y = \sum_i w_i (y_i - y_{ic})^2 \quad (2.1)$$

where the weight (w_i) assigned to each step is normally simply $1/y_i$. Since the diffraction peaks are not sharp, single point functions but have an appreciable breadth, the intensity at any step may contain contributions from a number of nearby peaks. The success of the Rietveld method lies with the fact that these contributions are not apportioned beforehand, but calculated and updated as a key part of the refinement. The calculated step intensity is therefore a sum over a number of peaks within a specified range :

$$y_{ic} = s \sum_{hkl} L_{hkl} M_{hkl} |F_{hkl}|^2 \phi(2\theta_i - 2\theta_{hkl}) P_{hkl} A + y_{bi} \quad (2.2)$$

Normally the summation range is defined in terms of the peak width, for example 5 times the width. The terms in Equation (2.2) are :

- s a scale factor to bring the calculated values in line with the arbitrarily measured number of counts;
- hkl the Miller indices defining the position of a Bragg peak;
- L the Lorentz and polarisation factors;
- M the peak multiplicity, *i.e.* the number of permutations of h, k and l which give rise to the same peak position;
- F the structure factor defining the intensity of a peak;
- ϕ an empirical peak shape function;
- P a function to account for preferred orientation;
- A an absorption factor, usually constant for the flat specimen geometry of Figure 2-1;
- y_{bi} the background intensity at the i th step.

The peak positions are given by the term $2\theta_{hkl}$ in Equation (2.2) and are defined by the unit cell parameters and space group in standard crystallographic fashion. The intensity of each peak is derived from its structure factor, which in turn depends on the type and placement of atoms within the unit cell. These two terms contain the structural information of interest in the refinement; the remaining terms represent the instrumental factors and diffraction effects.

The background is usually modelled as a simple polynomial function of 2θ containing terms up to $2\theta^5$. The Lorentz-polarisation factor describes geometric effects on the diffracted intensity. The first of these, the Lorentz factor, takes into consideration the opportunity of each diffracted beam to contribute to the measured intensity at a given 2θ value, and varies according to the instrumental conditions. For powder patterns of the type considered here, diffraction from each crystallite in the sample has a conical shape whose radius depends on the Bragg angle θ . At high angles the diffracted rays are spread around a large cone and comparatively few are intercepted by the detection system. The second effect, that of polarisation, is due to the electromagnetic character of X-rays which introduces an orientation dependence to their interaction with the sample. As a result, the scattered amplitude is proportional to the sine of the angle between the electric vector of the incident radiation and the scattering direction. For instruments with a monochromator, the polarisation of diffraction at the monochromator crystal also needs to be considered. These two factors combined lead to an expression for the Lorentz-polarisation factor :

$$L_{hkl} = \frac{1}{4 \cos \theta_{hkl} \sin^2 \theta_{hkl}} \cdot \frac{1 + \cos^2 2\alpha \cos^2 2\theta_{hkl}}{1 + \cos^2 2\alpha} \quad (2.3)$$

where α is the diffraction angle for the monochromator crystal.

The area of the refinement which usually introduces the largest errors is the function used to describe the peak shape. Although relatively simple analytical functions are used in Rietveld refinements, the observed diffraction profile is the combined result of a number of a number of different influences, including :

- (i) *The wavelength profile of the x-ray source.* This is approximately Lorentzian but not completely symmetric.
- (ii) *The use of a flat specimen.* Most XRD patterns are recorded from a flat bed of powder so that X-rays diffracted away from the centre of the specimen surface are not focused precisely to the detection system.
- (iii) *Divergence of the incident beam.* Like (ii) above, this introduces an asymmetry into the diffraction profile which is most notable at low angles when the irradiated length of the specimen is largest.

- (iv) *Specimen transparency.* The penetration depth of x-rays into the sample can be substantial, again producing diffraction from areas away from the ideal focus.
- (v) *Particle size/strain.* Decreasing the crystallite size below approximately $1\mu\text{m}$ or introducing strain both result in a broadening of the diffraction profile.

The complex origin of the peak shape means that it cannot be described perfectly by a simple mathematical function and, in addition, the nature of the shape changes somewhat with the diffraction angle. The function used cannot be made too complex, however, because the least-squares refinement requires all the derivatives of the variables used to be calculated. For X-rays, one of the best functions which provides a good approximation to the observed profile is the pseudo-Voigt function, defined as a mixture of Lorentzian and Gaussian curves :

$$\phi_{pV}(2\theta_i - 2\theta_{hkl}) = \eta L(2\theta_i - 2\theta_{hkl}) + (1-\eta)G(2\theta_i - 2\theta_{hkl}) \quad (2.4)$$

In this expression L and G refer to the Lorentzian and Gaussian lineshapes respectively, and the mixing parameter η may be allowed to vary across the 2θ range by refining the parameters NA and NB in the equation :

$$\eta = NA + NB(2\theta) \quad (2.5)$$

The Lorentzian and Gaussian are well established functions :

$$L(2\theta_i - 2\theta_{hkl}) = \frac{2}{\pi\Gamma} \left[1 + \frac{4(2\theta_i - 2\theta_{hkl})^2}{\Gamma^2} \right]^{-1} \quad (2.6)$$

$$G(2\theta_i - 2\theta_{hkl}) = \frac{1}{\Gamma} \sqrt{\frac{4 \ln 2}{\pi}} \exp \left[\frac{-4 \ln 2 (2\theta_i - 2\theta_{hkl})^2}{\Gamma^2} \right] \quad (2.7)$$

with a width at half maximum height defined by the parameter Γ . Because this width varies over the 2θ range, it too is defined by further refineable parameters, normally U , V , and W in the expression :

$$\Gamma^2 = U \tan^2 \theta + V \tan \theta + W \quad (2.8)$$

Finally, asymmetry in the profile must be taken into account. In Rietveld's original work and many subsequent programmes, this is achieved by multiplying the profile function by an asymmetry function A_s whose value depends on a refined asymmetry parameter A_p :

$$A_s(2\theta_i - 2\theta_{hkl}) = [1 - A_p(2\theta_i - 2\theta_{hkl})^2 \cdot s / \tan\theta_{hkl}] \quad (2.9)$$

where s takes the values +1, 0 or -1 according to whether $(2\theta_i - 2\theta_{hkl})$ is positive, zero or negative respectively.

The agreement between experimentally observed profiles and those calculated using the pseudo-Voigt function is good at high angles, but can be noticeably poorer at low angles. This is demonstrated in Figure 2-2 where two regions from a refinement of standard silicon powder are shown. The mismatch at the lower angle results in a characteristic deviation in the difference plot which rises above zero on the low 2θ side of the peak, then oscillates about zero as the peak is traversed. When the structural parameters have been refined to their correct values, the areas above and below zero in the difference curve should cancel, and the only effect is a poorer value for the agreement index between observed and calculated patterns (defined in the next section). This type of behaviour was observed in all of the Rietveld refinements

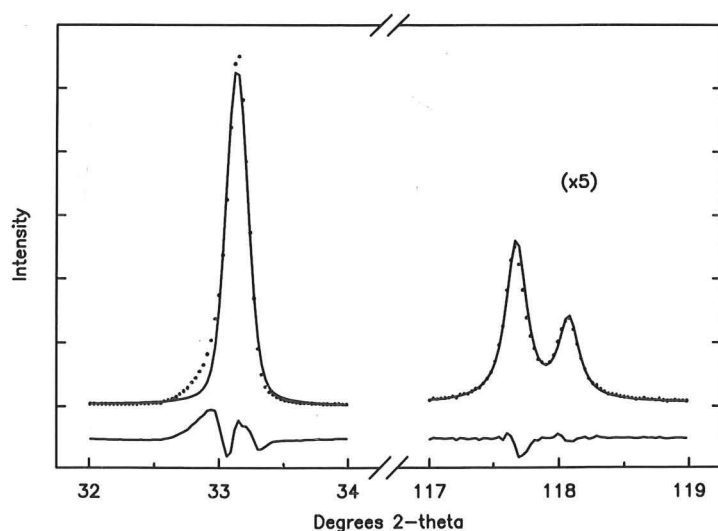


Figure 2-2

Selected regions from a Rietveld refinement of silicon powder ($\text{Co } K_\alpha$ radiation). Observed points are shown as dots, the calculated profile as a solid line, and the difference between the two beneath. Intensities for the high angle peak have been multiplied by a factor of five.

carried out in this study. The shape of the high angle peak, on the other hand, is described well by the psuedo-Voigt function.

2.2.2 Criteria of Fit

The refinement proceeds via a series of iterations, and is usually considered complete when the fractional change in each parameter is less than some prescribed amount, say 0.1%. At this stage it is important to assess how successful the refinement has been. Of course, a principal requirement is that the refined structure is chemically sensible, but there are also numerical techniques to evaluate how well the model matches the experiment. The methods used are based on those devised for single-crystal studies which calculate a number, called the R factor, which relates to the difference between calculated and observed quantities. The standard crystallographic agreement index is the Bragg R factor, defined as :

$$R_B = \frac{\sum_{hkl} |I_{hkl}(\text{obs}) - I_{hkl}(\text{calc})|}{\sum_{hkl} I_{hkl}(\text{obs})} \quad (2.10)$$

where I_{hkl} refers to the intensity of individual diffraction peaks. In the case of Rietveld data, the observed intensities ($I_{hkl}(\text{obs})$) may not be measured directly due to peak overlap and must instead be estimated by the computer programme based on the intensity ratio of calculated peaks. Nevertheless, this is a useful agreement index because it depends primarily on the structural model and is insensitive to misfits in, for example, the peak shape. Bragg R values are also helpful because they are most comparable to the R factors quoted in the literature for single-crystal studies.

The fit across the entire pattern is reflected in the weighted pattern R factor :

$$R_{wp} = \sqrt{\frac{\sum_i w_i (y_i - y_{ic})^2}{\sum_i w_i y_i^2}} \quad (2.11)$$

which is also commonly used to monitor the progress of the refinement since it contains in the numerator the quantity being minimised (see Equation (2.1)). From a statistical standpoint, the expected value for this factor may be calculated using the number of points (N) collected in the diffraction pattern and the total number of parameters (P) being refined :

$$R_{exp} = \sqrt{\frac{N - P}{\sum_i w_i y_i}} \quad (2.12)$$

This leads to a 'goodness of fit' indicator, S , which is simply the ratio of measured and expected R factors :

$$S = \frac{R_{wp}}{R_{exp}} \quad (2.13)$$

Ideally, S should be close to unity, say less than ≈ 1.5 . However, if the pattern has a number of intense poorly fitted peak profiles at low angles, then a considerably higher goodness of fit value may be obtained from an otherwise quite acceptable refinement. For this reason, an appraisal of the fit by examination of plots of the observed and calculated patterns is imperative. These should include a difference plot in which deficiencies due to poor peak shape, extra phases, or the structural model itself can be readily recognised. Often the fit can be improved by refining further parameters which do not significantly increase the understanding of the structural model. This practice is to be avoided - the best fit should be obtained using the minimum sensible number of refineable parameters.

2.2.3 Data Collection

When collecting a pattern for Rietveld analysis, it is initially tempting to record an extremely well-defined pattern by counting for long times at very narrow step widths. However, it is worth remembering that the purpose of the step data is to provide a means of estimating the intensities of the diffraction peaks, and collecting a pattern over a longer time is only worthwhile if it improves the precision of these estimates. This will only occur while the precision of counting makes a significant contribution to the overall errors of the model.

The primary factors to consider when designing the experiment are the angular range, the step size, and the counting time for each step. The range should be as wide as is necessary to encompass the maximum number of observable peaks. Attfield *et al.* (1988) have suggested that for structure solution there should be at least 10 times as many observable peaks as there are crystallographically distinct atoms in the unit cell. A similar claim can be made for structure refinement. To assist in making a sensible choice of step size and counting time, Hill and Madsen (1984, 1986, 1987) have carried out a series of studies to determine the effect of data collection conditions on the accuracy and precision of the refined model. The results of this work are summarised below.

The best choice of data collection conditions is, as might be expected, a trade-off between conflicting effects. At short counting times, the poor counting statistics lead to large values for R_B , indicating a deficiency in the refined structure. In addition, the estimated standard deviations (e.s.d.'s) of the refined parameters are large and therefore the refined model is relatively imprecise. Both R_B and the e.s.d.'s decrease as the counting time is increased, but at large counting times the goodness of fit statistic increases, suggesting that the instrumental model is no longer adequate. Under these conditions, the e.s.d.'s are not a true representation of the precision of the refined parameters and the additional time used to collect the data is of little benefit.

A similar situation is found for the variation of step size. If a relatively long counting time is used (say 5s per step) then, as the step size is reduced, R_B initially decreases but remains constant for step widths below about half the minimum peak width. No improvement in the structural model is therefore obtained by using narrow step widths, despite the further reduction in the e.s.d.'s of the refined parameters which occurs. By comparing the e.s.d.'s to true estimates of precision from replicate experiments, Hill and Madsen have shown that, as might be expected, the least-squares refinement offers reasonable e.s.d.'s only when counting statistics are the dominant source of error.

As a result of this work, the recommendations for data collection were that the step size should be between 1/5 to 1/3 the minimum peak width (at half maximum height) observed in the pattern, and that the counting time should give intensities for the largest peaks between 5000 and 10000 counts.

2.3 High-Resolution Electron Microscopy

The ultimate resolving power of a microscope with near-perfect lenses is determined by the effects of diffraction, which leads to a limit for the smallest details which can be observed as approximately the same dimension as the wavelength of radiation used. This explains why visible light, with a wavelength of several hundred nanometers, cannot be used for high-resolution microscopy where we wish to observe features on an atomic scale. X-rays have a suitable wavelength, but cannot be focused to form an image because no appropriate lens materials are known. It is therefore necessary to employ electrons which, being charged particles, may be focused with a magnetic field and can be accelerated to suitable wavelengths in an electric field.

The images produced by high-resolution electron microscopes are often termed 'structure images' because of the strong correlation between features in the image and the arrangement of atoms, primarily metal atoms, within the sample. However, it can be misleading to infer the crystal structure directly from the HREM image, and the only sure way to ascertain structure is to compare the experimental image with one simulated from a proposed structure. Unlike Rietveld refinement, the proposed structure cannot be revised numerically to provide the best match because there is no tractable analytical relationship between structure and image. Instead, images must be simulated from a succession of trial structures until satisfactory agreement is obtained.

The electron path through a transmission electron microscope is often drawn in the form of a schematic ray diagram similar to that shown in Figure 2-3. Such a diagram simplifies the action of electron lenses, which cause electrons to travel in a complex

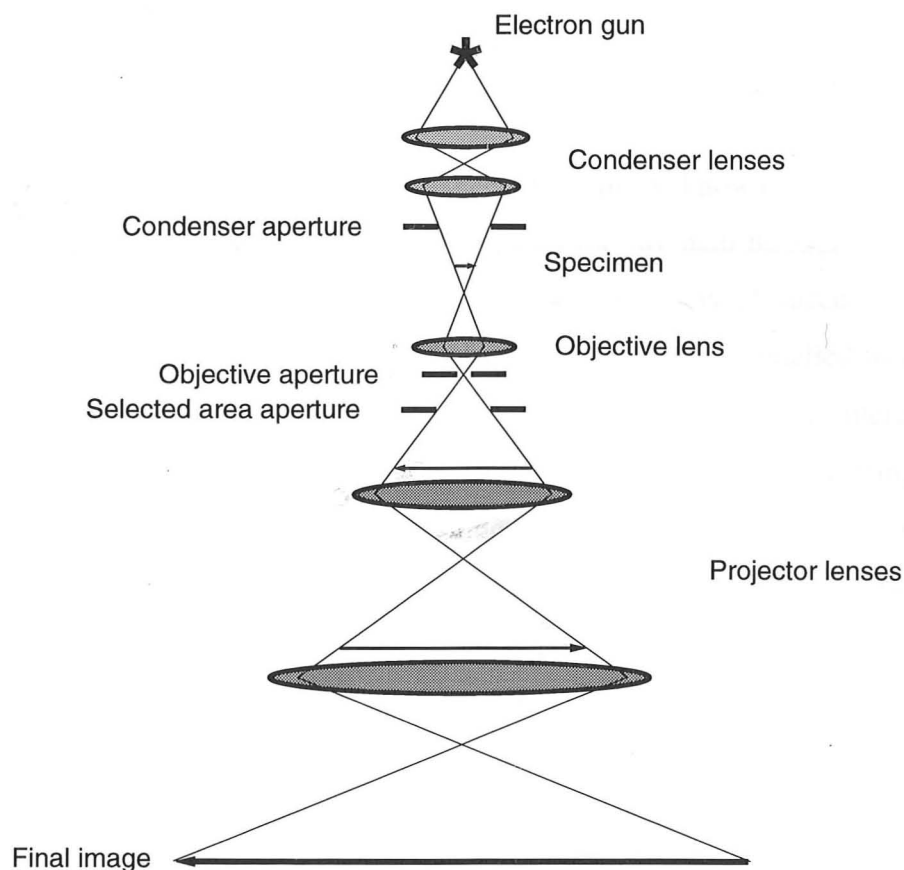


Figure 2-3 Schematic ray diagram of a transmission electron microscope.

spiral path rather than remaining in a given path containing the optical axis as the figure suggests. Nevertheless, since the electron path does not deviate greatly from the optical axis (known as a paraxial path) the only significant effect is a uniform rotation of the image, which for convenience may be ignored.

Electrons are emitted from a heated filament and accelerated in an electric field toward the specimen. Between the filament and the specimen a system of condenser lenses allows the beam to be focused onto the specimen for maximum brightness, or defocused to provide a broader field of view for use at lower magnifications. An intermediate image of the electron wavefunction emerging from the specimen is produced by the objective lens. This image is further magnified by a series of projector lenses to give a final image which may be recorded on photographic film or observed on a fluorescent screen. Controls on the microscope allow the imaging lens

currents to be adjusted so the electron diffraction pattern is brought to focus rather than the image itself.

Successful simulation of the image expected from a known sample involves calculating the electron wavefunction as it follows the ray path through the electron microscope. This procedure may be broken down into several successive stages. Firstly, the interaction of the sample with the electron beam is modelled to calculate the wavefunction at the exit surface, $\psi_e(xy)$. Because of the strong interaction of electrons with matter, due consideration must be taken of multiple scattering effects where the electrons scattered in one part of the sample may undergo further scattering in subsequent regions. Except in particularly favourable circumstances, the calculation of $\psi_e(xy)$ invariably involves some approximations - the method described here and in widespread use is the multi-slice method.

The second stage is to calculate the image of the exit wavefunction produced by the magnifying lens system. Electron lenses have inherent aberrations which are much worse than their optical counterparts, and the influence of these aberrations forms the basis of this part of the calculation. Lens aberrations increase markedly as the angle between the electron beam and optical axis increases but, since this angle is much greater for the objective lens than for subsequent lenses, only this lens need be considered. The final factors to be taken into account are instabilities in the lens current and the divergence of the incident beam. These factors are considered last because their effect is to produce an image averaged over a range of focus settings and beam angles.

A more detailed description of these stages of image simulation is given in the following sections. Several good texts are available on this subject, and much of what is discussed here is drawn from material in the books by Spence (1988) and by Buseck *et al.* (1988). Although the emphasis in the following sections is firmly placed on image simulation, the discussion is also relevant to understanding the physical processes occurring in the microscope which lead to the experimentally observed image.

2.3.1 Electron-Specimen Interactions

The electrons which impinge upon the sample may undergo both elastic and inelastic scattering, giving rise to various ways in which the contrast in electron microscope images may be observed. Contrast may arise from the variation of electron absorption across the sample as electrons are either completely absorbed or scattered outside the microscope aperture. This mechanism is responsible for images at low magnification and arises from an inelastic scattering process. Contrast in high-resolution images may be considered to arise from the interference of elastically scattered electrons whose phases have been modified by the atoms in the specimen. Because of the strong interaction of electrons with matter and the resultant multiple-scattering effects, calculating these phase changes is only successful for very thin specimens, of the order of less than 10\AA , depending on the atomic weight of the constituent atoms and the accelerating voltage of the microscope.

2.3.1.1 The Phase Object Approximation

As a first approximation, we can consider that an electron wave traversing a thin specimen experiences no sideways displacement, but undergoes only a phase change proportional to the total electrostatic potential it encounters within the crystal. Because we are only considering phase changes, this treatment is known as the phase object approximation. If we define a Cartesian coordinate system with the z direction parallel to the electron beam, then the phase change is proportional to the potential (represented by the function $\phi(xyz)$) projected in the z direction :

$$\phi(xy) = \int \phi(xyz) dz \quad (2.14)$$

The effect on the electron wave is to multiply the incident wavefunction by a transmission function $q(xy)$ related to this projected potential by the expression :

$$q(xy) = \exp[-i\sigma\phi(xy)] \quad (2.15)$$

where the interaction constant σ , which describes the strength of the electron interaction with matter, is given by :

$$\sigma = \frac{\pi}{\lambda E} = \frac{2\pi m e \lambda}{h^2} \quad (2.16)$$

Because of the large energies involved, it is important to use relativistically corrected values for the electron wavelength and mass in Equation (2.16).

Hence the only sample-dependent variable which modifies the electron wavefunction of a phase object is the projected potential, and this is related in an intuitive way to the arrangement of atoms within the sample. Mathematically, $\phi(xy)$ is obtained from a knowledge of the electron scattering factors of the atoms which comprise the sample, as well as their positions within a crystallographic unit cell.

A further simplification can be made if the phase changes are small, that is if $\sigma\phi(xy) \ll 1$. Since an arbitrary constant potential may be added which affects only the reference to which phases are measured, this condition need not apply to absolute values of potential but only to the range of potential across the specimen. In this case the transmission function can be approximated as :

$$q(xy) = 1 - i\sigma\phi(xy) \quad (2.17)$$

and is known as the kinematic or weak phase object approximation. Although it is rarely used in practice to calculate $q(xy)$ it is helpful in understanding aspects of the imaging process to be discussed later.

2.3.1.2 The Multi-Slice Method

The phase object approximation is unlikely to apply rigorously to many instances of specimens encountered in practice, and so if real experimental images are to be simulated then some consideration of multiple scattering as well as sideways displacement of the beam must be taken. One approach which has found widespread use is the multi-slice method devised by Cowley and Moodie (1957), which divides

the sample into a succession of thin slices. Within each slice, phase changes due to specimen potential are calculated as for phase objects, while the spreading of the electron wave is understood to occur by Fresnel diffraction. Although these two processes occur simultaneously, the multi-slice formulation positions all the specimen potential of successive slices onto a series of planes between which Fresnel diffraction takes place. As the slice thickness decreases, the error introduced by separating these two processes diminishes and for practical purposes becomes negligible in most cases for slices less than a few angstroms thick. Again, the validity of this approximation depends on the specimen and the atomic weight of the atoms it contains. The electron wavefunction calculated after each slice is used as the incident wavefunction for the following slice so that the wave function after n slices (Ψ_n) can be written as :

$$\Psi_n(xy) = [\Psi_{n-1}(xy) * p_{n-1}(xy)] \cdot q_n(xy) \quad (2.18)$$

where $q_n(xy)$ is the transmission function of the n th slice and the $*$ symbol indicates a convolution integral. $p_{n-1}(xy)$ is the propagation function describing the effects of Fresnel diffraction over the slice thickness Δz :

$$p(xy) = \exp[-\pi i(x^2 + y^2)/\Delta z \cdot \lambda] \quad (2.19)$$

Since this is an iterative method, it is ideally suited to numerical calculation by computer. An increase in computational efficiency can be obtained by carrying out the calculation in reciprocal space and using Fourier transforms of the functions. Following the recommended nomenclature of Buseck *et al.* (1988), we use lower case letters and xy coordinates for real space functions, and upper case letters and uv coordinates for their reciprocal space counterparts. Equation (2.18) can then be written in the form :

$$\Psi_n(uv) = F\{F^{-1}[\Psi_{n-1}(uv)P_{n-1}(uv)]F^{-1}[Q_n(uv)]\} \quad (2.20)$$

where the symbols F and F^{-1} denote the forward and inverse Fourier transforms respectively. This equation avoids the use of the convolution integral, taking advantage of the property of Fourier transforms which dictates that the convolution of two functions A and B is given by :

$$A * B = F[F^{-1}(A)F^{-1}(B)] \quad (2.21)$$

The reciprocal space wavefunction $\Psi(uv)$ is the Fourier transform of its real space counterpart $\Psi(xy)$ and corresponds to the electron diffraction pattern. This explains why it is more convenient for periodic specimens to carry out the calculations in reciprocal space. For such materials, diffraction occurs only to the reciprocal lattice points and the transmission function exists only at these discrete points. In addition, the iteration in this form leads directly to the calculated electron diffraction pattern. The drawback, of course, is the need to perform a number of Fourier transform operations. However, the calculation becomes much quicker than the direct iteration (Equation (2.18)) if the fast Fourier transform algorithm devised by Cooley and Tukey (1965) is used.

2.3.2 Lens Aberrations and the Transfer Function

The aberrations of the objective lens play an important role in high-resolution electron microscopy. Since the image intensity is the squared modulus of the image wavefunction and the specimen introduces primarily phase changes, a perfectly focused image in thin samples, *e.g.* a weak phase object, would exhibit little contrast. Much of the contrast seen in high-resolution images is brought about by multiple scattering and the imperfect action of the objective lens, so clearly any successful simulation must incorporate these aberrations. Since we are dealing with paraxial rays, only the simplest aberrations need be considered : astigmatism, chromatic aberration, defocus, and spherical aberration.

Although an expression for astigmatism can be derived, the degree and orientation of astigmatism is difficult to ascertain in practice, and so it is best if images are recorded without this defect present. Fortunately, objective lens astigmatism can be countered in most cases by careful adjustment of correcting coils installed in the microscope. We will defer discussion of chromatic aberration until the next section, since this is best treated after an account of defocus and spherical aberration.

The effects of these defects are accounted for by multiplying the wavefunction at the back focal plane by a function known as the lens transfer function $T(uv)$. Since the objective aperture is located in this plane, restricting the image-forming beams within a defined area of reciprocal space, the transfer function also includes an appropriate aperture function. When the lens is not adjusted to the ideal focus, rays emanating from a point in the sample converge to a point outside the image plane, introducing a phase change $\chi(uv)$ which is proportional to the defocus (Δf) and second order in u and v . Spherical aberration is a defect where the focal length of a lens varies as the ray path moves away from the optical axis, and produces a similar effect to defocus but with an additional dependence on u and v . These two aberrations are usually treated together to give an overall phase shift given by :

$$\chi(uv) = \pi\lambda\Delta f(u^2 + v^2) + \frac{1}{2}\pi C_s \lambda^3 (u^2 + v^2)^2 \quad (2.22)$$

where C_s is the spherical aberration coefficient. The lens transfer function is then :

$$T(uv) = A(uv) \exp[i\chi(uv)] \quad (2.23)$$

where the discontinuous aperture function $A(uv)$ is simply :

$$A(uv) = \begin{cases} 1, & \text{if } (u^2 + v^2)^{1/2} < \text{aperture radius} \\ 0, & \text{otherwise} \end{cases} \quad (2.24)$$

We now have sufficient information to compute the electron diffraction pattern and finally the simulated image itself for images free of astigmatism and chromatic aberration. The exit wavefunction calculated from the final multi-slice iteration (Ψ_e) gives the wavefunction for the diffraction pattern when multiplied by the transfer function :

$$\Psi_d(uv) = \Psi_e(uv) \cdot T(uv) \quad (2.25)$$

The observed image intensity is the squared modulus of the image wavefunction Ψ_i , which in turn is derived from the diffraction plane wavefunction by Fourier transform :

$$I(xy) = |\Psi_i(xy)|^2 = \left| \mathbb{F}[\Psi_d(uv)] \right|^2 \quad (2.26)$$

For weak phase objects, the relationship between image intensity and specimen detail becomes relatively simple and provides a means of understanding the behaviour of the lens transfer function. Under these conditions, an approximation for the image intensity in reciprocal space can be derived as :

$$I(uv) = \delta(uv) + 2\sigma\Phi(uv)A(uv) \sin[\chi(uv)] \quad (2.27)$$

where $\delta(uv)$ is the Dirac delta function describing the transmitted beam whose phase is unchanged by the transfer function. Second order terms in $\sigma\Phi$ have been neglected and since only the imaginary part of the phase factor $\exp[i\chi(uv)]$ is involved in producing image intensity, the transfer function contains only the sine term. Equation (2.27) shows that, for weak phase objects, the image intensity corresponds directly to the projected specimen potential multiplied by the imaginary part of the objective lens transfer function.

The form of this transfer function is shown in Figure 2-4 for the microscope used in the present study at several defocus settings, depicted in a one-dimensional form as $\sin\chi(U)$ where $U=(u^2+v^2)^{1/2}$. The curves begin with a gradual decrease in $\sin\chi(U)$,

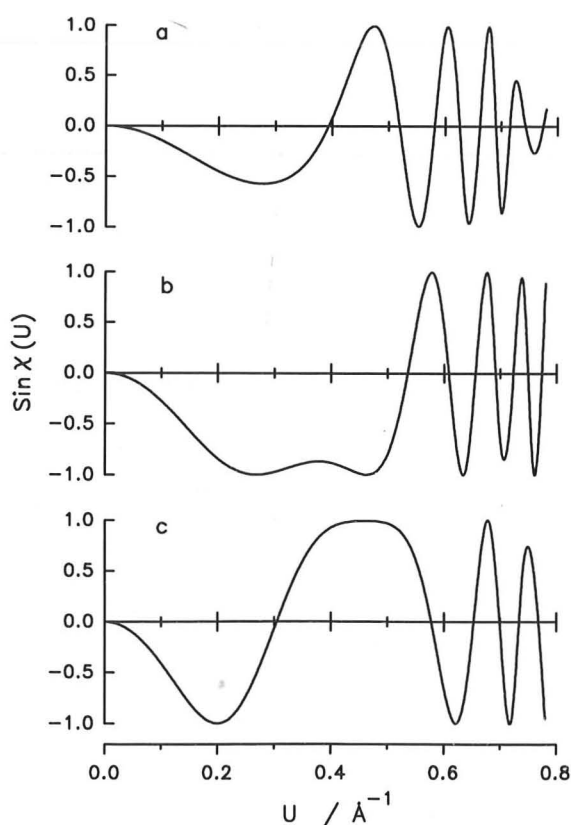


Figure 2-4

Imaginary component of the transfer function at defocus values of a) -200\AA ; b) -370\AA ; and c) -550\AA .

followed by a region where $\sin\chi(U)$ remains roughly constant before a region of rapid fluctuations. Hence for large periodicities (small U) little or no information is transferred to the image, while for small spacings the information is confused and uninterpretable. The useful specimen detail is transferred in the central portion of this function where $|\sin\chi(U)|$ is close to unity.

Clearly, the best imaging conditions are obtained when this portion is as large as possible so that the maximum number of diffracted beams contribute to the image with little change to their phase or amplitude. The defocus setting which provides this was first determined by Scherzer (1949) as the value of Δf which gives a minimum value for $\chi(U)$ of $-2/3\pi$ before increasing again. Then $d\chi/dU = 0$ and from (2.22) the optimum defocus, called the Scherzer focus, is :

$$\Delta f = -\left(\frac{4}{3} C_s \lambda\right)^{1/2} \quad (2.28)$$

Curve b in Figure 2-4 shows the imaginary component of the transfer function of the microscope used here at the Scherzer focus.

2.3.3 Chromatic Aberration and Beam Divergence

Chromatic aberrations arise from three main sources of instability in an electron microscope. The wavelength of electrons illuminating the sample is affected by variations in both the filament and the accelerating voltages, and the focal length of the objective lens changes as the current supplied to its coils fluctuates. All three instabilities lead to a corresponding variation in focus of the image and may be treated together. Since the time scale of these fluctuations is considerably shorter than the exposure time used to record HREM images, the simulated image corrected for focal spread may be calculated by averaging a series of images over a range of defocus values distributed about the mean, weighting each image according to its expected contribution. Normally, the distribution of focus can be represented as a Gaussian function.

A similar averaging technique can also be applied to account for beam divergence, which arises because the illuminating beam is usually focused onto the specimen to provide sufficient brightness at high magnification. In this case, the series of images to be calculated must cover the varying angles of incident radiation, each of which will give rise to a different wavefunction at the exit surface of the specimen. Hence, unlike focal spread, an exact integration over beam divergence requires a separate multi-slice calculation for each contributing image. A rigorous simulation incorporating both focal spread and beam divergence therefore requires a double integration involving an extremely large number of intermediate image calculations.

For most applications, an approximation is made to avoid this time-consuming calculation which gives a similar result to numerical averaging. The approximation works by modifying the objective lens transfer function and requires only one image to be computed. The following explanation is given for the simplest case, imaging of a weak phase object.

The basis of the approximation is to apply the integral to the transfer function rather than to a series of images. Figure 2-5 shows how a variation in defocus affects the transfer function by superimposing curves for two defocus values separated by approximately the amount resulting from lens instability. At low values of U the two curves coincide, but in the oscillating high U region the negative and positive values

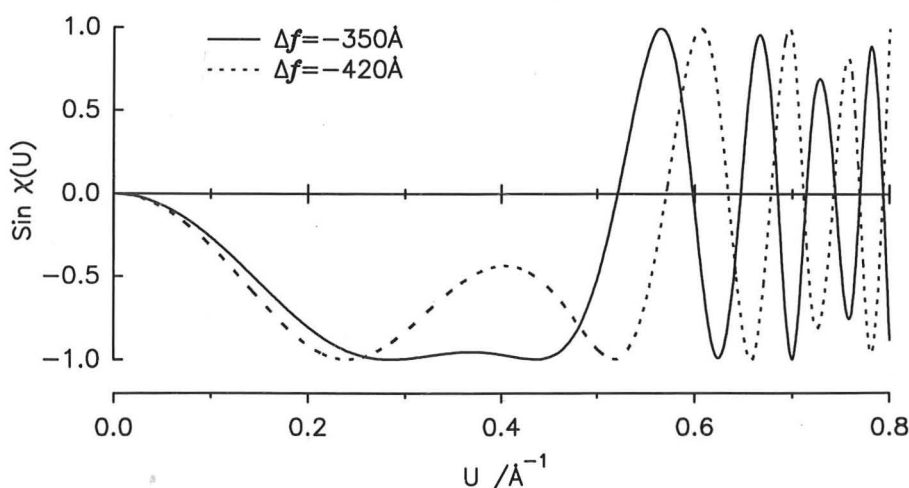


Figure 2-5 Variation in the transfer function due to a change in defocus of the magnitude expected from chromatic instabilities.

cancel and the average value tends toward zero. The effect is to multiply the transfer function by a so-called envelope function which is close to unity for low values of U , but drops to zero at higher values. If a Gaussian distribution of focal values has a spread D , then the envelope function for focal spread is :

$$C(uv) = \exp(-\frac{1}{2}\pi^2 \lambda^2 D^2 (u^2 + v^2)^2) \quad (2.29)$$

Similar arguments apply to the treatment of beam divergence, although in this case the averaging can be thought of as between transfer functions with slightly displaced origins. The envelope function which results is :

$$E(uv) = \frac{2J_1[2\pi\alpha(\Delta f(u^2 + v^2)^{1/2} + C_s \lambda^2 (u^2 + v^2)^{3/2})]}{2\pi\alpha(\Delta f(u^2 + v^2)^{1/2} + C_s \lambda^2 (u^2 + v^2)^{3/2})} \quad (2.30)$$

where the degree of divergence is given by the semi-angle α and J_1 is the first-order Bessel function. The transfer function incorporating all of these effects is :

$$T(uv) = A(uv)C(uv)E(uv)\exp[-i\chi(uv)] \quad (2.31)$$

Figure 2-6 shows the damping envelopes appropriate to the microscope used in the present study, and the transfer function which results at the Scherzer focus. It may be compared to the corresponding undamped function shown in Figure 2-4, curve b.

The description of imaging in terms of weak phase objects and damped transfer

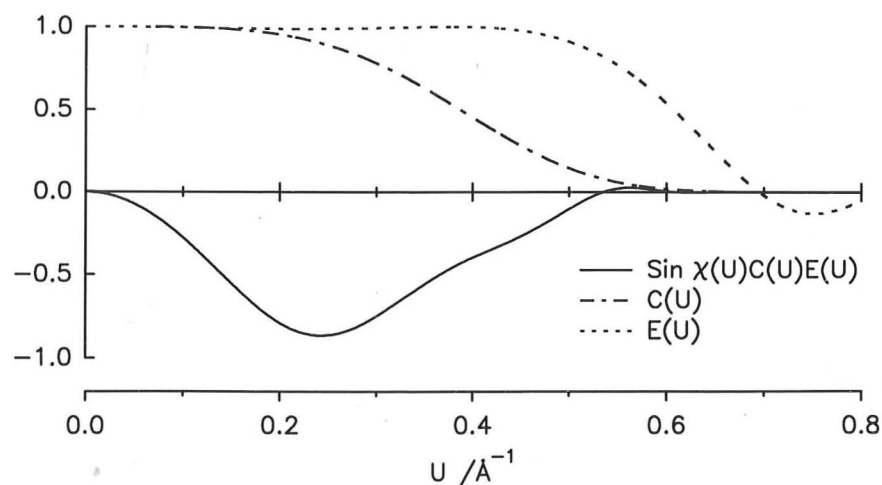


Figure 2-6 Transfer function incorporating damping due to focal spread (100Å) and beam divergence (1 mrad) at a defocus setting of -370Å.

functions is appealing because it provides a simple relationship between the specimen structure and the final image, with the additional advantage of portraying the effect of the objective lens in a graphical manner. However, it must be remembered that such a treatment is an *approximation* of the actual processes occurring in the microscope, and the extent to which a simulated image matches the experimental one depends on how satisfactory the approximation is.

The envelope functions given above in Equations (2.29) and (2.30) apply to weak phase objects because they describe linear imaging, where most of the intensity is carried by the zeroth order diffraction beams. Similar functions can also be derived for the non-linear case, where higher order beams also contribute to the image. In non-linear imaging, the image intensity at a position in reciprocal space (u, v) is not just a function of the image wavefunction $\Psi_i(u, v)$, but a sum over all the relevant reciprocal lattice points $(u+u', v+v')$ and (u', v') . Buseck *et al.* (1988) have described envelope functions for beam divergence and chromatic aberration using non-linear theory and a second order Taylor-series expansion for $\chi(uv)$.

The use of envelope functions involves two principle approximations. The first is a mathematical one: that changes in $\chi(uv)$ can be represented by a first or second order Taylor-series. Experience has shown this to be valid in most cases, particularly since the first order expansion gives an exact solution for the effects of chromatic aberration when there is no beam divergence. The use of the Taylor-series therefore only breaks down for large beam divergences. The other main approximation is that the wavefunction emerging from the specimen is assumed to be uninfluenced by the chromatic effects or beam divergence. In the case of chromatic effects, this is generally true since the wavelength of the incident radiation varies by only a few parts per million in modern high-resolution instruments. The influence of beam divergence on the exit wavefunction is less clear and more strongly specimen-dependent. If it is suspected that the approximation is not valid, then comparing simulated images for a crystal tilted by the angle of beam divergence with an untilted simulation should verify whether the envelope approximation is useful.

One special case where the use of envelope functions should be avoided is when the beam is aligned with a zone axis in which some diffracted beams are systematically absent, even with multiple scattering, but which appear when the beam is slightly off-axis. Under such conditions, the simulated image corrected for beam divergence must be obtained from numerical averaging of a number of images calculated over a range of beam tilts.

2.4 Experimental Procedures

2.4.1 Sample Preparation

The raw materials used for synthesis are listed in Table 2-1. Because of the strong tendency of La_2O_3 to form hydroxides when exposed to moist air, this material was weighed immediately after drying at 800°C . For many experiments, La was sourced from a stock of La_2TiO_5 prepared by reacting freshly dried La_2O_3 with TiO_2 overnight at 1100°C .

Compound	Purity	Supplier
SrCO_3	99%	BDH Chemicals Ltd.
TiO_2	99.9+%	Aldrich Chemical Co.
La_2O_3	99.9%	Ventron GMBH
CaCO_3	99.5%	BDH Chemicals Ltd.
CuO	99.9%	Johnson Matthey

Table 2-1 Origin of starting materials

For most preparations, appropriate quantities of the starting materials were weighed out to give a total sample weight of approximately 200mg and thoroughly dry-mixed in an agate mortar and pestle. They were then heated overnight at temperatures between 800 and 1450°C in an electric muffle furnace, which was allowed to cool to below 500°C before samples were removed. Preparations which did not contain La_2O_3 were weighed before and after reaction to monitor the loss of any volatile species.

Variations to this regime included longer heating times for some samples, and larger sample sizes for those specimens destined for Rietveld analysis. These changes are noted where appropriate in the text. Often several overnight heatings of the same sample were carried out until no further changes in the XRD pattern could be observed.

2.4.2 X-ray Diffraction

Two XRD instruments were used in the course of this investigation. Most patterns were collected on the Philips system in the Department of Chemistry, University of Cambridge. This instrument comprised a PW1050 vertical goniometer without a monochromator, controlled by the Philips PC-APD software. A Cu X-ray tube ($K_{\alpha 1}$ wavelength = 1.54056\AA) was operated at 40kV and 40mA. Patterns for Rietveld analysis of $\text{Sr}_{n+1}\text{Ti}_n\text{O}_{3n+1}$ and $\text{Sr}_{n-3}\text{La}_4\text{Ti}_n\text{O}_{3n+3}$ compounds were recorded using the facility at the Ceramics Group of the New Zealand Institute for Industrial Research and Development. This was a similar system, but included a post-diffraction monochromator and employed Co radiation ($K_{\alpha 1}$ wavelength = 1.78896\AA).

Routine survey scans to establish phase composition were collected between 15 and $80^\circ 2\theta$, counting for 1.5s at step intervals of 0.05° . Samples were front-loaded into shallow, glass-backed holders and pressed flat with a glass slide. Greater care to minimise preferred orientation was taken when loading samples for Rietveld analysis. The larger sample size used meant that samples could be back-loaded into deeper aluminium holders. Bearing in mind the recommendations of Hill and Madsen (1987, see Section 2.2.3), a step size of $0.04^\circ 2\theta$ and counting time of 5s were used.

The determination of unit cell parameters was carried out, except when part of Rietveld refinement, using the least-squares programme CELLREF (D.A. James, University of Oxford). The programme required as input a list of 2θ positions and h, k and l indices, and included a refineable zero offset to accommodate instrumental

misalignment. The 2θ positions were determined from X-ray diffraction patterns either visually using plots of expanded regions or, for structures with comparatively few peaks, by fitting peak profiles to individual reflections. Both of these were accomplished using the Philips PC-APD software.

Two programmes were used for carrying out Rietveld refinements. The first, used only for the refinement of $\text{Sr}_3\text{La}_2\text{Ti}_2\text{O}_{10}$, was that included with the GSAS programme suite (Larson and Von Dreele, 1987). The other programme (DBWS9006) was derived from that described by Wiles and Young (1981), incorporated into the CERius crystallographic software supplied by Molecular Simulations Incorporated. The instrumental parameters refined were the same regardless of which programme was used and are summarised in Table 2-2. The unit cell parameters and atomic coordinates were refined according to space group symmetry; in general, thermal parameters were only able to be refined individually for metal atoms. Further details relating to specific samples are given in the corresponding results sections.

Description	Parameters refined
Diffractometer zero	1
Background	3 to 5
Scale factor	1
Profile shape (psuedo-Voigt)	NA, NB
Profile width	U, V, W
Profile asymmetry	Ap

Table 2-2 Instrumental parameters refined during Rietveld analysis. A description of the terms and symbols is given in Section 2.2.1.

2.4.3 Electron Microscopy and Image Simulation

Samples for examination by HREM were suspended in acetone and dispersed onto a holey carbon film supported on a copper grid. This was then inserted into a JEOL 200CX electron microscope specially modified by Dr D.A. Jefferson to include a side-entry stage and high-resolution ($C_s=0.41\text{mm}$) objective lens pole piece (Jefferson *et al.*, 1986; Hewitt *et al.*, 1989). The microscope was operated with a LaB_6 filament and an accelerating voltage of 200 kV, giving an electron wavelength of 0.0251\AA .

High-resolution images were recorded by locating suitably thin crystals projecting over holes in the carbon film. These were brought into alignment so that a zone axis of the crystal was parallel to the viewing direction by adjusting the tilt controls until diametrically opposed spots in the electron diffraction pattern appeared to have equal intensity. Since tilting the crystal usually altered the height of the specimen within the pole piece, the beam tilt, voltage centre and objective lens astigmatism needed to be corrected for each individual crystal. The first two of these corrections were made with the aid of 'wobblers' fitted to the microscope which cause the beam or image to move when incorrectly aligned. Astigmatism was corrected by adjusting the controls until the fringes observed in the amorphous carbon film disappeared without any preferential orientation as the focus was adjusted through the Gaussian ($\Delta f=0$) defocus.

After the microscope had been aligned, images were recorded on photographic film over a range of defocus settings using exposures in the range 0.7-2s, and at a magnification of $\approx 500,000$ times. Electron diffraction patterns were taken at decreased illumination, resulting in exposure times between 5.6 and 16s. The exact magnification delivered by the microscope depends on the objective lens current, and so this was recorded for each series of images. A calibration was carried out by measuring the spacings recorded over a range of lens currents from a sample of SrTiO_3 viewed in the $[001]$ direction.

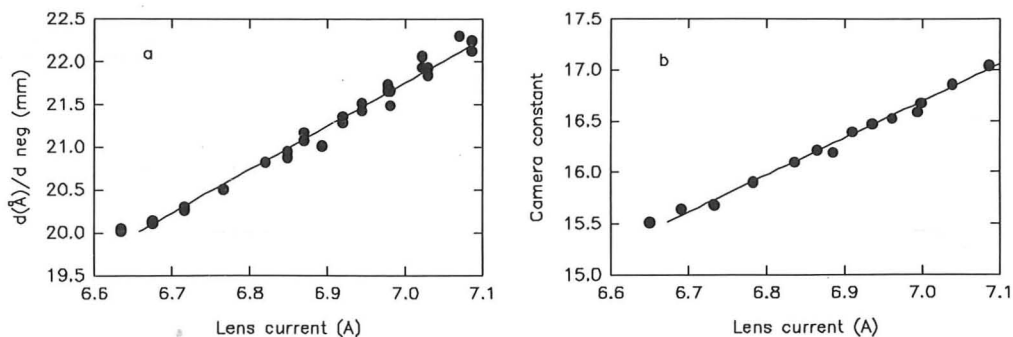


Figure 2-7 Calibration of the electron microscope against objective lens current for a) images; and b) electron diffraction patterns.

Figure 2-7 shows the linear nature of this variation which led, when coupled with the magnification due to photographic enlargement, to expressions relating measurements made directly from a print to the corresponding distance in angstroms :

$$d(\text{\AA}) = d(\text{print}) \times (5.098l - 13.93)(2.584 + 0.122h) \quad (2.32)$$

$$d(\text{\AA}) = (3.622l - 8.655)(2.584 + 0.122h)/d(\text{print}) \quad (2.33)$$

Equations (2.32) and (2.33) apply respectively to HREM images and electron diffraction patterns. In these equations, distances in the print are measured in mm, l is the lens current (in Amperes) and h is the height of the enlarger above the baseboard measured in cm.

Some of the images obtained from the electron microscope were affected by small distortions which caused skewing or an asymmetric expansion of the images. This was most easily seen in micrographs where the expected lattice was orthogonal, but the image displayed an angle other than 90° between lattice planes. The extent of the distortion depended on the orientation of the crystal and the lens current, and was not corrected in the images shown here.

Simulation of HREM images was carried out by the multi-slice method (see Section 2.3.1.2) using the CERIUS software package. The best match was sought over a range of simulated crystal thicknesses and defocus settings. Suitable values for focal spread (100\AA) and beam divergence (0.5 mrad) were established from previous studies, and were found to successfully simulate the images of known compounds.

Elemental analysis may be carried out in the electron microscope by measuring the energies of the secondary X-rays emitted from the electron-irradiated sample. The incident radiation is sufficiently energetic to displace core electrons from the atoms in the specimen and, when a higher level electron replaces the missing inner one, an X-ray photon is emitted with a well-defined energy corresponding to the difference in energy between the two electrons. Each type of atom has its own characteristic series of X-ray energies, enabling the elements in the sample to be identified. Quantitative analysis may also be carried out by measuring the relative intensities of the various

X-ray signals. The technique is known as energy-dispersive X-ray spectroscopy, abbreviated as EDS. Because the electron microscope has the facility to focus the electron beam onto small regions of the sample, the analysis can be confined to local areas, often smaller than 100\AA in diameter.

However, this technique was not applied to the specimens in the present study, for two main reasons. The first is that in order to obtain accurate quantitative results, a series of standards with known and well-defined elemental ratios must be analysed to establish a calibration. Ideally, these standards should contain all of the elements under investigation in compositions encompassing the expected range of unknown samples. For many of the samples studied in this work where EDS would have been of most benefit, suitable standards could not be found. For example, solid solution in the $\text{Sr}_2\text{TiO}_4\text{-La}_2\text{CuO}_4$ system (see Chapter 7) may have been investigated by EDS, but there are no known compounds which contain all four of these metals.

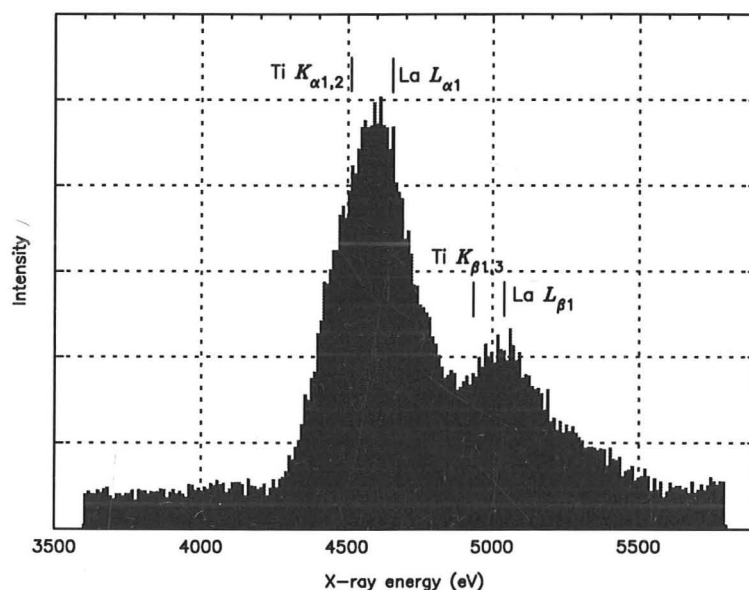


Figure 2-8 Portion of an EDS spectrum from a sample containing Ti and La. The positions of the expected peaks for these elements are marked.

The other problem concerns the overlap of signals from La and Ti. Most of the samples prepared in this study contained both of these elements, whose EDS peaks overlap considerably. Figure 2-8 shows an example where the expected positions of the Ti K_{α} and K_{β} , and La L_{α} and L_{β} peaks are marked. It is possible that these signals could be extracted from the data using a curve-fitting procedure, but the uncertainties

in such an approach would make the results questionable. A further possibility is that the La:Ti ratio could be determined from the intensity ratio of the two resolved peaks visible in Figure 2-8. This is because the expected Ti K_{α} :Ti K_{β} intensity ratio is quite different from the La L_{α} :La L_{β} ratio. Standards for this type of analysis could have been prepared, but because the method is still uncertain and provides only limited information, it was not attempted in this study.

Chapter 3

Compounds in the SrO-TiO₂ system

- 3.1 Introduction
 - 3.2 Ordered Compounds
 - 3.3 Disorder and Defects
 - 3.4 Summary and Conclusions
-

3.1 Introduction

The existence of strontium titanium oxides other than SrTiO₃ was discovered at approximately the same time by several groups independently. Drys and Trzebiatowski (1957) prepared both Sr₂TiO₄ and Sr₃Ti₂O₇, and examined their stability at elevated temperatures. Ruddlesden and Popper (1957,1958) also synthesised the same compounds and deduced their structures, basing them on the K₂NiF₄-type found by Balz and Pleith (1955). A further report of these compounds was given in a short article by Lukaszewicz (1958).

The structure of Sr₂TiO₄ (Figure 3-1) consists of layers of corner-sharing TiO₆ octahedra interleaved with layers of Sr atoms arranged in a body-centred tetragonal cell. A simple relationship between this structure and that of SrTiO₃ perovskite (see Chapter 1, Figure 1-6) may be seen - Sr₂TiO₄ can be derived from SrTiO₃ by removing alternate TiO₂ planes from the latter structure, leaving individual layers of TiO₆ octahedra bounded on either side by Sr atoms between the octahedral apices. The layers are then stacked above one another so that the octahedra in one layer are aligned with the gaps between octahedra in the adjacent layers. Successive layers are therefore related by a shift of ½ a unit cell in each of the *a* and *b* directions, providing a relationship between the Sr₂TiO₄ structure and the crystallographic shear structures

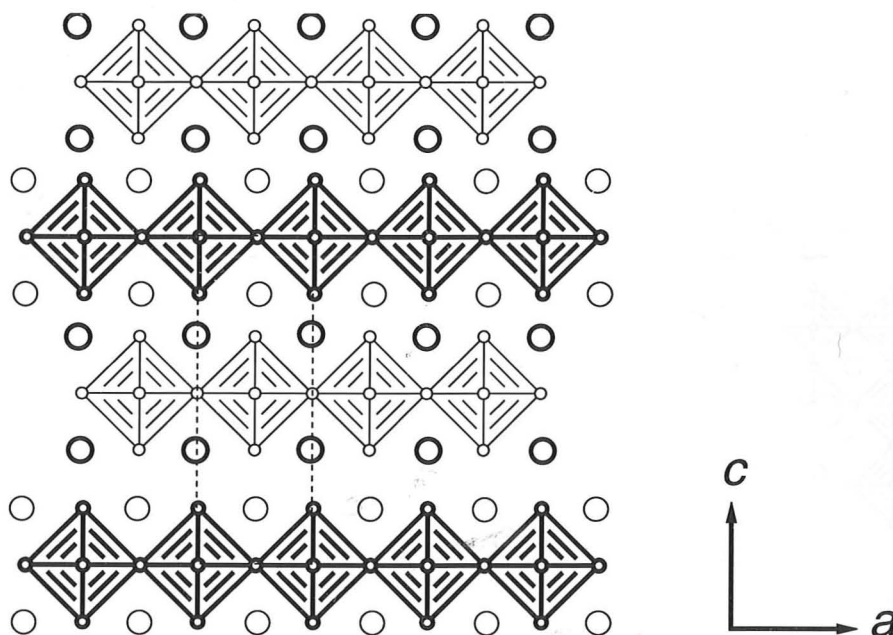


Figure 3-1 Polyhedral representation of the structure of Sr₂TiO₄. Ti atoms lie at the centres of the octahedra, Sr atoms are shown as large circles and O atoms as small circles. The heavy ruling indicates a difference in height of $b/2$ from the light ruling.

described in the Chapter 1. Ti atoms retain the octahedral coordination they have in SrTiO₃, but Sr now resides in asymmetric 9-fold sites rather than in the 12-fold ones of perovskite. Within the region bounded by the adjacent planes of Sr atoms, the coordination of Sr is much like that found in SrO which adopts the rocksalt structure. For this reason, Sr₂TiO₄ is often described as comprising alternating layers of perovskite SrTiO₃ and rocksalt SrO.

Once the relationship between perovskite and Sr₂TiO₄ has been established, it becomes clear how further compounds may be envisaged simply by increasing the thickness of the component perovskite layers. If the perovskite layers are two octahedra thick, then the resulting composition is Sr₃Ti₂O₇. Correspondingly, Sr₄Ti₃O₁₀ is obtained from perovskite layers three octahedra thick, and these two structures are depicted in Figure 3-2. In general, the uniform stacking of perovskite layers n octahedra thick gives rise to a compound Sr _{$n+1$} Ti _{n} O _{$3n+1$} , and this generic formula can be used to describe the family of structurally related materials. In such a formulation, the parent perovskite can be regarded as the $n=\infty$ member of the series. Ruddlesden and Popper (1958) were the first to describe this type of family, and so

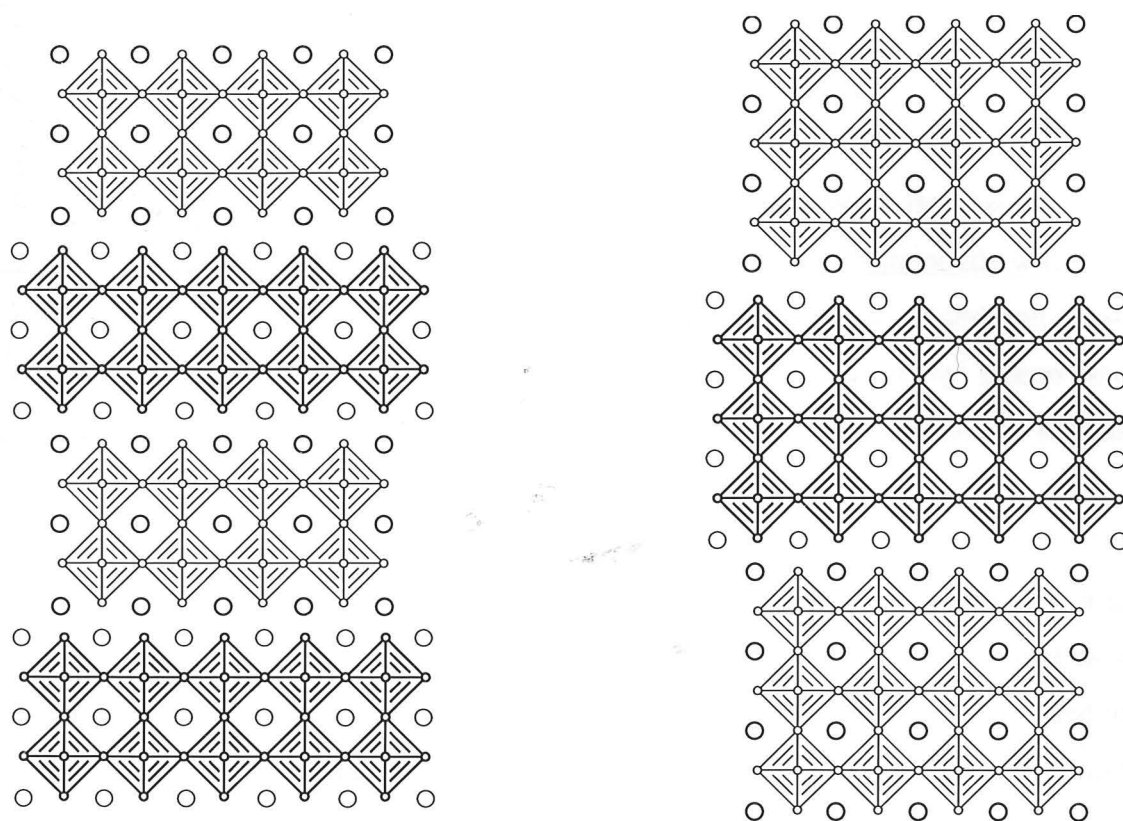


Figure 3-2 Structures of Sr₃Ti₂O₇ (left) and Sr₄Ti₃O₁₀ (right). The symbols and ruling are the same as for the previous figure.

compounds of this structure type are frequently referred to as “Ruddlesden-Popper compounds”. A large number of these materials have been discovered in a variety of chemical systems: those reviewed by Nomura (1978) will give some indication of the occurrence of this structure type.

Despite being the prototypes for the Ruddlesden-Popper family, there has not been a consensus amongst published studies as to how many of the Sr_{*n*+1}Ti_{*n*}O_{3*n*+1} compounds can be prepared. Ruddlesden and Popper published X-ray powder diffraction data for Sr₂TiO₄ and Sr₃Ti₂O₇, and reported the cell dimensions of Sr₄Ti₃O₁₀, although they were unable to prepare the latter compound as a single-phase product. Cocco and Massazza (1963) suggested that the Sr₄Ti₃O₁₀ composition lay in a range of solid solution between Sr₃Ti₂O₇ and SrTiO₃. However, by heating samples for over a week at 1475°C, M^cCarthy *et al.* (1969a) were able to synthesise what they believed to be phase-pure Sr₄Ti₃O₁₀ and published an indexed powder diffraction pattern.

With the advent of HREM, Tilley (1977a) was able to study the layer spacing and ordering in Sr_{n+1}Ti_nO_{3n+1} materials in some detail. No evidence could be found for ordered sequences with layers wider than two octahedra, although disordered intergrowth of layers up to eight octahedra thick were observed. Because of these wider intergrowths, Tilley did not discount the possibility that compounds with $n > 2$ may be able to be prepared under different experimental conditions. In addition, these observations suggested that the solid solution ranges proposed by Cocco and Massazza for SrTiO₃ and Sr₃Ti₂O₇ were likely to arise from intergrowths of various Sr_{n+1}Ti_nO_{3n+1} layers rather than cation disorder.

While there is no disagreement regarding the stability of Sr₂TiO₄ and Sr₃Ti₂O₇, it is not clear from the reports discussed above whether Sr₄Ti₃O₁₀ can be prepared as a single-phase, well ordered compound. Although several of these studies also tried to prepare materials with larger perovskite layers, all reported that compounds with $n > 3$ did not appear in XRD traces even as minor phases. This view was challenged by Balachandran and Eror (1980) who employed a liquid precursor technique to synthesise compounds with n ranging from 1 to 6. It is difficult to put their results into perspective, however, since they are only available as a conference abstract and phase identification was established by Raman spectroscopy rather than the more direct structural methods of XRD and HREM. White and Keramidas (1972) have published Raman spectra of $n=1,2$, and 3 materials and related the spectral features to the respective structures, but it is unclear how sensitive the technique is for determining structure in compounds with $n > 3$.

Most recently, Udayakumar and Cormack (1988) have examined the stability of Sr_{n+1}Ti_nO_{3n+1} compounds from a theoretical standpoint. Their approach was to calculate the energy of formation of each member from crystal structures obtained by atomistic simulation. In the simulation, the atomic coordinates and lattice vectors are adjusted in a least-squares procedure to minimise the lattice energy, which is in turn calculated from ionic pair potentials. The formation enthalpy was found to be -0.11eV for Sr₂TiO₄, and -0.14eV for all compounds with $2 \leq n \leq 12$. The authors therefore proposed that the absence of a thermodynamic driving force meant that

materials with $n > 2$ would not form ordered layer sequences but result in disordered intergrowths, in line with the experimental observations of Tilley (1977a).

One of the aims of the present study, therefore, was to clarify the extent of stability within the Sr_{*n*+1}Ti_{*n*}O_{3*n*+1} series, particularly that of Sr₄Ti₃O₁₀. Preparing single phase compounds also presented the opportunity to carry out a more detailed structural characterisation, for although the basic structural scheme proposed by Ruddlesden and Popper has never been called into question, surprisingly little has been published to provide precise cell parameters and atomic coordinates. Lukaszewicz (1959) refined the structures of Sr₂TiO₄ and Sr₃Ti₂O₇, to the level of precision available from powder diffraction photographs. Only Sr₃Ti₂O₇ has been the subject of a more recent analysis, the Rietveld refinement of neutron diffraction data described by Elcombe *et al.* (1991).

3.2 Ordered Compounds

3.2.1 Phase Stability

The preparation of $n=1,2,3$ and ∞ compounds was achieved in this study by conventional solid state reaction. The experimental conditions required to synthesise single-phase materials became progressively more severe in the sequence $\infty < 1 < 2 < 3$. For the $n=\infty$ material (SrTiO₃) a single overnight heating at 900°C was sufficient to produce XRD patterns with only a trace of reactants remaining, but the other compounds required longer times and higher temperatures. To give an approximate guide, temperatures of 950°C, 1200°C, and 1400°C were required to synthesise the $n=1,2$ and 3 materials respectively. The three weak diffraction peaks observed but unable to be indexed by Ruddlesden and Popper (1958) for Sr₃Ti₂O₇ were not detected in the current study, and it is therefore possible that they arose from traces of impurity phases. The peak at 2.26Å, for example, can be ascribed to SrTiO₃.

The only compound which presented difficulties in preparation was Sr₄Ti₃O₁₀. Interestingly, the formation of Sr₄Ti₃O₁₀ was greatly facilitated by the use of a series of overnight heatings in which the reaction temperature was gradually raised. To illustrate this, Figure 3-3 shows a key portion of the XRD traces from two sample treatments. The patterns on the left were obtained from a specimen heated only at 1400°C, and show no change after the first overnight reaction. The peaks attributable to Sr₄Ti₃O₁₀ are fairly broad, indicative of disorder, and some SrTiO₃ is also present. The patterns on the right, however, resulted from increasing the temperature with each overnight firing. Even though the maximum temperature used was the same as before, the greater success in preparing Sr₄Ti₃O₁₀ is evident from the narrower peaks, and particularly the presence of the (008) peak near 25°2θ.

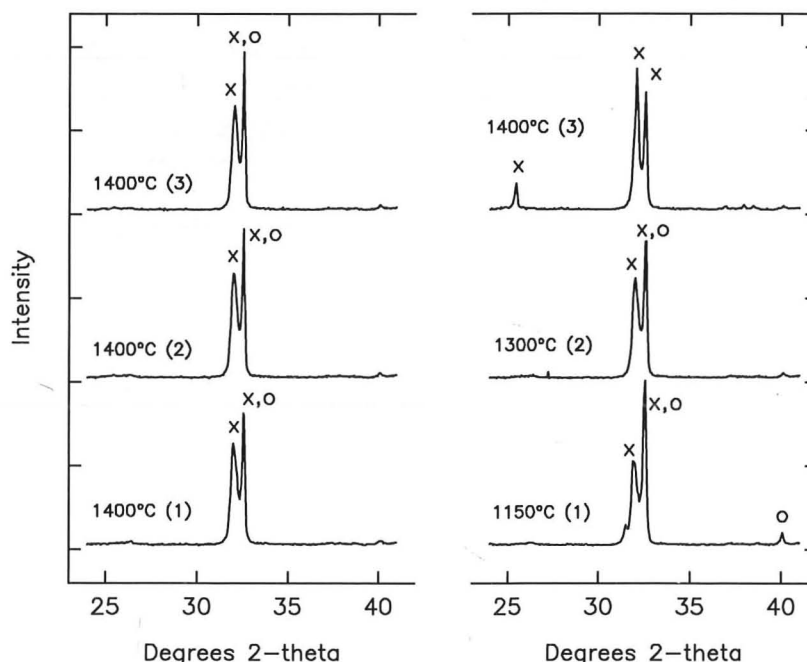


Figure 3-3 Comparison of a portion of the XRD traces resulting from two different sample treatments. The patterns on the left arose from successive overnight heatings at 1400°C, while those on the right resulted from an increase in temperature for each heating. The crosses indicate peaks due to Sr₄Ti₃O₁₀, the circles SrTiO₃.

The well-ordered nature of Sr₄Ti₃O₁₀ was confirmed by HREM, which showed crystals almost completely free of layer defects. The image shown in Figure 3-4 has a regular layer spacing of the expected dimension and the corresponding electron diffraction pattern (inset) displays no streaking which would be expected from

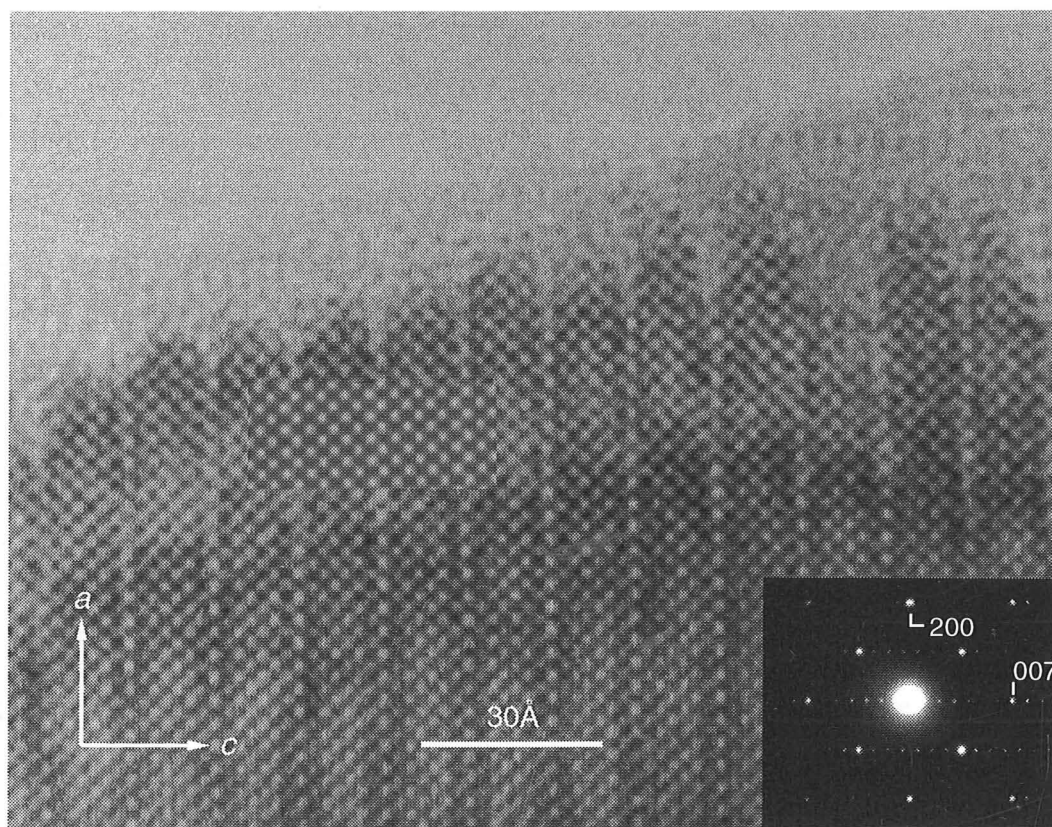


Figure 3-4 HREM image of well-ordered Sr₄Ti₃O₁₀ with simulated image (39 Å thick foil at -150 Å defocus) and electron diffraction pattern inset.

significant disorder in layer stacking. A simulated image is also inset in Figure 3-4 to verify that the crystal was in fact Sr₄Ti₃O₁₀.

Attempts to synthesise compounds with $n > 3$ invariably resulted in mixtures of the compounds already described above. This occurred regardless of whether the increasing temperature regime found to be successful for Sr₄Ti₃O₁₀ was used or not. All of the XRD peaks observed from these samples could be accounted for, indicating the absence of further compounds even as minor components of the phase assemblage. Increasing the reaction temperature to 1450°C and employing prolonged reaction times of several days did not produce any new phases, but led to a shift in phase composition toward more Ti-rich materials. This, coupled with the observation of a decreasing sample weight, indicated that Sr was being lost at the higher temperature through volatilisation.

In many layered structural families, ordered intergrowths containing regular sequences of two or more layer thicknesses are able to be prepared. For example, in the Aurivillius family (described in Chapter 1), Kikuchi *et al.* (1977) and Horiuchi *et al.* (1977) have characterised a mixed layer compound with the formula Bi₇Ti₄NbO₂₁. Electron diffraction and HREM showed this compound to comprise a regularly repeating sequence of one layer each of Bi₄Ti₃O₁₂ (3 octahedra across) and Bi₃TiNbO₉ (2 octahedra across). Jefferson *et al.* (1984) reported a similar intergrowth in a compound in which the perovskite layers were 4 and 3 octahedra across. Other more complex intergrowths in perovskite-related materials have also been observed in the Na-Ca-Nb-O system (Portier *et al.*, 1975).

Intergrowths of this type, however, were not found in the Sr_{n+1}Ti_nO_{3n+1} system. Specimens with compositions corresponding to $n=1.5$ and $n=2.5$ were reacted in an effort to produce ordered intergrowths, but XRD indicated that in each case the product formed comprised a two phase mixture of the neighbouring integral members. This was confirmed by HREM which showed no intergrowth, even over the scale of a few layer repeats.

3.2.2 Structure Refinement

Diffraction data suitable for structure refinement by the Rietveld method were collected for the single-phase specimens of SrTiO₃, Sr₂TiO₄, Sr₃Ti₂O₇, and Sr₄Ti₃O₁₀. The first three of these rapidly converged to give good agreement between observed and calculated diffraction patterns, but difficulties were experienced in obtaining a satisfactory refinement for Sr₄Ti₃O₁₀. Examination of the difference plot indicated that the (00 l) reflections were especially strong in the experimental pattern, and so the fit was improved markedly by incorporating preferred orientation in this direction. The appearance of preferred orientation in this sample and not the others is understandable since a considerably higher reaction temperature was required for Sr₄Ti₃O₁₀, encouraging greater grain growth. The relative difficulty locating crystals oriented with the layer plane parallel to the electron beam encountered during electron

microscopy is consistent with a propensity for the grains to cleave parallel to the layer plane, another feature of samples prone to preferred orientation.

The refined structural parameters are presented in Table 3-1 to Table 3-3, and plots of the observed and calculated diffraction profiles are shown in Figure 3-5 to Figure 3-7. SrTiO₃ has not been included here, as all of the atoms are on fixed coordinate sites and this refinement was carried out primarily to ensure the instrument functions incorporated in the refinement were appropriate to the experimental system used.

Sr ₂ TiO ₄ $a=3.8859(2)$; $c=12.597(1)$					
Atom	Site	x	y	z	B
Sr	4e	0	0	0.3542(1)	0.47(5)
Ti	2a	0	0	0	0.80(8)
O(1)	4c	½	0	0	0.46(18)
O(2)	4e	0	0	0.1590(5)	0.26(17)
$R_B=4.6\%$; $S=1.6$					

Table 3-1 Refined structural parameters for Sr₂TiO₄ in space group *I4/mmm*. The figures in parentheses indicate the estimated standard deviations in the final digit(s). The agreement indices R_B and S are defined in Section 2.2.2

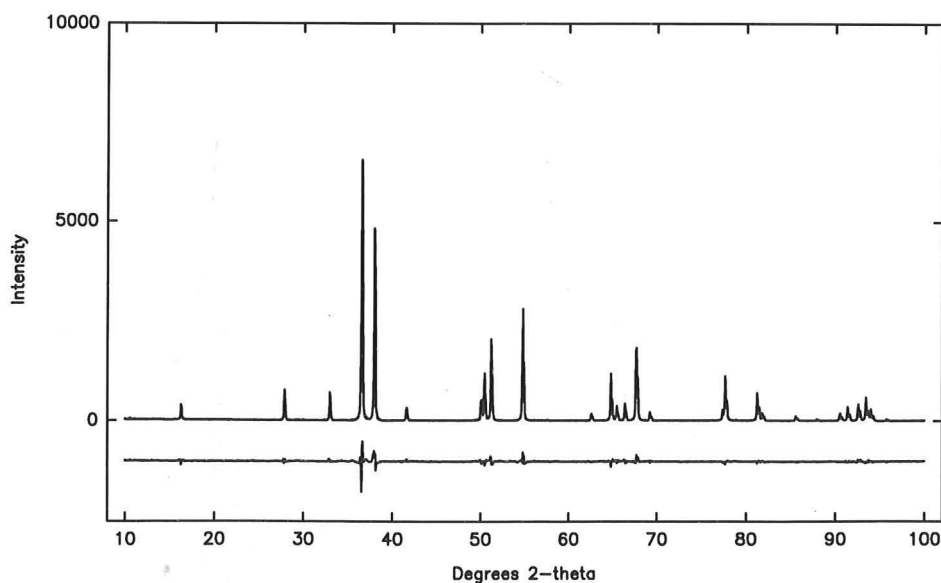
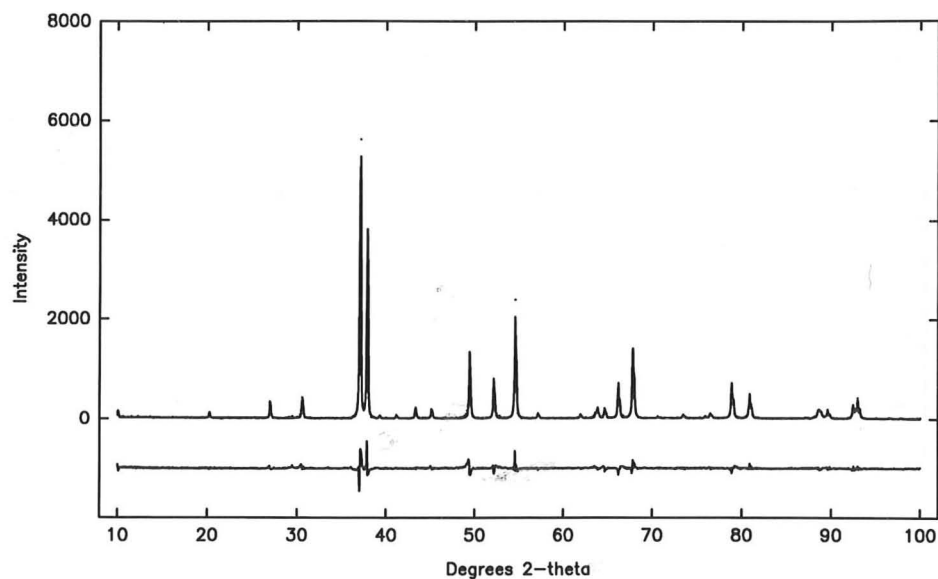


Figure 3-5 Plot from Rietveld refinement of Sr₂TiO₄ (Co radiation) with observed (dots), calculated (line) and difference (lower) XRD patterns.

Figure 3-6 Plots from Rietveld refinement of Sr₃Ti₂O₇ (Co radiation).

Sr ₃ Ti ₂ O ₇ $a=3.9005(3)$; $c=20.351(3)$					
Atom	Site	x	y	z	B
Sr(1)	2b	½	½	0	0.60(11)
Sr(2)	4e	½	½	0.1855(1)	1.07(8)
Ti	4e	0	0	0.0985(2)	0.14(10)
O(1)	2a	0	0	0	1.5(6)
O(2)	4e	0	0	0.1898(7)	1.9(5)
O(3)	8g	0	0	0.0960(4)	1.3(3)
$R_B=6.4\%$; $S=1.8$					

Table 3-2 Refined structural parameters for Sr₃Ti₂O₇ in space group *I4/mmm*.

Sr ₄ Ti ₃ O ₁₀ $a=3.904(1)$; $c=28.150(4)$					
Atom	Site	x	y	z	B
Sr(1)	4e	0	0	0.2981(1)	0.35(8)
Sr(2)	4e	0	0	0.4317(1)	"
Ti(1)	2a	0	0	0	"
Ti(2)	4e	0	0	0.1404(2)	"
O(1)	4c	0	½	0	0.6(2)
O(2)	4e	0	0	0.0722(7)	"
O(3)	8g	0	½	0.1408(4)	"
O(4)	4e	0	0	0.2066(6)	"
$R_B=11.8\%$; $S=2.1$					

Table 3-3 Refined structural parameters for Sr₄Ti₃O₁₀ in space group *I4/mmm*.

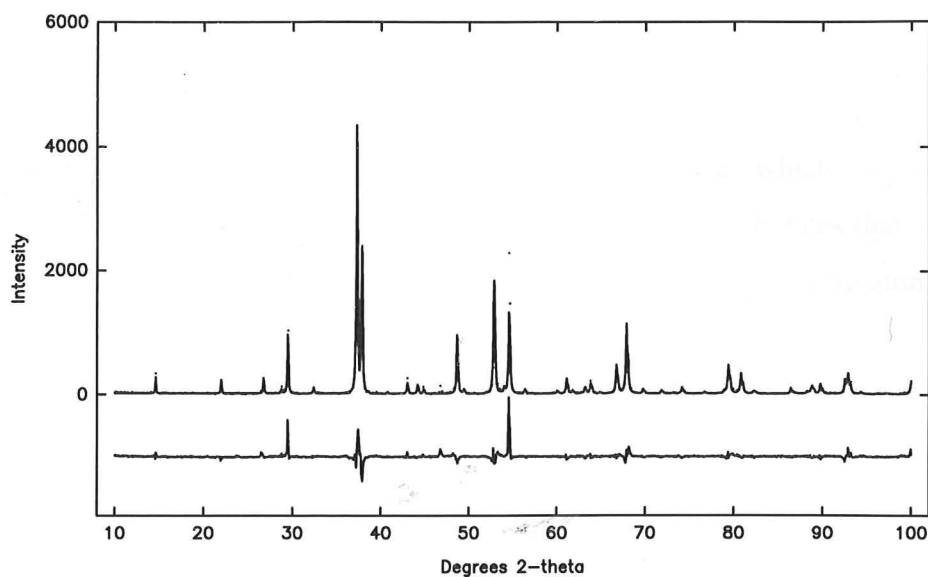


Figure 3-7 Rietveld plots for Sr₄Ti₃O₁₀ (Co radiation).

The major features of the refined Sr₂TiO₄ structure are the distortions away from ideal symmetry, in particular the elongation of the TiO₆ octahedra along the *c* axis. In their original calculations, Ruddlesden and Popper (1957) placed the Sr atoms level with the apical oxygens of the octahedra, which were slightly flattened compared to their width in the *a-b* plane. The refined structure, on the other hand, has the Sr atoms pushed away from the rocksalt layer toward the centre of the octahedral plane, while the oxygens at the apices of the octahedra are moved in the opposite direction. This results in a considerable elongation of the octahedra, with Ti-O distances of 1.974Å in the *c* direction compared to 1.943Å in the *a-b* plane.

The refined structure is predicted extremely well by a method used to relate bond distances and valences described by Brown (1987). In this model, the valence (s_{ij}) of a bond between atoms *i* and *j* is related to the interatomic distance by the empirical expression :

$$s_{ij} = \exp[(R_0 - R_{ij}) / 0.37] \quad (3.1)$$

where R_{ij} is the distance in angstroms between the two atoms and R_0 is the expected distance for atoms of that type. Values of R_0 for most common atom pairs have been tabulated by Brown and Altermatt (1985). The valence of atom *i* is found by summing its bond valences :

$$V_i = \sum_j s_{ij} \quad (3.2)$$

This should be equivalent to the expected chemical valence in what Brown terms the “valence sum rule”. The other feature of the bond valences which may be used to analyse structures is known as the “equal valence rule”. This dictates that if any path through the bond network is taken which returns to the original starting atom, the sum of bond valences traversed should be zero :

$$0 = \sum_{loop} s_{ij} \quad (3.3)$$

and is equivalent to saying that the bonds formed by each atom are, as near as possible, equal (see the appendix in Brown, 1992). An ideal structure obeys both the valence sum and equal valence rules. However, this may not always be possible and in such cases the observed structure represents a balance with the least disruption to both rules.

The bond valence model has been used to predict the structure of La₂NiO₄ (Brown, 1992) which, like Sr₂TiO₄, possesses the K₂NiF₄ structure. We have followed the same procedure here to derive a complete structure for Sr₂TiO₄ without using any experimental data. The first step is to construct a finite bond graph, given in Figure 3-8, which shows the network of bonds between all of the atoms. Figure 3-8 also includes a portion of the structure to help identify the atoms and their coordinations.

The procedure begins by equalising the valences of all the bonds to each metal atom

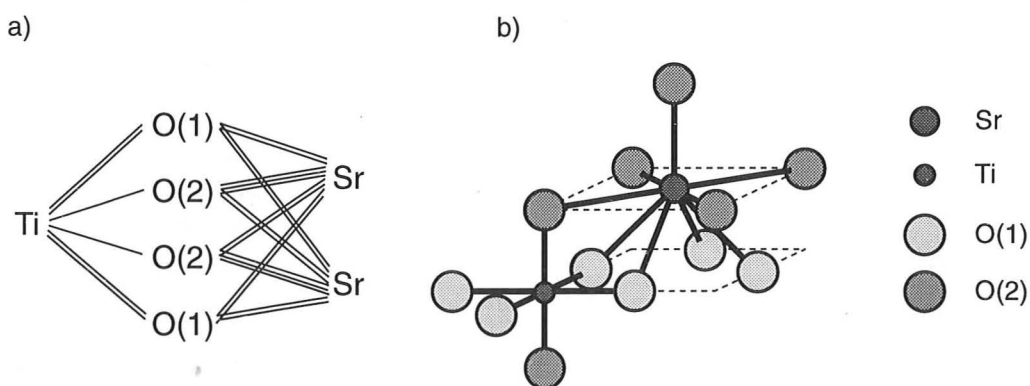


Figure 3-8 a) Bond network graph for Sr₂TiO₄. b) Portion of the Sr₂TiO₄ structure showing metal coordination and oxygen atom labels.

and thereby calculating the bond distances. Titanium has an expected valence of +4 and is in 6-fold coordination, and so the expected Ti-O bond valence is 2/3. Using Equation (3.1) and a value for R_0 of 1.815 Å (Brown and Altermatt, 1985) leads to Ti-O bond lengths of 1.965 Å. Similarly, the bond distances between Sr and O (bond valence = 2/9, $R_0 = 2.118$ Å) are expected to be 2.675 Å. However, these ideal lengths cannot be achieved in the real structure because they lead to different periodicities in the a - b plane. As a first approximation, the a dimension is taken as the mean of the two values, in this case 3.857 Å. With Ti at the origin, O(2) is positioned so that the Ti-O(2) distance corresponds to the ideal 1.965 Å, and Sr located to give ideal Sr-O(1) distances. Four of the Sr-O(2) bond lengths are now defined by the positions already established for Sr and O(2), but the fifth may be set to the ideal value by choosing an appropriate dimension for the c axis.

The structure which results is one which has the maximum number of bonds with the expected valences while retaining structural coherence in the a - b plane. The atomic valences, however, show a significant deviation from their ideal valences, at 4.28 and 1.88 for Ti and Sr respectively. They may be restored to their expected values by moving Sr closer to, and O(2) further away from the Ti-O(1) plane, but this is at the expense of enlarging the range of bond valences around each atom, in violation of the equal valence rule. The optimal structure chosen is one in which Sr and O(2) have been moved half the distance required to restore the ideal metal valences, and this structure is compared to the refined structure in Table 3-4.

Parameter	Refined value	Bond Valence value
a	3.8859(2)	3.857
c	12.597(1)	12.598
z for Sr	0.3542(1)	0.356
z for O(2)	0.1590(5)	0.159

Table 3-4 Comparison of refined structural parameters for Sr₂TiO₄ with those predicted by the bond valence model.

The agreement between the two is remarkable; only the a dimension is not predicted accurately by the bond valence model. Although some rather arbitrary assumptions have been made in deriving the bond valence structure, we have not chosen these to produce the best match, but directly followed the approach Brown (1992) took for

La₂NiO₄. The necessity to make these assumptions may make the extent of the agreement with the refined structure somewhat coincidental, but it is clear that the attempts to minimise the disruption to atomic and bond valences correctly predict the observed distortions in the Sr₂TiO₄ structure.

The refined structures of Sr₃Ti₂O₇ and Sr₄Ti₃O₁₀ also possess similar distortions to those encountered in Sr₂TiO₄, especially the movement of Sr away from the middle of the rocksalt layer, although both elongation and flattening of TiO₆ octahedra were observed. The octahedral distortions are drawn in Figure 3-9 which shows that within a given structure the Ti-O bond lengths parallel to *c* become larger as the centre of the perovskite layer is approached. A similar trend can be seen in the structures of Sr₃V₂O_{7.1} and Sr₄V₃O_{9.6} refined by Suzuki *et al.* (1991a,1991b) and may represent the effect of repulsion away from the rocksalt layer. However, care must be taken when interpreting these distortions as they rely on the refined oxygen positions, the least well-defined in X-ray Rietveld refinements. In addition, the contrary trend has been observed in a neutron Rietveld refinement of Sr₃Ti₂O₇ (Elcombe *et al.*,1991) and in a single-crystal X-ray determination of Sr₄V₃O_{9.7} (Gong *et al.*,1991b).

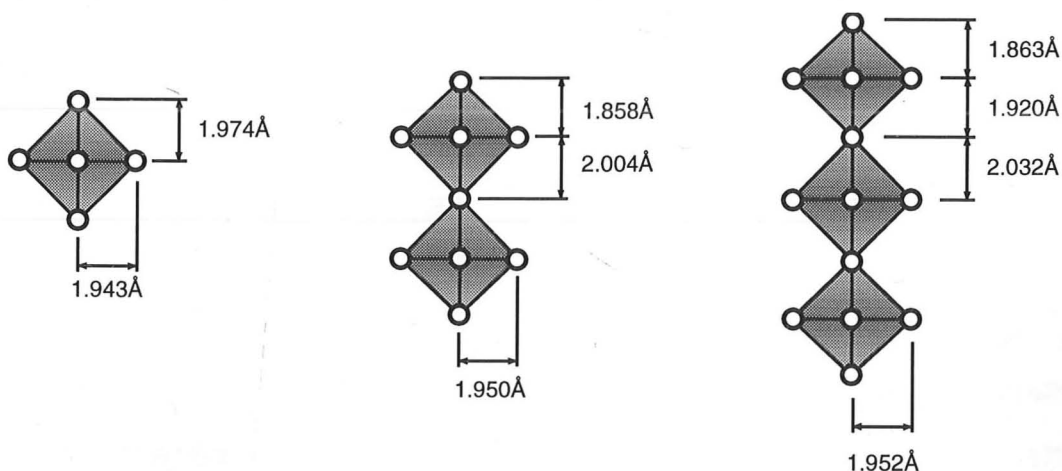


Figure 3-9 Octahedral distortions in, from left to right, Sr₂TiO₄, Sr₃Ti₂O₇, and Sr₄Ti₃O₁₀.

Attempts to apply the bond valence equations to Sr₃Ti₂O₇ and Sr₄Ti₃O₁₀ did not produce satisfactory results, since further assumptions are needed to determine the placement of atoms in these more complex structures. Unlike Sr₂TiO₄, there was more than one way to construct a model with minimal bond valence or valence sum disruptions.

3.3 Disorder and Defects

3.3.1 Layer Stacking

Disorder in the regularity of layer spacing was observed, as might be expected, primarily in those samples which had been reacted at lower temperatures or for shorter times, and for samples with compositions corresponding to $n > 3$. An example from a relatively Sr-rich specimen is shown in Figure 3-10. This particular fragment contains primarily $n=3$ layers which extend beyond the range of the figure, but there are intergrowths of wider lamellae, up to $n=8$, clearly present. All of the intergrowths found in this study involved individual layers with $n > 3$, and usually the 'foreign' layers were wider than those of the matrix they inhabited.

At compositions closer to SrTiO₃ where the frequency of rocksalt layers is correspondingly lower, it becomes more appropriate to refer to rocksalt layers within a perovskite matrix rather than intergrowth of different Sr_{*n*+1}Ti_{*n*}O_{3*n*+1} layers. In some cases, individual rocksalt layers quite distant from their nearest neighbours were observed, as in the micrograph shown in Figure 3-11. More common, however, was

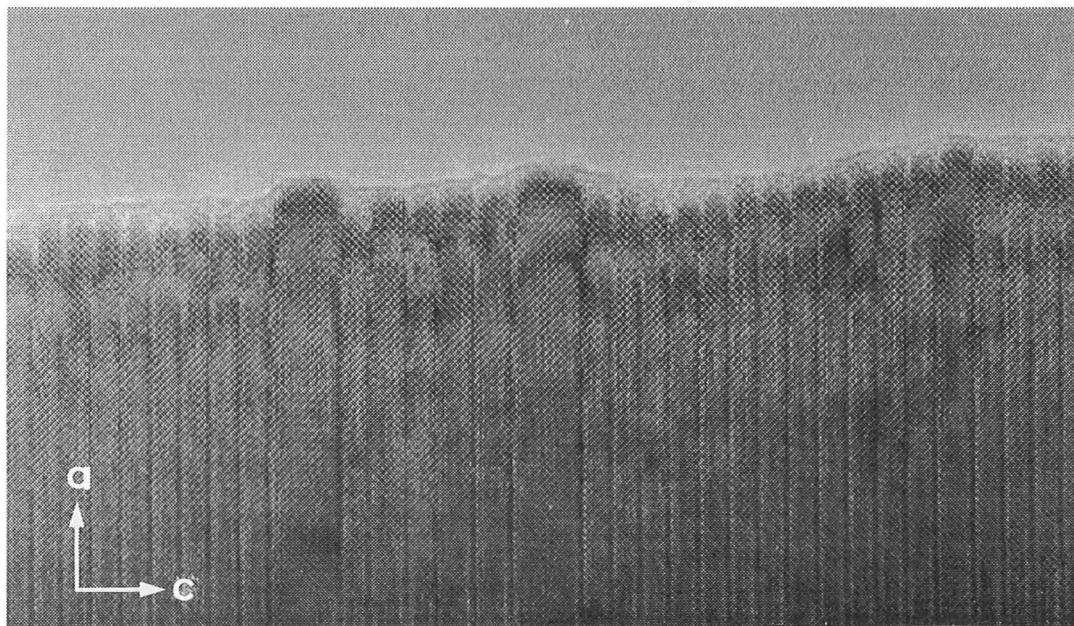


Figure 3-10 HREM image of a specimen with composition close to Sr₄Ti₃O₁₀. Intergrowth of wider layers, up to $n=8$, can be seen in the $n=3$ matrix.

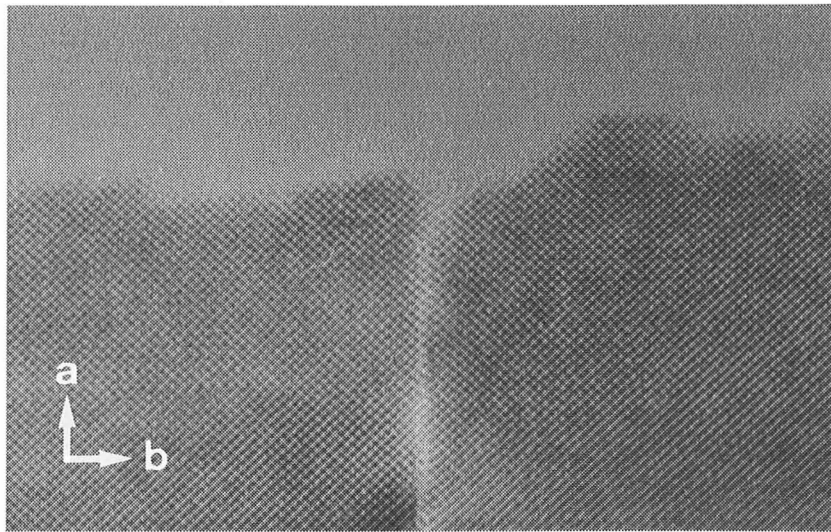


Figure 3-11 An isolated rocksalt layer, from a specimen with the composition Sr_{1.1}TiO_{3.1}

the appearance of small clusters of rocksalt layers such as those in Figure 3-12, recorded from the same specimen as the previous example. The spacing between layers in these clusters was about 20-30Å, corresponding to lamellae of $n=4$ to $n=6$ compounds. When this is compared to the overall composition ($n=10$), it indicates that the distribution of Sr, and therefore of the rocksalt layers, is inhomogeneous on a local scale. The electron diffraction patterns of these samples showed primarily spots arising from SrTiO₃, although some faint streaking along the [100] direction was also noticeable.

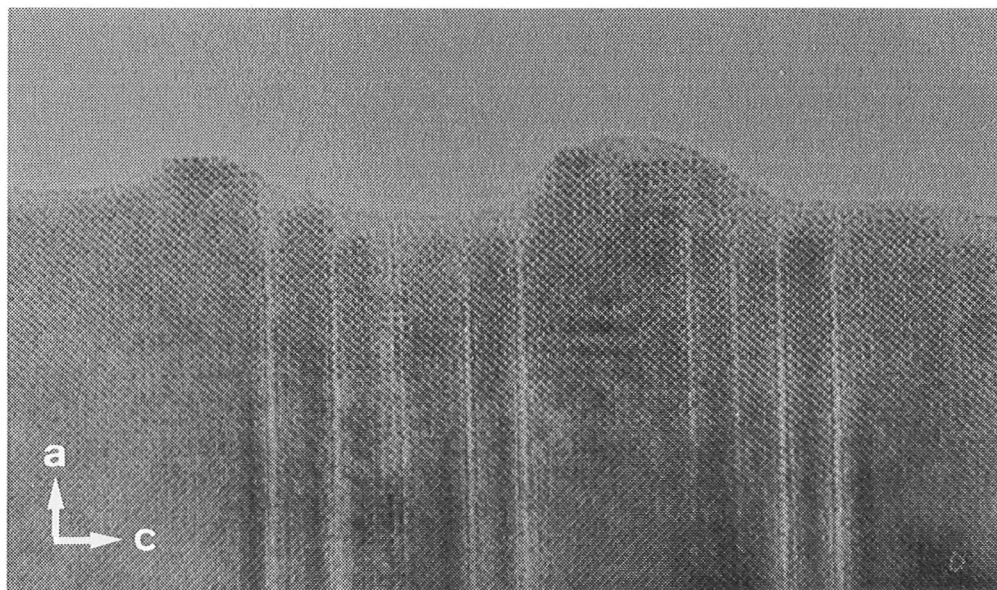


Figure 3-12 HREM image, again from a Sr_{1.1}TiO_{3.1} sample, showing clusters of rocksalt layers.

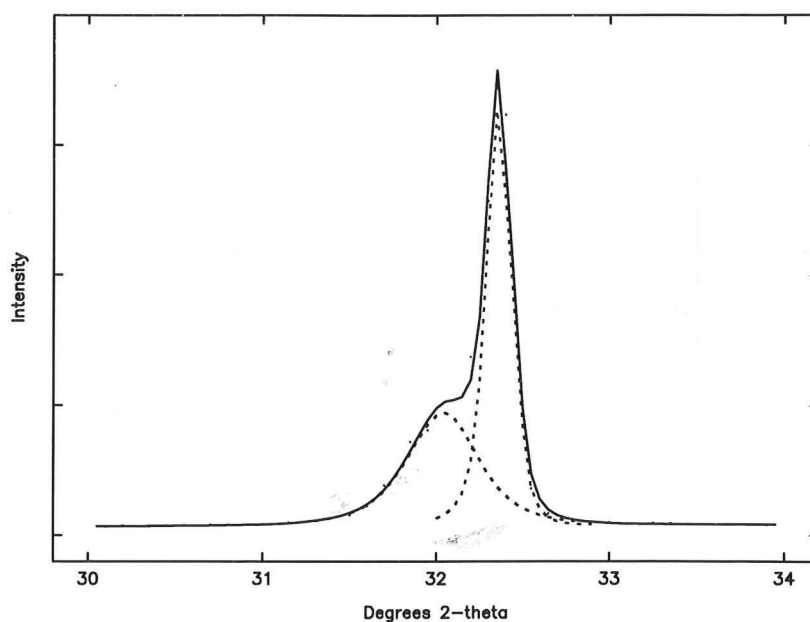


Figure 3-13 Region of XRD trace from a sample with composition equivalent to $n=6.67$. The two peaks have been resolved by least-squares profile fitting.

The inhomogeneity in layer spacing is also consistent with XRD patterns, which displayed peaks in addition to those expected from SrTiO₃ for compositions between $n=5$ and $n=10$. The most significant of these was the peak near $32.0^\circ 2\theta$ which could be resolved from the neighbouring SrTiO₃ peak by fitting peak profiles in this diffraction range like those shown in Figure 3-13. Two peaks in this area are also present in patterns from ordered Sr _{$n+1$} Ti _{n} O _{$3n+1$} phases, and their separation decreases as n becomes larger. An indication of the average layer spacing which gave rise to the $\approx 32.0^\circ$ peak could therefore be obtained by comparing the measured peak separation with those expected from various Sr _{$n+1$} Ti _{n} O _{$3n+1$} compounds.

The peak separation has been established experimentally for $n=1,2$ and 3 , and the separation for larger values of n has been predicted by extrapolating the trends in the unit cell parameters. The higher angle peak of the two considered has Miller indices (110) , and the lower angle peak $(1.0.2n+1)$. The expected peak separation is plotted in Figure 3-14 as a function of n and was used to estimate the average layer spacing in preparations with $n>4$. Of course, the broadening observed for the lower angle peak is indicative of considerable disorder, and the values obtained from this method should

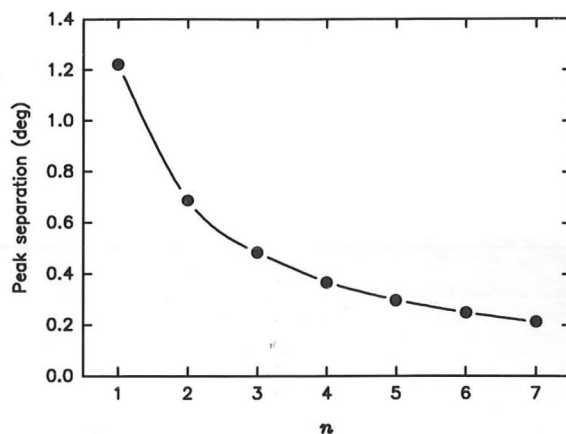


Figure 3-14 Variation of the separation between the XRD peaks near $32^\circ 2\theta$ as a function of n for the $\text{Sr}_{n+1}\text{Ti}_n\text{O}_{3n+1}$ compounds. Values for $n > 3$ have been calculated by extrapolating the measured unit cell dimensions of $n \leq 3$ samples.

be regarded as a rough estimate of the mean layer spacing. It should also be noted that this analysis is only valid if the disorder is of the random type. If association between defects (short range order) occurs, the lower angle peak will invariably be of a more complex shape and only "average" values of n will be obtained.

For the $n=10$ sample the measured peak separation was 0.27° , corresponding to a average layer spacing around $n=5.5$. This is remarkably consistent with the HREM images (see Figure 3-12) of clusters of layers 20-30Å apart. Preparations with more Sr-rich compositions had correspondingly smaller average layer spacings, but no clear trend emerged as to how the spacing changed with heating temperature or time.

3.3.2 Changes in Layer Direction

In principle, the rocksalt layer may be orientated along any of the three equivalent planes in perovskite - *i.e.* the (100), (010), or (001) planes. It is not surprising then that disordered crystals contained regions where layers in more than one of these directions were present. An example is shown in Figure 3-15 where several right-angled deviations are clearly visible. In the basic structure of $\text{Sr}_{n+1}\text{Ti}_n\text{O}_{3n+1}$ compounds (Section 3.1), the octahedra either side of the rocksalt plane are displaced with respect to one another by half a body diagonal in both the a and b directions.

This means that in the image shown in Figure 3-15 the perovskite regions either side of any layer are at different heights in the plane of projection. Even in a disordered crystal such as this, the defects are placed so that each perovskite region bounded by a series of rocksalt layers is at a constant height.

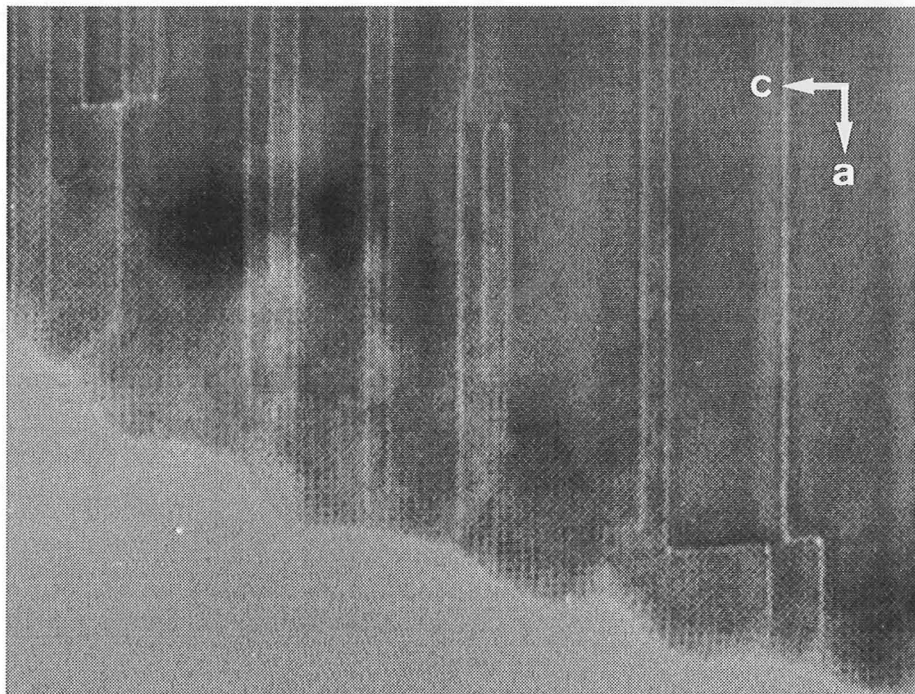


Figure 3-15 Disordered crystal with right-angled deviations in rocksalt plane orientation.

One simple way in which the height of perovskite blocks in these crystals may be held constant is through the formation of U-shaped layers. An example of this configuration is shown in the micrograph in Figure 3-16a; several of these defects were present in this particular crystal. To show that this defect requires comparatively little structural relaxation, a computer-based model was constructed (Figure 3-16c) with the same layer separations as the observed image. Small atomic shifts away from the atoms near the top of the U-bend were applied to counteract the anomalously short Sr-Sr distances in this region which were otherwise present. These shifts also improved the match of the simulated image (shown in Figure 3-16b) with the experimental one. A perspective view of a slice of the model structure is also shown in Figure 3-16d to emphasise the differences in height which cannot be seen in the other view.

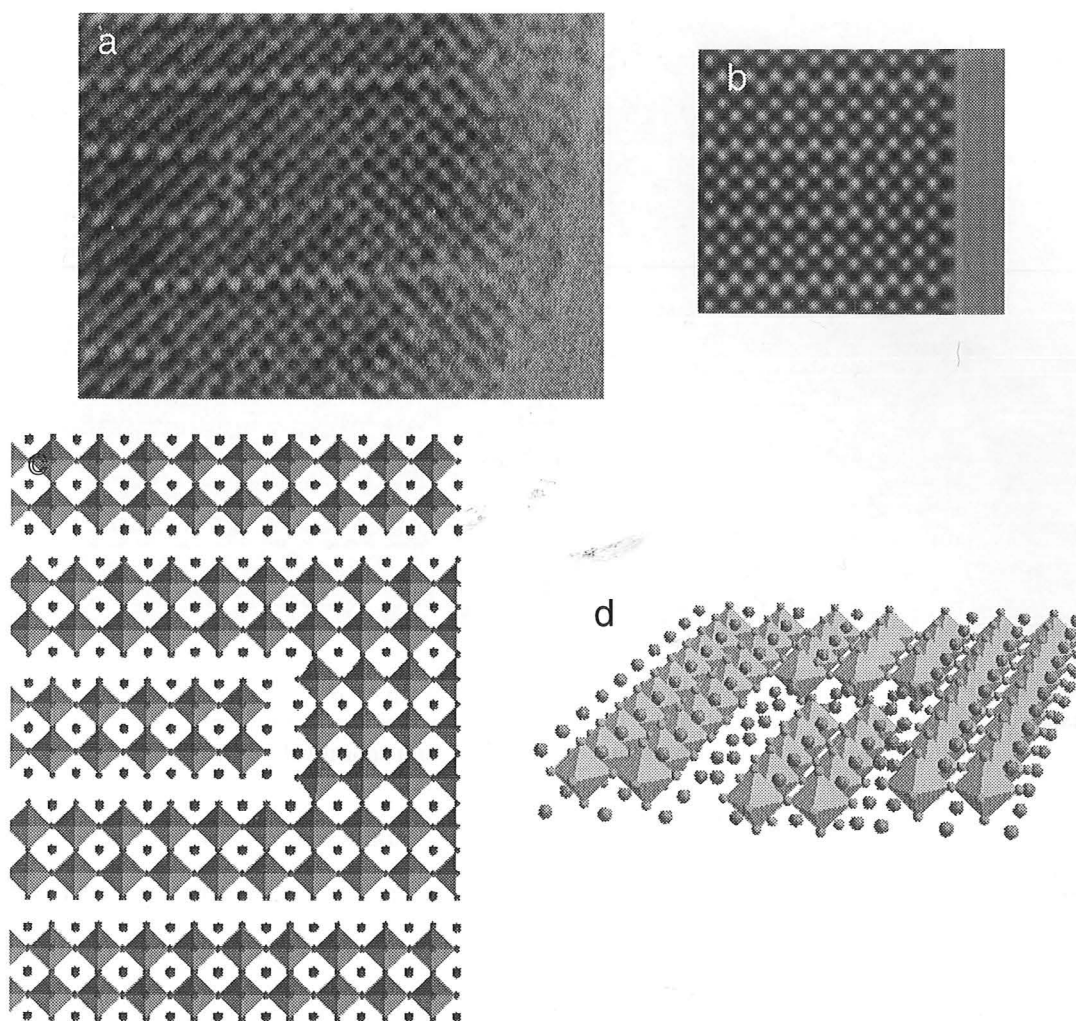


Figure 3-16 A U-shaped rocksalt layer. a) Observed HREM image; b) simulated image (thickness = 31.2Å, defocus = -150Å). The model used for the simulated image is shown in c) and d).

Right-angled changes in layer orientation were also evident, albeit indirectly, in images recorded from the (110) direction relative to perovskite. At first glance, the image shown in Figure 3-17 appears to contain a rocksalt layer which terminates inside the perovskite matrix, and perhaps another which begins a little further up (marked by arrows). However, careful examination shows that these two features are part of the same rocksalt layer which is bent by two right-angled turns. The horizontal portions are easily seen because the direction of observation is parallel to the plane of the layer, but the vertical step is not imaged clearly because it is at 45° from the plane of the micrograph. This is not immediately apparent from the micrograph, and so a representation of the geometry of the bent rocksalt layer is shown in Figure 3-18.

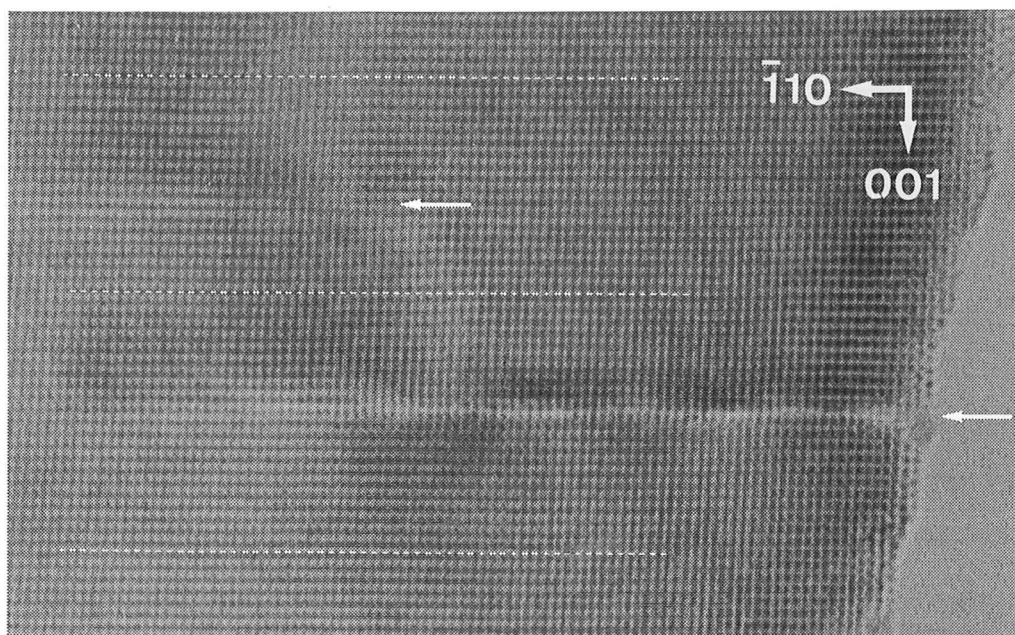


Figure 3-17 [110] HREM image of SrTiO₃ with rocksalt layers (arrowed) present. The purpose of the dotted lines is explained in the text. The deviation from orthogonal symmetry is due to distortions introduced by the microscope.

The evidence for the true nature of this defect comes from two observations. Firstly, one layer appears to start as the other ends, and there is some disturbance of the lattice between the two. Secondly, and more importantly, the contrast in the perovskite matrix is displaced by exactly half an octahedron as the vertical step is traversed. This is highlighted by the horizontal lines drawn on the micrograph (Figure 3-17). At the

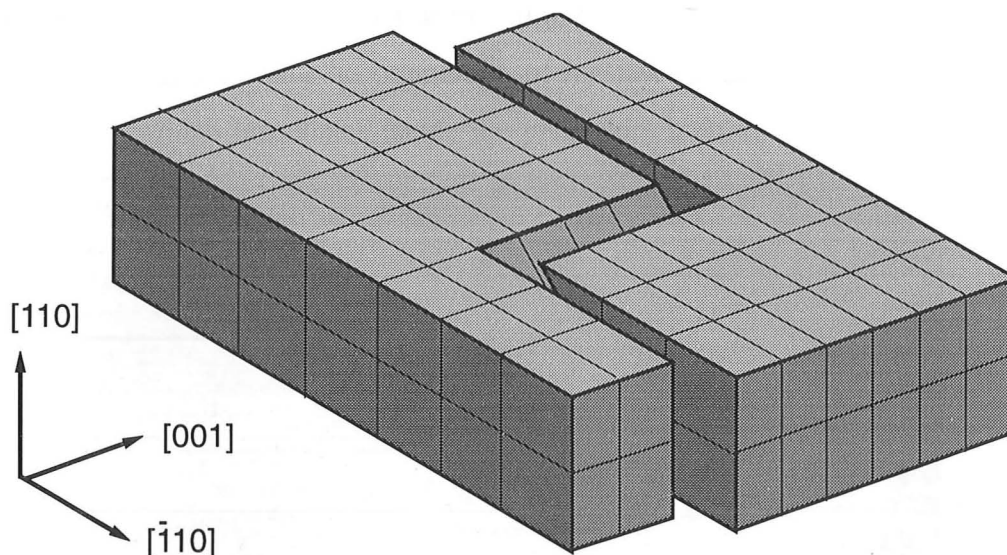


Figure 3-18 Schematic illustration of stepped rocksalt layer in SrTiO₃ as seen in the previous figure. When running parallel to $[\bar{1}10]$, the layer is also parallel to the viewing direction ($[110]$). However, the portion of the layer parallel to $[001]$ lies obliquely to the direction of view.

bottom of the picture, the line connects an unbroken sequence of white dots, indicating an undisturbed perovskite region. The central line, however, connects white spots on the right hand side but lies midway between these spots on the left hand side. This is precisely the displacement expected from a rocksalt layer and provides strong evidence for the presence of a vertical step in the rocksalt plane.

Exactly the same displacement can also be seen at the top of the image. This arises from a second vertical step to another horizontal portion visible in the original negative, but excluded from the enlarged area shown in Figure 3-17 for the sake of clarity. The second step also explains why the short horizontal portion in the enlarged area is only weakly imaged.

3.3.3 Termination of the Layer Structure

The foregoing discussion has emphasised that most of the defects observed require relatively small structural rearrangements, since layer intergrowths and right-angled bends can be accommodated using much the same structural principles as the ordered Sr_{n+1}Ti_nO_{3n+1} compounds. This was not always the case, as the image in Figure 3-19 shows. This feature was observed deep within the interior of a crystal making image simulations unreliable, but the orientation of the layer suggests it must surely be a rocksalt layer which terminates inside the perovskite matrix. Since this image was

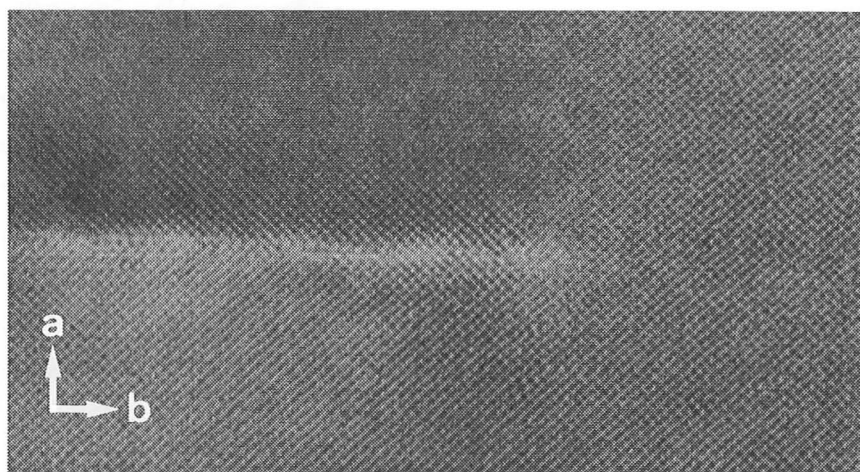


Figure 3-19 HREM image of a rocksalt layer terminating inside SrTiO₃, viewed in the [100] direction.

bottom of the picture, the line connects an unbroken sequence of white dots, indicating an undisturbed perovskite region. The central line, however, connects white spots on the right hand side but lies midway between these spots on the left hand side. This is precisely the displacement expected from a rocksalt layer and provides strong evidence for the presence of a vertical step in the rocksalt plane.

Exactly the same displacement can also be seen at the top of the image. This arises from a second vertical step to another horizontal portion visible in the original negative, but excluded from the enlarged area shown in Figure 3-17 for the sake of clarity. The second step also explains why the short horizontal portion in the enlarged area is only weakly imaged.

3.3.3 Termination of the Layer Structure

The foregoing discussion has emphasised that most of the defects observed require relatively small structural rearrangements, since layer intergrowths and right-angled bends can be accommodated using much the same structural principles as the ordered Sr_{n+1}Ti_nO_{3n+1} compounds. This was not always the case, as the image in Figure 3-19 shows. This feature was observed deep within the interior of a crystal making image simulations unreliable, but the orientation of the layer suggests it must surely be a rocksalt layer which terminates inside the perovskite matrix. Since this image was

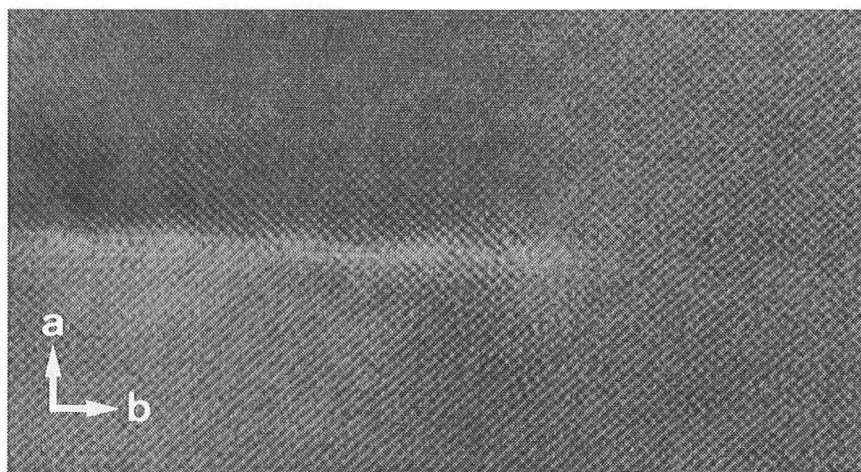


Figure 3-19 HREM image of a rocksalt layer terminating inside SrTiO₃, viewed in the [100] direction.

recorded in the [100] direction, it is not possible for this layer to continue unseen in a vertical direction as was the case in the previous [110] example.

This type of defect requires a considerable degree of structural rearrangement, and so computer modelling was undertaken to see how this might occur. The first attempts were made with the end of the layer running parallel to the perovskite [100] direction, but the atomic movements required to bring the octahedra into registration beyond the layer end were too severe. It was quickly realised that the least disruption occurred when the layer plane ended along the perovskite [110] direction, and the resulting model is presented in Figure 3-20. The left hand view shows how the layer 'closes up' to continue as defect-free perovskite, while the perspective view (right) highlights how the height difference across the rocksalt plane is accounted for. Although some of the octahedra are quite distorted, the model nevertheless illustrates how termination of the rocksalt plane can be achieved. Unfortunately, none of these defects were found close enough to the edge of crystals to confirm the model by image simulation.

When the terminating layer is seen from the [100] direction, as in the micrograph shown in Figure 3-19, it is possible that it is a layer which terminates along a single [110] axis viewed obliquely, in which case the actual termination point varies with the

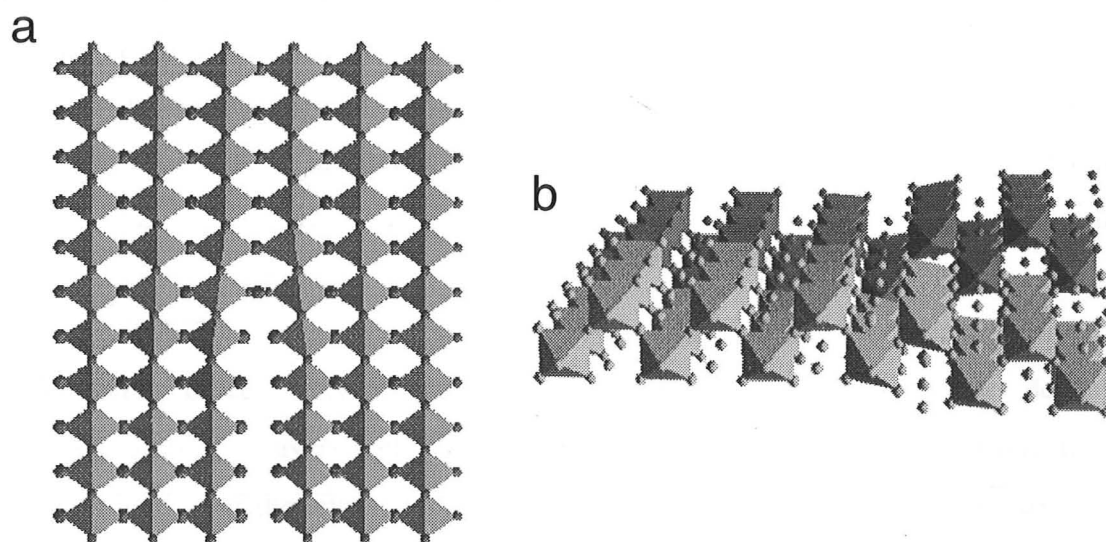


Figure 3-20 Model of terminating rocksalt layer. In the perspective view (b) the atoms darkly shaded are displaced upwards in the rocksalt layer, while those shaded lightly are displaced downwards.

thickness of the crystal. Alternatively, the layer may terminate in a saw-tooth fashion along alternating [110] and [1 $\bar{1}$ 0] directions. Both these possibilities would seem to more likely than termination along [100] which requires greater structural distortion.

3.4 Summary and Conclusions

The stability of phases in the Sr_{n+1}Ti_nO_{3n+1} series has been shown to extend as far as the $n=3$ compound (Sr₄Ti₃O₁₀), in agreement with the findings of M^cCarthy *et al.* (1969a). The regularity of layer spacing in this compound has been confirmed for the first time by HREM. Preparation of phase-pure Sr₄Ti₃O₁₀ is assisted by using a heating programme consisting of several reactions at successively higher temperatures up to 1400°C. Temperatures higher than this result in the loss of Sr through volatilisation. Evidence for the presence of compounds with $n>3$ could not be found, contrary to the report of Balachandran and Eror (1980).

The structures of Sr₂TiO₄, Sr₃Ti₂O₇, and Sr₄Ti₃O₁₀ were refined by Rietveld analysis which revealed deviations in atomic positions from their ideal positions. Sr atoms were found to be displaced away from the rocksalt plane, and TiO₆ octahedra were distorted from the perfect configuration. The octahedral distortion was observed to change in a uniform manner across the perovskite blocks. Calculations based on the bond valence model (Brown, 1987) were able to generate the Sr₂TiO₄ structure with a considerable degree of accuracy. This suggested that the atomic displacements in Sr_{n+1}Ti_nO_{3n+1} compounds were in accord with the equalisation of valences inherent in the bond valence approach.

A number of defects were observed in HREM images, classified into those dealing with intergrowth of layers with different thicknesses, deviation in the layer direction, and termination of the layer structure. These defects were similar to those observed by Hawkins and White (1991) in isostructural Ca-containing compounds, but here we have been able to construct computer-based models to demonstrate how the structure adapts to incorporate such defects.

Chapter 4

Investigation of Reported Compounds in the Sr-La-Ti-O System

- 4.1 Introduction
 - 4.2 La-substituted SrTiO₃
 - 4.3 Other Reported Sr-La-Ti-O compounds
 - 4.4 Summary and Conclusions
-

4.1 Introduction

The reports of materials in the Sr-La-Ti-O system may be classified into three main groups:

- (i) Compounds resulting from the substitution of La for Sr in SrTiO₃;
- (ii) The series of layered compounds corresponding to the formula Sr_{n-3}La₄Ti_nO_{3n+3}; and
- (iii) The three materials given by $n=2,3,$ and 4 in the series SrLa₂Ti_nO_{2n+4}.

In this chapter, each of these groups will be examined in turn to establish the structure and stability of compounds in the Sr-La-Ti-O system. Although it may appear confusing to treat several different types of compound in the same chapter, a common structural theme may be seen to emerge. The experimental work has been confined to materials prepared in air, with the expectation that the metals are in their most oxidised valence state. The ternary system SrO-La₂O₃-TiO₂ is therefore being considered, and the reported compounds are depicted for this system on the composition diagram shown in Figure 4-1.

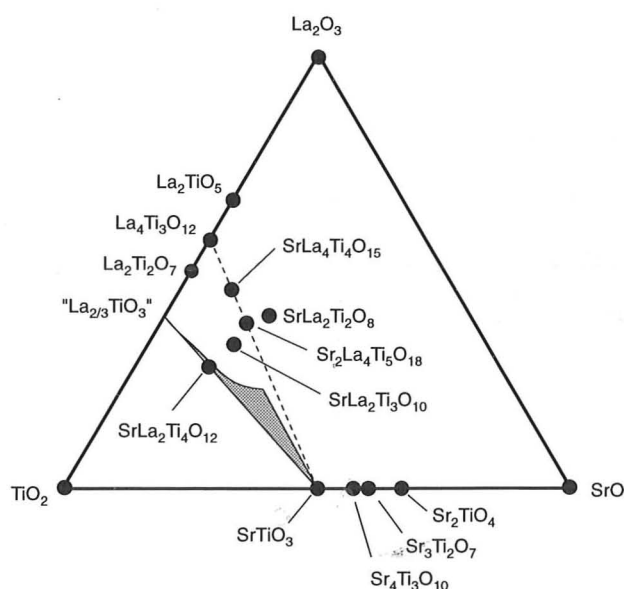


Figure 4-1 Summary of reported compositions in the SrO-La₂O₃-TiO₂ system, in the form of a phase diagram. Solid solution in SrTiO₃ is shown as a shaded region, and the fixed compositions as dark circles.

4.1.1 Solid Solutions in SrTiO₃

Initially, the substitution of La³⁺ for Sr²⁺ in SrTiO₃ seems unlikely because the difference in valence between these two ions requires additional oxygen to be incorporated if charge neutrality is to be maintained. The oxygen sites of the SrTiO₃ perovskite structure are fully occupied, and so one must propose interstitial oxygen positions or some other structural modification if extensive solid solution is to be believed. It is not surprising then, that the initial reports suggested that the solubility of La in SrTiO₃ only occurred to a limited extent (Tofield and Scott, 1974). These authors examined a sample with the composition Sr_{0.8}La_{0.2}TiO_{3.1}, and found it to contain additional peaks in its XRD pattern, assigned to La₂O₃.

However, subsequent studies provided evidence for a significant solid solution range. Bouwma *et al.* (1976), confirming the work of Tien and Hummel (1967), described an intuitively more acceptable solid solution between SrTiO₃ and La_{2/3}TiO₃ in which the oxygen content remains constant, and cation vacancies counteract the difference in charge between Sr²⁺ and La³⁺. Although La_{2/3}TiO₃ has not been observed as a pure phase, small amounts of other cations or Ti³⁺ ($\approx 2\%$, Kestigan and Ward, 1955) are

known to stabilise this cation-deficient perovskite. Bouwma *et al.* also reported solid solution, albeit more limited, between SrTiO₃ and LaTiO_{3.5}, and it is from this work that the solid solution is shown in Figure 4-1 as a shaded region.

The direct substitution of La for Sr may be represented by the formula Sr_{1-x}La_xTiO_{3+1/2x}, and Balachandran and Eror (1981) showed that solid solution up to $x=0.4$ could occur. Only the peaks from a perovskite phase were detected in XRD patterns up to this solubility limit, and the cubic unit cell dimension was found to decrease linearly with increasing La substitution.

These authors (Eror and Balachandran, 1981) also measured the reversible weight change which occurred when samples were heated in alternately reducing and oxidising atmospheres. They found that the charge imbalance was compensated by partial reduction of Ti⁴⁺ to Ti³⁺ in reducing atmospheres, and by incorporation of additional oxygen into the structure in oxidising atmospheres. The difference in weight corresponded to the amount of oxygen predicted by the Sr_{1-x}La_xTiO_{3+1/2x} formulation. Because of the relatively large concentrations involved, Eror and Balachandran ruled out the possibilities that extra oxygen was located at grain boundaries, in interstitial sites, or in an additional phase. Instead, they proposed that planes of SrO formed within the perovskite matrix with the same structure as those in the Ruddlesden-Popper compounds (see Chapter 3). To maintain the correct cation ratio, it was also necessary to propose some vacancies of the Sr sites. The work described in the previous chapter, and that of Tilley (1977a), has shown that SrO planes in perovskite do not form extensive ordered arrays when present in low concentrations, and therefore do not appear as a new phase in XRD patterns.

Several later publications supported this model for the accommodation of extra oxygen on the basis of conductivity measurements (Balachandran and Eror, 1982; Odekirk *et al.*, 1982), thermogravimetry (Flandermeyer *et al.*, 1984) and X-ray Rietveld refinement (Howard *et al.*, 1989). In the last of these studies, the structural model did not incorporate the planar defects directly, but instead refined the cell size, strain, and site occupancies of the perovskite phase. At high substitution levels, new

small peaks were discerned in the XRD patterns which were attributed to planar faulting or lamellar intergrowth.

While the evidence for the presence of additional oxygen in La-substituted SrTiO₃ is strong, the manner in which it has been accommodated has so far been investigated only by indirect methods. Particularly at the higher substitution levels, the structural changes which must occur ought to be visible in HREM images, and this formed one of the major objectives in the present study.

4.1.2 Fixed Composition Phases

The compounds in the SrO-La₂O₃-TiO₂ system which have been characterised best are those in the series Sr_{n-3}La₄Ti_nO_{3n+3} with $n=3,4$, and 5. The $n=3$ compound, which has no Sr and has the formula La₄Ti₃O₁₂, was first described by Federov *et al.* (1979) who determined the hexagonal unit cell and noted the similarity between this compound and the so-called hexagonal perovskite phases. Katz and Ward (1964) have described the structural principles underlying this family of compounds by considering perovskite to be composed of layers with the composition AO₃, as opposed to the framework description used mostly throughout this study. A short description of the perovskite structure in terms of AO₃ layers was given in Chapter 1 (Section 1.4). Cubic stacking of the AO₃ layers leads to the familiar perovskite structure with corner-sharing octahedra, but hexagonal stacking is also possible and results in face-sharing octahedra. Further structural description and HREM images of hexagonal perovskites are given by Hutchison and Jacobson (1977).

As in the case of Ruddlesden-Popper compounds, the structure of La₄Ti₃O₁₂ can be described in terms of layers of perovskite separated by some different interlayer structure. Whereas in Ruddlesden-Popper materials the perovskite layers are bounded by planes parallel to perovskite {001} planes, for La₄Ti₃O₁₂ the planar boundaries are parallel to perovskite {111} planes. This can be seen in the structural diagram shown in Figure 4-2. The perovskite layers are 3 octahedra thick, and are separated by what

may be considered as planes of empty octahedra. These share faces with the octahedra in neighbouring perovskite blocks as opposed to the corner-sharing arrangement in perovskite, which presumably explains why they are not occupied by Ti atoms.

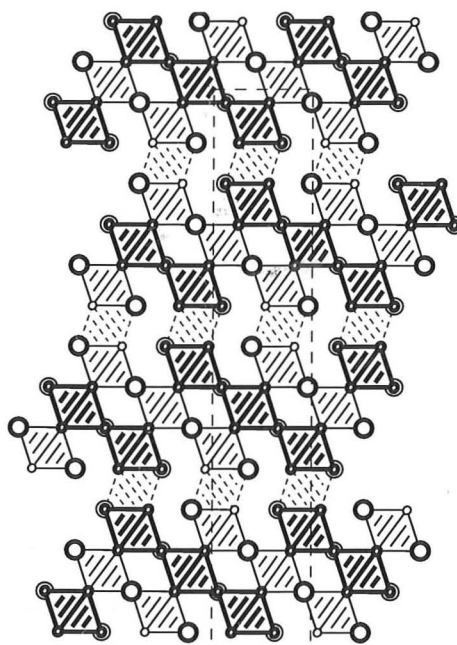


Figure 4-2 Structure of $\text{La}_4\text{Ti}_3\text{O}_{12}$ viewed in the $[100]$ direction. The dashed octahedra are the vacant face-sharing ones between perovskite lamellae.

If the thickness of the perovskite blocks is varied, then a series of compounds $\text{La}_{n+1}\text{Ti}_n\text{O}_{3n+3}$ arises where n denotes the number of octahedra across each perovskite layer. Note that the average valence of Ti decreases with increasing n , which must be greater than or equal to 3 if Ti valences larger than +4 are to be avoided. Such materials have been prepared by Bontchev *et al.* (1993) and Van Tendeloo *et al.* (1994) who have confirmed the structures by XRD and HREM. These authors have also outlined the general structural principles and prepared ordered intergrowths of neighbouring members in the $\text{La}_{n+1}\text{Ti}_n\text{O}_{3n+3}$ series. Because of the reduced Ti valence, compounds with $n > 3$ must be synthesised under non-oxidising conditions.

As well as preparing materials with lower Ti valences, it is also possible to produce isostructural compounds by substituting a divalent metal in place of La^{3+} . This is precisely what occurs in the $\text{Sr}_{n-3}\text{La}_4\text{Ti}_n\text{O}_{3n+3}$ series, and the $n=4$ (German and Kovba,

1983,1985) and $n=5$ (Saltykova *et al.*, 1989) members have been isolated. Although the XRD patterns of these compounds bear a strong resemblance to those of the $\text{La}_{n+1}\text{Ti}_n\text{O}_{3n+3}$ phases, their structures have not yet been verified by simulation of XRD patterns or by electron microscopy.

The final group of compounds to be considered are those represented by yet another general formulation, $\text{SrLa}_2\text{Ti}_n\text{O}_{2n+4}$. Sidorova *et al.* (1982) have reported the existence of compounds corresponding to $n=2,3$, and 4 in this series. However, the composition diagram (Figure 4-1) shows that the $n=4$ compound lies in the range of solid solution described in the previous section for La-substituted SrTiO_3 . This material may therefore be a special case of the solid solution structure. In addition, the existence of the $n=2$ compound has been disputed by German and Kovba (1983) who suggested that this composition gives a mixture of three separate phases. Structural models have not been proposed for the $\text{SrLa}_2\text{Ti}_n\text{O}_{2n+4}$ materials, and so further investigation including structural determination is required if they are to be accepted as true single phase compounds.

4.2 La-Substituted SrTiO_3

4.2.1 Structural Determination

A number of preparations covering the entire range of $\text{Sr}_{1-x}\text{La}_x\text{TiO}_{3+1/2x}$ compositions were reacted at 1350°C , and portions of the XRD patterns obtained from four of these samples are shown in Figure 4-3. The lowest trace, as expected, showed only the peaks arising from perovskite SrTiO_3 . As the level of La substitution was increased, the SrTiO_3 peaks broadened and diminished in intensity, most clearly seen in the diffraction peak near $58^\circ 2\theta$. In samples with compositions corresponding to $x=0.4-0.5$, new weak peaks could be discerned in the XRD trace which were strongest at ≈ 28 and $30^\circ 2\theta$ (pattern 'c', Figure 4-3). These peaks continued to grow at the expense of perovskite peaks with further La substitution until only the peaks of a new phase were

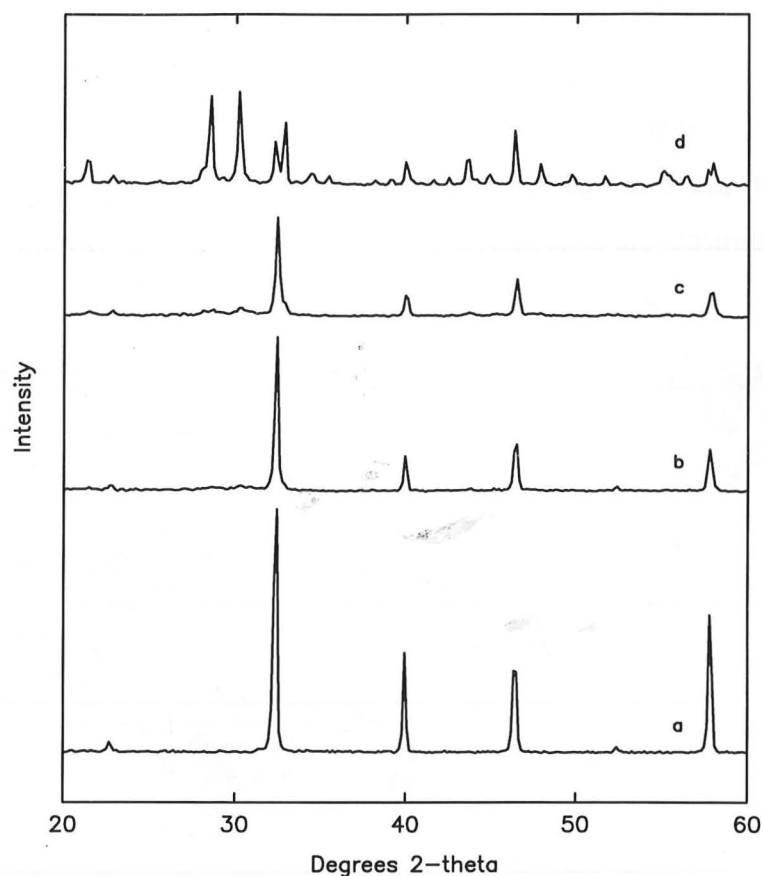


Figure 4-3 Region of XRD patterns from several representative Sr_{1-x}La_xTiO_{3+1/2x} specimens. The compositions were a) $x=0$; b) $x=0.2$; c) $x=0.5$; d) $x=0.8$.

observed for the composition $x=0.8$ (pattern 'd'). Although there was considerable overlap between the diffraction peaks of the new phase and those of SrTiO₃, the fact that the intensity ratios between the new peaks did not change with further La substitution suggested that the perovskite phase was no longer present in significant concentrations at the $x=0.8$ composition.

The structural changes which occurred as a result of La substitution were determined by HREM. This indicated that throughout the substitution range, layered features were present in the perovskite matrix whose frequency correlated with the extent of La substitution. The layer structure was most easily identified for the new phase ($x=0.8$) and so this composition shall be considered first. Figure 4-4 shows a micrograph recorded from an $x=0.8$ sample which is characterised by a regularly spaced array of layers with a strong, distinctive contrast. The appearance of these layers strongly resembled those in HREM images published recently by Williams *et*

al. (1991a) for a reduced lanthanum titanate, $\text{La}_5\text{Ti}_5\text{O}_{17}$. The composition of the sample prepared here, $\text{SrLa}_4\text{Ti}_5\text{O}_{17}$, gave a further indication that the two compounds might be isostructural. This was confirmed by simulating images of $\text{La}_5\text{Ti}_5\text{O}_{17}$ which showed excellent agreement with the experimental image of $\text{SrLa}_4\text{Ti}_5\text{O}_{17}$ (see inset, Figure 4-4). Further confirmation that the two compounds are isostructural was given by the close similarity of their XRD patterns.

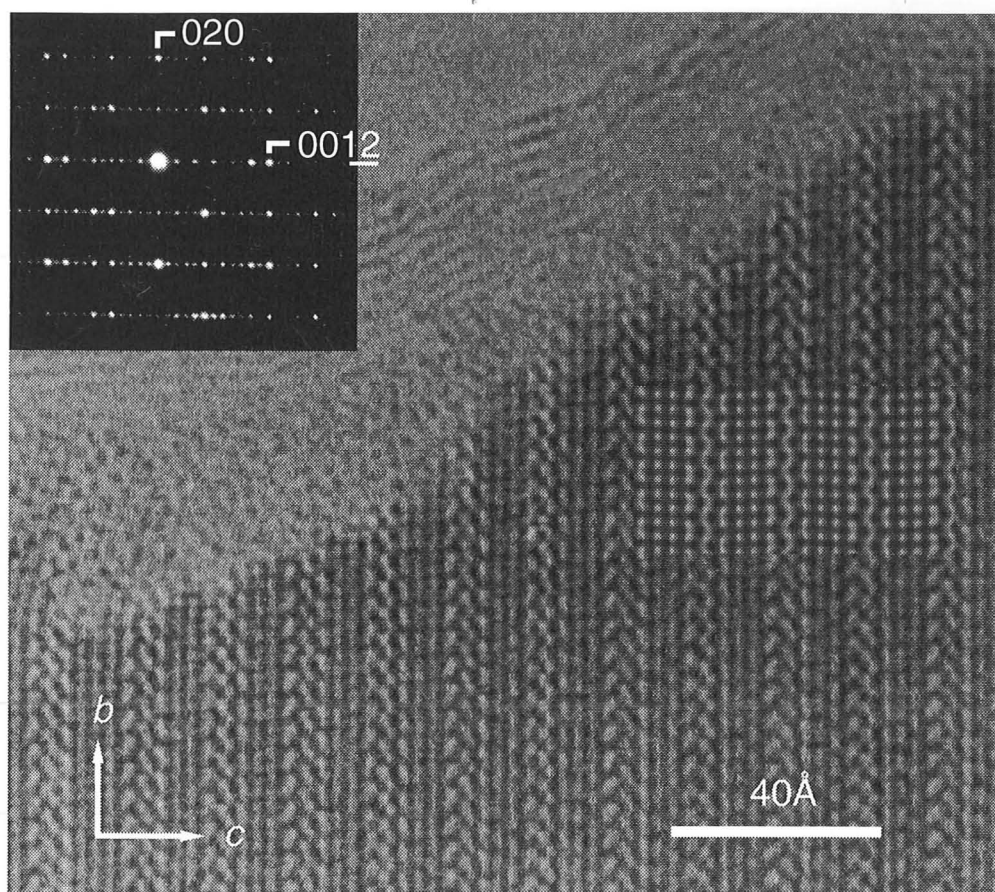


Figure 4-4 HREM image of $\text{SrLa}_4\text{Ti}_5\text{O}_{17}$ taken in the $[100]$ direction, with simulated image inset for a 23.6\AA thick crystal at a defocus of -225\AA .

$\text{La}_5\text{Ti}_5\text{O}_{17}$ is another variant of a layered structure based on perovskite, in this case composed of perovskite layers 5 octahedra across bounded by planes parallel to a $\{110\}$ perovskite plane (Figure 4-5). Adjacent layers are displaced perpendicular to this plane, and also by half an octahedron body diagonal in the a direction. The $[010]$ projection drawn in Figure 4-5b shows how the cooperative tilting of octahedra leads to monoclinic symmetry and a doubling of the a cell dimension. As for Ruddlesden-Popper compounds, a series of related materials can be formed by varying the

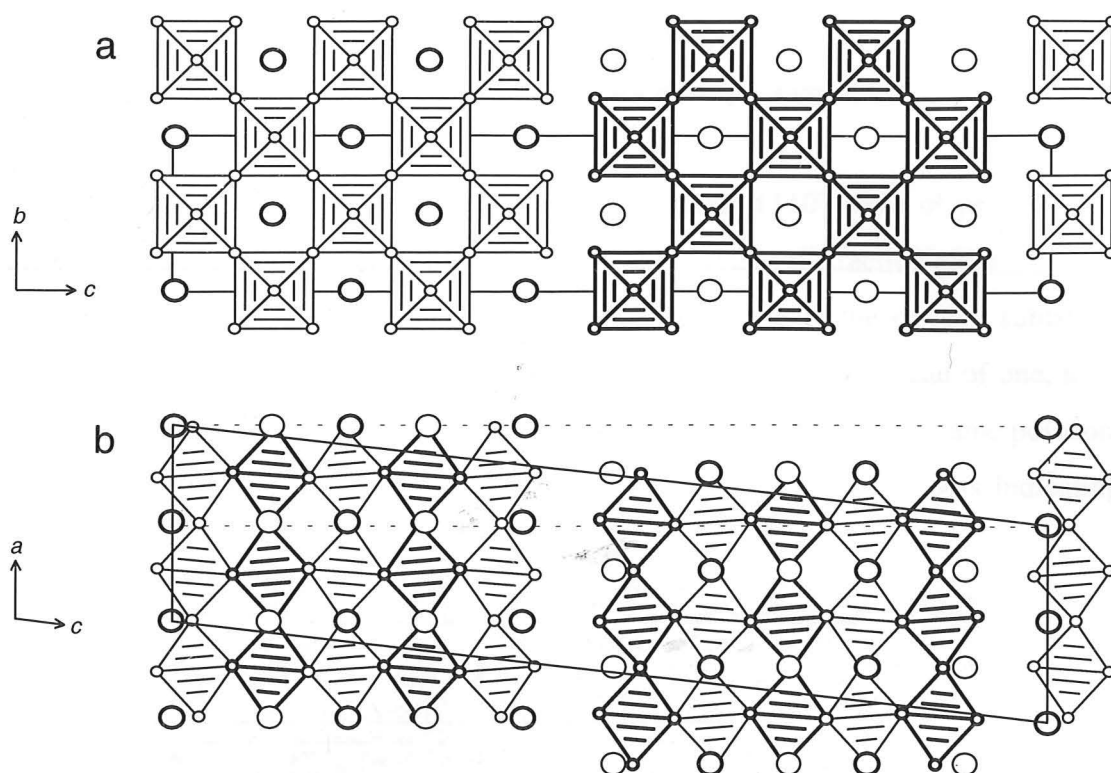


Figure 4-5 Schematic structure of $\text{La}_5\text{Ti}_5\text{O}_{17}$ in a) [100] and b) [010] projections. As in other structural diagrams, the light and heavy ruling indicate a difference in height along the viewing direction. Unit cells are outlined; in b) the dotted cell shows the orthogonal subcell determined by the cation positions only.

thickness of the perovskite slabs. For example, $\text{La}_2\text{Ti}_2\text{O}_7$ has a similar structure in which the perovskite blocks are 4 octahedra across (Gasperin, 1975).

In samples with less La substitution, *i.e.* $x < 0.8$, the same layered features were observed but in a lower concentration. For example, Figure 4-6 shows HREM images from an $x=0.4$ sample in which an individual $\text{La}_2\text{Ti}_2\text{O}_7$ -type layer and a small cluster of such layers were observed within the perovskite host. The impression gained from examining a number of crystals was that the layers were present predominantly in clusters rather than as isolated features.

Although several attempts were made to image features such as these in specimens with a small degree of La substitution ($x \leq 0.2$), no suitable crystals could be found in the electron microscope. This was thought to be due to the difficulty in locating suitably oriented crystals rather than an absence of $\text{La}_2\text{Ti}_2\text{O}_7$ -type layers. However,

images were readily obtained which were consistent with this layer structure positioned perpendicular to the electron beam, for example Figure 4-7.

The only feature which distinguishes this from a simple {110} view of perovskite is the weak doubling of the a dimension visible in the electron diffraction pattern (inset). The presence of $\text{La}_2\text{Ti}_2\text{O}_7$ -type layers causes a disturbance in the oxygen sublattice which increases the periodicity along the a axis to two octahedra instead of one, as in $\text{La}_5\text{Ti}_5\text{O}_{17}$ (Figure 4-5b). The metal atoms remain in approximately the same position, and since diffraction from oxygen is relatively weak the diffraction spots indicating

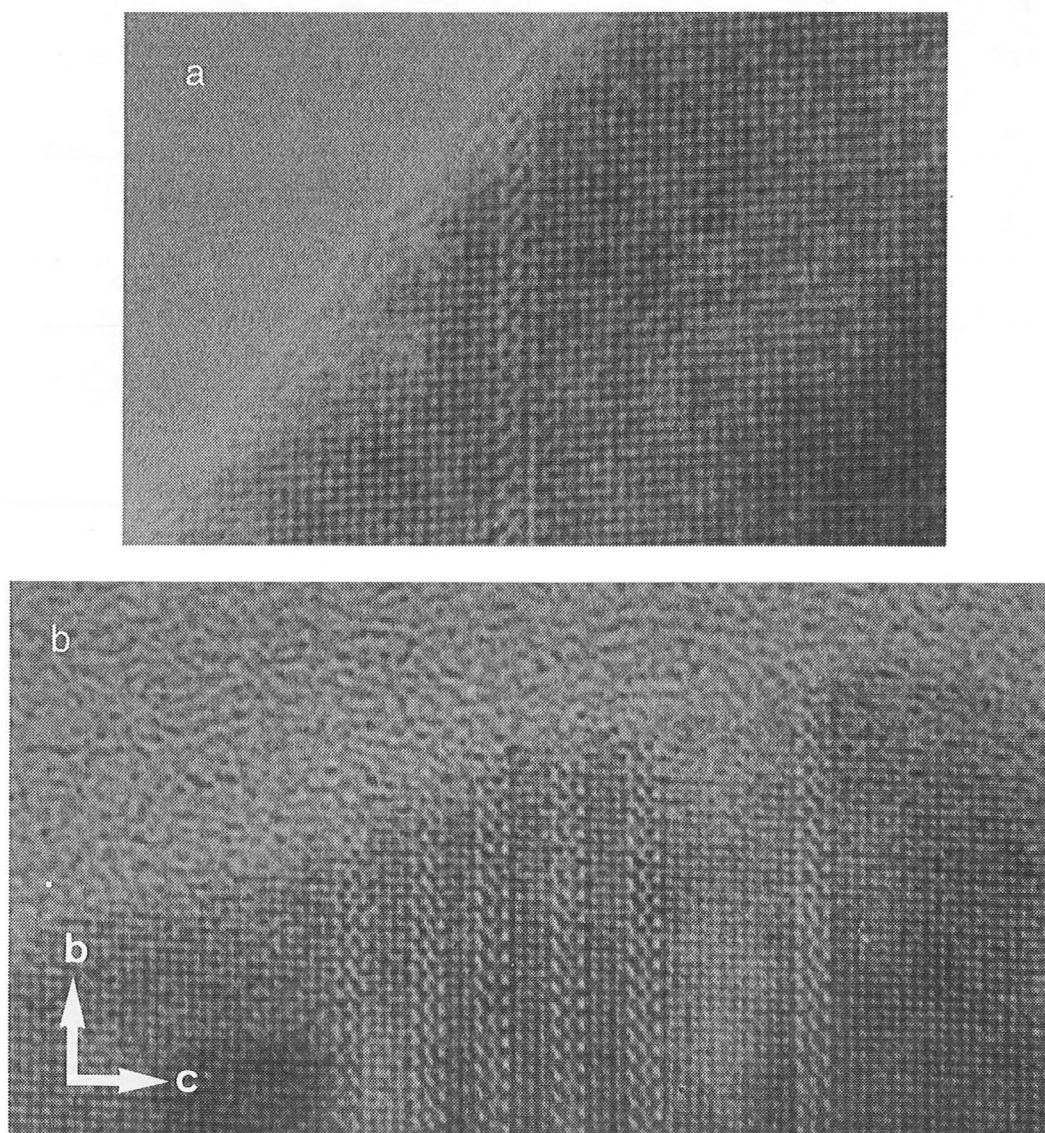


Figure 4-6 HREM images of a) an isolated layer, and b) a group of layers from a sample with a composition corresponding to $x=0.4$. The layer structure can be identified by comparison with the previous micrograph.

the true a repeat are quite faint. It would appear that $\text{Sr}_{1-x}\text{La}_x\text{TiO}_{3+1/2x}$ materials have a preference for cleaving along planes parallel to the layer structure and the likelihood of locating suitable crystals with layers parallel to the electron beam diminishes with decreasing La substitution. No evidence was found for the presence of Ruddlesden-Popper SrO layers in any of the $\text{Sr}_{1-x}\text{La}_x\text{TiO}_{3+1/2x}$ preparations, which would have been expected from the proposal of Eror and Balachandran (1981).

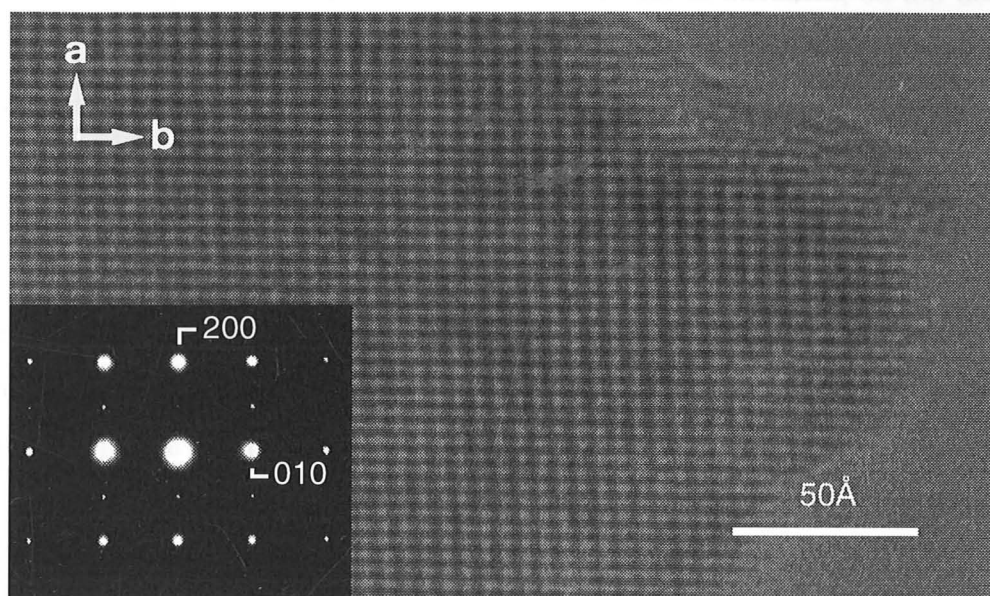


Figure 4-7 HREM image from an $x=0.2$ specimen. The electron diffraction pattern is consistent with $\text{La}_2\text{Ti}_2\text{O}_7$ -type layers viewed perpendicular to the electron beam.

4.2.2 The Accommodation of Extra Oxygen

The formation of layers with a $\text{La}_2\text{Ti}_2\text{O}_7$ -type layer structure provides a good explanation of how the additional oxygen is incorporated into SrTiO_3 when La^{3+} is substituted for Sr^{2+} . The octahedra at the surfaces of the perovskite blocks corner-share oxygens with only four other octahedra instead of the usual six, effectively inserting an additional plane of oxygen atoms at the planar boundary. Unlike the suggestion of SrO layers, this mechanism does not require the presence of lattice vacancies to explain the observed stoichiometries, and provides a consistent structural evolution from SrTiO_3 through to $\text{La}_2\text{Ti}_2\text{O}_7$, the end members of the $\text{Sr}_{1-x}\text{La}_x\text{TiO}_{3+1/2x}$ composition range.

For compositions close to SrTiO_3 , the occurrence of these oxygen-rich layers is relatively infrequent. For example, each layer in an $x=0.2$ specimen will be separated by, on average, 20 octahedra of the perovskite structure. HREM has shown that the layers are not uniformly distributed and so large regions of perovskite remain. This accounts for the corresponding XRD patterns which show only perovskite peaks broadened by the strain and reduction in effective crystallite size produced by the incorporation of planar discontinuities. As substitution is increased, so too does the frequency of layers and they begin to form larger clusters with similar layer spacings, reflected in XRD traces as the emergence of new weak peaks. Only at very high levels of substitution do the layers order into recognisable new compounds.

The structural scheme outlined in this study is also consistent with the evidence presented in previous studies of the $\text{Sr}_{1-x}\text{La}_x\text{TiO}_{3+1/2x}$ system which supported the model based on SrO layers and Sr vacancies. Both the conductivity measurements and the thermogravimetric treatment used to substantiate the SrO layer model conform equally well to the scheme proposed in the present study. Although Howard *et al.* (1989) considered $\text{Sr}_3\text{Ti}_2\text{O}_7$ as the phase most likely responsible for the weak peaks observed in XRD traces of samples with high La contents, the XRD pattern of $\text{La}_5\text{Ti}_5\text{O}_{17}$ was not available at the time of these authors' study. In fact this compound, or the isostructural $\text{SrLa}_4\text{Ti}_5\text{O}_{17}$, provides a better match to the XRD peaks.

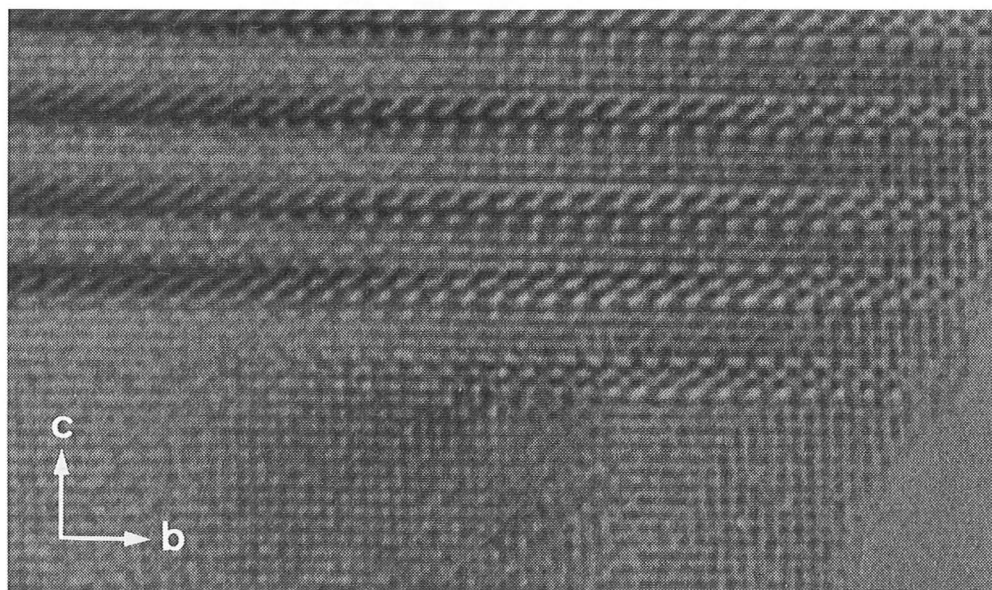


Figure 4-8 HREM image showing a $\text{La}_2\text{Ti}_2\text{O}_7$ -type layer (lower) terminating within a perovskite domain.

The formation of $\text{La}_2\text{Ti}_2\text{O}_7$ -type layers within SrTiO_3 requires the insertion of a plane of oxygen atoms coupled with a relative displacement of the perovskite blocks either side. This does not involve a dramatic structural rearrangement, and may explain the readily reversible nature of the transformation between oxidised and reduced states described earlier. Indeed, Williams *et al.* (1993) have observed the layer structure retreating away from the edge of a crystal in analogous Sr-La-Nb oxides due to *in situ* reduction by the electron microscope. As oxygen was removed, the perovskite blocks either side of the retreating layer were rejoined in the style of a 'molecular zip'. For the present materials, a few examples of layers terminating inside the perovskite matrix were observed, for example Figure 4-8, but there was no change noted with exposure to the electron beam. Presumably, this was due to the greater tendency of Ti to remain in its highest oxidation state compared to Nb.

As in the case of terminating $\{100\}$ layers, a computer-based model has been built to demonstrate how $\{110\}$ layers can terminate within a perovskite matrix. This is presented in Figure 4-9, and shows how the difference in octahedral positions across

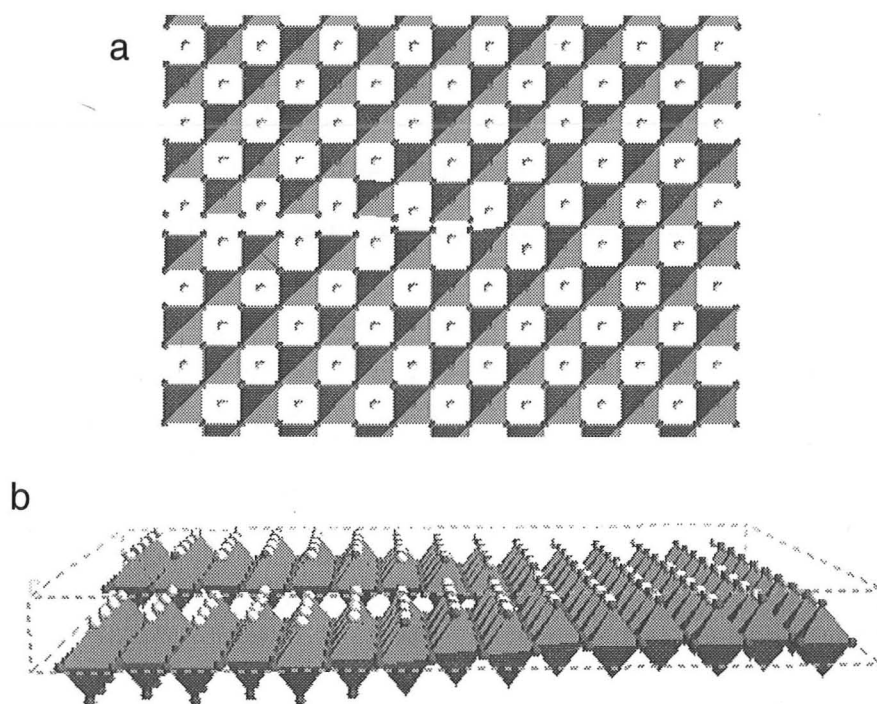


Figure 4-9

Computer-based model of terminating $\text{La}_2\text{Ti}_2\text{O}_7$ -type layer. The plan view (a) shows the layer structure closing up, while the perspective view (b) highlights the variation in height across the layer not present in the perovskite region.

the layer can be gradually brought into registration to form an unlayered perovskite region.

4.2.3 Characterisation of New Compounds

The incorporation of $\text{La}_2\text{Ti}_2\text{O}_7$ -type layers into SrTiO_3 provides the opportunity for a new series of compounds with various ordered layer sequences. This series can be represented by the general formula $\text{Sr}_{n-4}\text{La}_4\text{Ti}_n\text{O}_{3n+2}$ where $n \geq 4$. We have already described the $n=5$ member of this series in Section 4.2.1 when discussing La substitution at the $x=0.8$ composition. The monoclinic unit cell of this compound was refined from the XRD peak positions to give the dimensions $a=7.812(4)\text{\AA}$, $b=5.529(1)\text{\AA}$, $c=31.51(1)\text{\AA}$, and $\beta=97.13(3)^\circ$. Although the XRD peaks could also be indexed on an orthorhombic cell with half the a dimension, [010] electron diffraction patterns confirmed the monoclinic symmetry, which almost certainly arises from the small shifts in the oxygen sublattice depicted in Figure 4-5. The indexed XRD pattern is tabulated in the Appendix.

The only other ordered compound in this series able to be prepared was the $n=4.5$ member, identified by HREM and XRD as an ordered intergrowth of layers 4 and 5 octahedra thick (Figure 4-10). The HREM image (Figure 4-11) displayed a strict alternation of $n=4$ and $n=5$ layers, and the electron diffraction pattern shown inset

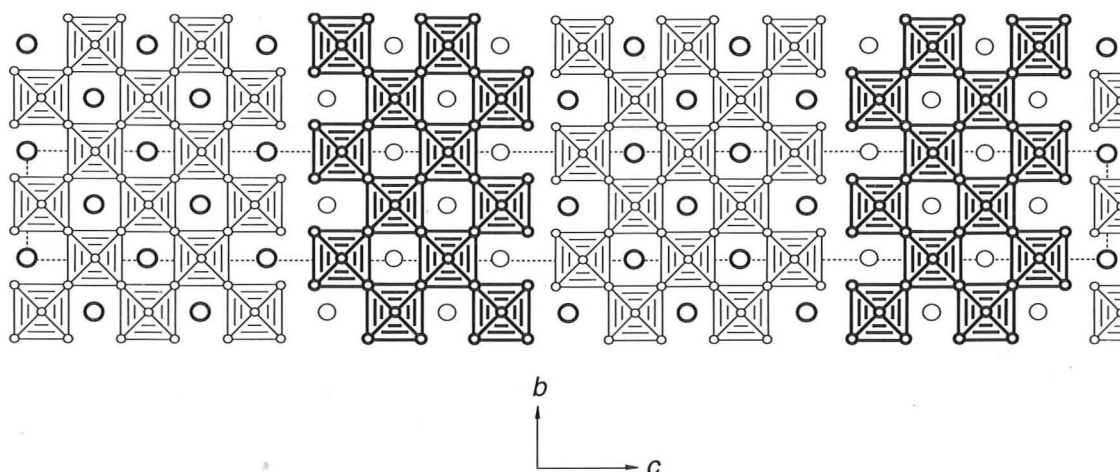


Figure 4-10 [100] diagram of the $\text{SrLa}_8\text{Ti}_9\text{O}_{31}$ structure, comprising regularly alternating perovskite layers 4 and 5 octahedra across.

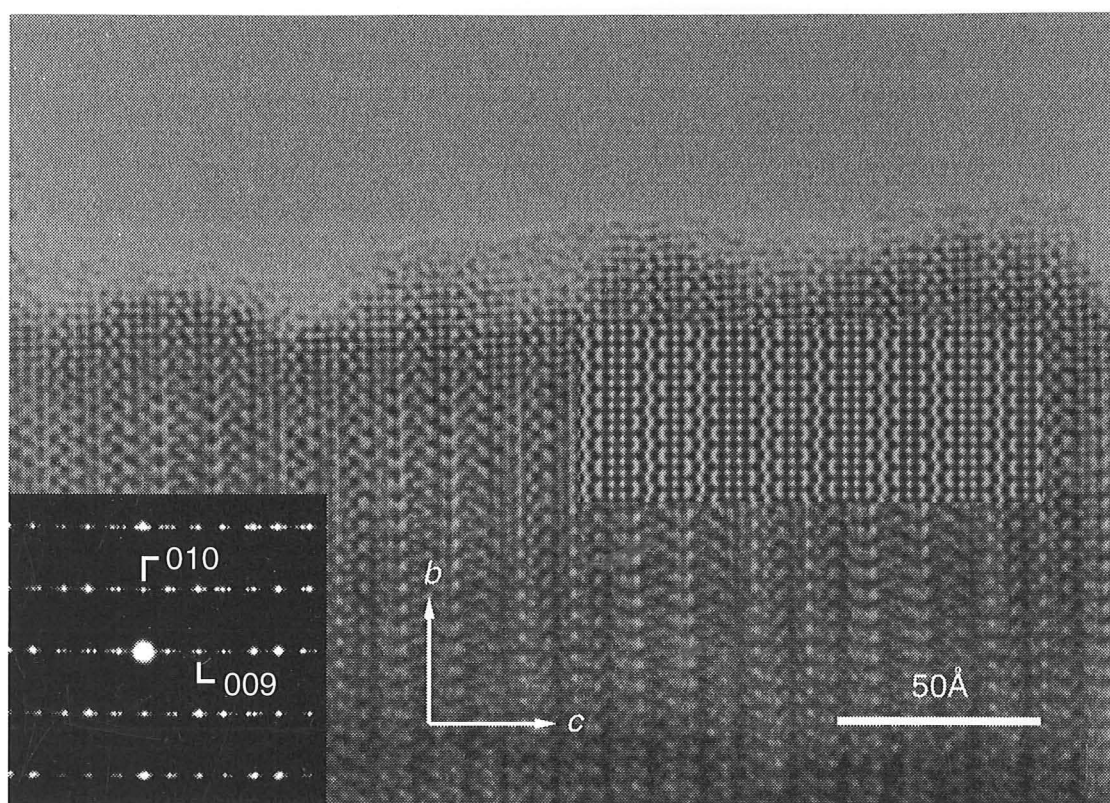


Figure 4-11 HREM image and electron diffraction pattern of an ordered intergrowth of $n=4$ and $n=5$ $\{110\}$ layers. The simulated image inset is for a 23.4\AA thick crystal at a defocus of -275\AA .

indicated a long axis with the expected spacing of $\sim 57\text{\AA}$. The simulated HREM image also shown in this figure was calculated from a set of idealised atomic coordinates generated on the basis of interatomic distances found in $\text{La}_5\text{Ti}_5\text{O}_{17}$.

To confirm that this microscopic observation was representative of the bulk structure, an XRD pattern was calculated from the idealised structure and used to assign Miller indices to the observed peaks. All the peaks in the XRD pattern could be ascribed to an orthorhombic cell with the refined dimensions $a=7.810(2)\text{\AA}$, $b=5.533(2)\text{\AA}$, $c=57.01(2)\text{\AA}$. Note that it is not necessary to consider a monoclinic cell for this compound because the oxygen sublattice reverts to its original configuration after the layer repeat of two layers each of the $n=4$ and $n=5$ members. The XRD pattern of this compound is also tabulated in the Appendix.

Nanot *et al.* (1973) have reported the analogous $n=4.5$, 5 and 6 compounds in the Ca-La-Ti-O system. However, the $n=6$ member of the Sr-containing series could not be

synthesised, despite prolonged reactions at temperatures up to 1450°C. After a single heating of this composition overnight at 1350°C, the XRD pattern showed primarily broadened perovskite peaks with minor peaks attributed to SrLa₄Ti₅O₁₇. With further heating, the perovskite peaks sharpened and the SrLa₄Ti₅O₁₇ peaks grew to finally yield a steady state mixture of the two oxides, which was assumed to be the equilibrium state. This slow ordering process may also account for the early conflict over whether La has appreciable solubility in SrTiO₃. The very high synthesis temperature (1500°C) employed by Tofield and Scott (1974) led to the ordering of a second phase and their conclusion that SrTiO₃ could accept only limited substitution. Balachandran and Eror (1981), on the other hand, used more modest reaction conditions (1350°C) and therefore observed the disordered "solid solution" indicated by the presence of only perovskite peaks in the XRD pattern.

Layer disorder in the Sr_{n-4}La₄Ti_nO_{3n+2} series was observed more frequently than well-ordered compounds. An example of stacking disorder is shown in Figure 4-12.

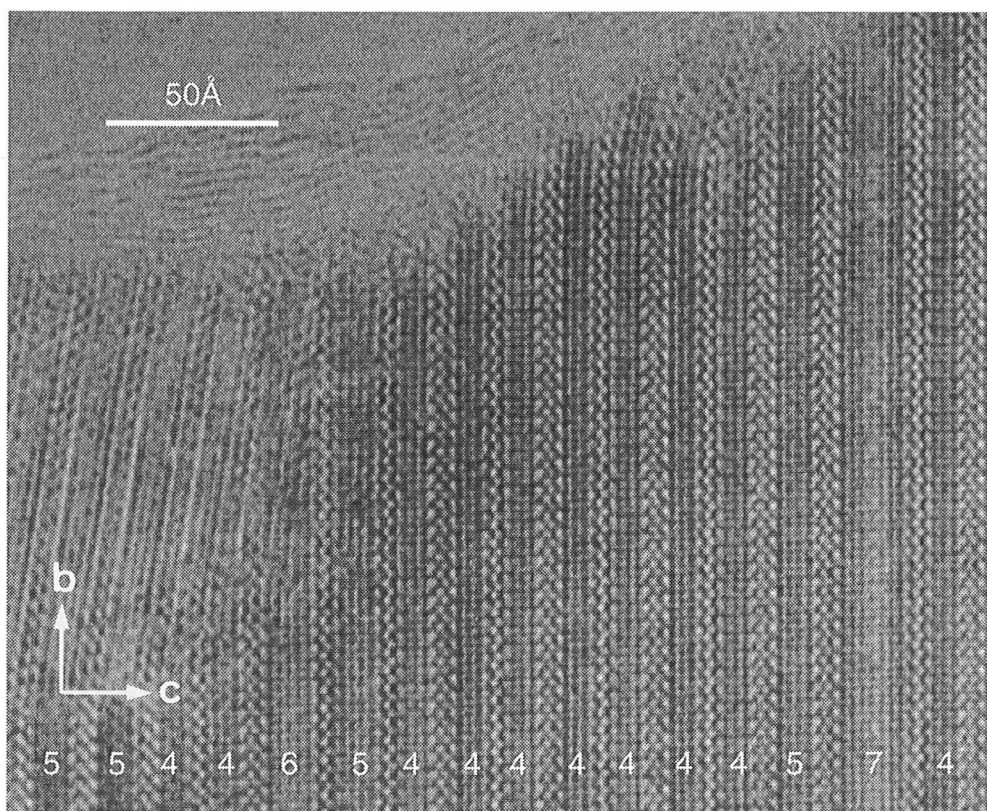


Figure 4-12 Random intergrowth of different Sr_{n-4}La₄Ti_nO_{3n+2} layers. The values of *n* are marked for individual layers.

The tilt boundary near the surface give the impression of a defect caused by grinding during sample preparation.

4.3 Other Reported Sr-La-Ti-O Compounds

4.3.1 $\text{SrLa}_2\text{Ti}_n\text{O}_{2n+4}$ Compounds

The results of experiments described in the previous section also provide information relevant to the $\text{SrLa}_2\text{Ti}_n\text{O}_{2n+4}$ compounds reported by Sidorova *et al.* (1982). The $n=3$ composition of this series has precisely the same stoichiometry as the $n=6$ member of the $\text{Sr}_{n-4}\text{La}_4\text{Ti}_n\text{O}_{3n+2}$ series discussed above, and it has already been demonstrated how syntheses with this composition tend toward a two phase mixture of other compounds.

Similarly, Sidorova *et al.*'s $n=4$ compound lies on the SrTiO_3 - $\text{La}_{2/3}\text{TiO}_3$ solid solution described by Tien and Hummel (1967) and Bouwma *et al.* (1976). Both these latter studies reported ordering of cation vacancies in this system which gave rise to extra peaks in XRD patterns, which may also be the origin of Sidorova *et al.*'s phase.

Efforts to prepare the remaining composition, $n=2$, again resulted in multiphase mixtures, this time containing La_2TiO_5 and SrTiO_3 . It was therefore concluded that the $\text{SrLa}_2\text{Ti}_n\text{O}_{2n+4}$ compositions are not unique phases, and there does not appear to be any structural theme linking them together. It is unfortunate that these are the only ternary Sr-La-Ti oxides listed in the ICDD database of XRD patterns.

4.3.2 $\text{Sr}_{n-3}\text{La}_4\text{Ti}_n\text{O}_{3n+3}$ Compounds

It was possible, however, to confirm the single phase nature of materials in the $\text{Sr}_{n-3}\text{La}_4\text{Ti}_n\text{O}_{3n+3}$ series for $n=3,4$ and 5. An example is presented in Figure 4-13 which shows an HREM image taken from a sample of $\text{Sr}_2\text{La}_4\text{Ti}_5\text{O}_{18}$ ($n=5$) together

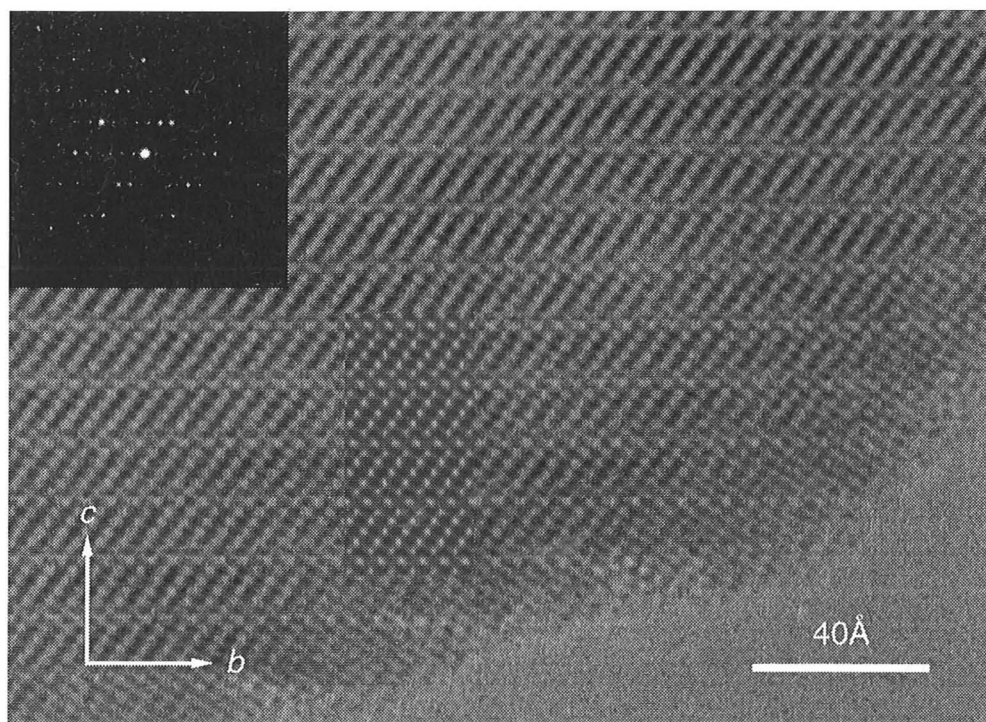


Figure 4-13 HREM image of Sr₂La₄Ti₅O₁₈ with electron diffraction pattern and simulated image (thickness=44.4Å, defocus=-280Å) inset.

with a simulated image which confirms the structure proposed by German and Kovba (1985) for the isostructural Ca-containing compound. Attempts to synthesise materials with $n > 5$ resulted in multiphase samples, in agreement with the findings of Saltkyova *et al.* (1989).

In the La-Ti-O system, Bontchev *et al.* (1993) have carried out Rietveld refinements for the analogous structures with $n=4$ and $n=3.5$. The latter compound is a regularly alternating intergrowth of perovskite layers 3 and 4 octahedra thick. However, no refined structures have been reported for the $n=3$ compound (La₄Ti₃O₁₂) and, aside from the HREM evidence found in the present study, structures for the Sr-containing materials have only been inferred from the similarity of their XRD patterns to other compounds. Rietveld refinements were therefore carried out for the $n=3,4$ and 5 members in the Sr _{$n-3$} La₄Ti _{n} O_{3 $n+3$} family. The results are presented in Table 4-1 to Table 4-3 and Figure 4-14 to Figure 4-16. In these refinements, it was necessary to constrain the thermal parameters to prevent the values for some atoms becoming negative and therefore meaningless. This was achieved by refining a single thermal parameter for groups of atoms, although in La₄Ti₃O₁₂ fixed values were required.

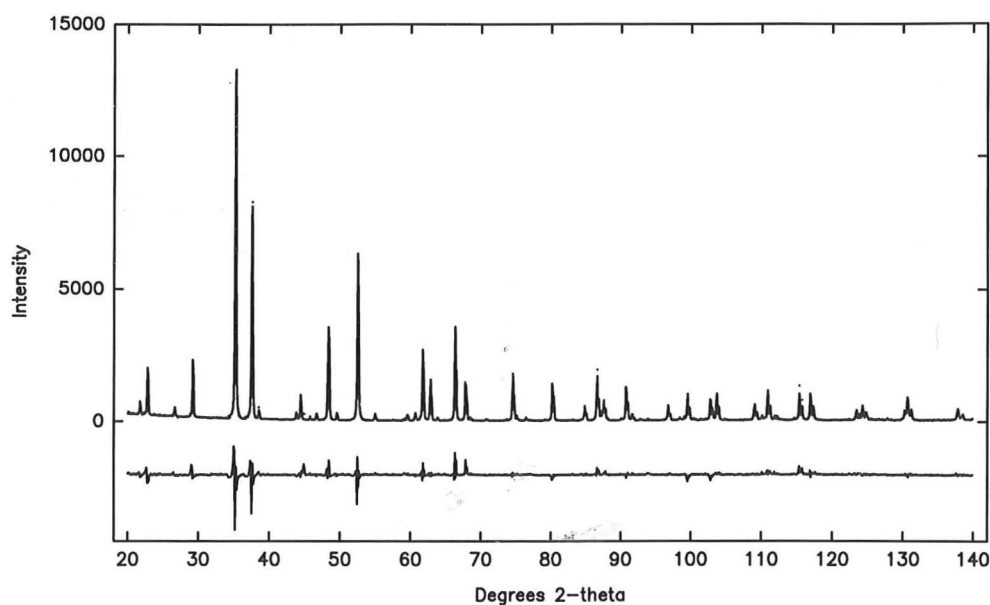


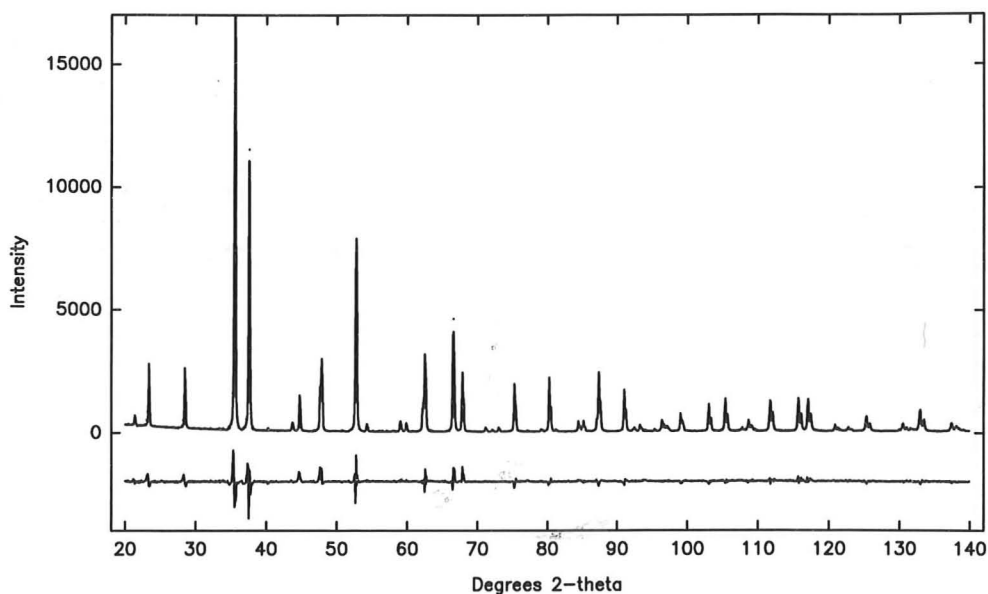
Figure 4-14 Observed (dots), calculated (line) and difference (lower) XRD profiles from the Rietveld refinement of $\text{La}_4\text{Ti}_3\text{O}_{12}$ (Co K_α radiation).

Atom	Site	x	y	z	B
La(1)	6c	0	0	0.1343(1)	0.2
La(2)	6c	0	0	0.2880(1)	"
Ti(1)	3a	0	0	0	"
Ti(2)	6c	0	0	0.4251(2)	"
O(1)	18h	0.169(3)	0.339(3)	0.6239(6)	0.8
O(2)	18h	0.174(3)	0.348(3)	0.4520(5)	"

Table 4-1 Refined coordinates for $\text{La}_4\text{Ti}_3\text{O}_{12}$ in space group $R\bar{3}m$. The cell parameters were $a=5.5527(2)\text{\AA}$ and $c=28.186(2)\text{\AA}$. Agreement indices $R_B=8.60\%$ and $S=2.72$ were obtained.

Atom	Site	x	y	z	B
Sr/La(1)	2b	0	0	0	0.2(2)
Sr/La(2)	4d	1/3	2/3	0.2136(1)	"
Sr/La(3)	4d	1/3	2/3	0.3927(1)	"
Ti(1)	4d	1/3	2/3	0.0518(4)	"
Ti(2)	4c	0	0	0.1598(3)	"
O(1)	6e	1/2	0	0	1.1(2)
O(2)	12g	0.130(6)	0.784(6)	0.0970(11)	"
O(3)	12g	0.203(8)	-0.141(8)	0.3026(10)	"

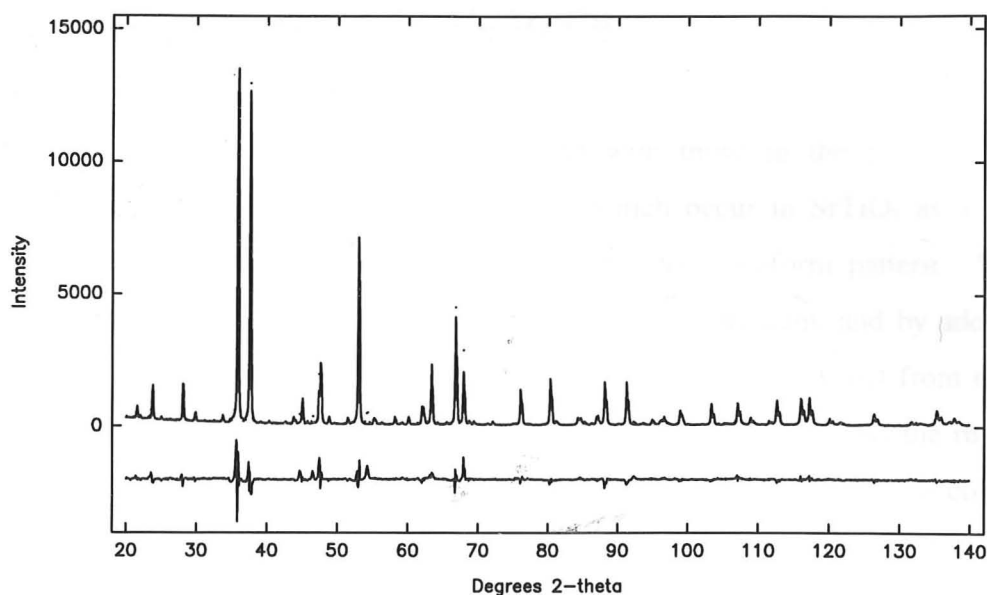
Table 4-2 Refined coordinates for $\text{SrLa}_4\text{Ti}_4\text{O}_{15}$, space group $P\bar{3}c1$. The cell parameters were $a=5.5479(2)\text{\AA}$ and $c=22.1347(8)\text{\AA}$. Agreement indices obtained were $R_B=6.06\%$, $S=2.48$.

Figure 4-15 Rietveld plot for SrLa₄Ti₄O₁₅.

Atom	Site	x	y	z	B
Sr/La(1)	6c	0	0	0.0877(1)	0.16(10)
Sr/La(2)	6c	0	0	0.1867(1)	0.64(12)
Sr/La(3)	6c	0	0	0.3627(2)	0.33(11)
Ti(1)	3a	0	0	0	0.31(8)
Ti(2)	6c	0	0	0.4505(3)	"
Ti(3)	6c	0	0	0.2754(3)	"
O(1)	18h	0.1667(19)	0.8333(19)	0.1351(7)	2.4(2)
O(2)	18h	0.1609(24)	0.8391(24)	0.2498(8)	"
O(3)	18h	0.169(3)	0.831(3)	0.6926(9)	"

Table 4-3 Refined coordinates for Sr₂La₄Ti₅O₁₈, space group $R\bar{3}m$. The cell parameters were $a=5.5433(3)\text{\AA}$ and $c=40.047(4)\text{\AA}$. Agreement indices obtained were $R_B=9.94\%$, $S=2.97$.

The most notable feature of the refined structures was the shortening of the Ti-O distances at the surfaces of the perovskite lamellae. Whereas the bond lengths within the lamellae were in the range 1.854-2.180Å, those at the surface were between 1.754 and 1.859Å. Accompanying this distortion was a movement of Sr/La atoms in the opposite direction, which resulted in the shortest metal-metal distances for these atoms across the layer plane. A gradation in behaviour was observed for metal-metal distances across the perovskite lamellae, summarised in Table 4-4. Distances between

Figure 4-16 Rietveld plot for $\text{Sr}_2\text{La}_4\text{Ti}_5\text{O}_{18}$.

nearest Sr/La atoms generally increased toward the centres of the perovskite lamellae, while the Ti-Ti distances exhibited the opposite trend.

Atoms	$n=3$	$n=4$	$n=5$
		3.997	3.984
Ti-Ti	4.005	3.940	3.953
Sr/La-Sr/La	3.990	3.988	3.972
	3.963	3.975	3.961
	3.626	3.586	3.978
			3.579

Table 4-4 Metal-metal distances (\AA) for the refined $\text{Sr}_{n-3}\text{La}_4\text{Ti}_n\text{O}_{3n+3}$ structures. The dotted lines represent the positions of the layer of vacant face-sharing octahedra.

Samples were also reacted with compositions equivalent to $n=3.5$ and $n=4.5$ in an effort to synthesise ordered intergrowths similar to the one reported by Bontchev *et al.* (1993). As was the case in the {100} layered family, this resulted in two-phase mixtures of compounds with a single layer repeat. In fact, HREM showed the samples prepared in the {111} layered family to be remarkably free of stacking defects.

4.4 Summary and Conclusions

The results presented in this chapter, along with those in the previous chapter, demonstrate that the structural modifications which occur in SrTiO₃ as a result of three different changes in stoichiometry conform to a uniform pattern. We have altered the stoichiometry by adding oxygen, removing titanium, and by adding both strontium and oxygen together. The last of these changes is distinct from removing titanium in that it alters the (Sr+La):O ratio from 1:3. In each case, the result is to introduce layered defects into the perovskite matrix which order into new compounds at high concentrations.

The addition of oxygen, effected by substituting La³⁺ for Sr²⁺, produced layers oriented along {110} perovskite planes and gave rise to compounds with $n=4, 4.5$ and 5 in the series Sr _{$n-4$} La₄Ti _{n} O_{3 $n+2$} . The $n=4$ phase corresponds to La₂Ti₂O₇, a material known and characterised for some time. The additional oxygen is accommodated by the different arrangement of octahedra at the layer boundary, and unlike a previously proposed model, does not require the presence of lattice vacancies.

Removal of titanium without changing the oxygen content was accomplished by simultaneously replacing 4 moles of Sr²⁺ with La³⁺ for each mole of Ti⁴⁺ removed. The layers formed by this substitution are parallel to perovskite {111} planes and contain sheets of face-sharing octahedra which remain unoccupied by titanium. Compounds corresponding to $n=3, 4$ and 5 in the family Sr _{$n-3$} La₄Ti _{n} O_{3 $n+3$} were able to be prepared using this procedure.

Addition of strontium and oxygen resulted in the formation of SrO rocksalt layers along perovskite {100} planes (Chapter 3). When the concentration of additional SrO was high enough, the rocksalt layers formed regularly spaced arrays to give the Ruddlesden-Popper compounds Sr _{$n+1$} Ti _{n} O_{3 $n+1$} with $n=1, 2$ and 3.

In each of these families the general formula is arranged so that n indicates the number of octahedra in the perovskite blocks between successive layers. When n

exceeded the values given, the layers were no longer found in regularly spaced sequences but in a disordered fashion which gave a variety of layer spacings within any local region. Rather than being distributed in a truly random fashion throughout the sample, a tendency for clusters of irregularly-spaced layers was observed. These layers are not detectable in X-ray diffraction patterns, and have led to the belief that these compositions are part of a solid solution range. However, the structural changes which occur are much greater than those found in traditional solid solutions, and we therefore suggest that a better description would be of a "structural solid solution" of layered features within the perovskite host.

A revised composition diagram for the SrO-La₂O₃-TiO₂ system based on these findings is given in Figure 4-17, in which those compounds which were not considered single-phase have been excluded. However, a new compound not discussed so far is also shown on the diagram with the composition Sr₃La₂Ti₂O₁₀. This new phase was discovered during the course of investigating the reported Sr-La-Ti-O materials, and the determination of its structure is the subject of the next chapter.

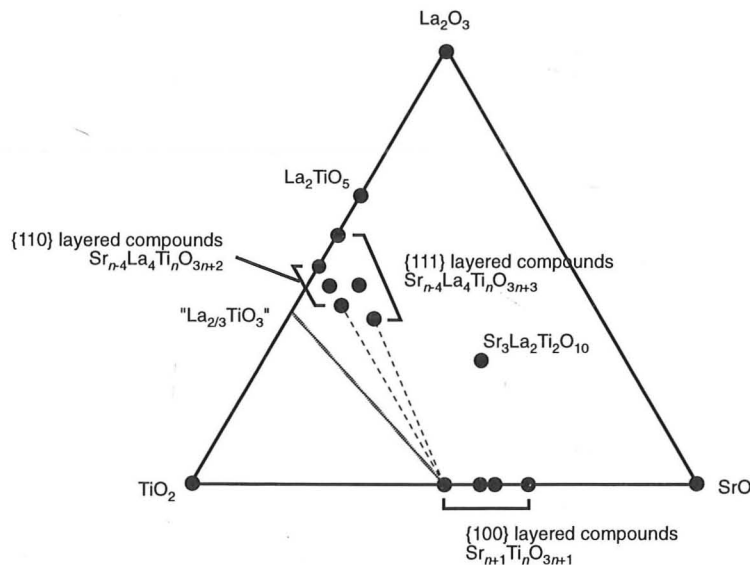


Figure 4-17 Composition diagram for the SrO-La₂O₃-TiO₂ system based on the findings in this study. The dotted lines indicate "structural solid solutions" between SrTiO₃ and ordered layered compounds in which the layers are irregularly intergrown.

Chapter 5

Sr₃La₂Ti₂O₁₀, a New Compound in the SrO-La₂O₃-TiO₂ System

- 5.1 Introduction
 - 5.2 Formulation of a Draft Structure
 - 5.3 Confirmation by Rietveld and HREM
 - 5.4 Defects and Intergrowths
 - 5.5 Surface Modification Under the Electron Beam
 - 5.6 Summary and Conclusions
-

5.1 Introduction

It has been shown in the previous chapter how substituting La³⁺ for Sr²⁺ in SrTiO₃ resulted in the formation of oxygen-rich planes along perovskite {110} planes. With this in mind, the possibility of La substitution in Ruddlesden-Popper compounds was investigated to see if similar layers could be introduced into these compounds, which already possess layered features in a different orientation. The results indicated that these two layer types could not be combined in simple intergrowths. However, new peaks appeared in XRD patterns which could not be explained by any of the phases considered so far. By varying the composition in a systematic fashion it was possible to prepare samples whose XRD patterns displayed only the peaks from this new phase. This established the composition as Sr₃La₂Ti₂O₁₀, and further experiments were undertaken to determine the structure of this phase.

5.2 Formulation of a Draft Structure

A possible unit cell was proposed by examining a number of electron diffraction patterns taken from different crystals lying in different orientations. It was difficult to obtain diffraction patterns from different zone axes of the same crystal in the available microscopes due to the limited range of tilt possible. The most likely unit cell which

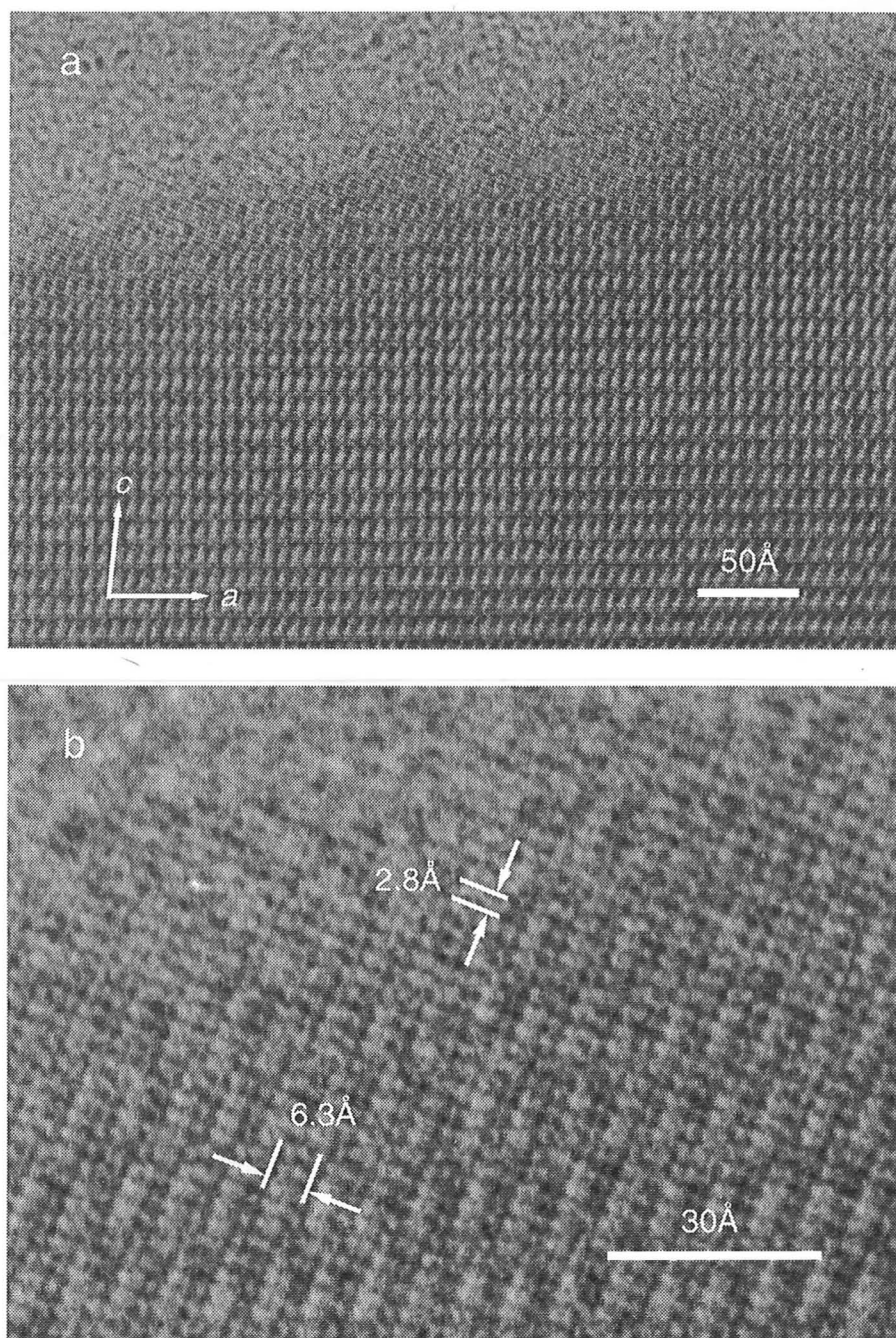


Figure 5-1 HREM images of $\text{Sr}_3\text{La}_2\text{Ti}_2\text{O}_{10}$ viewed along the b axis. The lower magnification in (a) emphasises the layered nature, while the enlarged region in (b) shows more detail.

emerged was a monoclinic one with the approximate dimensions $a=6.9\text{\AA}$, $b=5.5\text{\AA}$, $c=12.2\text{\AA}$, and $\beta=85^\circ$. All of the peaks observed in the XRD pattern could also be indexed using this cell.

HREM images taken along the b axis proved to be the most fruitful in locating possible atom positions. Micrographs recorded from this orientation, for example Figure 5-1a, indicated that $\text{Sr}_3\text{La}_2\text{Ti}_2\text{O}_{10}$ possesses a layered structure, with the layer plane oriented approximately perpendicular to c . Between the layers, rows of dots could be discerned spaced at $\approx 2.8\text{\AA}$ intervals and inclined at $\approx 70^\circ$ to the plane of the layers (Figure 5-1b). The perpendicular separation between the rows of dots was $\approx 6.3\text{\AA}$.

The spacing of 2.8\AA is consistent with a perovskite-based structure since this is the width of the TiO_6 octahedra found in SrTiO_3 . Although the spacing of 6.3\AA is not encountered in perovskite, it can be recognised as the distance between layers in the Ruddlesden-Popper compound Sr_2TiO_4 (see Chapter 3).

From all of these considerations a structure was proposed (Figure 5-2) consisting of ribbons of TiO_6 octahedra one octahedron high and four octahedra wide extending down

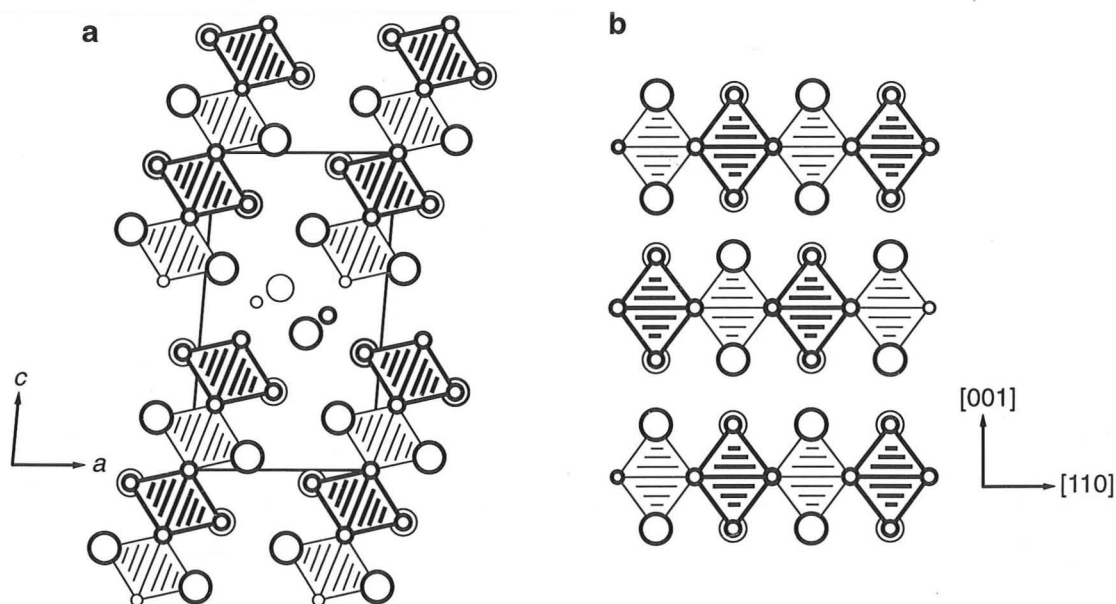


Figure 5-2 a) Structure of $\text{Sr}_3\text{La}_2\text{Ti}_2\text{O}_{10}$ viewed along b . Large circles represent Sr/La atoms, small circles O atoms, and Ti atoms lie at the centres of the octahedra. Heavy ruling indicates a difference in position of $b/2$ over the light ruling. b) $(\bar{1}10)$ projection of the Sr_2TiO_4 structure.

the b axis. The configuration of these ribbons and intervening Sr/La atoms resembles blocks of the Sr_2TiO_4 structure cut along (112) planes. To highlight this, a view of the Sr_2TiO_4 structure is also shown in Figure 5-2. The blocks are layered above one another, and additional Sr/La atoms positioned in the interlayer spaces that result. Preliminary HREM image simulations showed good agreement with the observed micrographs, and so this structure was used for input to the Rietveld refinement programme.

5.3 Confirmation by Rietveld and HREM

Choosing a space group on the basis of systematic absences proved to be impossible, as the large number of potential diffraction peaks did not allow unambiguous indexing of all reflections. Instead, the most symmetric space group which accounted for all the observed peaks was chosen by testing several different space groups in a series of preliminary Rietveld refinements. The most important constraint was that the selected space group had to be consistent with the basic symmetry elements of the trial structure. Using this procedure, space group $P2_1/m$ was selected for further refinements.

With all the atomic parameters unconstrained, the refinement converged to give a good agreement between observed and calculated diffraction patterns, although two structural considerations made the result questionable. Firstly, the refinement gave large standard deviations, and an unreasonably wide variation, for the oxygen temperature factors. To avoid this, a single thermal parameter was refined for all the oxygens in the structure. The second problem was that the positions of oxygen atoms around TiO_6 octahedra resulted in considerable distortion where there seemed no structural reason why this should be so. For example, oxygens linking adjacent TiO_6 octahedra were placed much closer to one of the titanium atoms than the other. For the final refinement, the positions of oxygen atoms forming TiO_6 octahedra were adjusted to give little distortion and bond lengths close to the expected distance of 2.0\AA . The fit with these oxygen positions constrained was only slightly poorer, with the agreement index R_{wp} equal to 10.5% as

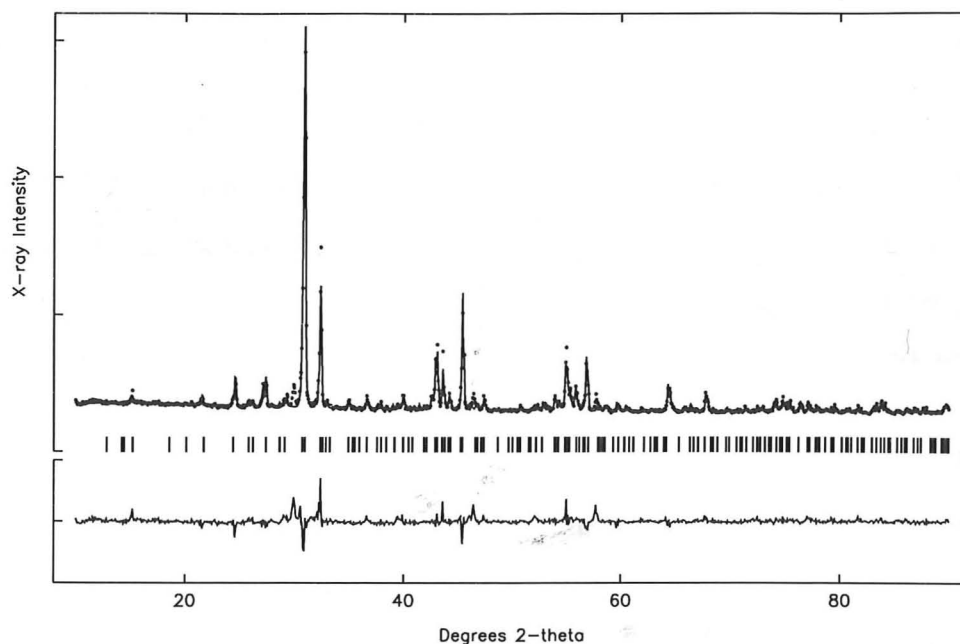


Figure 5-3 Observed (dots), calculated (line) and difference (lower) diffraction patterns for $Sr_3La_2Ti_2O_{10}$. The short vertical lines mark the positions of all potential reflections.

opposed to 10.1% for the unconstrained refinement. The difficulty in defining oxygen positions and temperature factors was considered to be due to the relative insensitivity of the calculated XRD pattern to these parameters.

Figure 5-3 compares the observed and calculated diffraction patterns, and the refined structural parameters are presented in Table 5-1 for a uniform distribution of strontium

Atom	Site	<i>x</i>	<i>y</i>	<i>z</i>	B
Ti(1)	2e	0.073(7)	3/4	0.104(4)	1.7(8)
Ti(2)	2e	0.170(5)	1/4	0.3222(26)	1.0(8)
Sr/La(1)	2e	0.3109(24)	1/4	0.0530(13)	2.1(5)
Sr/La(2)	2e	0.4372(24)	3/4	0.2483(16)	2.0(5)
Sr/La(3)	2e	-0.1865(26)	1/4	0.1586(15)	4.2(6)
Sr/La(4)	2e	-0.0509(27)	3/4	0.3945(17)	2.4(3)
Sr/La(5)	2e	0.4128(18)	3/4	0.5602(11)	0.0(3)
O(1)	2a	0	0	0	2.6(4)
O(2)	4f	0.122	0	0.216	2.6(4)
O(3)	4f	0.214	0	0.434	2.6(4)
O(4)	2e	0.351	3/4	0.042	2.6(4)
O(5)	2e	0.448	1/4	0.269	2.6(4)
O(6)	2e	-0.197	3/4	0.171	2.6(4)
O(7)	2e	-0.110	1/4	0.380	2.6(4)
O(8)	2e	0.374(13)	1/4	0.621(7)	2.6(4)

Table 5-1

Final refined coordinates. Figures in parentheses indicate the estimated standard deviation of the last significant figures. The refined lattice parameters were $a=6.9214(4)\text{\AA}$, $b=5.5294(3)\text{\AA}$, $c=12.3048(8)\text{\AA}$ and $\beta=85.439(4)^\circ$.

and lanthanum over the available sites. Partitioning of strontium and lanthanum between these sites was not able to be determined because the refinement programme did not allow the partial occupancy of these elements to be refined while maintaining a constant overall stoichiometry. Nevertheless, when the occupancies were relaxed a tendency for high lanthanum occupation in the site between the Sr_2TiO_4 blocks was noted. This is also reflected in the anomalously low temperature factor for this site (Sr/La(5) in Table 5-1) compared to the other Sr/La positions. The indexed XRD pattern is listed in the Appendix.

The refined titanium positions led to a slight buckling of the Ti-O ribbons rather than the linear arrangement shown in the idealised view of Figure 5-2. The Sr/La sites within the Sr_2TiO_4 blocks have the same 9-fold coordination as found in Sr_2TiO_4 itself, except for Sr/La(4) which has two additional oxygen neighbours from the adjacent Sr_2TiO_4 block. Since most of the structure is derived directly from Sr_2TiO_4 , the key as to whether it is structurally sensible lies with the additional site placed between the Sr_2TiO_4 blocks. A stereoscopic view of the coordination around this site is presented in Figure 5-4 which shows it to be 9-coordinate with its oxygen atoms reasonably distributed around the central metal atom. The metal-oxygen distances are in the range 2.17-2.94Å, comparable to the other Sr/La atoms.

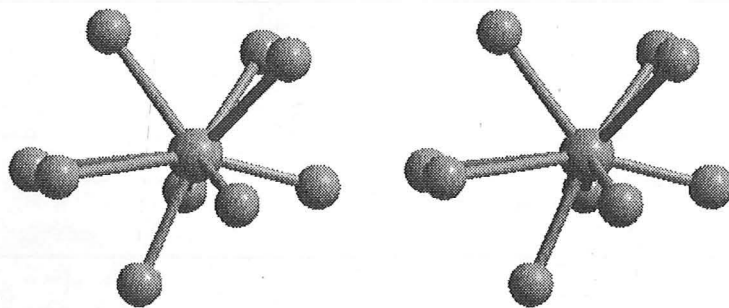


Figure 5-4 Stereo projection of the coordination around Sr/La(5), viewed slightly off the direction of the b axis.

Further confirmation of the proposed structure was sought by comparing simulated and observed HREM images. The agreement was good, shown in Figure 5-5 and Figure 5-6

for images taken in the [100] and [010] directions respectively. A notable feature of [100] images was the dramatic change in contrast with increasing distance from the crystal edge, presumably due to increasing crystal thickness. The image simulations reproduced this behaviour well. Near the crystal edge the simulation matches the observed image in general appearance, but exhibits a greater level of detail than the micrograph (Figure 5-5B). In fact, most of the images recorded from this compound showed poorly ordered or amorphous regions near the edge, and it was thought that some degree of surface disorder was always present.

Further from the edge, the micrograph contained a region of confused detail but with strong diagonal fringes, also contained in the simulated image (Figure 5-5C) for 145 Å thick crystals. It was only at comparatively large crystal thicknesses that the micrograph displayed a clear and regular pattern. The simulated images (Figure 5-5D,E) provided the best match in these regions. It should be noted that although this micrograph exhibited the greatest detail of those recorded in the [100] direction, a consistent beam tilt of 2 mrad around b needed to be incorporated into image simulations to achieve

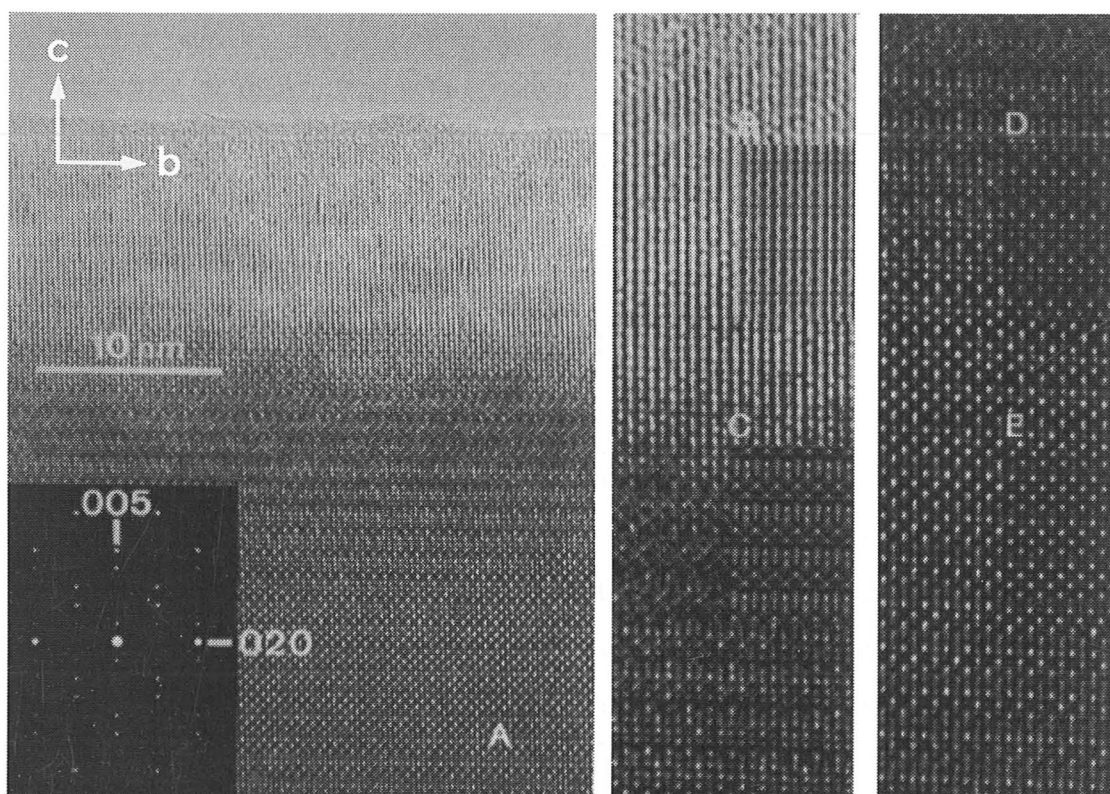


Figure 5-5 A) [100] HREM image and electron diffraction pattern. The enlarged regions (right) include simulated images for: B) thickness 35 Å, defocus -275 Å; C) thickness 145 Å, defocus -325 Å; D) thickness 221 Å, defocus -400 Å; and E) thickness 242 Å, defocus -425 Å. A beam tilt of 2 mrad around b has been included in the simulations.

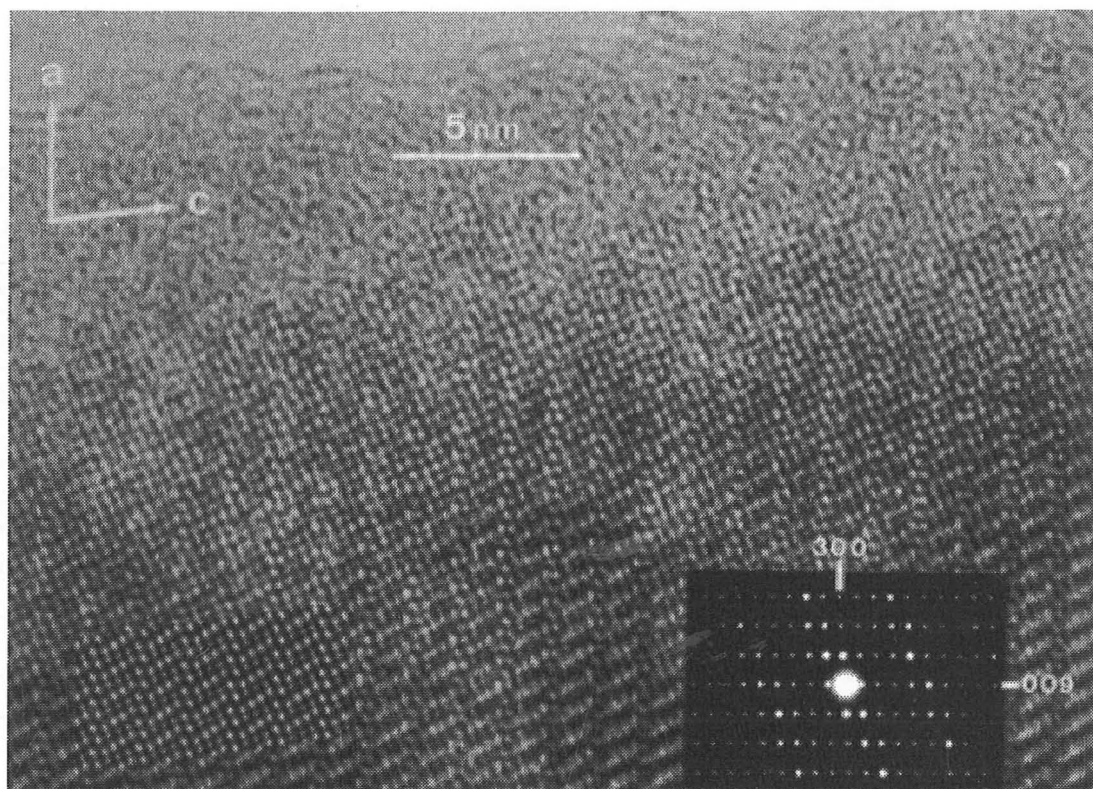


Figure 5-6 [010] HREM image and electron diffraction pattern. The simulated image inset is for a 33\AA thick crystal at a defocus of -225\AA

satisfactory comparisons. Nevertheless, the fact that good agreement was obtained over a large range of thicknesses with sensible defocus values strongly suggests that the cation positions in the proposed structure are correct.

5.4 Defects and Intergrowths

Most of the HREM images obtained from the $\text{Sr}_3\text{La}_2\text{Ti}_2\text{O}_{10}$ sample were, apart from surface disorder, relatively free of defects. A notable exception to this observation is shown in Figure 5-7 which shows a coherent boundary between $\text{Sr}_3\text{La}_2\text{Ti}_2\text{O}_{10}$ on the right and, on the left, a region with a different structure containing irregular faults. Direct measurement of the lattice combined with image simulations confirmed that this was a region of perovskite structure, viewed in the $[110]$ direction. Identification of perovskite and $\text{Sr}_3\text{La}_2\text{Ti}_2\text{O}_{10}$ is further facilitated by the electron diffraction patterns recorded from the different regions of the crystal (inset in Figure 5-7). The arrangement

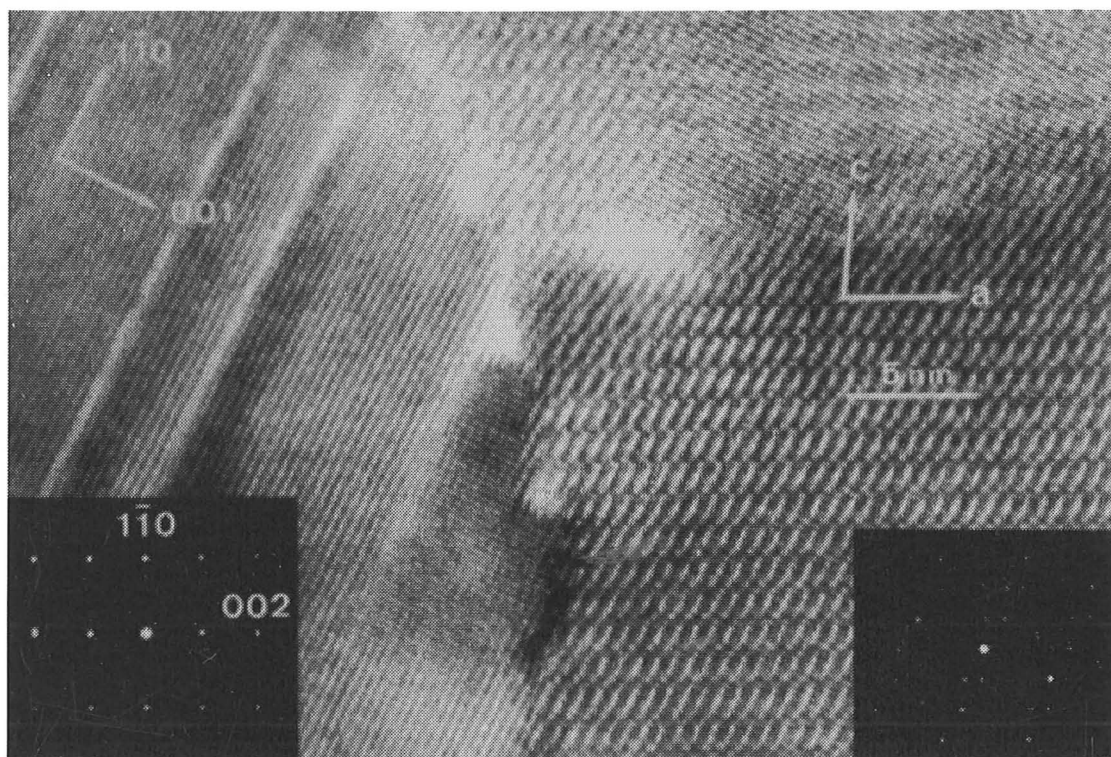


Figure 5-7 Disordered region from a $Sr_3La_2Ti_2O_{10}$ fragment showing a coherent boundary with faulted $SrTiO_3$ (left).

of octahedra in $Sr_3La_2Ti_2O_{10}$ is such that a transition to the perovskite structure can be achieved without undue strain. Figure 5-8 illustrates how this is accomplished through the registration of perovskite octahedra with those in the $Sr_3La_2Ti_2O_{10}$ ribbons. The linear faults visible within the perovskite region in Figure 5-7 can be identified as Ruddlesden-Popper layers.

As in the other layered structures discussed in this study, $Sr_3La_2Ti_2O_{10}$ presents the potential for a family of related compounds containing different layer thicknesses. Because $Sr_3La_2Ti_2O_{10}$ has two layer types, related materials could be generated by either varying the parent Ruddlesden-Popper compound that forms each block, or by altering the block width. The first of these possibilities was considered unlikely since registration of overlying blocks does not occur with structures comprising Ruddlesden-Popper compounds other than Sr_2TiO_4 . On the other hand, compounds containing Sr_2TiO_4 blocks of different widths appear structurally feasible and lead to a family with the general formula $Sr_{2n-2}La_4Ti_nO_{4n+4}$. In this formula, n represents the number of TiO_6 octahedra across the width of the Sr_2TiO_4 block, making $Sr_3La_2Ti_2O_{10}$ the $n=4$ member.

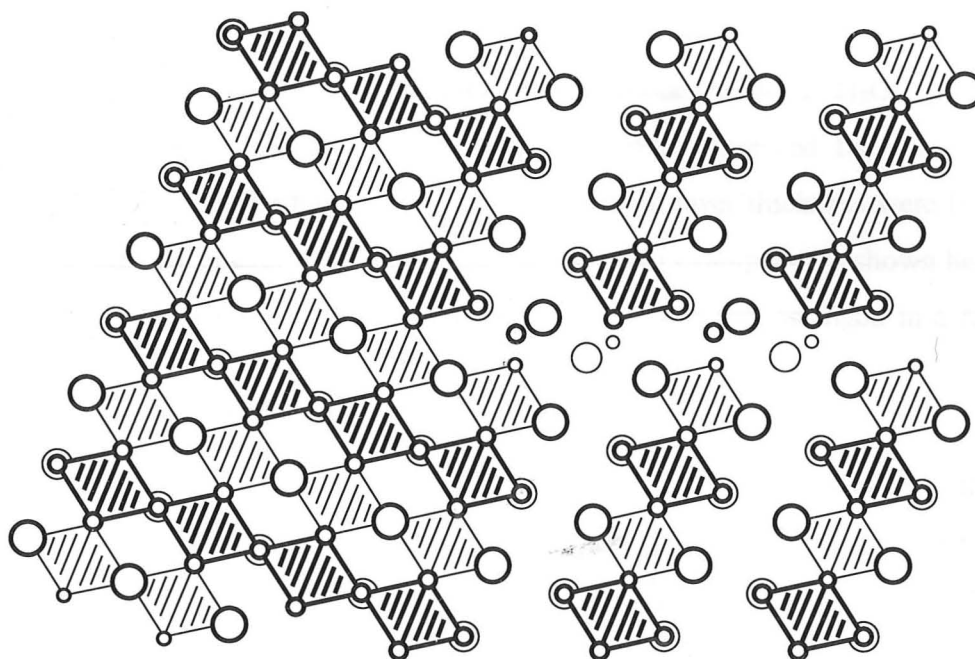


Figure 5-8 Model depicting coherent joining of perovskite (left) and $Sr_3La_2Ti_2O_{10}$ (right) structures. Symbols as for previous structural diagrams.

Samples with values of n ranging from 3 to 7 were reacted in an effort to prepare other members of the $Sr_{2n-2}La_4Ti_nO_{4n+4}$ family. No ordered compounds beside $Sr_3La_2Ti_2O_{10}$

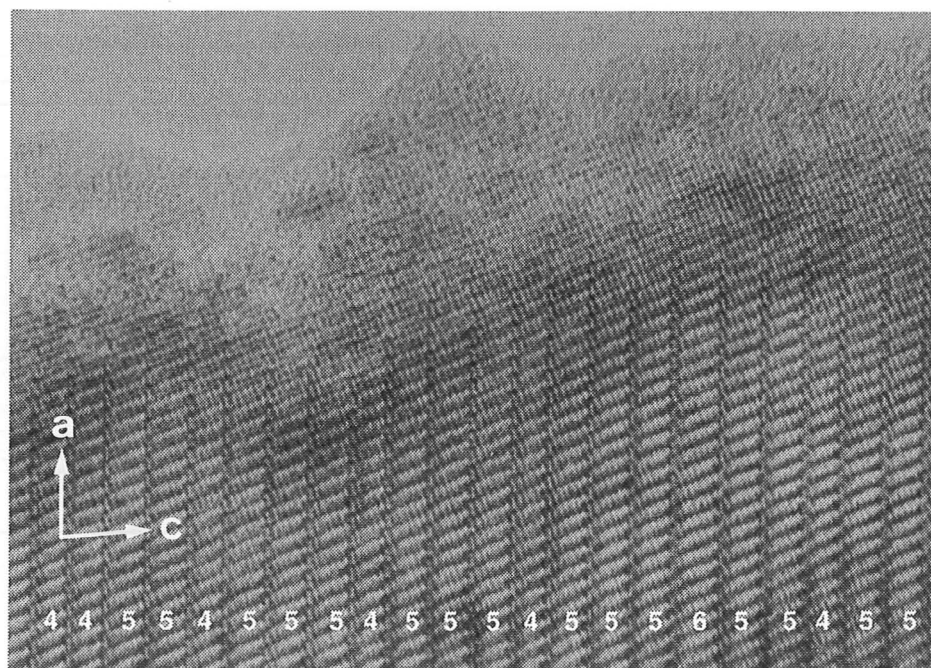


Figure 5-9 Disordered intergrowth amongst $Sr_{2n-2}La_4Ti_nO_{4n+4}$ layers. The values of n for individual layers are marked.

could be detected by either HREM or XRD. For the $n=3$ composition XRD showed the sample to contain $Sr_3La_2Ti_2O_{10}$ and La_2O_3 , while broadened $Sr_3La_2Ti_2O_{10}$ peaks and minor amounts of Ruddlesden-Popper compounds were observed for compositions between $n=5$ and 7. Disordered intergrowths of varying layer thickness were however observed in HREM images of higher n specimens. Two examples are shown here, the first (Figure 5-9) contains layers ranging between $n=4$ and $n=6$ arranged in a random order.

The other example, shown in Figure 5-10, was recorded from a sample close to the $n=5$ composition. For the most part, this area contains layers of the $n=6$ structure seen in the [110] orientation, but considerably wider layers are also clearly visible. Atomic coordinates for the $n=6$ structure were calculated based on $Sr_3La_2Ti_2O_{10}$ and used for the simulated image inset in Figure 5-10.

Although this particular region contains predominantly $n=6$ layers, the electron diffraction pattern indicated a different layer spacing. Disorder in layer stacking was evident from the streaking of the diffraction spots along the c^* direction, but the presence of recognisable spots suggested a principle average distance of 14.9\AA between layers, which is the separation expected for the $n=5$ compound. This discrepancy can be

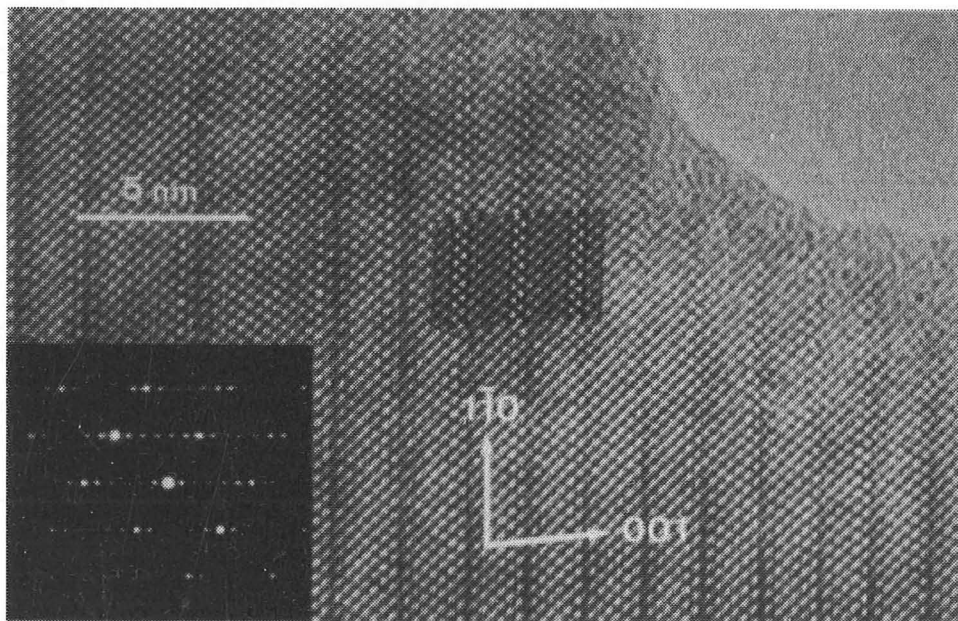


Figure 5-10 Intergrowth of wide lamellae, viewed in the [110] orientation. The simulated image is for an $n=6$ crystal 53\AA thick at a defocus of -600\AA .

reconciled by noting that the diffraction aperture used covers a considerably larger area ($\approx 6500\text{\AA}$ diameter) than that displayed in the micrograph. Hence it appears that while the average structure of this fragment may approximate to that expected for $n=5$, the microscopic detail shows that considerable local variation in layer thickness exists.

5.5 Surface Modification Under the Electron Beam

It was noted in Section 5.3 how the surfaces of $Sr_3La_2Ti_2O_{10}$ crystals examined in the electron microscope invariably seemed to be covered by a layer of disordered material. Since images taken from several orientations showed similar characteristics, the disordered coating was presumably present over all surfaces of the crystal. This may explain why even regions a considerable distance from the edge were still not able to be imaged as clearly as might be expected (see, for example, Figure 5-6).

Amorphous surface coatings are found frequently during HREM examination due to build-up of amorphous carbon, despite the use of a cryogenic anti-contamination device. However, images of the surface of $Sr_3La_2Ti_2O_{10}$ did not always resemble

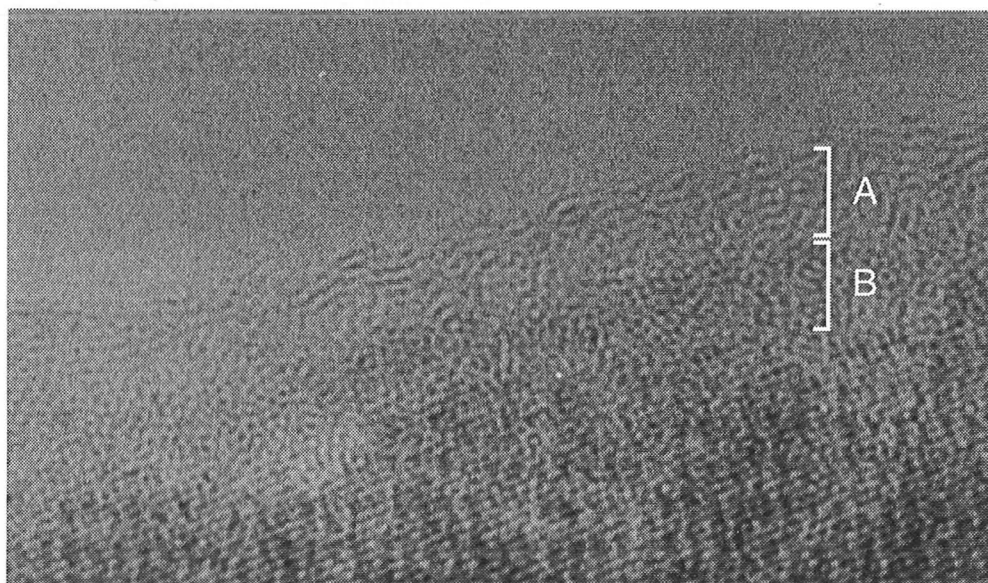


Figure 5-11 Region of $Sr_3La_2Ti_2O_{10}$ crystal with disordered surface. Although not very clear in this reproduction, two zones can be distinguished in the amorphous coating. The outermost, marked 'A', consists of fringes of alternating dark and light contrast often parallel to the surface. The inner zone ('B') is darker and contains irregularly patterned spots in addition to fringes.

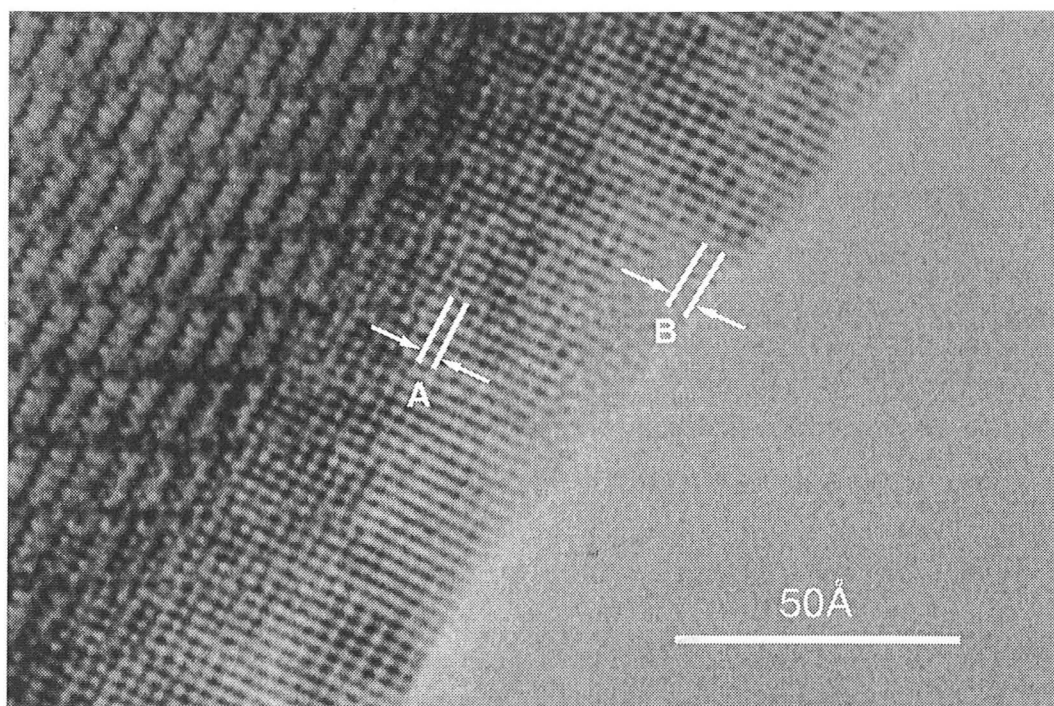


Figure 5-12 $\text{Sr}_3\text{La}_2\text{Ti}_2\text{O}_{10}$ crystal with well-defined surface structure. The difference in lattice spacing at the surface is highlighted by the annotations.

amorphous carbon, which often appears as short fringes $\approx 3.5\text{\AA}$ apart, sometimes becoming aligned to the crystal surface on irradiation. An example is shown in Figure 5-11, in which two zones within the amorphous coating can be recognised. The outer layer resembles carbon, but the inner zone with strongly imaged but disordered spots was considered to be a region of disordered metal oxide.

In some crystals, however, clear images of crystalline structure were observed extending all the way to the edge of the specimen. These samples were ones which had been exposed to the electron beam for some time, and an example is shown in Figure 5-12. Close inspection of this micrograph suggests that the structure near the surface is different from that of the bulk material. Within the interior of the crystal, an array of spots can be seen with a lattice spacing of $\sim 3.2\text{\AA}$ (marked 'A' in Figure 5-12), corresponding to half the distance between adjacent Ti-O ribbons in $\text{Sr}_3\text{La}_2\text{Ti}_2\text{O}_{10}$. However, near the surface the lattice spacing is $\sim 3.9\text{\AA}$ (marked 'B' in Figure 5-12) which does not correspond to features of the $\text{Sr}_3\text{La}_2\text{Ti}_2\text{O}_{10}$ structure and could not be reproduced by image simulations. In addition, the orientation of this lattice spacing is

slightly different from that within the bulk, which is best observed by looking across Figure 5-12 in a direction perpendicular to the arrows marking the lattice spacings.

The most likely explanation for the surface structure was considered to be an overgrowth of perovskite, for example $SrTiO_3$ whose (001) and (110) spacings (3.90\AA and 2.76\AA respectively) are consistent with the observed surface image. The ability of $SrTiO_3$ to mesh with $Sr_3La_2Ti_2O_{10}$ has already been noted in disordered crystals in the previous section. To verify this hypothesis, a computer model where the surface of $Sr_3La_2Ti_2O_{10}$ is covered by a coherent region of $SrTiO_3$ was constructed, as shown in Figure 5-13a.

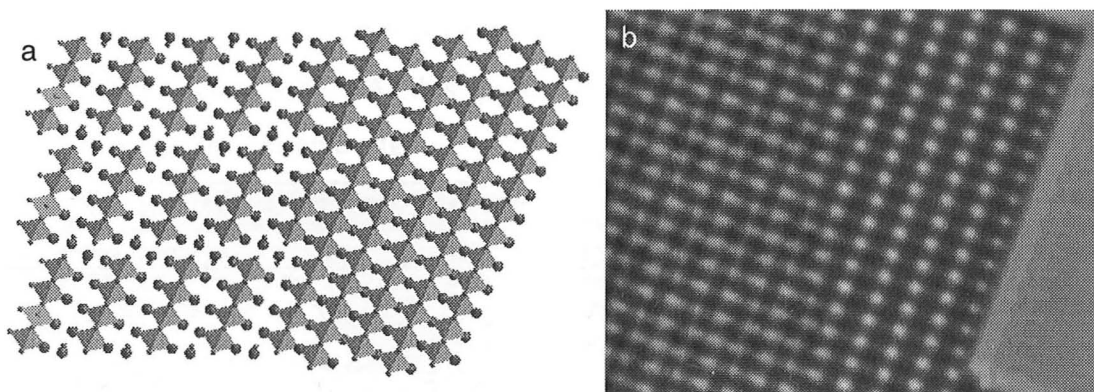


Figure 5-13 a) Computer-based model of perovskite on the surface of $Sr_3La_2Ti_2O_{10}$. b) HREM image simulated from this model with thickness= 45\AA at defocus of -300\AA .

The model was input to the multi-slice image simulation program and a series of HREM images calculated for a range of values for crystal thickness and microscope defocus. A good match with the experimental image was found for a 45\AA thick crystal at a defocus of -300\AA . An image simulated under these conditions is shown in Figure 5-13b, and may be compared with the experimental micrograph given in Figure 5-12. The simulation reproduced not only the general appearance of the lattice image both near the edge and within the bulk, but also the slight difference in alignment between these two regions discussed earlier. This is initially surprising given that the inclination of TiO_6 octahedra is the same throughout the model structure, but arises because of the way that octahedra in adjacent Sr_2TiO_4 blocks are slightly misaligned with respect to one another in $Sr_3La_2Ti_2O_{10}$. The white spots seen in HREM images

correspond to regions of low electron density between the metal atoms, and in $Sr_3La_2Ti_2O_{10}$ these extend in a direction slightly different to that formed by the linkage of TiO_6 octahedra.

Further experiments were undertaken in an attempt to discover how the transformation from amorphous coating to perovskite takes place. Crystals lying in the [010] orientation were sought in the electron microscope and series of images recorded from each as a function of beam exposure time. Several such time-lapse sequences were obtained and all showed a similar development of surface structure, although the precise timescale differed according to individual crystals. Figure 5-14 shows a selection of images recorded from one of these crystals. At the outset (Figure 5-14a), the edge of the crystal is characterised by a rim of amorphous-like material approximately 30\AA wide. At this stage, the amorphous region appears to contain some carbon at the extreme edge.

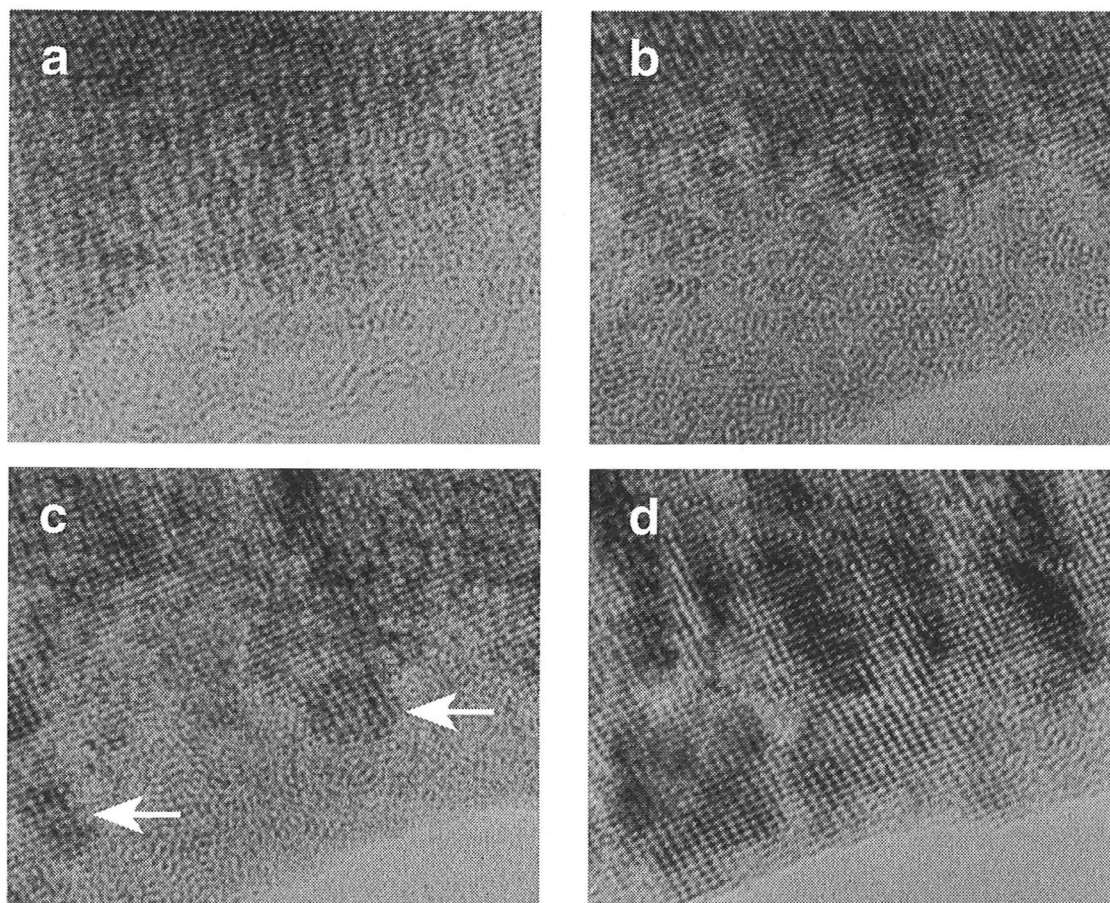


Figure 5-14 Time-lapse sequence showing development of perovskite on the surface of $Sr_3La_2Ti_2O_{10}$. Approximate times after initial observation (a) are: b) 45 minutes; c) 70 minutes; and d) 225 minutes.

After approximately 45 minutes in the electron microscope (Figure 5-14b), the disordered rim is still evident, but no longer resembles amorphous carbon. The contrast is much stronger and appears more like a disordered arrangement of spots rather than the loose network of fringes associated with amorphous carbon. It is most likely, then, that the surface of the crystal is at this stage covered by a layer of amorphous metal oxide, the carbon having been removed. This may take place by the water-gas reaction since there is usually some residual water vapour present in the electron microscope. Further exposure to the electron beam results in the nucleation of perovskite at the interface between the crystalline and amorphous regions, clearly visible in the areas marked in Figure 5-14c. The perovskite continues to grow at the expense of the amorphous material, eventually reaching the edge of the crystal (Figure 5-14d). The $Sr_3La_2Ti_2O_{10}$ structure is still evident in the interior of the crystal, but is now marked by regions of alternate dark and light contrast. This effect can arise from comparatively rapid changes of thickness, and indicates that structural changes may not have been confined to the extreme edge of the crystal.

Another explanation may be that the structure is bent somewhat to accommodate the surface growth of perovskite. In the earlier example shown in Figure 5-12, the perovskite formed on a surface approximately parallel to $(\bar{2}01)$, where the perovskite structure may easily join with $Sr_3La_2Ti_2O_{10}$ along a coherent boundary. In Figure 5-14, however, perovskite is seen to grow on a surface approximately parallel to (001) , where there is no comparable way in which the two structures may be joined in a relatively strain-free manner. Nevertheless, there are regions in this crystal where the boundary does appear to be coherent, and the structural alterations required to allow this may be responsible for the broad dark and light bands visible in Figure 5-14d. In any case, the nucleation of perovskite at the edge of the crystalline $Sr_3La_2Ti_2O_{10}$ region leads to an alignment of the octahedra in the two structures. Hence the lattice planes running roughly parallel to the crystal surface in Figure 5-14d have the same orientation in both regions of structure.

5.6 Summary and Conclusions

A new compound with the formula $Sr_3La_2Ti_2O_{10}$ has been identified in the $SrO-La_2O_3-TiO_2$ system. It can be envisaged as comprising blocks of the Sr_2TiO_4 structure cut parallel to the (112) plane. The blocks are 4 octahedra across and are stacked above one another with additional Sr/La atoms occupying the inter-block sites which are created. To our knowledge, this is the first reported compound which possesses this structure.

Atomic coordinates were determined in a constrained Rietveld refinement where the positions of oxygen atoms were held in chemically sensible positions. The refined structure produced simulated HREM images which agreed closely with observed micrographs in several different orientations. In addition, the manner in which the $Sr_3La_2Ti_2O_{10}$ structure was seen to mesh with that of perovskite verified the arrangement of oxygens in corner-sharing octahedra.

Mixed-layer intergrowths of layers with larger Sr_2TiO_4 blocks were observed which indicated that $Sr_3La_2Ti_2O_{10}$ may be part of a larger family of compounds. However, despite some local ordering seen in the electron microscope, single-phase specimens of other members of this family could not be prepared.

It is possible that $Sr_3La_2Ti_2O_{10}$ may be a metastable compound, since crystals were usually covered with a coating of amorphous metal oxide. No evidence was sought as to whether this layer was present in the 'as-prepared' compound or was formed during preparation for microscopic examination. Under the influence of the electron beam, domains with the perovskite structure nucleate at the interface between the crystalline and amorphous regions. These were observed to grow to the surface of crystals as a result of continued electron irradiation until the $Sr_3La_2Ti_2O_{10}$ fragments became covered with an overgrowth of perovskite.

Chapter 6

The Importance of Elastic Strain

- 6.1 Introduction
 - 6.2 Brief Literature Review
 - 6.3 Application to the Present Materials
 - 6.4 Similarities to Other Systems
 - 6.5 Summary and Conclusions
-

6.1 Introduction

In previous chapters, it has been shown how layers of varying orientation within a perovskite host behave as a function of their concentration, from which several common features emerged. Firstly, there appears to be a definite limit to the number of compounds which may be prepared with a single, regularly repeating, layer thickness. Such compounds are limited to two or three members of a homologous series with a relatively small layer spacing - up to 3 octahedra wide in the case of {100} layered materials, and up to 5 octahedra wide for {110} and {111} layered compounds. When this limit is exceeded, disordered layer growth was observed, firstly as an intergrowth of occasional wider layers. As the frequency of layers decreased further, they appeared primarily in clusters rather than in a more evenly dispersed arrangement. This observation is interesting, because consideration of entropy would predict a more random distribution. The occurrence of clusters suggests there may be an energetic or kinetic preference for this arrangement.

For the $\text{Sr}_{n+1}\text{Ti}_n\text{O}_{3n+1}$ compounds discussed in Chapter 3, it was found that only the first three members of the series could be prepared. This also appears to be the case

Chapter 6

The Importance of Elastic Strain

- 6.1 Introduction
 - 6.2 Brief Literature Review
 - 6.3 Application to the Present Materials
 - 6.4 Similarities to Other Systems
 - 6.5 Summary and Conclusions
-

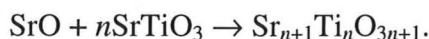
6.1 Introduction

In previous chapters, it has been shown how layers of varying orientation within a perovskite host behave as a function of their concentration, from which several common features emerged. Firstly, there appears to be a definite limit to the number of compounds which may be prepared with a single, regularly repeating, layer thickness. Such compounds are limited to two or three members of a homologous series with a relatively small layer spacing - up to 3 octahedra wide in the case of {100} layered materials, and up to 5 octahedra wide for {110} and {111} layered compounds. When this limit is exceeded, disordered layer growth was observed, firstly as an intergrowth of occasional wider layers. As the frequency of layers decreased further, they appeared primarily in clusters rather than in a more evenly dispersed arrangement. This observation is interesting, because consideration of entropy would predict a more random distribution. The occurrence of clusters suggests there may be an energetic or kinetic preference for this arrangement.

For the $\text{Sr}_{n+1}\text{Ti}_n\text{O}_{3n+1}$ compounds discussed in Chapter 3, it was found that only the first three members of the series could be prepared. This also appears to be the case

for most other {100} layered compounds in different chemical systems. Exceptions include the inability to make an $n=3$ member, for example in the Sr-Ru-O system (Williams *et al.*, 1991b), and the instability of the $n=1$ member of the $\text{Ca}_{n+1}\text{Ti}_n\text{O}_{3n+1}$ series (Hawkins and White, 1991). In the latter case, the authors considered this to be due to the pronounced orthorhombic distortion of the parent perovskite. Ordered compounds with $n>3$ are not known except in the $\text{CaNa}_n\text{Nb}_n\text{O}_{3n+1}$ system where the $n=4$ and $n=5$ materials have been reported (Carpy *et al.*, 1974). Electron microscopy revealed the presence of mixed-layer intergrowths in these samples, however. Interestingly, compounds with $n<4$ have not been reported for this system which differs from many other Ruddlesden-Popper compounds by possessing three different metal ions. This is significant in the light of the suggestion by Williams *et al.* (1991b) that higher n materials might be stabilised by the ordering of different sized cations.

The overall picture which emerges when considering all of the $\text{A}_{n+1}\text{B}_n\text{O}_{3n+1}$ -type compounds is that up to three members of any particular family can be prepared, usually with n between 1 and 3. Udayakumar and Cormack (1989) have addressed why this should be so for the Sr-Ti-O system. Their technique was to use atomistic simulation to calculate the crystal structure and lattice energies of a range of $\text{Sr}_{n+1}\text{Ti}_n\text{O}_{3n+1}$ compounds. Idealised structural coordinates were input to a computer programme and adjusted iteratively to minimise bulk lattice strains, in turn calculated from ionic pair interactions between the constituent atoms. This allowed the formation enthalpy of individual members to be evaluated according to the equation:



The enthalpies obtained were -0.11eV for the $n=1$ member and -0.14eV for all members with $n\geq 2$, prompting the conclusion that an absence of thermodynamic driving force precludes the ordering of compounds with $n>2$. While this agrees with the HREM observations of Tilley (1977a), the present study has shown that an ordered $n=3$ material ($\text{Sr}_4\text{Ti}_3\text{O}_{10}$) can be prepared relatively easily. Hence although the atomistic simulations of Udayakumar and Cormack successfully predict an upper limit for ordered phases, this limit appears to be at $n=3$ rather than $n=2$. In the present consideration of phase stability, we have sought a physical interpretation which underlies the thermodynamic behaviour in the Sr-Ti-O system.

A number of studies have explored the reasons behind the observed behaviour of other layered systems, notably the crystallographic shear (CS) compounds formed in the TiO_{2-x} , WO_{3-x} and related systems. From these studies, elastic strain emerges as the dominant physical factor which governs the distribution of layers. The treatment of elastic strain can be broadly categorised into three distinct groups differing in the model used to represent the structure, and the techniques for evaluating the strain energy. The basic idea in each, however, is similar: the layer structure represents a structural discontinuity which is stabilised by a readjustment of atomic positions in the neighbouring vicinity. The following sections present a brief summary of these ideas, grouped into methods dealing with continuum elasticity, atomistic simulation, and layer mismatch. Much of this work is concerned with the orientation of layers in CS phases and is therefore less relevant to the present work, but some is directly concerned with the extent to which ordering of layers occurs.

6.2 Brief Literature Review

6.2.1 Continuum Elasticity Models

Stoneham and Durham (1973) were the first to apply continuum elasticity to layered structures, following the successful application of this method to the ordering of voids within certain irradiated metals (Stoneham, 1971). They modelled the planar defect by an array of "defect forces" which represented the distortion of the lattice created by the shear plane and which possessed the periodicity of the crystal structure. These forces were assumed to exist in an elastic continuum which represented the intervening structure, and were used to calculate the elastic energy as a function of interplanar spacing. The specific model was based on hypothetical $\{100\}$ CS planes in an ReO_3 structure, but because the model is somewhat idealised the results are more general.

For an infinite array of planes, the calculations displayed a minimum in energy at a separation equal to about four times the spacing of the forces within the planes (*i.e.* four times the unit cell size parallel to the layer plane). This optimum spacing varied little with the relative magnitudes of the various defect forces and was considered to be of about the right magnitude by comparison with observed spacings in TiO_{2-x} . The shape of the interaction function suggested an attractive interaction between layers.

For isolated pairs of planes, the interaction function was found to be oscillatory, with the first minimum at about twice the separation found for arrays of planes. This was again compared favourably to experimental results from TiO_{2-x} , where the spacing at the outside of large clusters of planes was found to be about twice the spacing at the centre (Bursill and Hyde, 1971).

Iguchi and Tilley (1977) extended this work by performing calculations which corresponded more directly to real structures, calculating strain energies for {100}, {102} and {103} planes in reduced WO_3 . Like Stoneham and Durham (1973), they considered *CS* planes to be a source of forces acting on the surrounding matrix, but modelled them as ionic interactions while the intervening lattice was, as before, treated as an elastic continuum. Classical elastic theory was used to obtain the strain energy induced in the ions near the *CS* plane. For single planes, the strain energy was found to increase in the order {100} < {102} < {103} so that {100} planes would always be energetically preferred. This is in contrast to experimental observations which show {102} planes to form initially, followed by {103} planes when the concentration of defects becomes larger. The authors concluded that factors other than strain, for example chemical interactions, are responsible for determining the defect plane orientation.

However, when a family of *CS* planes in an ordered array was considered, the calculations provided a basis for understanding the observed microstructures of WO_{3-x} compounds. The predominance of layered structures with an even number of octahedra between successive layers was related to strain calculations which indicated

that disproportionation of an odd-numbered member into a mixture of the two neighbouring even members was energetically favourable.

6.2.2 Atomistic Simulation

The same kind of atomistic simulation techniques described in the context of $\text{Sr}_{n+1}\text{Ti}_n\text{O}_{3n+1}$ formation enthalpies (Section 6.1) have been applied by Cormack *et al.* (1983) to shear planes in ReO_3 -type structures. Their calculations of shear plane formation energies emphasised the importance of structural relaxation whether considering isolated shear planes, pairs of planes, or those in infinite arrays.

As in the WO_{3-x} oxides discussed above, shear planes in ReO_{3-x} are found in different orientations as their concentration increases. Initial reduction results in $\{102\}$ planes, but as the amount of oxygen removed increases then $\{103\}$, $\{104\}$ and finally $\{001\}$ planes are observed. The atomistic calculations predicted this sequence correctly only when the atoms around the CS plane were relaxed to adopt positions with lower overall strain. This relaxation was also responsible for stabilising the planar defect with respect to a collection of point defects.

A relationship with the continuum studies was found for isolated pairs of planes in an otherwise undisturbed lattice. Here the atomistic simulations produced an oscillating interaction as a function of spacing, similar to that presented by Stoneham and Durham (1973). Cormack *et al.* (1983), however, were able to show a physical explanation for this behaviour by examining the perpendicular cation displacements of their simulated structures. These also showed an oscillatory trend, which became less pronounced with increasing distance from the shear plane. Hence the most stable separations between planes were those in which the individual displacements from each plane were closest to being in phase. Again, a similarity can be seen between this result and the predominance of the even-membered WO_{3-x} phases discussed by Iguchi and Tilley (1977).

6.2.3 Layer Mismatch

In the types of layer compounds under discussion, the structure at the layer interface would usually prefer to adopt a different periodicity within the layer plane than that of the host it inhabits. For example, the a and b dimensions of the rocksalt layer in Ruddlesden-Popper compounds is unlikely to exactly match those of the perovskite structure which lies between if the two were separated. The structure must, however, possess the same cell dimensions within this plane throughout the entire compound, which gives rise to compressive and tensile strains in successive regions of the structure. Although this has long been realised (see, for example, the discussion in the final section of Eyring and O'Keefe, 1970), few publications have dealt with this issue in relation to the stability of layered compounds.

Armstrong and Newnham (1972) considered layer mismatch to be important in determining the stability of substituted Aurivillius compounds. These workers were able to explain the lower limit of solid solution in such compounds by use of Goldschmidt's (1926) long-established tolerance factor for ionic radii, but found the upper limit more difficult to explain. They proposed that the upper solubility limit occurred when the a dimension of the perovskite unit exceeded a critical size ($\approx 4.0\text{\AA}$) which became too large to enable coherence with the intervening Bi_2O_2 layers without causing excessive strain. By analogy with PbO , they estimated that the a dimension of the Bi_2O_2 layers should be approximately 3.80\AA .

Kikuchi (1979) extended this idea by considering families of Aurivillius phases with an increasing number of octahedra in their perovskite layers. The structure was idealised as comprising a repeating sequence of n perovskite layers, each one octahedron high, followed by a single Bi_2O_2 layer which, if unconstrained, would have differing a dimensions. In the assembled crystal, the a dimensions of these layers must coincide, and so each contains an component of stress generated by their enforced registration (see Figure 6-1). If both of the layer types are elastic, then the stress (F) can be represented by an equation of the type:

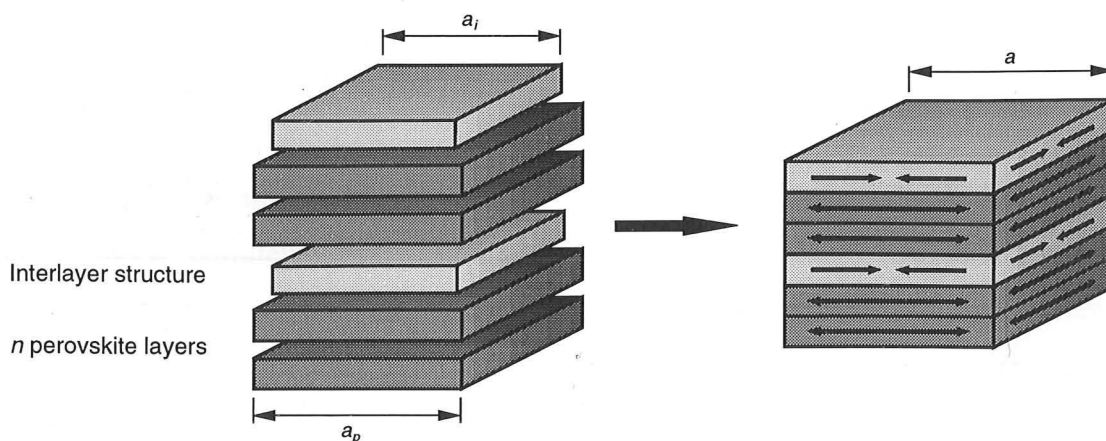


Figure 6-1 Schematic assembly of perovskite layers with a different sized interlayer structure. The strains resulting in the coherent crystal (right) are marked by arrows.

$$F = M \frac{(V' - V)}{V'} \quad (6.1)$$

where M is the elastic bulk modulus and V and V' are the layer volumes in the constrained and unconstrained states respectively. Kikuchi assumed the variation in volume to occur significantly only as a result of changes in a , and so Equation (6.1) can be transformed into the following:

$$F_p = M_p \left(1 - \frac{a^2}{a_p^2} \right) \quad F_i = M_i \left(1 - \frac{a^2}{a_i^2} \right) \quad (6.2)$$

where the subscripts p and i refer to the perovskite and interlayer (in this case Bi_2O_2) components respectively, and the subscripted a dimensions refer to the unconstrained state. In the assembled crystal, not only must the a dimension be coherent, but the two stresses must balance ($F_i = -nF_p$) and so, by rearrangement:

$$a = \sqrt{\frac{a_i^2 a_p^2 (nK + 1)}{a_p^2 + a_i^2 nK}} \quad (6.3)$$

where K is the ratio of the bulk moduli ($= M_p/M_i$). By using Armstrong and Newnham's (1972) value for a_i and estimating a_p from published ionic radii (Shannon and Prewitt, 1969), Kikuchi was able to calculate the expected a dimension of a number of Aurivillius compounds. This could only be achieved where the cells of several members of a series were known in order to establish a suitable value for K , and the agreement with measured cell dimensions was good. In addition, the values

of K obtained increased with increasing Madelung constant of the perovskite component, as expected from theory.

The idea of layer mismatch was also used by Kittel (1978) to explain the existence of the so-called 'infinitely adaptive structures' described by Anderson (1973). These are compounds which can take on any composition between prescribed limits by forming an appropriate ordered array of layer sequences. The sequences can be extraordinarily long, and Kittel sought an explanation for the long-range forces involved. He argued that interaction between layers must be repulsive, for if an attractive interaction existed then the assemblage would be unstable with respect to a two phase mixture where in one phase the layers were more closely spaced. Using a similar approach to Kikuchi, Kittel derived an expression for the elastic energy at the planar interface as a function of separation. This was interpreted as a repulsive force because the elastic energy decreased as the separation increased.

6.3 Application to the Present Materials

6.3.1 Description in Terms of Elastic Strain

We return, then, to the compounds prepared in the present study, and in particular to the $\text{Sr}_{n+1}\text{Ti}_n\text{O}_{3n+1}$ family. Can similar arguments to those described above for crystallographic shear structures also be used to explain the stability of layered perovskites? In attempting to answer this question, the ideas connected with atomistic simulation and, in particular, layer mismatch will be most suitable since these have the closest relation to the structural information gathered in this investigation.

Examination of the unit cell parameters of the $\text{Sr}_{n+1}\text{Ti}_n\text{O}_{3n+1}$ compounds reveals an interesting trend: as the number of layers increases so too does the a dimension, and the a dimension of the $n=3$ member is almost that of the parent perovskite. Such

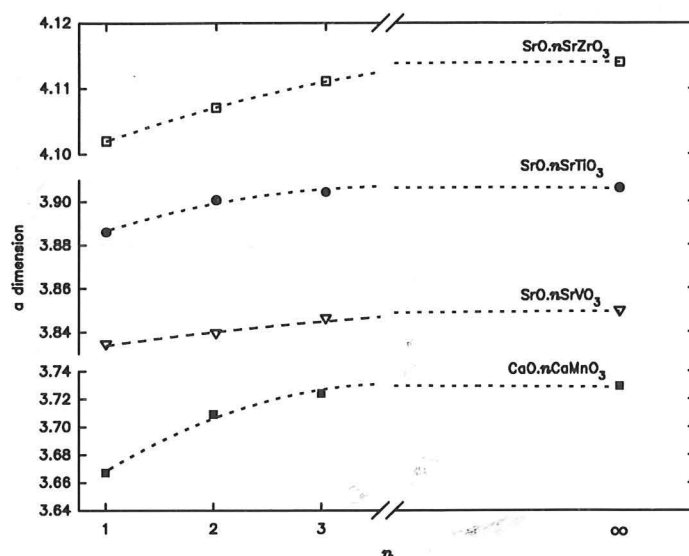


Figure 6-2 Variation in a dimension of several $A_{n+1}B_nO_{3n+1}$ families as a function of the layer spacing n .

behaviour is also observed for a wide range of $A_{n+1}B_nO_{3n+1}$ compounds, as the data in Table 6-1 and Figure 6-2 show. The change in a is noticeable but relatively small which makes the identification of trends rather difficult, particularly if the parameters of different members of the same series were determined by different workers. In such cases, the reported values can vary considerably; for example the a dimension of $Sr_4V_3O_{10}$ has been reported as variously 3.84(1)Å (Nozaki *et al.*, 1991), 3.8457(1)Å (Suzuki *et al.*, 1991b), 3.852(1)Å (Gong *et al.*, 1991b), and 3.8428(3)Å (Itoh *et al.*, 1990). Although the difference in these reported values may seem minor, it becomes significant when compared to the difference in a between the $n=2$ and $n=3$ members (approximately 0.01Å).

n	$Sr_{n+1}Ti_nO_{3n+1}$	$Sr_{n+1}V_nO_{3n+1}$	$Sr_{n+1}Zr_nO_{3n+1}$	$Ca_{n+1}Mn_nO_{3n+1}$	$Eu_{n+1}Ti_nO_{3n+1}$
1	3.8859(7) ¹	3.8341(1) ²	4.102 ⁴	3.667(2) ⁵	3.833 ⁶
2	3.9005(3) ¹	3.839(1) ²	4.107 ⁴	3.709(2) ⁵	3.899 ⁶
3	3.904(1) ¹	3.8457(1) ³	4.111 ⁴	3.724(2) ⁵	3.90 ⁶
∞	3.9061(5) ¹	3.849(2) ³	4.114 ⁴	3.729 ⁵	3.905 ⁸

Table 6-1 a cell dimensions for a variety of $A_{n+1}B_nO_{3n+1}$ compounds. References : 1. This study; 2. Nozaki *et al.* (1991); 3. Suzuki *et al.* (1991b); 4. Tilloca and Perez Y Jorba (1964); 5. MacChesney *et al.* (1967); 6. M^cCarthy *et al.* (1969b); 7. Holzapfel and Sieler (1966).

The trend in lattice parameter with increasing n is what would be expected from the layer mismatch model. Using this notion, the a dimension of any $A_{n+1}B_nO_{3n+1}$ compound represents a compromise between those of the perovskite component and

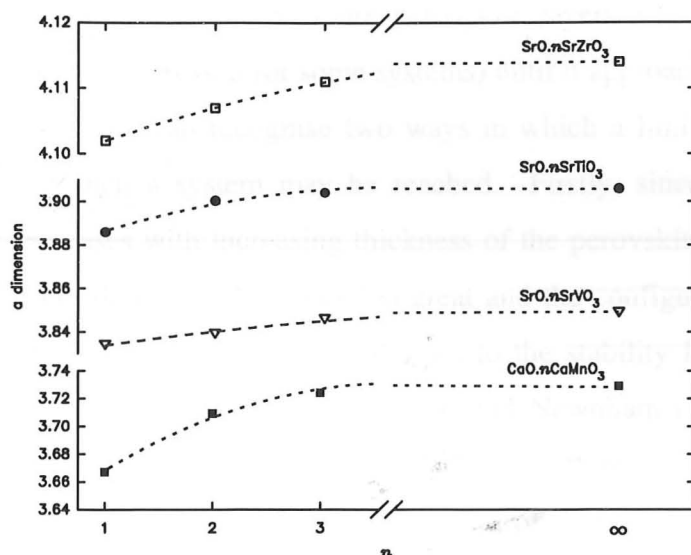


Figure 6-2 Variation in a dimension of several $A_{n+1}B_nO_{3n+1}$ families as a function of the layer spacing n .

behaviour is also observed for a wide range of $A_{n+1}B_nO_{3n+1}$ compounds, as the data in Table 6-1 and Figure 6-2 show. The change in a is noticeable but relatively small which makes the identification of trends rather difficult, particularly if the parameters of different members of the same series were determined by different workers. In such cases, the reported values can vary considerably; for example the a dimension of $Sr_4V_3O_{10}$ has been reported as variously $3.84(1)\text{\AA}$ (Nozaki *et al.*, 1991), $3.8457(1)\text{\AA}$ (Suzuki *et al.*, 1991b), $3.852(1)\text{\AA}$ (Gong *et al.*, 1991b), and $3.8428(3)\text{\AA}$ (Itoh *et al.*, 1990). Although the difference in these reported values may seem minor, it becomes significant when compared to the difference in a between the $n=2$ and $n=3$ members (approximately 0.01\AA).

n	$Sr_{n+1}Ti_nO_{3n+1}$	$Sr_{n+1}V_nO_{3n+1}$	$Sr_{n+1}Zr_nO_{3n+1}$	$Ca_{n+1}Mn_nO_{3n+1}$	$Eu_{n+1}Ti_nO_{3n+1}$
1	3.8859(7) ¹	3.8341(1) ²	4.102 ⁴	3.667(2) ⁵	3.833 ⁶
2	3.9005(3) ¹	3.839(1) ²	4.107 ⁴	3.709(2) ⁵	3.899 ⁶
3	3.904(1) ¹	3.8457(1) ³	4.111 ⁴	3.724(2) ⁵	3.90 ⁶
∞	3.9061(5) ¹	3.849(2) ³	4.114 ⁴	3.729 ⁵	3.905 ⁸

Table 6-1 a cell dimensions for a variety of $A_{n+1}B_nO_{3n+1}$ compounds. References : 1. This study; 2. Nozaki *et al.* (1991); 3. Suzuki *et al.* (1991b); 4. Tilloca and Perez Y Jorba (1964); 5. MacChesney *et al.* (1967); 6. M^cCarthy *et al.* (1969b); 7. Holzapfel and Sieler (1966).

The trend in lattice parameter with increasing n is what would be expected from the layer mismatch model. Using this notion, the a dimension of any $A_{n+1}B_nO_{3n+1}$ compound represents a compromise between those of the perovskite component and

the rocksalt interface structure. As more perovskite layers are added, the rocksalt layer is stretched (or compressed for some systems) until it approaches the dimensions of pure perovskite. We can recognise two ways in which a limit to the number of ordered phases in such a system may be reached. Firstly, since the strain in the interface layer increases with increasing thickness of the perovskite blocks, we could reach a point where this strain becomes too great and the configuration is no longer energetically stable. This situation is analogous to the stability limit of substituted Aurivillius compounds described by Armstrong and Newnham (1972) (see Section 6.2.3). Alternatively, we would predict that the difference in strain between successive $A_{n+1}B_nO_{3n+1}$ members becomes smaller with increasing n because the difference in the a dimension also diminishes. The experimental data given in Table 6-1 show that this occurs when n becomes greater than about 2 or 3. For these compounds, the mechanism and kinetics of formation will dominate the microstructure rather than the thermodynamics of the most stable configuration. Of the two situations, the latter explanation seems the most likely to apply to $A_{n+1}B_nO_{3n+1}$ materials given the small difference in lattice size between the $n=3$ compounds and the corresponding perovskites, and in the light of HREM observations of disordered intergrowth among higher n members (see Chapter 3).

There is also a connection between this argument and the results of enthalpy calculations derived from atomistic simulation which were described earlier in Section 6.2.2. The simulations predicted that ordering of $Sr_{n+1}Ti_nO_{3n+1}$ compounds ceased beyond a small value of n because the difference in thermodynamic stability between successive members became vanishingly small. Elastic strain provides a physical interpretation for these results: the thermodynamic stability arises from the minimisation of strain energy and significant minima exist only for ordered arrangements where $n \leq 3$.

The same reasoning can be applied to the other layered perovskite compounds outlined in this study. These also showed similar trends in cell dimensions, converging toward the $SrTiO_3$ value as the layer thickness increased. Figure 6-3

graphs the relevant cell parameters against n for the {100}, {110}, and {111} layered compounds, converted to allow direct comparison with the a dimension of SrTiO₃.

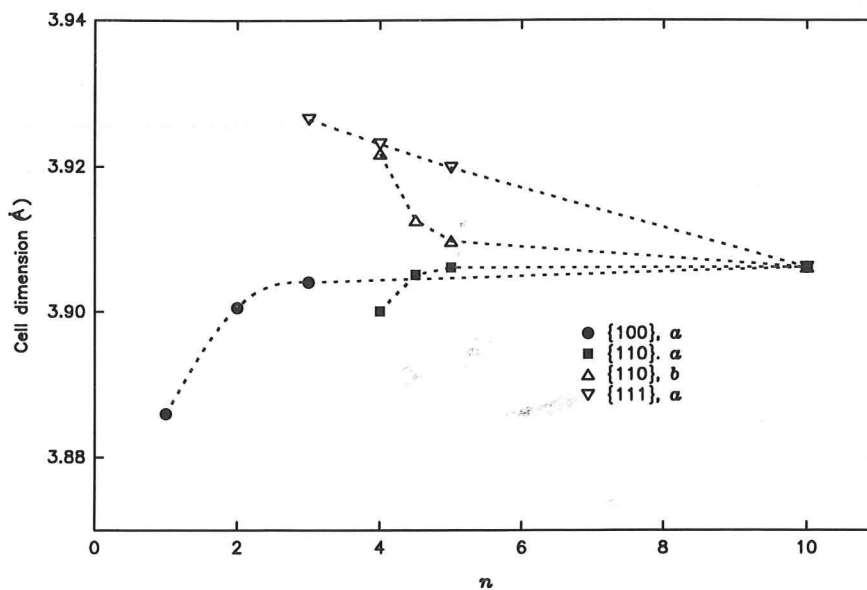


Figure 6-3 Variation in lattice dimensions of the layered compounds based on SrTiO₃ as a function of layer separation. To enable direct comparison with SrTiO₃ (shown here as $n=10$) the a dimensions of {110} layered compounds have been halved, and the b dimensions of {110} and a dimensions of {111} layered compounds divided by $\sqrt{2}$.

Two other features may also be explained in the context of elastic strain, and in particular the layer mismatch model. The first is the observation of disordered intergrowths of different layer thicknesses. In most cases, this was observed amongst relatively wide layers, for example perovskite blocks larger than 3 octahedra across in the {100} layered compounds. The predicted a dimensions of these layers are all roughly equivalent, allowing intergrowth without a significant increase in elastic strain. Intergrowth of narrow layers, for example $n=2$ lamellae in a Sr₄Ti₃O₁₀ matrix, would involve more strain since the difference in the respective a dimensions is greater. Such intergrowth was not observed in the present study, although Tilley (1977a) shows a micrograph with Sr₂TiO₄ lamellae intergrown in Sr₃Ti₂O₇.

A related aspect is the preferential appearance of clusters of layered defects for compositions close to SrTiO₃. Even a single layer plane must exert some distortion on the surrounding lattice and so, if a second layer is to be introduced, it will be more favourable for it to form close to the existing layer where the perovskite matrix is already deformed some way toward the preferred dimensions of the layer structure.

This cannot be the complete story, however, because continuing this line of reasoning leads to the extreme case of clustering - a two phase mixture of layered and unlayered perovskite. The effects of configurational entropy must also be taken into account.

Of course, other factors may influence the distribution of layers in such materials, especially the mechanism and kinetics of reaction. The appearance of clustered layers may simply reflect the inhomogeneous distribution of reactants, arising from the mechanically mixed powders used for sample preparation. An attempt was made to investigate whether the layer distribution changed as a function of annealing time by examining samples periodically during their heating programme. The results were largely inconclusive, with no clear changes evident in either XRD patterns or HREM images. Certainly, no major changes occurred over the annealing period used (several days), but longer experiments may reveal further information. Unlike the migration of crystallographic shear planes in reduced rutile (Bursill and Hyde, 1972), there is no simple mechanism by which the layers in $\text{Sr}_{n+1}\text{Ti}_n\text{O}_{3n+1}$ compounds may be displaced.

6.3.2 Quantitative Models

If the layer mismatch is qualitatively appealing in explaining stability of $\text{A}_{n+1}\text{B}_n\text{O}_{3n+1}$ materials, it may also be amenable to a quantitative treatment similar to that used by Kikuchi (1979). In order to calculate the a dimension of any $\text{Sr}_{n+1}\text{Ti}_n\text{O}_{3n+1}$ compound, values are required for the a dimensions of the parent perovskite (a_p), the interlayer structure (a_i), and the ratio of the bulk moduli (K) of the two components (see Equation (6.3)). The first of these has been measured, but the other two parameters cannot be obtained experimentally or determined *a priori*. This is largely because the interlayer structure is not found as an extended 3-dimensional structure in any known compound. Although it is frequently referred to as the rocksalt layer, this only describes the atomic arrangement in the narrow region between the two layers of Sr atoms between perovskite units (the structure is described in Chapter 3, Figure 3.1), and ignores the fact that the Sr coordination in this region is 9-fold rather than the octahedral arrangement in the SrO rocksalt structure.

It is, however, possible to arrive at values for a_i and K by a process of least-squares minimisation, where initial estimates are iteratively adjusted to provide the best agreement between observed and calculated cell dimensions. This procedure has been carried out for the $n=1, 2$ and 3 members of the $\text{Sr}_{n+1}\text{Ti}_n\text{O}_{3n+1}$ series using a commercial spreadsheet package. Although the optimal solution gave an unrealistically small value for a_i ($<1\text{\AA}$), it was found that the agreement between the observed and calculated cell lengths was within experimental error for values of a_i less than about 3.4\AA . Table 6-2 shows the values for $a_i=3.35\text{\AA}$. For comparison, the corresponding distance in rocksalt SrO ($a=5.160\text{\AA}$; Swanson *et al.*, 1955) is 3.65\AA ; however it is difficult to make a direct comparison for the reasons noted above regarding the nature of the rocksalt layer in Ruddlesden-Popper compounds. Similarly, the value of K found by this technique cannot meaningfully be compared to experimentally measured quantities. The predicted a dimension of the $n=4$ compound is extremely close to that of the parent perovskite, which in terms of the layer mismatch model explains why we have been unable to prepare $n=4$ materials.

n	a_{observed}	$a_{\text{calculated}}$
1	3.8859	3.8871
2	3.9005	3.8995
3	3.904	3.904
4	-	3.9059
∞	3.9061	

Table 6-2 Comparison of a dimensions for $\text{Sr}_{n+1}\text{Ti}_n\text{O}_{3n+1}$ compounds with those calculated from Equation (6.3), using $K=26.66$ and $a_i=3.35\text{\AA}$.

Although this treatment shows that the a cell dimensions of the $\text{Sr}_{n+1}\text{Ti}_n\text{O}_{3n+1}$ compounds are quantitatively consistent with the ideas of the layer mismatch model, the predictive capacity of the model is limited because of the requirement to use all of the experimentally measured quantities to evaluate the unknown parameters. The utility of the model is further undermined by a graphical treatment designed to eliminate the need to find values for a_i and K . Beginning with the equations for stress within each layer (Equation (6.2)) and the requirement for these stresses to be balanced ($F_i = -nF_p$), we find that:

$$a_i^2 - a^2 = -nK \frac{a_i^2}{a_p^2} (a_p^2 - a_i^2) \quad (6.4)$$

where the constant K has the same value as before. By defining a parameter $\delta = a_p^2 - a_i^2$ and substituting into the above equation, we can rearrange to give the dependence of a upon n :

$$\frac{1}{a^2 - a_p^2} = \frac{nKa_i^2}{\delta a_p^2} + \frac{1}{\delta} \quad (6.5)$$

Hence a plot of $1/(a^2 - a_p^2)$ against n should be linear and a_i may be determined from the y-intercept. Figure 6-4 shows several plots for the cell dimensions listed in Table 6-1, where accurate cell parameters are available for three members of a Ruddlesden-Popper series and the parent perovskite. The plots do not conform exactly to the straight line model, with all exhibiting a convex-up curve shape. In addition, the values of a_i calculated for the Sr-based compounds are different, despite each having the same SrO interface layer.

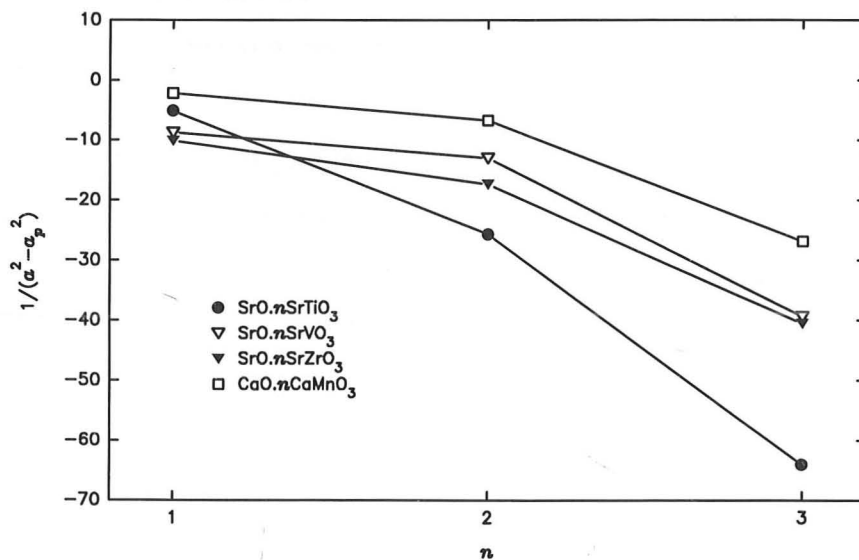


Figure 6-4 Plot of cell dimensions of $A_{n+1}B_nO_{3n+1}$ compounds according to the relationship in Equation (6.5).

The deviations from the predicted straight line were thought to be due to the simplifications of the model used. Firstly, it was assumed that the strain results in negligible changes in the c dimensions of the individual layers. But the trend in cell parameters (Chapter 3, Tables 3-1 to 3-3) shows that this is not the case. If the only difference between the $Sr_{n+1}Ti_nO_{3n+1}$ phases is the number of perovskite layers, then the additional layer added to convert $n=1$ to $n=2$ is 3.877\AA thick, and the further layer required to produce $n=3$ is 3.900\AA thick. Although this change is most likely to be

distributed amongst all the layers in the structure, it does highlight how changes in the c direction are as significant as those in a .

Accounting for the variation in c is not straightforward. The equations for force may be left in terms of volume changes (Equation (6.1)) and the forces balanced as before, in which case no simple variation of the lattice parameters with n emerges. Alternatively, the layers may be treated in the same manner as for larger bodies and the change in c linked to the force (F) present in the a - b plane. In the perovskite layer, for example, this results in an expression for the change in c as:

$$\Delta c_p = \frac{-2\nu_p F}{a_p E_p} \quad (6.6)$$

where ν is Poisson's ratio and E Young's modulus for the material in question. Continuing the argument leads to a similar result as found when neglecting changes in c , but without the squared dependence on the lattice parameters.

However, there is another problem with the model which makes the effort to account for changes in the c direction unworthwhile. In order to provide a consistent progression with an increasing number of perovskite layers, it has been assumed that the stress is taken up uniformly by each layer. But the refined structures (Chapter 3, Figure 3-9) have shown that this is not the case. The height of the octahedra along the c direction in $\text{Sr}_4\text{Ti}_3\text{O}_{10}$, for example, is different for each layer. This is also mirrored in the positions of Sr atoms, which are defined better by the Rietveld analysis. The octahedral distortions are smallest near the centre of the perovskite blocks, and become greater close to the rocksalt layer.

Hence, while the cell parameters give a good indication that elastic strain plays a major role in determining the stability of layered perovskite compounds, the detailed structure shows that quantitative analysis cannot be satisfactorily achieved using a simple layer mismatch model.

6.4 Similarities to Other Systems

The behaviour noted in $\text{Sr}_{n+1}\text{Ti}_n\text{O}_{3n+1}$ compounds, where the perovskite structure becomes progressively more distorted closer to the rocksalt layer, has also been observed in other systems. Gong *et al.* (1991b) defined a distortion index (*DI*) for VO_6 octahedra in $\text{Sr}_{n+1}\text{V}_n\text{O}_{3n+1}$ compounds based on the difference in V-O bond lengths parallel and perpendicular to the *c* axis:

$$DI = \frac{(\text{V}-\text{O})_{c \text{ axis}} - (\text{V}-\text{O})_{a-b \text{ plane}}}{(\text{V}-\text{O})_{a-b \text{ plane}}} \quad (6.7)$$

The single crystal x-ray refinement of $\text{Sr}_4\text{V}_3\text{O}_{9.7}$ by Gong *et al.* (1991b) showed the outermost octahedron ($DI = 0.021$) to be considerably more distorted than the octahedron at the centre of the perovskite block ($DI = 0.004$). The octahedron in Sr_2VO_4 was even more distorted ($DI = 0.036$), reflecting the greater strain in the single perovskite layer of this compound.

A similar progressive distortion was also proposed by Jefferson *et al.* (1984) in Aurivillius compounds comprising a regular intergrowth of perovskite units 3 and 4 octahedra across. These authors believed elastic strain to be responsible for the formation of such recurrent intergrowths. In order to obtain a good match between simulated and observed HREM images, the proposed structures needed to be distorted in two ways. Firstly, the Bi atoms in the Bi_2O_2 layer were shifted along the *c* axis to bring them closer together. In addition, the cations in the perovskite units needed to be shifted in the same direction. This was accomplished by a proportional expansion of the perovskite layer so that atoms near the outside underwent the largest shifts and therefore possessed the greatest distortion. The agreement with the observed HREM image improved markedly when this structural modification was performed.

Although we have shown that variations in cell dimensions and structural distortions are common to a number of different layered systems, one of the limitations of the compounds considered so far is that only a few members of any one family can be prepared. This means that we are examining trends defined by only 3 or 4 points and,

although a consistent picture emerges, it would be better if we could examine a system where more compounds representing a larger variation in layer separation were available.

The best known series which fulfils this criterion is the family of titanium suboxides, described in Chapter 1 and represented by the general formula Ti_nO_{2n-1} . These compounds comprise blocks of the rutile structure n octahedra wide separated by shear planes where octahedra share faces in a manner akin to those in $\alpha-Al_2O_3$. Ordered compounds with values of n ranging between 4 and 9 have been prepared, and well characterised in single crystal studies by Marezio *et al.* (1973, 1977) and by Le Page and Strobel (1982a, 1982b). The unit cell parameters show a steady progression across the series, with the greatest variation occurring in the a dimension. Like all the layered compounds considered here, a becomes progressively closer to the corresponding dimension of the $n=\infty$ compound (in this case rutile) as n increases. Le Page and Strobel (1982a) noted this trend, and showed how a varied linearly when plotted as a function of $1/n$. The intercept at $1/n=0$ corresponded to the a dimension of rutile, but no theoretical justification for this relationship was offered.

As in the case of layered perovskites, the variation in a can be attributed to elastic strain resulting from the different size of the interlayer structure. It has not proved possible to derive the $1/n$ dependence from considerations of elastic strain, but

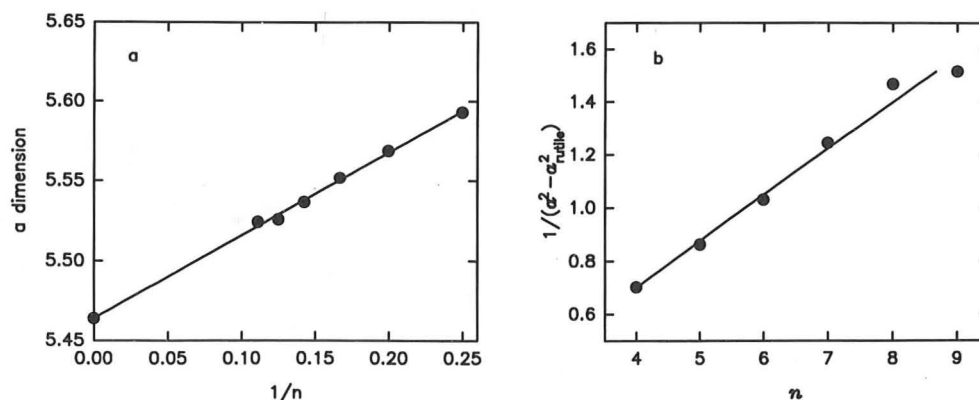


Figure 6-5 a) Empirical relationship for the a cell parameter in Ti_nO_{2n-1} compounds noted by Le Page and Strobel (1982a). The intercept at $1/n=0$ corresponds to the equivalent distance in rutile. b) The same data plotted according to Equation (6.5).

interestingly the equation resulting from strain considerations (Equation (6.5)) provides a fit to the data which seems to be as good as the empirical function observed by Le Page and Strobel (1982a), shown in Figure 6-5. This simplistic model again breaks down, however, when the a dimension of the interface structure is calculated from the graph - in this case a negative value results.

In their second publication, which dealt with the refined structures, Le Page and Strobel (1982b) examined trends in atomic coordination. They found that the Ti-O bond lengths and TiO_6 octahedral distortions varied in a consistent manner with increasing distance from the shear plane. They related Ti-O bond distances to valence, and were able to show that the Ti valence varied from about +3.5 at the shear plane to almost +4 in the centre of the rutile slabs.

Of more interest, however, was the variation in octahedral distortion. Le Page and Strobel used the standard deviation in Ti-O distances as a measure of distortion in the TiO_6 octahedra. The greatest distortion was always found in those octahedra closest to the shear plane, and diminished progressively toward the centre of the rutile slabs

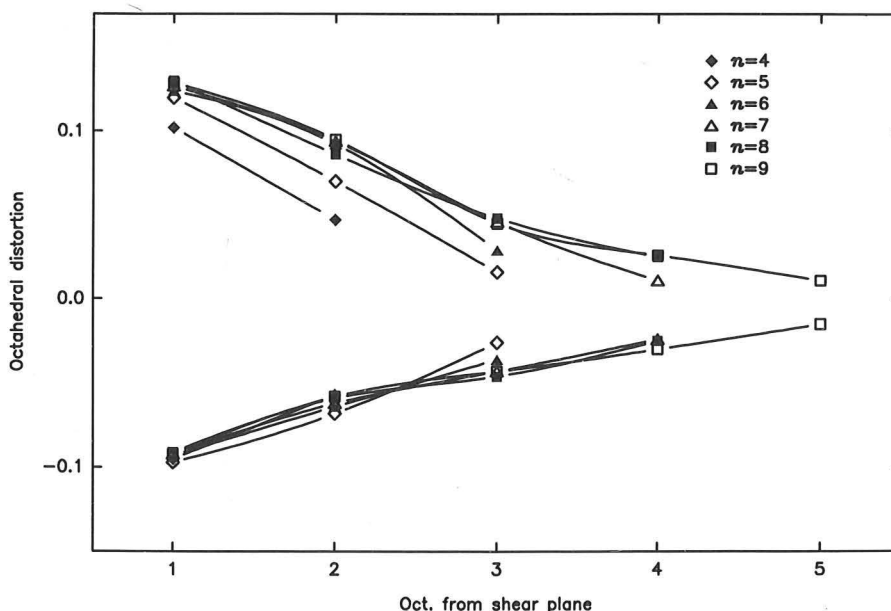


Figure 6-6

Octahedral distortion in $\text{Ti}_n\text{O}_{2n-1}$ compounds, estimated as the standard deviation of Ti-O distances, and plotted as a function of distance from the shear plane. The two crystallographically distinct sets of octahedra are distinguished by making the distortions negative for one set. Data from Le Page and Strobel (1982b).

(see Figure 6-6). The distortion at the centre of the slabs is approximately the same as that found in pure rutile; using the single crystal data of Abrahams and Bernstein (1971) gives a standard deviation of 0.015 for the Ti-O distances. The Ti_nO_{2n-1} compounds are crystallographically more complex than the perovskite-based materials prepared in this study, and contain two distinct sets of TiO_6 octahedra which are distinguished in Figure 6-6 by assigning a negative distortion to one set. Hence the clear trend which emerges from these distortions represents data from a considerable number of atoms, and provides the most detailed picture yet of how elastic strain affects the structures of layered compounds.

6.5 Summary and Conclusions

The introduction of layered defects exerts a physical effect on the surrounding matrix which has a considerable influence in determining the stabilities of the resulting compounds. This arises primarily because the ideal layer structure has a different periodicity in a direction parallel to the layer plane than that of the host structure. In the assembled crystal, however, these periodicities must coincide and so one component is stretched and the other compressed. The effects of this have been observed in the lattice parameters of all the layered compounds prepared in this study, which showed a gradual change with increasing layer separation toward the lattice parameter of the unlayered material, $SrTiO_3$.

A distortion of the structure between the layered defects accompanies the change in lattice parameter. The distortion is not distributed evenly throughout the material, but is strongest near the layered defect and diminishes progressively as the distance from the layer increases. This explains why attempts to quantify the variations in lattice parameter with a simple elastic strain model have met with only partial success. The structural distortions have been observed in the $Sr_{n+1}Ti_nO_{3n+1}$ and $Sr_{n-3}La_4Ti_nO_{3n+3}$ compounds prepared here, but the trend is most clearly seen in the homologous series of titanium suboxides where more data from 6 members are available.

The elastic strain represented by the lattice and structural distortions is important in determining the stability of ordered sequences of layers. Ordered compounds were found only when the lamellae from which they are composed had lattice parameters significantly different from the corresponding unlayered material. In the materials synthesised in this study, this occurred for perovskite lamellae up to 3 or 5 octahedra thick, depending on the orientation of the layer plane. Lamellae wider than this all have similar lattice dimensions and can form random intergrowths without a significant increase in elastic strain.

Chapter 7

Ruddlesden-Popper Compounds Containing Copper

- 7.1 Introduction
 - 7.2 Solid Solutions Between Copper and Titanium
 - 7.3 Three-layered Cuprates
 - 7.4 Summary and Conclusions
-

7.1 Introduction

In this chapter, the attention is shifted from SrTiO_3 to include compounds based on copper oxide in addition to titanium oxide. The major emphasis is to examine the possibility of preparing compounds with the Ruddlesden-Popper structure type, particularly those with larger numbers of copper-oxygen layers. Of course, a vast amount of work has been published recently on layered cuprates in the wake of the discovery of high- T_c superconductivity, but it is beyond the scope of this work to try and review all the structural chemistry of these compounds. Instead, the focus will be directed at cuprates which comprise elements of the perovskite structure interleaved with rocksalt layers of the type found in the $\text{Sr}_{n+1}\text{Ti}_n\text{O}_{3n+1}$ phases described in Chapter 3. It should also be stressed that the interest is from the standpoint of crystal chemistry and the physical properties, for example superconductivity, will not be addressed.

7.1.1 Mixed Cuprates-Titanates

As a means of providing a bridge between titanates and cuprates, mixed titanium-copper compounds will be examined first. Several studies have been published which

show that materials with the perovskite structure may be prepared using a combination of copper and titanium. Ramadass *et al.* (1977) reported the synthesis of $\text{La}_2\text{CuTiO}_6$ and described its structure as a cubic perovskite with an a dimension (7.872 Å) approximately twice that found for simple perovskites (*e.g.* SrTiO_3 , 3.906 Å). The authors expressed surprise that the cell was not tetragonal as would be expected from the Jahn-Teller distortion of Cu^{2+} , and interpreted this result as indicating incomplete ordering of copper and titanium over the octahedral sites.

Later work with this material (Anderson *et al.*, 1993) has suggested a completely random distribution of copper and titanium, although the symmetry was determined as orthorhombic rather than cubic. These workers noted the similarity between the powder diffraction patterns of $\text{La}_2\text{CuTiO}_6$ and $\text{Nd}_2\text{CuTiO}_6$. The latter compound has been characterised by Rietveld analysis of neutron diffraction data and possesses orthorhombic symmetry due to the cooperative tilting of octahedra, as opposed to any ordering of elements over the lattice sites.

Two studies have dealt with elemental substitution in the $\text{La}_2\text{CuTiO}_6$ composition. Rojas and Fierro (1990) investigated $\text{LaTi}_{1-x}\text{Cu}_x\text{O}_3$ compounds, and found single-phase perovskites for values of x between 0.3 and 0.8. The end members of this series contain Ti^{3+} (LaTiO_3 ; Kestigan and Ward, 1955) and Cu^{3+} (LaCuO_3 ; Demazeau *et al.*, 1972), but the experimental conditions employed by Rojas and Fierro were not appropriate to synthesise phase pure samples of either material. Nevertheless, the observation of the extensive solid solution range suggests that mixed perovskites may form over the entire range if suitable synthesis conditions are used.

Jones and McKinnon (1990) examined compositions including Sr^{2+} , which enabled perovskites to be formed with copper and titanium in their more usual oxidation states of 2+ and 4+ respectively. They found a complete solid solution between $\text{La}_2\text{CuTiO}_6$ (or $\text{La}(\text{Cu}_{0.5}\text{Ti}_{0.5})\text{O}_3$) and SrTiO_3 , over which the cubic cell dimension dropped from 3.934 to 3.903 Å in a roughly linear fashion. From the perspective of ionic radii, the substitution involves two competing effects. Sr^{2+} (ionic radius=1.58 Å; Shannon, 1976) is larger than La^{3+} (1.50 Å), while Ti^{4+} (0.745 Å) is smaller than Cu^{2+} (0.87 Å).

The observed cell dimensions suggest that the latter effect predominates, perhaps because it is proportionally more significant,.

These authors also substituted Sr^{2+} for La^{3+} in $\text{La}_2\text{CuTiO}_6$ without simultaneously replacing copper. They found a small range of solid solution, equivalent to $x \leq 0.3$ in the formula $\text{La}_{1-x}\text{Sr}_x(\text{Cu}_{0.5}\text{Ti}_{0.5})\text{O}_3$. The copper valence in these materials was partly Cu^{3+} , determined by iodometric titration. Overall, perovskite compounds were found in the triangular region of the phase diagram bounded by SrTiO_3 , $\text{La}(\text{Cu}_{0.5}\text{Ti}_{0.5})\text{O}_3$ and $(\text{La}_{0.7}\text{Sr}_{0.3})(\text{Cu}_{0.5}\text{Ti}_{0.5})\text{O}_3$.

In all of the materials discussed so far, titanium and copper were found to have been, or were assumed to have been, disordered over the available octahedral sites. Examples of compounds which displayed an ordered arrangement of metal atoms have been reported in oxygen-deficient perovskites by Palacín *et al.* (1994). The oxygen vacancies in these materials are ordered into layers which leave BO_5 square pyramids in place of BO_6 octahedra. A Rietveld refinement of $\text{Eu}_2\text{Ba}_2\text{Cu}_2\text{Ti}_2\text{O}_{11}$ found ordering not only of copper and titanium on the B sites, but also of europium and barium over the A sites. The structure is shown in Figure 7-1 and comprises 2

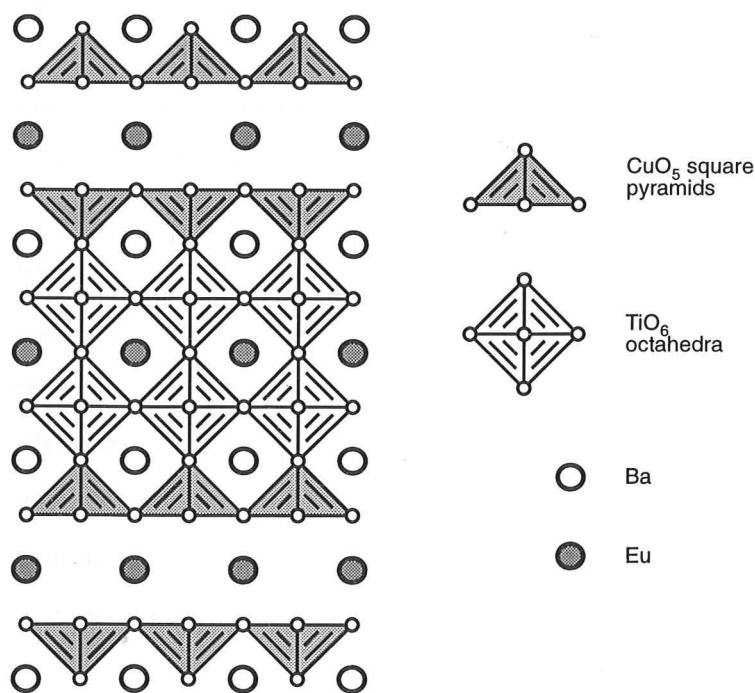


Figure 7-1 Structure of the oxygen-defect perovskite $\text{Eu}_2\text{Ba}_2\text{Cu}_2\text{Ti}_2\text{O}_{11}$.

layers of TiO_6 octahedra alternating with 2 layers of CuO_5 square pyramids. Single layers of europium and barium alternate in the A sites.

As a final example of perovskites with both Cu and Ti, Bochu *et al.* (1979) have reported compounds with copper in the 12-coordinate A site, as opposed to the more usual octahedral B site. Both $(\text{CaCu}_3)\text{Ti}_4\text{O}_{12}$ and $(\text{SrCu}_3)\text{Ti}_4\text{O}_{12}$ were found to have cubic unit cells approximately twice the size of simple perovskites. The neutron diffraction pattern of the former compound was found to be consistent with a model where Ca and Cu were ordered over the A sites, giving rise to the doubled unit cell.

The foregoing summary shows that there is a considerable body of work dealing with perovskite structures containing both copper and titanium. However, layered perovskite structures of the type discussed in previous chapters which contain both of these elements do not appear to have been investigated. In this report, an account is given of Cu substitution in one of the layered families, the Ruddlesden-Popper compounds $\text{Sr}_{n+1}\text{Ti}_n\text{O}_{3n+1}$.

7.1.2 Ruddlesden-Popper Cuprates

La_2CuO_4 has been known for some time as a K_2NiF_4 -type oxide containing single sheets of corner-linked CuO_6 octahedra interleaved with rocksalt layers of lanthanum atoms. This structure has been described in Chapter 3 as the $n=1$ structure of the Ruddlesden-Popper family of compounds which have the general formula $\text{A}_{n+1}\text{B}_n\text{O}_{3n+1}$. La_2CuO_4 has lower symmetry than the tetragonal strontium titanates, owing to a cooperative tilting scheme of the octahedra about one of their two-fold axes. This leads to an orthorhombic unit cell where a and b are approximately $\sqrt{2}$ times the a dimension of tetragonal compounds (Longo and Raccach, 1973). The material changes to tetragonal symmetry when small amounts of other cations (*e.g.* Sr) are substituted for La (Michel and Raveau, 1984).

Following reports of superconductivity in Ba-doped La_2CuO_4 (Bednorz and Müller, 1986; Chu *et al.*, 1987), a number of publications have addressed the question of whether further lanthanum cuprates might exist with wider perovskite lamellae, *i.e.* the Ruddlesden-Popper series $\text{La}_{n+1}\text{Cu}_n\text{O}_{3n+1}$. Davies and Tilley (1987) reported the preparation in air of ordered compounds in this series with values of n between 2 and 5. These were identified by XRD and HREM; the latter technique revealing disordered intergrowths in some samples with individual lamellae as wide as 7 octahedra. Torrance *et al.* (1987) reported that the $n=2$ compound was not yet known, but prepared "mostly single-phase" samples of the $n=3$ and $n=4$ materials. In both of these papers, the authors indicated that further details including X-ray diffraction data were to be published elsewhere, but subsequent papers were unable to be located.

Other workers have been unable to prepare $\text{La}_{n+1}\text{Cu}_n\text{O}_{3n+1}$ compounds with $n>1$. Maletta *et al.* (1987), Sekizawa *et al.* (1987) and Takano *et al.* (1987) all reported efforts to prepare $n=2$ and $n=3$ materials. In each case, only the $n=1$ compound was observed, sometimes with minor unidentified peaks in the XRD traces. In the last of these studies, the authors tried heating specimens in air as well as in sealed tubes containing KClO_3 to generate a high oxygen partial pressure.

The reason for trying to react La_2O_3 and CuO under high oxygen pressures is that the $n=\infty$ compound, LaCuO_3 , contains copper in the trivalent oxidation state. Demazeau *et al.* (1972) have reported the synthesis of this compound under high oxygen partial pressures (estimated as >400 bar) generated by the *in situ* decomposition of KClO_4 . Hence the $\text{La}_{n+1}\text{Cu}_n\text{O}_{3n+1}$ series entails an increase in copper valence from 2+ in the $n=1$ compound through to 3+ in $n=\infty$. This change in oxidation state is analogous to that for Ni in the corresponding Ruddlesden-Popper series $\text{La}_{n+1}\text{Ni}_n\text{O}_{3n+1}$ (Drennan *et al.*, 1982). The difficulty in preparing $\text{La}_{n+1}\text{Cu}_n\text{O}_{3n+1}$ compounds may therefore be related to the need to control the copper valence and corresponding oxygen stoichiometry.

An alternative, and closely related, way of increasing the thickness of the perovskite lamellae is by the addition of ACuO_2 sheets instead of ACuO_3 octahedra. The

perovskite unit is therefore oxygen deficient, but copper remains in the more usual 2+ oxidation state. Nguyen *et al.* (1981) described such a structure for materials with the formula $\text{La}_{2-x}\text{A}_{1+x}\text{Cu}_2\text{O}_{6-1/2x}$ where A was Sr or Ca, shown in Figure 7-2. It is essentially the same as an $n=2$ Ruddlesden-Popper material, but with the plane of oxygens in the centre of the perovskite lamellae removed. Copper is therefore 5-coordinate in square pyramidal sites, and the A cation between the copper planes 8-coordinate instead of the 12-coordinate arrangement in fully oxygenated perovskite. The A cations in the rocksalt layer possess the same 9-fold coordination as in conventional Ruddlesden-Popper compounds.

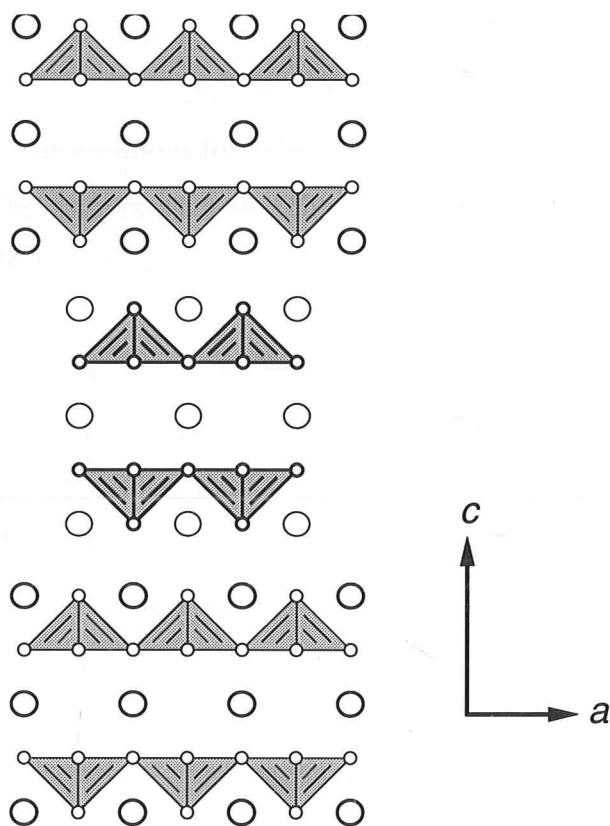


Figure 7-2 Structure of the oxygen-deficient Ruddlesden-Popper compound $\text{La}_2\text{ACu}_2\text{O}_6$ (A=Sr,Ca). Cu atoms are in the square pyramidal sites, and the large circles represent La or A cations. Light and heavy ruling indicate a difference in height of $b/2$.

Nguyen *et al.* (1981) also observed a difference in behaviour according to whether the A cation was Sr or Ca. For Sr-containing compounds, a small range of compositional variation was tolerated, given by the range $0 \leq x \leq 0.14$ in the formula $\text{La}_{2-x}\text{A}_{1+x}\text{Cu}_2\text{O}_{6-\delta}$. Sr and La were disordered over the available lattice sites, so that the 8-coordinate site between Cu planes was occupied equally by Sr and La, and the 9-coordinate rocksalt

site 75% La. The Ca-containing compound, on the other hand, produced single-phase samples only when x was equal to 0.1. Limited disorder of Ca and La was observed, so that the 8-coordinate site was 90% Ca and the 9-fold site 90% La. An account of this difference in behaviour was given in terms of the variation in ionic radii, and was subsequently confirmed by Rietveld analysis of neutron diffraction data (Santoro *et al.*, 1990).

Further substitutions in these compounds were investigated by Doverspike *et al.* (1989). These authors were also only able to produce the Ca-containing compound for the composition $\text{La}_{1.9}\text{Ca}_{1.1}\text{Cu}_2\text{O}_{6.8}$. They reported substitution of other lanthanides for La, and of Sr or Ba for Ca. In the case of Sr-substitution, materials between $\text{La}_{1.9}\text{Ca}_{1.1}\text{Cu}_2\text{O}_{6.8}$ and $\text{La}_{1.9}(\text{Ca}_{0.9}\text{Sr}_{0.2})\text{Cu}_2\text{O}_{6.8}$ were able to be synthesised as pure phases. By contrast, substitutions for either La or Sr in $\text{La}_2\text{SrCu}_2\text{O}_6$ resulted in mixed-phase products. The authors attributed this to the difference in the cation ordering schemes between the two systems.

Following the structural evolution from La_2CuO_4 through $\text{La}_2\text{ACu}_2\text{O}_6$ leads to a series of compounds akin to conventional Ruddlesden-Popper compounds, but deficient in oxygen with the general formula $\text{La}_2\text{A}_{n-1}\text{Cu}_n\text{O}_{2n+2}$. The structure of the $n=3$ member of this series is depicted in Figure 7-3, and comprises triple layers of oxygen-deficient perovskite interleaved with rocksalt layers. The perovskite component has two rows of vacant oxygen sites, leaving a central sheet of corner-sharing CuO_4 square planes sandwiched between layers of CuO_5 square pyramids. The A cations either side of the square planar sheet have 8-fold coordination.

It is not clear whether materials with this structure have been synthesised or not. Rouillon *et al.* (1989) assigned this structure to the material $\text{PbBaYSrCu}_3\text{O}_8$, on the basis of calculated XRD patterns. Tokiwa *et al.* (1989) disputed this, claiming instead the material had the same structure as $\text{Pb}_2\text{Sr}_2\text{YCu}_3\text{O}_8$ with a missing PbO layer. This compound contains alternating double and single copper layers separated by layers of the other elements.

Triple copper-oxygen layers with the same arrangement as depicted in Figure 7-3 are found in some of the high- T_c superconductors, for example $\text{Bi}_2\text{Ca}_2\text{Sr}_2\text{Cu}_3\text{O}_{10}$ (Tarascon *et al.*, 1988) and $\text{Tl}_2\text{Ba}_2\text{Ca}_2\text{Cu}_3\text{O}_{10}$ (Toradi *et al.*, 1988). The interlayer structure in these materials are rocksalt-based, but with four layers of metal atoms instead of the two found in La_2CuO_4 and $\text{La}_2\text{ACu}_2\text{O}_6$.

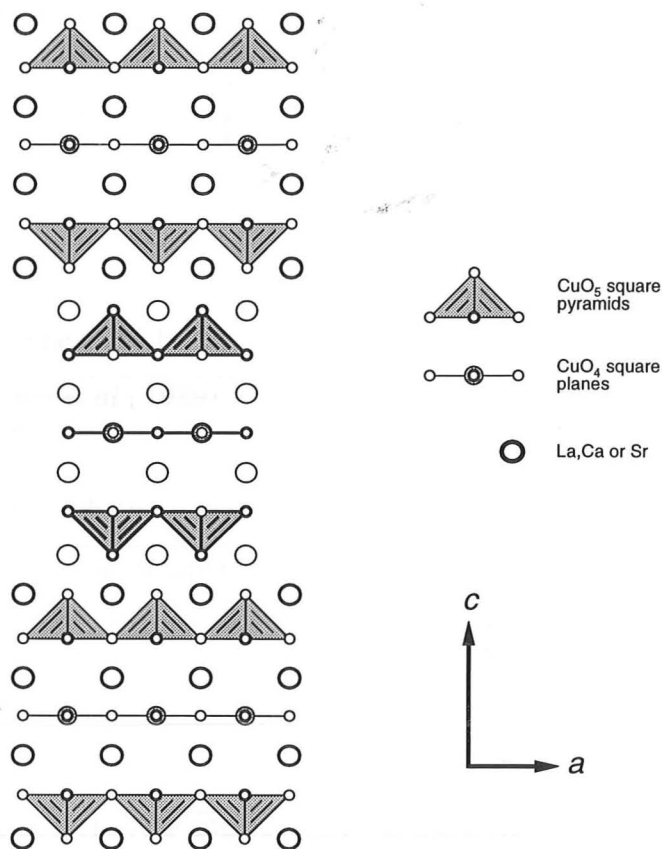


Figure 7-3 Structure of the $n=3$ member of the oxygen deficient Ruddlesden-Popper series $\text{La}_2\text{A}_{n-1}\text{Cu}_n\text{O}_{2n+2}$. As in other structural diagrams, light and heavy ruling differentiate between atoms at positions differing by $b/2$; however here this convention is extended to include the oxygens in polyhedra for additional clarity.

The $n=\infty$ member of the $\text{La}_2\text{A}_{n-1}\text{Cu}_n\text{O}_{2n+2}$ series has the formula ACuO_2 and consists entirely of sheets of CuO_4 square planes interleaved with layers of 8-coordinate A cations (Figure 7-4). This may be thought of as a perovskite structure with parallel planes of oxygens removed at the level of the A cations. Siegrist *et al.* (1988a) prepared single crystals with the composition $\text{Ca}_{0.86}\text{Sr}_{0.14}\text{CuO}_2$ and confirmed the structural arrangement. In an examination of the SrO-CaO-CuO system, Roth *et al.* (1989) reported that the perovskite-like structure was only stable over a very narrow range of compositions, approximately between $\text{Ca}_{0.83}\text{Sr}_{0.17}\text{CuO}_2$ and $\text{Ca}_{0.87}\text{Sr}_{0.13}\text{CuO}_2$.

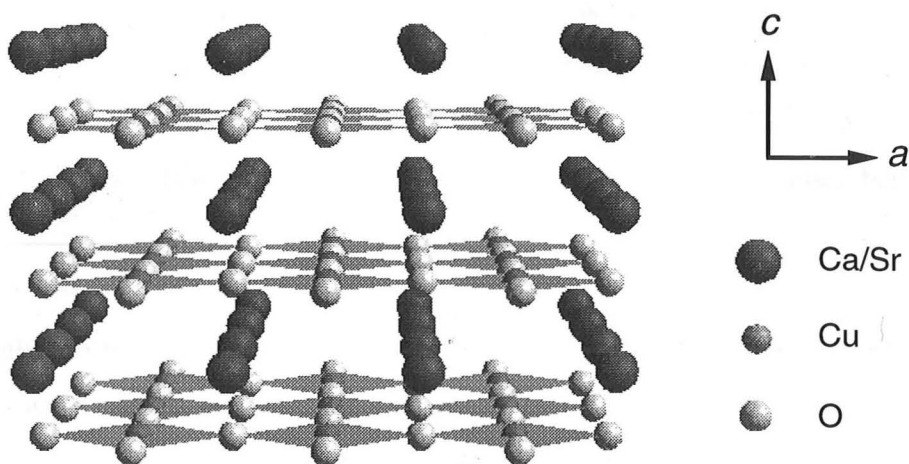


Figure 7-4 Perspective view of the $ACuO_2$ ($A=Ca,Sr$) structure.

A broader range appears to be obtainable if high pressures are used during synthesis (Okai, 1989; Takano *et al.*, 1989).

Using a knowledge of the $n=\infty$ structure, experiments were undertaken in this study in an attempt to synthesise compounds with triple copper-oxygen layers of the type depicted in Figure 7-3. Efforts were also made to prepare fully oxygenated structures in the $La_{n+1}Cu_nO_{3n+1}$ series.

7.2 Solid Solutions Between Copper and Titanium

Samples were prepared with compositions between Sr_2TiO_4 and La_2CuO_4 in an effort to synthesise $n=1$ Ruddlesden-Popper compounds containing both TiO_6 and CuO_6 octahedra. Initial experiments, reacted up to $1000^\circ C$, suggested that such materials could not be prepared, as XRD traces displayed only peaks attributable to the two end members.

Since solid solution has been observed for the corresponding perovskites (*e.g.* Jones and McKinnon, 1990), it was considered more likely that solid solution would be found in Ruddlesden-Popper compounds with $n>1$, as these materials contain larger perovskitic elements. In accordance with the perovskite solid solution, and to

maintain the usual oxidation states of metal atoms, samples were reacted with compositions given by the formula $\text{Sr}_{3-y}\text{La}_y\text{Ti}_{2-1/2y}\text{Cu}_{1/2y}\text{O}_7$. This represents solid solution in the $n=2$ Ruddlesden-Popper structure between Ti^{4+} and Cu^{2+} with complete oxygen occupancy. The compositional parameter y may take on values between 0 and 3.

Interestingly, no $n=2$ compounds based on either Ti or Cu were observed when such specimens were reacted with intermediate values of y . Instead, XRD patterns showed the samples to contain a mixture of $n=1$ and perovskite phases. At lower temperatures, below 1000°C , some of the diffraction peaks were quite broad, indicating a measure of structural disorder and perhaps a departure from equilibrium. As the temperature was raised, the peaks sharpened but were still attributable to the perovskite and $n=1$ phases. The highest temperature, 1150°C , was close to the melting temperature of these samples.

Sample	a (perovskite)	a ($n=1$)	c ($n=1$)	x (estimated)	x (predicted)
$y=0.75$	3.9701(8)	3.863(5)	12.87(2)	0.34	0.38
$y=1.5$	3.905(3)	3.825(2)	13.064(7)	0.67	0.75
$y=2.25$	3.9163(17)	3.7915(12)	13.196(5)	0.91	1.0
Sr_2TiO_4		3.8859(2)	12.597(1)		
La_2CuO_4		3.7783(2)	13.229(1)		

Table 7-1 Cell parameters (\AA) obtained after reaction of $\text{Sr}_{3-y}\text{La}_y\text{Ti}_{2-1/2y}\text{Cu}_{1/2y}\text{O}_7$ samples. The $n=1$ phase may be represented by the solid solution $\text{Sr}_{2-2x}\text{La}_{2x}\text{Ti}_{1-x}\text{Cu}_x\text{O}_4$, and values of x for the samples have been estimated from the cell dimensions of the end members. The parameters for La_2CuO_4 are taken from Godwod *et al.* (1987) and actually correspond to the composition $(\text{La}_{1.93}\text{Sr}_{0.07})\text{CuO}_4$. Predicted values of x arise from assuming all La and Cu is positioned in the $n=1$ phase, as described in the text.

Inspection of the unit cell parameters measured from these samples showed that the cell of the $n=1$ phase lay between those of Sr_2TiO_4 and La_2CuO_4 , indicating the existence of a solid solution. This was the case even for materials reacted at lower temperatures, where the direct reaction of $n=1$ compositions did not display any solid solution at all. The cell parameters obtained from the $n=2$ preparations reacted at 1050°C are summarised in Table 7-1. The perovskite cell is close to that of SrTiO_3 for the $y=0.75$ and $y=1.5$ samples, but the $n=1$ cells of all three samples lie between those of the end members. If we represent solid solution in the $n=1$ phase by the formula $\text{Sr}_{2-2x}\text{La}_{2x}\text{Ti}_{1-x}\text{Cu}_x\text{O}_4$, then the value of x may be estimated by comparing the

measured cell dimensions to a linear interpolation between those of the two end members. To make best use of the experimental data, this has been carried out using the ratio c/a , and the resulting values of x included in Table 7-1. Because La_2CuO_4 has an orthorhombic unit cell, the cell dimensions of the closest tetragonal compound ($\text{La}_{1.93}\text{Sr}_{0.07}\text{CuO}_4$; Godwod *et al.*, 1987) have been used for the La end member.

The observed diffraction patterns may be understood by assuming that the $n=2$ ($\text{A}_3\text{B}_2\text{O}_7$) composition results in an equimolar mixture of A_2BO_4 and ABO_3 , and that Sr preferentially occupies the ABO_3 phase and La the A_2BO_4 phase. On this basis, the perovskite phase would be pure SrTiO_3 for the $y=0.75$ and $y=1.5$ samples, and contain a small amount of La- and Cu-substitution for the $y=2.25$ sample, since there is insufficient Sr and Ti at this composition. This is consistent with the measured cell parameters, as the only cell different from SrTiO_3 ($a=3.906\text{\AA}$) was found for the $y=2.25$ specimen, and this was increased toward the value expected for $\text{La}(\text{Cu}_{0.5}\text{Ti}_{0.5})\text{O}_3$ ($\approx 3.934\text{\AA}$; Jones and McKinnon, 1990).

The compositions of the $n=1$ phase are also in agreement with this scheme of cation distribution. The predicted values of x (in $\text{Sr}_{2-2x}\text{La}_{2x}\text{Ti}_{1-x}\text{Cu}_x\text{O}_4$) are also included in Table , calculated by positioning as much La and Cu from the starting compositions in the $n=1$ phase as is possible. These compare favourably to the measured values and show, to a first approximation at least, that La and Cu occupy the $n=1$ structure in preference to perovskite. This may be because the octahedra in $n=1$ materials share corners in only two dimensions as opposed to the three-dimensional arrangement in perovskite. A two-dimensional network allows greater freedom for octahedral distortion arising from the Jahn-Teller effect frequently observed in Cu^{2+} compounds, where the apical oxygens are positioned further away from the Cu atom than those in the corner-sharing sites. The distortion in La_2CuO_4 is quite marked - the apical Cu-O distances are 2.40\AA , compared to 1.90\AA in the basal plane (Longo and Raccach, 1973). This explanation may also account for why $n=2$ solid solutions were not observed, but resulted in the two-phase assemblage of perovskite and $n=1$ materials.

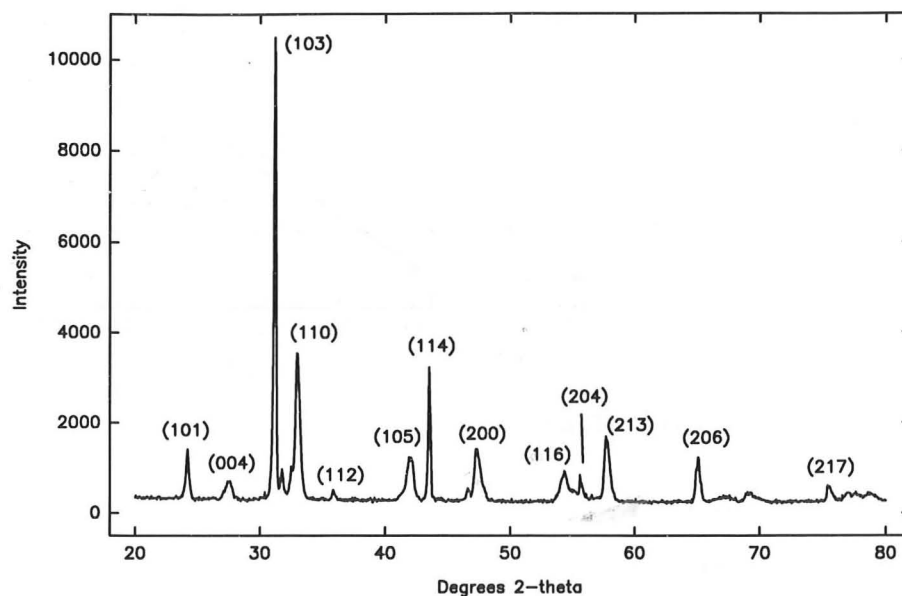


Figure 7-5 Indexed XRD pattern of $(\text{SrLa})_2(\text{Ti}_{0.5}\text{Cu}_{0.5})\text{O}_4$ reacted at 1140°C . The unindexed peaks near 32° and $46^\circ 2\theta$ have not been identified.

These results prompted a re-examination of the samples prepared to investigate solid solution directly in $n=1$ structures. By increasing the temperature to a little below the melting temperature, approximately 1150°C , XRD patterns were obtained which contained a single $n=1$ phase with a few minor unidentified peaks. An example is shown in Figure 7-5 for the $x=0.5$ composition in which some variation in the sharpness of the peaks can be seen. Unit cell parameters obtained from these samples are given in Table 7-2 and graphed in Figure 7-6 for samples reacted at 1140°C . The linear change in both a and c over the entire composition range confirmed that complete solid solution does take place.

Composition, x	a (Å)	c (Å)
0	3.8859(2)	12.597(1)
0.25	3.864(5)	12.741(16)
0.5	3.837(4)	12.951(12)
0.75	3.8088(12)	13.122(4)
1.0	3.7783(2)	13.229(1)

Table 7-2 Unit cell dimensions of $n=1$ solid solutions, $\text{Sr}_{2-2x}\text{La}_{2x}\text{Ti}_{1-x}\text{Cu}_x\text{O}_4$. The value for the $x=1.0$ composition is derived from the same source as the previous table.

As the degree of La substitution proceeds, the a dimension decreases while c increases. This means that the 2θ positions of some diffraction peaks move to higher angles, some move to lower angles, and some remain in approximately the same

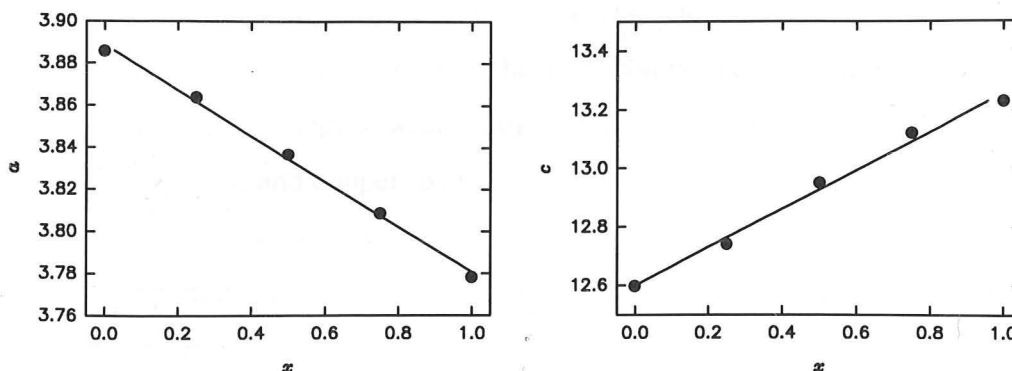


Figure 7-6 Variation in unit cell parameters of $\text{Sr}_{2-2x}\text{La}_{2x}\text{Ti}_{1-x}\text{Cu}_x\text{O}_4$ samples

position according to their dependence on a and c . The broadest diffraction peaks obtained were also those whose positions changed the most, indicating that the broadening was primarily due to compositional inhomogeneity rather than small particle sizes or strain.

The possibility of cation ordering in these samples was also considered, since the size and shape of the CuO_6 octahedra in La_2CuO_4 are somewhat different from the TiO_6 octahedra in Sr_2TiO_4 (see Table 7-3). A superstructure might also explain the weak unidentified peaks in the diffraction patterns. However, no superstructure reflections or a decrease in the tetragonal symmetry could be detected in electron diffraction patterns or HREM images recorded from individual crystal fragments. The solid solution therefore seems to involve a random disorder of cation positions, as that observed in perovskites containing Cu and Ti.

Compound	Apical B-O distance	Basal B-O distance
La_2CuO_4	2.40Å	1.90Å
Sr_2TiO_4	1.974Å	1.943Å

Table 7-3 Comparison of octahedral bond lengths in La_2CuO_4 (Longo and Raccach, 1973) with those in Sr_2TiO_4 (this study, Chapter 3).

7.3 Three-layered Cuprates

Several different approaches were taken in an effort to synthesise 3-layered cuprates with the Ruddlesden-Popper structure. Initial experiments were carried out using only

La and Cu to prepare the $\text{La}_{n+1}\text{Cu}_n\text{O}_{3n+1}$ materials described by Davies and Tilley (1987) and Torrance *et al.* (1987). The $n=1$ compound (La_2CuO_4) was prepared relatively easily, but samples with compositions corresponding to $n>1$ resulted in mixtures of La_2CuO_4 and copper oxide.

Because compounds with $n>1$ require some copper in the 3+ oxidation state if the oxygen stoichiometry is to be maintained, experiments were also carried out using a tetravalent A cation in addition to La^{3+} . This allowed specimens with the appropriate overall stoichiometry to be prepared with divalent Cu, for example $\text{La}_2\text{CeCu}_2\text{O}_7$. Ce was chosen for this purpose because it had the largest ionic radius of any of the 4+ metals available. However, these experiments did not produce the desired products, resulting instead in mixtures of La_2CuO_4 , CuO and CeO_2 . The unit cell of the CeO_2 phase was significantly larger than that found in the pure compound, which was assumed to be a result of substitution of La for Ce. Minkova and Aslanyan (1989) have described an extensive (up to 68%) solid solution of La_2O_3 in CeO_2 in which the cubic unit cell parameter increased from 5.45Å to 5.65Å.

It is possible that both of these approaches failed because in each case the parent perovskite is unable to be prepared under the synthesis conditions used. LaCuO_3 requires a high oxygen partial pressure (Demazeau *et al.*, 1972), and CeCuO_3 is not known at all. Perovskites have not been reported where the A cation is tetravalent and the B cation divalent.

For these reasons, efforts were shifted to the oxygen-deficient Ruddlesden-Popper compounds where the $n=\infty$ member (ACuO_2) can be synthesised under ambient conditions for appropriate mixtures of CaO, SrO and CuO. Because of the narrow composition range reported for the perovskite-based structure (Roth *et al.*, 1989), samples were reacted initially with $n=\infty$ compositions ($\text{Ca}_{1-x}\text{Sr}_x\text{CuO}_2$) to ensure that this compound could be prepared with the equipment used in this study.

The results indicated a considerably wider homogeneity range than Roth *et al.* reported. Whereas these authors found perovskite-based materials only for values of x

in the range $0.13 \leq x \leq 0.17$, the samples prepared here produced this compound for values of x between 0.05 and 0.20. The reaction temperature (950°C) was the same in both studies. Although the present XRD traces also contained small peaks due to impurity phases, the unit cell dimensions of the $n=\infty$ phase supported the notion of solid solution in $\text{Ca}_{1-x}\text{Sr}_x\text{CuO}_2$ over the $0.05 \leq x \leq 0.20$ range. These are given in Table 7-4 and Figure 7-7, and show a linear increase with increasing Sr content, in line with the larger ionic radius of Sr^{2+} (1.26\AA) compared to Ca^{2+} (1.12\AA). Below $x=0.05$, samples displayed large quantities of Ca_2CuO_3 and CuO , and above $x=0.20$ a solid solution based on SrCuO_2 was observed. These results are consistent with the phase diagram given by Roth *et al.* (1989). The structure of SrCuO_2 is quite different from the perovskite-based $\text{Ca}_{1-x}\text{Sr}_x\text{CuO}_2$, containing zig-zag ribbons of edge-sharing CuO_4 square planes separated by rows of Sr atoms (Teske and Müller-Buschbaum, 1970).

Composition, x	a (\AA)	c (\AA)
0.05	3.8548(12)	3.1915(10)
0.10	3.8614(15)	3.2042(12)
0.15	3.8637(12)	3.2125(12)
0.20	3.8692(10)	3.2263(9)

Table 7-4 Cell parameters for $n=\infty$ samples, with compositions $\text{Ca}_{1-x}\text{Sr}_x\text{CuO}_2$.

The cell parameters obtained here appear to be consistent with those reported from high pressure syntheses, although direct comparisons are difficult. This is because Okai (1989) only presented cell dimensions in graphical form, and the solid solution reported by Takano *et al.* (1989) was in the range $0.33 \leq x \leq 1.0$, outside that of the present materials.

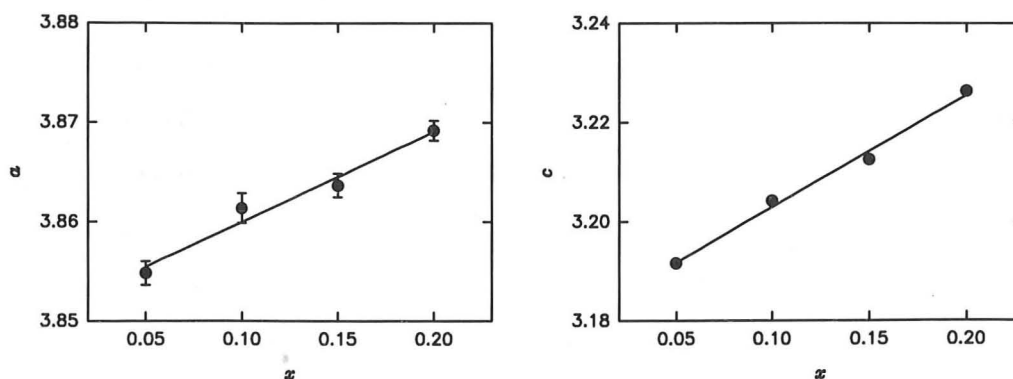


Figure 7-7 Unit cell parameters measured from the oxygen-deficient perovskite phase in $\text{Ca}_{1-x}\text{Sr}_x\text{CuO}_2$ specimens.

The $n=3$ member of the oxygen-deficient Ruddlesden-Popper cuprates may be represented by the formula $\text{La}_2\text{A}_2\text{Cu}_3\text{O}_8$. Samples were reacted with $\text{A}=\text{Ca}, \text{Sr}$ and Ba , but no evidence of any compounds with the $n=3$ structure could be found. XRD traces of Ca -containing samples showed the $n=2$ compound, CaO , and peaks attributed to the $(\text{La}, \text{Ca})_{14}\text{Cu}_{24}\text{O}_{41}$ phase described by Siegrist *et al.* (1988b). The latter compound was identified by calculating a diffraction pattern from the crystal structure given by Siegrist *et al.* In a recent study of the $\text{La}_2\text{O}_3\text{-CaO-CuO}$ system, Skakle and West (1994) identified this compound as having the stoichiometry $\text{LaCa}_2\text{Cu}_5\text{O}_{8+\delta}$.

The Sr -containing specimen produced an $n=2$ compound as well, with SrCuO_2 also detected in XRD patterns. The Ba -containing sample did not show any Ruddlesden-Popper phases, containing instead the oxygen deficient perovskite $\text{Ba}_3\text{La}_3\text{Cu}_6\text{O}_{14.1}$ reported by Er-Rakho *et al.* (1981). A few unidentified peaks remained in the XRD pattern which, on the basis of the overall composition, were assumed to have arisen from an unknown Ba - and La -rich phase.

According to the discussion in the previous chapter, an $n=3$ phase in the $\text{La}_2\text{A}_{n-1}\text{Cu}_n\text{O}_{2n+2}$ series should have an a dimension close to that of the corresponding $n=\infty$ perovskite compound. This conclusion must be tempered by the realisation that the Ruddlesden-Popper compounds considered before this chapter contained fully oxygenated octahedra, whereas the Cu-O polyhedra in the oxygen-deficient series include octahedra, square pyramids, and square planes. Nevertheless, there are further reasons for thinking that the $n=3$ and $n=\infty$ a dimensions might be similar. Although the composition range of the $n=\infty$ material was found in this study to be larger than previously reported, it is still fairly restricted with a varying between 3.885\AA and 3.869\AA . It would appear that the structural arrangement with sheets of CuO_4 square planes is only stable within a limited range of cell sizes, provided by a suitable balance of the Ca^{2+} and larger Sr^{2+} ions. This is supported by the a dimensions of other compounds known to have sheets of CuO_4 square planes which fall in a similar range (Table 7-5).

Compound	a (Å)	Reference
TlBa ₂ Ca ₂ Cu ₃ O ₉	3.853(1)	Subramanian <i>et al.</i> (1988)
Tl ₂ Ba ₂ Ca ₂ Cu ₃ O ₁₀	3.8503(6)	Toradi <i>et al.</i> (1988)
Tl _{1.6} Hg _{0.4} Ba ₂ Ca ₂ Cu ₃ O ₁₀	3.843(1)	Goutenoire <i>et al.</i> (1994)

Table 7-5 Reported a cell parameters for compounds with a layer of corner-sharing square planar copper oxide polyhedra.

With this in mind, a series of samples was made across the composition range La_{1.9}Ca_{2.1-x}Sr_xCu₃O_{8-δ}. The La stoichiometry, slightly lower than the ideal value of 2.0, was chosen because of the stability of the Ca-based $n=2$ compound with the same La content (Nguyen *et al.*, 1981). The a dimensions of the analogous $n=2$ phases are 3.825(2)Å and 3.863(2)Å for the Ca and Sr end members respectively (Nguyen *et al.*, 1981). The Sr end member approaches the a dimension of the $n=\infty$ phases which appeared to have been stabilised by an appropriate combination of Sr and Ca. It was therefore hoped that a combination of Ca and Sr might lead to a cell size suitable for stabilising an $n=3$ phase.

The samples were reacted at 950°C, but again no evidence of an $n=3$ phase could be observed in XRD patterns, which displayed primarily peaks attributed to $n=2$ compounds. The additional diffraction peaks arose from materials similar to those described earlier for the end-member compositions. In particular, peaks corresponding to the $n=\infty$ phase were not found in the diffraction patterns from intermediate compositions. The predominance of $n=2$ materials was confirmed by HREM studies, which did not locate any $n=3$ structures, even on a local scale. Figure 7-8 shows a micrograph from a sample where the Ca:Sr ratio was similar to that found in $n=\infty$ compounds. It contains well-ordered $n=2$ lamellae without any intergrowths, and the corresponding electron diffraction pattern does not display any streaking which would arise from disordered intergrowths.

The unit cell parameters of the $n=2$ phases prepared from the $n=3$ compositions are listed in Table 7-6 and graphed in Figure 7-9. Both a and c show a roughly linear variation over the entire composition range, suggesting complete solid solution between La₂CaCu₂O₆ and La₂SrCu₂O₆. This is in contrast to earlier reports (Doverspike *et al.*, 1989) which indicated only a restricted solid solution near the Ca

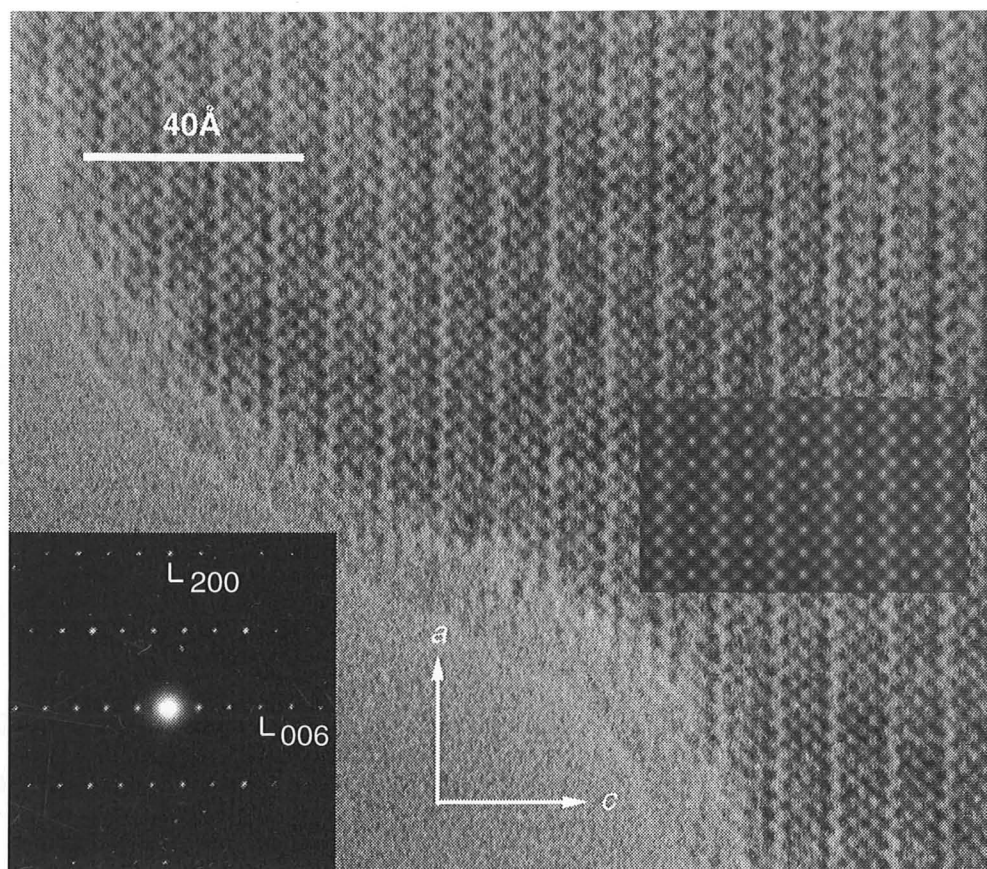


Figure 7-8 HREM image from a $\text{La}_{1.9}\text{Ca}_{1.8}\text{Sr}_{0.3}\text{Cu}_3\text{O}_{8-\delta}$ sample, showing ordered $\text{La}_2\text{ACu}_2\text{O}_6$ -type structure. The simulated image inset is for a 30.6Å thick crystal at a defocus of -180Å , where A corresponds to $(\text{Ca}_{0.8}\text{Sr}_{0.2})$.

end member. However, the present materials are not single-phase, and contain excess Ca and/or Sr over the $\text{La}_2\text{ACu}_2\text{O}_6$ composition.

Composition, x	a (Å)	c (Å)
0	3.8279(3)	19.4301(17)
0.1	3.8305(8)	19.511(7)
0.19	3.8312(4)	19.530(2)
0.35	3.8308(14)	19.541(13)
0.8	3.8387(10)	19.709(6)
1.0	3.8434(8)	19.772(4)
1.2	3.8453(9)	19.811(9)
1.5	3.8525(8)	19.949(3)
1.8	3.8573(10)	20.043(7)
2.1	3.8596(6)	20.038(4)

Table 7-6 Cell dimensions of $n=2$ compounds formed from preparations with $n=3$ compositions $\text{La}_{1.9}\text{Ca}_{2.1-x}\text{Sr}_x\text{Cu}_3\text{O}_{8-\delta}$.

It is therefore possible that the solid solution indicated by the cell parameters corresponds to compositions where some of the A cations substitute for La, represented by the formula $\text{La}_{2-y}(\text{Ca}_{1-x}\text{Sr}_x)_{1+y}\text{Cu}_2\text{O}_{6-\delta}$. This type of substitution has

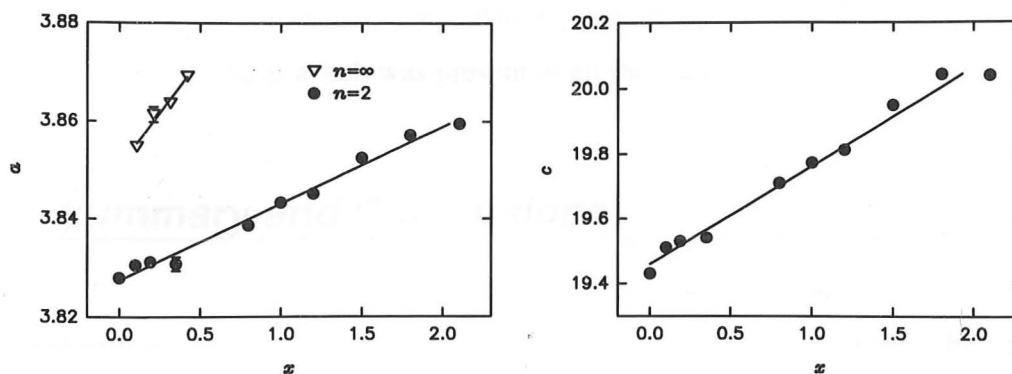


Figure 7-9 Unit cell parameters of the $n=2$ phase prepared from the $n=3$ compositions $\text{La}_{1.9}\text{Ca}_{2.1-x}\text{Sr}_x\text{Cu}_3\text{O}_{8-\delta}$. The a measured from $n=\infty$ samples discussed earlier are also shown, positioned according to the same Ca/Sr ratio.

been observed where Sr substitutes onto the La (rocksalt) site, and is in fact important for initiating superconductivity in these materials (Cava *et al.*, 1990). The cell parameters obtained in the present study were consistent with this idea, where primarily Sr substitutes onto the rocksalt site.

For the Ca end member, the only reported composition is $\text{La}_{1.9}\text{Ca}_{2.1}\text{Cu}_2\text{O}_{6-\delta}$, which has the cell parameters $a=3.8248(1)\text{Å}$ and $c=19.4286(5)\text{Å}$ (Santoro *et al.*, 1990). The unit cell of the sample containing Ca only ($x=0$, Table 7-6) compares favourably with these values. For the Sr end member, Nguyen *et al.* (1981) obtained cell parameters of $a=3.865(2)\text{Å}$ and $c=19.887(4)\text{Å}$ for $\text{La}_2\text{SrCu}_2\text{O}_6$, and $a=3.859(2)\text{Å}$, $c=19.956(4)$ for $\text{La}_{1.86}\text{Sr}_{1.14}\text{Cu}_2\text{O}_{6-\delta}$ where there was greater substitution of Sr onto the rocksalt site. The cell parameters obtained here for the Sr end member ($x=2.1$, Table 7-6) are closest to the latter values. Hence it appears that complete solid solution is attainable between $\text{La}_{1.9}\text{Ca}_{1.1}\text{Cu}_2\text{O}_{6-\delta}$ and $\text{La}_{2-y}\text{Sr}_{1+y}\text{Cu}_2\text{O}_{6-\delta}$, and is stabilised by Sr substitution onto the 9-fold rocksalt site.

The linear nature of the graphs in Figure 7-9 suggests that the Sr/Ca ratio adopted by the $n=2$ phase is roughly the same as the initial $n=3$ composition. The a dimensions of the $n=2$ phases obtained are closest to those for $n=\infty$ materials at Sr-rich compositions. However, the $n=\infty$ phase is only found for Ca-rich stoichiometries, highlighted in Figure 7-9 by plotting the $n=\infty$ a dimensions on the same graph. The disparity between the cells of the two systems may explain the lack of success in

preparing $n=3$ in the current samples. Another reason may be the apparent stability of the $(\text{Ca},\text{La})_{14}\text{Cu}_{24}\text{O}_{41}$ phase which was present in all the Ca-rich specimens.

7.4 Summary and Conclusions

A solid solution between Sr_2TiO_4 and La_2CuO_4 has been observed where the unit cell parameters displayed a linear correlation with composition. A similar solid solution in layered materials with thicker perovskite lamellae was not found, despite previous reports of solid solution between the corresponding perovskites. Attempts to prepare $n=2$ solid solutions resulted instead in mixtures of $n=1$ and perovskite phases. The unit cell parameters of these compounds showed that La and Cu preferentially occupied the $n=1$ phase. This was thought to be due to the greater freedom for Jahn-Teller distortion of the CuO_6 octahedra in the $n=1$ structure, which has only a 2-dimensional network of corner-sharing octahedra.

Attempts to synthesise a three-layered Ruddlesden-Popper cuprate were not successful. The simple $\text{La}_4\text{Cu}_3\text{O}_{10}$ composition resulted in a mixture of La_2CuO_4 and CuO , presumably because the experimental conditions were not adequate to oxidise $2/3$ of the Cu atoms to the $3+$ oxidation state. Substitution of Ce^{4+} for La^{3+} was also unsuccessful, despite Cu in the theoretical structure remaining divalent. However, the incorporation of A^{4+} cations in perovskites or Ruddlesden-Popper compounds has not been reported before.

A suitable combination of A cations amongst La, Sr, Ca and Ba could not be found which would produce a three-layered cuprate with an oxygen-deficient Ruddlesden-Popper structure. However, two new solid solutions were discovered. Firstly, the range of perovskite-related $\text{Ca}_{1-x}\text{Sr}_x\text{CuO}_2$ compounds which can be prepared under ambient conditions was found to be larger than previously reported, covering the limits $0.05 \leq x \leq 0.20$. Secondly, complete solid solution between the Ca- and Sr-containing $n=2$ oxygen-deficient structures was found. This appeared to have been stabilised by the substitution of Sr onto the 9-fold rocksalt site between perovskite-like lamellae.

Chapter 8

Summary and Concluding Remarks

- 8.1 Layers in Perovskite Compounds
 - 8.2 The Nature of the Intergrowth Phases
 - 8.3 Layered Perovskites Containing Copper
 - 8.4 New Structures and Future Possibilities
-

8.1 Layers in Perovskite Compounds

Various layered compounds based on perovskite have been described in previous studies where the layered component of the structure is oriented parallel to {100}, {110} or {111} planes in the parent perovskite. In this thesis, the existence of layered components in all three orientations has been demonstrated *within the same parent perovskite*, and similarities in the way in which their distribution is affected by changes in stoichiometry have been demonstrated. The work presented here has also shown the existence of a new compound with a more complex composite layered structure, and has indicated the presence of solid solutions in layered perovskites containing copper.

Perovskite-based layer structures are produced as a result of departures in composition away from the ideal ABO_3 perovskite stoichiometry. Tilley (1977b) has suggested that the dielectric constant of the parent perovskite is important in determining whether layered structures or point defects form, with the layered configuration dominating in materials having a high dielectric constant. Catlow and James (1980) believed that this was related to the ability of high dielectric materials to accept large cation displacements within the structure, this in turn permitting the structural relaxation necessary to stabilise the intergrowth of a layered component within the perovskite lattice. For the perovskite studied here ($SrTiO_3$), three different layer

orientations were investigated, which corresponded to three different types of compositional change. In each case, a series of ordered compounds was found where the complete layers were distributed in a regular sequence. They are summarised in the following paragraphs:

- (i) Layers oriented along a {100} perovskite plane, formed by an excess of SrO over the SrTiO₃ composition. The layered component contains double rows of Sr atoms in a rocksalt-like configuration, and phases containing this feature give rise to a family of compounds Sr_{n+1}Ti_nO_{3n+1}, where *n* is the number of TiO₆ octahedra between each rocksalt component. The number of ordered members in this family has not been firmly established before, and in particular it had not been established whether an ordered *n*=3 compound could be prepared. The stability of the *n*=3 phase has been verified in the current work, both by HREM imaging and Rietveld refinement of X-ray powder diffraction data.
- (ii) Layers oriented parallel to the {110} perovskite planes, resulting from an excess of oxygen, in turn caused by substituting La³⁺ for Sr²⁺. The layered component of the structure contains an additional plane of oxygen atoms where the corner-sharing octahedra are separated along the layer plane. Ordering of these components within the perovskite gives rise to a family of structures with the formula Sr_{n-4}La₄Ti_nO_{3n+2} in which the *n*=4, 4.5 and 5 members have been prepared here. Of these, the *n*=4 compound (La₂Ti₂O₇) has been described before, but the others have not been reported previously. Isostructural compounds are known in other chemical systems, however. The *n*=4.5 compound contains a regularly alternating sequence of perovskite lamellae 4 and 5 octahedra thick, and was the only such recurrent intergrowth found in this study.
- (iii) Layers oriented parallel to the {111} perovskite planes, in response to a deficiency of titanium. The oxygen stoichiometry in these phases was maintained by replacing simultaneously four Sr²⁺ atoms with La³⁺ for each

Ti⁴⁺ atom removed. The layered component of the structure consists of vacant face-sharing octahedra and leads to a family of compounds Sr_{n-3}La₄Ti_nO_{3n+3}. Previous studies have reported the $n=3, 4$ and 5 members of this family and proposed the general structural principles. In this investigation, the existence of these compounds has been confirmed, and their structures verified by HREM and refined by Rietveld analysis.

8.2 The Nature of the Intergrowth Phases

Rietveld refinements have been carried out for all members of the {100} and {111} layered families of structures. As well as verifying the structures of these compounds, the refinements have characterised the considerable distortions, primarily in the cation lattice, that are present in the perovskite lamellae. These distortions are greatest near the layered component of the structure, and decrease uniformly into the centres of the perovskite units. For the {100} oriented materials, the Sr atoms were pushed away from the centre of the rocksalt layer toward the interior of the perovskite region, while the reverse trend was found in the {111} layered compounds. In these latter materials, Sr/La atoms were found to be positioned closer to the planes of vacant octahedra than an ideal perovskite structure would predict. Distortions were also found in the anion framework and were especially evident in the TiO₆ octahedra. These results support the proposal that structural distortions are important in stabilising a layered structure, this in turn requiring materials with a high dielectric constant which will permit such extensive distortions.

In addition to the ordered materials, extensive disorder in these compounds has also been investigated, primarily using HREM. Disordered states could be classified into two main types, namely those involving irregular intergrowths of layered components, and disorders within the layered component itself. Random intergrowth of perovskite lamellae of varying thicknesses has been observed in both the {100} and {110} families of structures, particularly for compositions close to ordered materials having the thickest perovskite lamellae. As the composition approaches SrTiO₃, the

separation of the layered components of the structure becomes correspondingly larger, but HREM has revealed that the distribution of layers is not completely random. As has been reported in slightly reduced rutile (Bursill and Hyde, 1972), the layered components in the present investigation displayed a tendency to appear in clusters, leaving large regions of undisturbed perovskite.

HREM has also shown defects within the layer structure. For both the {100} and {110} systems, layers were imaged which terminated inside the perovskite matrix. The {100} materials additionally displayed deviations in the layer direction, where a single layer underwent right-angled changes in orientation. These occasionally formed complex mosaic patterns, as well as more simple structures such as U-shaped rocksalt layers. For all of these defects, computer-based models have been constructed to demonstrate how the structure adapts to accommodate the defect. Often, this is not as simple as first appears, since the perovskite regions either side of a layer are displaced relative to one another along more than one crystal axis. In the case of U-shaped rocksalt layers, the HREM images were clear enough to allow comparison with an image simulated from the computer-based model.

In qualitative terms, much of the behaviour of the layered structures derived from perovskite may be reconciled with the phenomenon of elastic strain. The perovskite structure is inevitably deformed by the presence of the layered component, which appears in all cases to possess a different 'ideal' periodicity in the intergrowth plane than the parent perovskite. Registration of the two structures requires that a single, common periodicity must prevail, however, and adjacent regions of the final structure must therefore contain alternate compressive and tensile stresses. Many of the observations made in this study can be interpreted in terms of this elastic model. The lattice dimensions of all three layered families displayed a regular progression where the cell dimensions within the plane of the layers tended towards the corresponding perovskite dimension as the separation of the layered components increased. Elastic considerations suggest that the observed lattice dimensions will be a compromise between those of the layered and perovskite components, with the values of the latter predominating as the perovskite component becomes thicker. Consequently, the

formation of the higher members of all series is restricted by the ensuing reduced relaxation at the interface between perovskite and layered components, as found experimentally. Although the trend in lattice parameters is also a feature of many other layered compounds, it does not seem to have been highlighted in previous publications.

Ordered compounds were only observed when the periodicity in the layered component differed significantly from the corresponding perovskite values, which occurred only for relatively narrow perovskite lamellae. The periodicities of these lamellae were also distinct from one another, and so they tended not to form disordered intergrowths. If larger lamellae occur, we may expect these to have very similar periodicities within the plane of the layers, and they will therefore intergrow randomly without excessive strain. Nevertheless, strain is still introduced by the presence of larger lamellae, and the clustering of layered components found in practice may also be the result of elastic interactions, since the overall strain in the parent perovskite will be minimised when the structural distortions are confined to a smaller region containing the cluster, rather than spread throughout the crystal.

However, a fully quantitative treatment which explains the observed structures in terms of elastic strain has yet to be formulated. The approach taken in this work was only partially successful because of the assumptions made in order to quantify the trends. The perovskite lamellae were considered as a collection of individual layers, each one octahedron thick, which behaved identically. However, the refined structures showed that distortions occurred progressively across the perovskite lamellae, and so a realistic model must take this into account.

8.3 Layered Perovskites Containing Copper

The structural chemistry of layered perovskites which contain copper has received considerable attention recently following the discovery of high- T_c superconductivity

in the layered cuprates. Part of the present study was directed toward the {100} layered perovskites containing copper, and several attempts were made to prepare materials with perovskite-like lamellae containing three copper-oxygen layers. These proved unsuccessful, probably due to the difficulty in preparing the corresponding perovskites for the $A_4Cu_3O_{10}$ formulations. The oxygen-deficient analogue ($A_4Cu_3O_8$), where the corresponding $n=\infty$ compound ($ACuO_2$) can be prepared relatively easily under ambient conditions, was also unable to be synthesised. In this case, there appears to be a requirement for a carefully-controlled lattice size to stabilise the $ACuO_2$ plane.

A possible way to synthesise a 3-layered copper Ruddlesden-Popper compound may be to use a halide in place of oxygen. Many ABX_3 perovskites are known, as well as Ruddlesden-Popper A_2BX_4 compounds where X is a halogen. A candidate for this approach is the K-Cu-F system, where $KCuF_3$ (Edwards and Peacock, 1959), K_2CuF_4 and $K_3Cu_2F_7$ (Herdtweck and Babel, 1981) have all been prepared. $K_4Cu_3F_{10}$ would be the next member of the series, but experimental details make investigation of this family somewhat difficult. KF is extremely hygroscopic, forming a dihydrate which melts below 100°C. Care must also be taken to eliminate oxygen when heating samples, which must be carried out at temperatures high enough to allow reaction but low enough to avoid loss of fluorine.

One unexpected result found in copper-containing samples was the complete solid solution in $n=1$ {100} layered compounds, between Sr_2TiO_4 and La_2CuO_4 . Given the previous reports of solid solution in unlayered perovskites, it was initially assumed that the greatest chance to observe similar behaviour in layered materials would be in those compounds with the greatest resemblance to perovskite, namely those with the thicker perovskite lamellae. However, the $n=1$ solid solution was found to form in preference to an $n=2$ solid solution. A probable reason for this was the greater freedom for octahedral distortion available in the $n=1$ structure, particularly the elongation of octahedra in line with the Jahn-Teller effect frequently found in Cu^{2+} compounds.

8.4 New Structures and Future Possibilities

During the investigation of the SrO-La₂O₃-TiO₂ system, a new compound was found with the formula Sr₃La₂Ti₂O₁₀. The structure of this material was elucidated by examination of HREM images, and refined by Rietveld analysis of X-ray powder diffraction data. It consists of lamellae of the Sr₂TiO₄ structure, cut obliquely to the sheets of TiO₆ octahedra, and stacked above one another. The result is an arrangement of TiO₆ octahedra in ribbons one octahedron high and 4 wide, interspersed with Sr and La atoms. Although efforts to prepare compounds with larger Sr₂TiO₄-type lamellae (*i.e.* wider ribbons) were not successful, mixed-layer intergrowths were observed. If elastic strain is also the dominating force behind the formation of these structures, it may well be possible to synthesise other compounds in this series, perhaps by introducing other elements to manipulate the effect of elastic strain.

Because this is a new structure, the potential for related materials is considerable. In addition to compounds with thicker Sr₂TiO₄ units, the observation of coherent joining

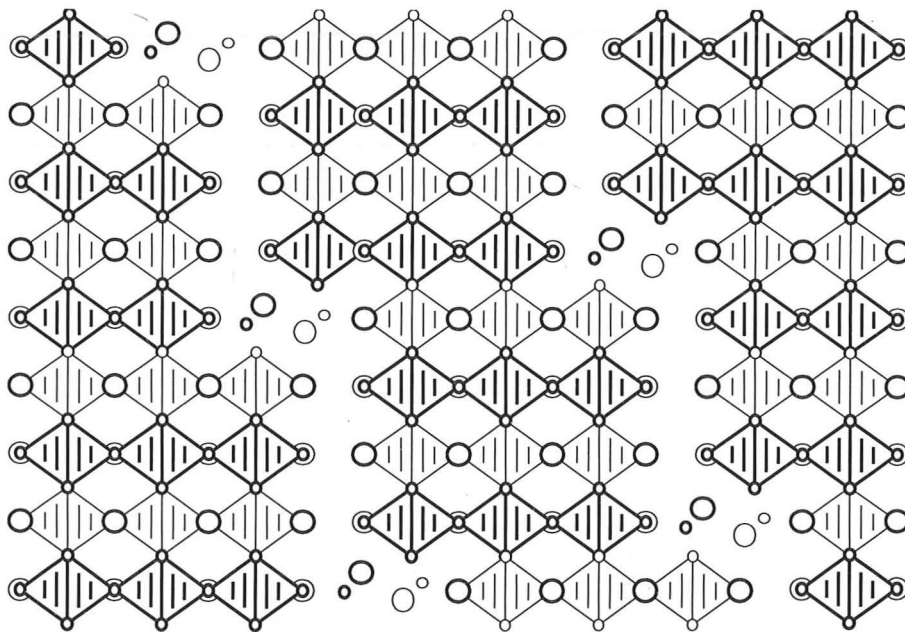


Figure 8-1 Possible structure resulting from the combination of Sr₃La₂Ti₂O₁₀ and perovskite elements. The portions of structure arising from Sr₃La₂Ti₂O₁₀ may be recognised from Chapter 5 (for example, Figure 5-2), and the perovskite regions are viewed in the [110] orientation.

between $\text{Sr}_3\text{La}_2\text{Ti}_2\text{O}_{10}$ and perovskite suggests possible structures based on alternating $\text{Sr}_3\text{La}_2\text{Ti}_2\text{O}_{10}$ and perovskite regions. An example of this is shown in Figure 8-1, where a single a repeat of $\text{Sr}_3\text{La}_2\text{Ti}_2\text{O}_{10}$ alternates with perovskite, leading to what is in effect a stepped rocksalt layer.

Isostructural compounds may also be of interest, particularly those based on copper oxide. Since the two-dimensional nature of materials such as $(\text{La},\text{Sr})_2\text{CuO}_4$ is thought to be important for their superconducting properties, a further reduction in dimensionality from sheets to ribbons may yield further improvements to their electronic behaviour.

The investigation described here is by no means an exhaustive account of the possible structures which might be synthesised based on SrTiO_3 . Oxygen-deficient compositions have not been investigated, not only those formed by direct reduction, but also any phases which may result from the substitution of Na^+ for Sr^{2+} , for example. It may also be possible to combine elements of the crystallographic shear compounds into the perovskite structure. Figure 8-2 shows one such hypothetical structure, where an ReO_3 -like $\{100\}$ CS plane is interspersed between perovskite lamellae. Layers based on configurations such as these have been observed, albeit in metastable high temperature phases, in the system Bi-Mo-W-O (Jefferson *et al.*,

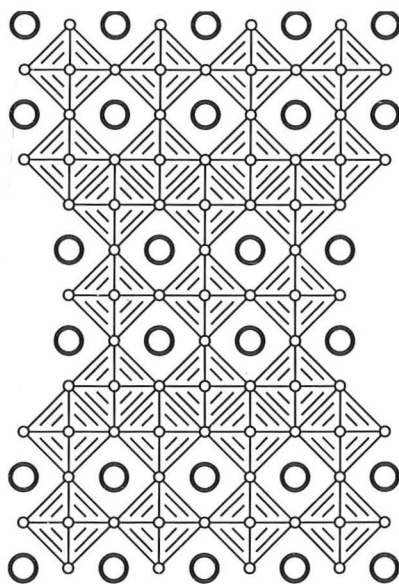


Figure 8-2 Hypothetical structure resulting from $\{100\}$ CS planes in a perovskite matrix. The formula of this compound would be $\text{Sr}_2\text{Ti}_3\text{O}_8$.

1983). If this configuration were possible, it would open the door for a large range of compounds, analogous to reduced WO_3 , containing different layer separations and orientations. Alternatively, intergrowth compounds can be envisaged where the interlayer structure alternates, as opposed to an alternation of the perovskite lamellae. An example would be a compound containing a succession of rocksalt and Bi_2O_2 layers, since both are oriented along perovskite $\{100\}$ planes.

The appearance of right-angled deviations in rocksalt layers also offers the opportunity for new structures. The coordination of the A cations at the corner site is different from the other cations, and so if this coordination could be preferentially generated, then a series of block structures bounded by rocksalt layers can be imagined. An example is shown in Figure 8-3, comprising 3×3 and 4×4 perovskite blocks.

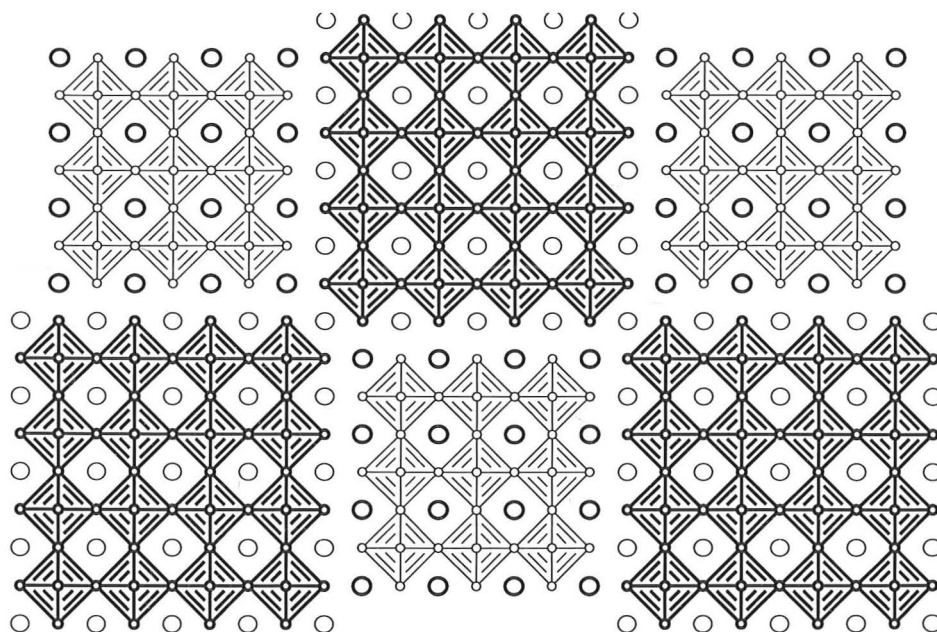


Figure 8-3 Hypothetical structure containing blocks of perovskite separated by rocksalt-like layers. Presumably, the key to generating such structures lies in the A sites near the corners of the blocks, which have a different coordination than the planar rocksalt compounds.

The compounds prepared in this study all contained titanium in its most oxidised state, and are therefore expected to be electrical insulators. The electrical properties of mixed-valence compounds could be intriguing; in fact reduced SrTiO_3 exhibits

superconductivity at low temperatures (Schooley *et al.*, 1965). Compounds containing Ti^{3+} as well as Ti^{4+} have been prepared in the {110} and {111} layered families, but it should also be possible to synthesise mixed-valence {100} layered materials by, for example, substituting La^{3+} for Sr^{2+} to counteract the reduction in Ti valence. The main experimental limitations at present are a lack of knowledge of experimental conditions and the need to work at only moderate pressures; if these limitations can be overcome, it may then be possible to realise all the many structural possibilities which exist in the Sr-Ti-O system and its derivatives.

Appendix

X-ray Diffraction Data

The X-ray diffraction peaks of compounds which have not been reported before are tabulated in this appendix.

<i>h</i>	<i>k</i>	<i>l</i>	<i>d</i> (calc)	<i>d</i> (obs)	<i>I</i> / <i>I</i> ₀	<i>h</i>	<i>k</i>	<i>l</i>	<i>d</i> (calc)	<i>d</i> (obs)	<i>I</i> / <i>I</i> ₀
0	0	6	5.211	5.185	3.0	4	0	-2	1.9530	1.9518	65.7
0	1	5	4.124	4.131	35.9	0	2	12	1.8892	1.8957	20.5
2	0	0	3.876	3.867	9.7					1.8907	7.5
0	1	6	3.778	3.783	3.5	1	1	15	1.8399	1.8287	11.9
0	1	7	3.464	3.468	3.3	4	1	-7	1.7652	1.7657	13.2
0	0	10	3.127	3.120	82.8	2	0	16	1.6639	1.6649	22.6
2	1	-5	2.947	2.946	74.1					1.6556	18.2
0	2	0	2.743	2.759	45.8					1.6459	4.8
2	1	-7	2.716	2.718	100.0					1.6295	10.4
2	0	-10	2.596	2.591	13.1	2	3	-5	1.6203	1.6261	5.9
0	1	11	2.524	2.526	8.0					1.5947	26.0
2	1	8	2.346	2.351	4.0	4	2	-2	1.5910	1.5873	26.7
2	0	-12	2.298	2.296	9.7	0	0	20	1.5633	1.5629	3.4
2	2	0	2.239	2.248	35.0	2	1	-19	1.5247	1.5264	8.4
0	0	14	2.233	2.231	7.2					1.4211	21.1
2	2	-5	2.158	2.165	5.1	0	4	0	1.3716	1.3770	5.6
2	1	-12	2.120	2.121	6.7	4	2	-14	1.3579	1.3611	12.6
0	2	10	2.062	2.069	43.2	0	0	24	1.3028	1.3028	3.5
2	0	12	2.048	2.049	5.5	0	4	9	1.2757	1.2687	8.0
2	1	-13	2.016	2.026	9.3	2	-3	15	1.2634	1.2640	7.2

Table A-1

X-ray diffraction peaks recorded from SrLa₄Ti₅O₁₇ (Cu *K*_α radiation). Indices have been assigned according to the data published by Williams *et al.* (1991a) for the isostructural La₅Ti₅O₁₇, using the cell *a*=7.812Å, *b*=5.529Å, *c*=31.51Å, β=97.13° (see Section 4.2.3).

<i>h</i>	<i>k</i>	<i>l</i>	<i>d</i> (calc)	<i>d</i> (obs)	<i>I</i> / <i>I</i> ₀
0	1	9	4.167	4.153	40
1	0	2	3.869	3.861	14
0	1	18	3.437	3.438	3
0	0	18	3.167	3.161	70
1	1	3	3.146	3.124	70
1	1	7	2.971	2.975	78
0	1	17	2.868	2.870	6
0	2	0	2.767	2.762	58
1	1	11	2.717	2.714	100
1	0	16	2.632	2.630	13
0	0	22	2.591	2.595	5
1	0	20	2.302	2.300	9
1	2	2	2.250	2.249	40
1	1	19	2.186	2.190	3
0	2	18	2.084	2.082	15
1	1	21	2.068	2.069	26
2	0	0	1.9525	1.9518	64
0	2	22	1.8913	1.8919	18
1	1	25	1.8553	1.8536	6
2	1	9	1.7681	1.7675	15
1	1	29	1.6737	1.6734	8
2	0	18	1.6621	1.6629	18
1	3	7	1.6338	1.6337	9
2	2	0	1.5952	1.5950	29
1	3	11	1.5875	1.5874	27
1	1	33	1.5193	1.5203	7
2	2	18	1.4247	1.4249	20
2	2	22	1.3585	1.3593	9
3	1	7	1.2520	1.2524	8
3	1	11	1.2308	1.2316	8

Table A-2

X-ray diffraction pattern for SrLa₈Ti₉O₃₁ (Cu K_α radiation). Indices have been assigned using a pattern calculated from a conceptual structure in an orthorhombic cell with the dimensions $a=7.810\text{\AA}$, $b=5.533\text{\AA}$, and $c=57.01\text{\AA}$ (see Section 4.2.3).

<i>h</i>	<i>k</i>	<i>l</i>	<i>d</i> (calc)	<i>d</i> (obs)	<i>I</i> / <i>I</i> ₀	<i>h</i>	<i>k</i>	<i>l</i>	<i>d</i> (calc)	<i>d</i> (obs)	<i>I</i> / <i>I</i> ₀
1	0	-1	5.819	5.824	3	2	1	7	1.5501	1.5497	1
1	1	1	4.135	4.135	2	4	0	-3	1.5457	1.5455	1
0	1	2	4.106	4.103	1	3	1	6	1.5298	1.5302	1
1	0	3	3.647	3.644	2	4	1	4	1.4988	1.4986	1
1	1	2	3.614	3.614	7	2	2	-6	1.4483	1.4483	5
2	0	0	3.450	3.451	1	4	2	2	1.4456	1.4446	6
1	0	-3	3.401	3.404	2	2	0	8	1.4443		
0	1	3	3.287	3.285	6	4	1	5	1.4178	1.4172	1
2	0	-1	3.254	3.252	9	4	2	3	1.4082	1.4077	1
0	0	4	3.066	3.070	2	0	4	0	1.3822	1.3820	5
1	1	3	3.044	3.042	3	4	2	-3	1.3492	1.3489	1
1	1	-3	2.897	2.897	68	4	1	-5	1.3215	1.3211	1
2	1	1	2.899	2.890	100	2	0	9	1.3034	1.3035	1
1	0	4	2.889			2	3	6	1.2962	1.2960	1
0	2	0	2.765	2.764	41	1	1	-9	1.2813	1.2807	2
2	1	2	2.713	2.713	2	3	3	-4	1.2778	1.2773	3
1	2	0	2.566	2.563	2	0	3	7	1.2699	1.2692	4
0	0	5	2.453	2.453	3	5	1	4	1.2632	1.2631	2
2	0	4	2.388	2.387	1	4	3	0	1.2593	1.2592	3
1	0	5	2.372	2.372	2	1	4	4	1.2468	1.2470	3
1	2	-2	2.343	2.341	1	4	1	-6	1.2372	1.2371	3
1	0	-5	2.255	2.257	4	5	2	2	1.2273	1.2271	2
1	2	3	2.2030	2.2008	1	3	2	-7	1.2081	1.2079	1
3	1	0	2.1233	2.1229	4	3	3	6	1.2048	1.2047	2
3	1	1	2.1185	2.1167	4	2	1	-9	1.2047		
2	2	-1	2.1068	2.1059	14	1	0	-10	1.1914	1.1912	1
3	0	-2	2.0991	2.0996	16	2	2	9	1.1789	1.1787	2
3	0	3	2.0761	2.0760	15	4	2	7	1.1624	1.1621	1
2	1	-4	2.0492	2.0478	4	5	2	-3	1.1593	1.1590	2
0	0	6	2.0442	2.0441	3	3	4	-2	1.1544	1.1542	3
1	2	4	1.9972	1.9967	28	3	4	3	1.1506	1.1506	2
1	0	-6	1.9188	1.9183	5	5	1	-5	1.1388	1.1387	1
1	2	5	1.8000	1.8006	1	5	0	7	1.1285	1.1283	1
0	0	7	1.7521	1.7556	1	0	2	10	1.1211	1.1210	1
1	2	-5	1.7476	1.7476	1	6	1	-1	1.1132	1.1129	1
2	1	6	1.7316	1.7321	2	3	1	-9	1.1104	1.1103	1
2	0	-6	1.7003	1.7005	4	1	2	-10	1.0941	1.0940	2
3	1	-4	1.6886	1.6890	2	6	1	-2	1.0923	1.0925	2
3	2	-2	1.6718	1.6707	16	5	1	-6	1.0828	1.0824	1
0	1	7	1.6703			1	3	-9	1.0716	1.0716	1
3	2	3	1.6601	1.6601	5	6	2	1	1.0645	1.0644	1
4	1	0	1.6465	1.6460	6	5	3	4	1.0609	1.0607	1
1	3	-3	1.6203	1.6200	14	1	5	-3	1.0516	1.0513	3
2	3	1	1.6194			5	2	7	1.0448	1.0448	2
1	1	-7	1.5960	1.5971	4	4	1	10	1.0215	1.0213	1
1	2	-6	1.5763	1.5761	2						

Table A-3

X-ray diffraction pattern of Sr₃La₂Ti₂O₁₀ (Cu K_α radiation). The indices and calculated positions are from the Rietveld refinement described in Section 5.3, giving a monoclinic unit cell with the dimensions $a=6.9214\text{\AA}$, $b=5.5294\text{\AA}$, $c=12.3048\text{\AA}$, $\beta=85.439^\circ$.

References

- S.C. Abrahams and J.L. Bernstein (1971), "Rutile: normal probability plot analysis and accurate measurement of crystal structure" *J. Chem. Phys.* **55** 3206-3211.
- M.A. Alario-Franco and M. Vallet-Regi (1977), "Anion deficiency in strontium titanate" *Nature* **270** 706-708.
- M.A. Alario-Franco, M.J.R. Henche, M. Vallet, J.M.G. Calbert, J.-C. Grenier, A. Wattiaux and P. Hagemuller (1983), "Microdomain texture and oxygen excess in the calcium-lanthanum ferrite $\text{Ca}_2\text{LaFe}_3\text{O}_8$ " *J. Solid State Chem.* **46** 23-40.
- S. Andersson, B. Collén, U. Kuylenstierna and A. Magnéli (1957), "Phase analysis studies on the titanium-oxygen system" *Acta. Chem. Scand.* **11** 1641-1652.
- J.S. Anderson (1973), "On infinitely adaptive compounds" *J. Chem. Soc., Dalton Trans.* 1107-1115.
- J.S. Anderson and B.G. Hyde (1967), "On the possible role of dislocations in generating ordered and disordered shear structures" *J. Phys. Chem. Solids* **28** 1393-1408.
- M.T. Anderson, V.E. Balbarin, D.A. Groenke, G.A. Bain and K.R. Poeppelmeier (1993), " La_2O_3 -CuO-TiO₂ phase diagram and the crystal structure of $[\text{La}_{0.86}\square_{0.14}\text{Cu}_3][\text{Ti}_{3.42}\text{Al}_{0.58}]\text{O}_{12}$ " *J. Solid State Chem.* **103** 216-227.
- R.A. Armstrong and R.E. Newnham (1972), "Bismuth titanate solid solutions" *Mat. Res. Bull* **7** 1025-1034.
- J.P. Attfield, A.K. Cheetham, D.E. Cox and A.W. Sleight (1988), "Synchrotron X-ray and neutron powder diffraction studies of the structure of α -CrPO₄" *J. Appl. Cryst.* **21** 452-457.
- B. Aurivillius (1949a), "Mixed bismuth oxides with layer lattices. I The structure type of $\text{CaNb}_2\text{Bi}_2\text{O}_9$ " *Arkiv for Kemi* **1** 463-480.
- B. Aurivillius (1949b), "Mixed bismuth oxides with layer lattices. II Structure of $\text{Bi}_4\text{Ti}_3\text{O}_{12}$ " *Arkiv for Kemi* **1** 499-512.
- B. Aurivillius (1950), "Mixed bismuth oxides with layer lattices. III Structure of $\text{BaBi}_4\text{Ti}_4\text{O}_{15}$ " *Arkiv for Kemi* **2** 519-527.
- U. Balachandran and N.G. Eror (1980), *Extended Abstracts* (158th meeting of the Electrochem. Soc.) **80-82** 914-915.
- U. Balachandran and N.G. Eror (1981), "Solubility of lanthanum in strontium titanate" *J. Am. Ceram. Soc.* **64** C75-C76.
- U. Balachandran and N.G. Eror (1982), "Electrical conductivity in lanthanum-doped strontium titanate" *J. Electrochem. Soc.* **129** 1021-1026.

- D. Balz and K. Pleith (1955), "Die Struktur de Kaliumnickelfluorids, K_2NiF_4 " *Z. Elektrochem.* **59** 545-551.
- Y. Bando, Y. Sekikawa, H. Yamamura and Y. Matsui (1981), "Crystal structure analysis of $Ca_4YFe_5O_{13}$ by combining 1MeV high-resolution electron microscopy with convergent-beam electron diffraction" *Acta Cryst.* **A37** 723-728.
- J.G. Bednorz and K.A. Müller (1986), "Possible high- T_c superconductivity in the barium-lanthanum-copper-oxygen system" *Z. Phys. B* **64** 189-193.
- J. Berggren (1971), "Refinement of the crystal structure of dicalcium ferrite, $Ca_2Fe_2O_5$ " *Acta Chem. Scand.* **25** 3616-3624.
- M. Bochu, M.N. Deschizeaux, J.C. Jourbet, A. Collomb, J. Chenavas and M. Marezio (1979), "Synthèse et caractérisation d'une série de titanates pérowskites isotypes de $[CaCu_3](Mn_4)O_{12}$ " *J. Solid State Chem.* **29** 291-281.
- J. Booth, T. Ekström, E. Iguchi and R.J.D. Tilley (1982), "Notes on phases occurring in the binary tungsten-oxygen system" *J. Solid State Chem.* **41** 293-307.
- R. Bontchev, B. Darriet, J. Darriet, F. Weill, G. Van Tendeloo and S. Amelinckx (1993), "New cation deficient perovskite-like oxides in the system $La_4Ti_3O_{12}$ - $LaTiO_3$ " *Eur. J. Solid State Inorg. Chem.* **30** 521-537.
- J. Bouwma, K.J. DeVries and A.J. Burggraaf (1976), "Nonstoichiometry, defect structure, and dielectric relaxation in lanthana-substituted $SrTiO_3$ " *Phys. Stat. Solidi A* **35** 281-290.
- I.D. Brown (1987), "Recent developments in the bond valence model of inorganic bonding" *Phys. Chem. Min.* **15** 30-34.
- I.D. Brown (1992), "Modelling the structures of La_2NiO_4 " *Z. Krist.* **199** 255-272.
- I.D. Brown and Altermatt (1985), "Bond valence parameters obtained from a systematic analysis of the Inorganic Crystal Structure Database" *Acta Cryst.* **B41** 244-247.
- L.A. Bursill and B.G. Hyde (1971), "Crystal structures in the $\{1\bar{3}2\}$ family of higher titanium oxides" *Acta Cryst.* **B27** 210-215.
- L.A. Bursill and B.G. Hyde (1972), "Crystallographic shear in the higher titanium oxides: structure, texture, mechanisms and thermodynamics" *Prog. Solid State Chem.* **7** 177-259.
- L.A. Bursill, B.G. Hyde and D.K. Philp (1971), "New crystallographic shear families derived from the rutile structure, and the possibility of continuous ordered solid solution" *Phil. Mag.* **23** 1501-1513.
- L.A. Bursill, D.J. Netherway and I.E. Grey (1978), "Composition waves in iron-doped rutile and the relationship between Young's modulus minima and crystallographic shear orientations" *Nature* **272** 405-410.
- P. Buseck, J. Cowley and L. Eyring (Eds) (1988), "High-resolution transmission electron microscopy and associated techniques" Oxford University Press, New York.

- A. Carpy, P. Amestoy and R. Portier (1974), "Étude par diffraction X et microscopie électronique de deux phases inédites de la série $A_{n+1}B_nO_{3n+1}$ (A=Na et Ca, B=Nb) ($n=4$ et 5)" *C.R. Acad. Sci. Paris, Serie C* **278** 1255-1258.
- C.R.A. Catlow and R. James (1980), "The formation and ordering of shear planes in non-stoichiometric oxides" *Chem. Phys. Solids and their Surf.* **8** 108-120.
- R.J. Cava, B. Batlogg, R.B. van Dover, J.J. Krajewski, J.V. Waszczak, R.M. Fleming, W.F. Peck Jr, L.W. Rupp Jr, P. Marsh, A.C.W.P. James and L.F. Schneemeyer (1990), "Superconductivity at 60K in $La_{2-x}Sr_xCaCu_2O_6$: the simplest double-layer cuprate" *Nature* **345** 602-604.
- C.W. Chu, P.H. Hor, R.L. Meng, L.Gao and Z.J. Huang (1987), "Superconductivity at 52.5K in the lanthanum-barium-copper-oxide system" *Science* **235** 567-569.
- A. Cocco and F. Massazza (1963), "Esame microscopio sistema SrO-TiO₂" *Annali di Chimica (Rome)* **53** 883-893.
- J.W. Cooley and J.W. Tukey (1965), "An algorithm for the machine computation of complex Fourier transforms" *Math. Computation* **19** 297.
- A.N. Cormack, C.R.A. Catlow and P.W. Tasker (1983), "Long-range ordering of extended defects in non-stoichiometric oxides" *Radiation Effects* **74** 237-245.
- J.M. Cowley and A.F. Moodie (1957), "The scattering of electrons by atoms and crystals, I. A new theoretical approach" *Acta Cryst.* **10** 609-619.
- A.H. Davies and R.J.D. Tilley (1987), "New layer structures in the La-Cu-O system" *Nature* **326** 859-861.
- G. Demazeau, C. Parent, M. Pouchard and P. Hagenmuller (1972), "Sur deux nouvelles phases oxygénées du cuivre trivalent: $LaCuO_3$ et $La_2Li_{0.5}Cu_{0.5}O_4$ " *Mat. Res. Bull* **7** 913-920.
- K. Doverspike J.-H. Liu, K. Dwight and A. Wold (1989), "Preparation and characterisation of members of the system $La_{2-x}A_{1+x}Cu_2O_{6\pm y}$ where A=Ca,Sr" *J. Solid State Chem.* **82** 30-34.
- J. Drennan, C.P. Tavares and B.C.H. Steele (1982), "An electron microscope investigation of phases in the system La-Ni-O" *Mat. Res. Bull* **17** 621-626.
- M. Drys and W. Trzebiatowski (1957), "System strontium oxide-titanium oxide" *Roczniki Chem.* **31** 489-96.
- A.J. Edwards and R.D. Peacock (1959), "The structures of potassium trifluorocuprate(II) and potassium trifluorochromate(II)" *J. Chem. Soc.* 4126-4127.
- A. Eikman and R.E. Smallman (1964), "A note on the transformation in non-stoichiometric rutile" *Phil. Mag.* **11** 627-632.
- T. Ekström and R.J.D. Tilley (1980), "The crystal chemistry of the ternary tungsten oxides" *Chem. Scr.* **16** 1-23.

- M.M. Elcombe, E.H. Kisi, K.D. Hawkins, T.J. White, P. Goodman and S. Matheson (1991), "Structure determinations for $\text{Ca}_3\text{Ti}_2\text{O}_7$, $\text{Ca}_4\text{Ti}_3\text{O}_{10}$, $\text{Ca}_{3.6}\text{Sr}_{0.4}\text{Ti}_3\text{O}_{10}$ and a refinement of $\text{Sr}_3\text{Ti}_2\text{O}_7$ " *Acta Cryst.* **B47** 305-314.
- N.G. Eror and U. Balachandran (1981), "Self-compensation in lanthanum-doped strontium titanate" *J. Solid State Chem.* **40** 85-91.
- L. Er-Rakho, C. Michel, J. Provost and B. Raveau (1981), "A series of oxygen-defect perovskites containing Cu^{II} and Cu^{III} : The oxides $\text{La}_{3-x}\text{Ln}_x\text{Ba}_3[\text{Cu}^{\text{II}}_{5-2y}\text{Cu}^{\text{III}}_{1+2y}]\text{O}_{14+y}$ " *J. Solid State Chem.* **37** 151-156.
- L. Eyring and M. O'Keefe (eds) (1970), "The chemistry of extended defects in non-metallic solids" North-Holland, Amsterdam.
- N.F. Federov, O.V. Mel'nikova, V.A. Saltykova and M.V. Chistyakova (1979), "New perovskite-like compound (12H) $\text{La}_4\text{Ti}_3\text{O}_{12}$ " *Zh. Neorg. Khim.* **24** 1166-1170.
- B.F. Flandermeyer, A.K., Agarinal, H.U. Anderson and M.M. Nasrallah (1984), "Oxidation-reduction behaviour of La-doped SrTiO_3 " *J. Mater. Sci.* **19** 2593-2598.
- P. Gado and A. Magnéli (1965), "Shear structure of the wolfram oxide $\text{WO}_{2.95}$ " *Acta Chem. Scand.* **19** 1514-1515.
- F.S. Galasso (1969), "Structure, properties and preparation of perovskite-type compounds" Pergamon, Oxford.
- M. Gasperin (1975), "Dititanate de lanthane" *Acta Cryst.* **B31** 2129-2130.
- M. German and L.M. Kovba (1983), "Hexagonal 'perovskite' phases in the La_2O_3 - TiO_2 -MO systems (M=Mg,Ca,Sr,Ba)" *Zh. Neorg. Khim.* **28** 2377-2379.
- M. German and L.M. Kovba (1985), "The structure of the hexagonal phases $\text{A}_n\text{B}_{n-1}\text{O}_{3n}$ " *Zh. Neorg. Khim.* **30** 317-322.
- A. M. Glazer (1972), "The classification of tilted octahedra in perovskites" *Acta Cryst.* **B28** 3384-3392.
- K. Godwod, J. Gorecka, G. Jasidek, J. Majewski and P. Przyslupski (1987), "X-ray characterisation of La-Sr-Cu-O system" *Z. Phys.* **B67** 313-317.
- V.M. Goldschmidt (1926), *Skifter Nordske Videnkaps-Akad. Oslo, I. Mat.-Naturv. Kl.* **8** 2.
- W. Gong, H. Yun, Y.B. Nong, J.E. Greedan, W.R. Datars and C.V. Stager (1991a), "Oxygen-deficient SrTiO_{3-x} , $x=0.28, 0.17$ and 0.08 . Crystal growth, crystal structure, magnetic and transport properties" *J. Solid State Chem.* **90** 320-330.
- W. Gong, J.S. Xue and J.E. Greedan (1991b), "Single crystals of new Ruddlesden-Popper phases $(\text{SrLa})_3\text{V}_2\text{O}_7$ and $\text{Sr}_4\text{V}_3\text{O}_{9.7}$: preparation, crystal structure, and electrical resistivity" *J. Solid State Chem.* **91** 180-185.
- J.-C. Grenier, G. Schiffmacher, P. Caro, M. Pouchard and P. Hagenmuller (1977), "Etude par diffraction X et microscopie electronique du système CaTiO_3 - $\text{Ca}_2\text{Fe}_2\text{O}_5$ " *J. Solid State Chem.* **20** 365-379.

- J.-C. Grenier, F. Menil, M. Pouchard and P. Hagenmuller (1978), "Mössbauer resonance studies in the $\text{CaTiO}_3\text{-Ca}_2\text{Fe}_2\text{O}_5$ system" *Mat. Res. Bull.* **13** 329-337.
- K. Hawkins and T.J. White (1991), "Defect structure and chemistry of $(\text{Ca}_x\text{Sr}_{1-x})_{n+1}\text{Ti}_n\text{O}_{3n+1}$ layer perovskites" *Phil. Trans. Roy. Soc. Lond.* **A336** 541-569.
- E. Herdtweck and D. Babel (1981), "X-ray single crystal structure determinations of the potassium copper(II) fluorides K_2CuF_4 and $\text{K}_3\text{Cu}_2\text{F}_7$ " *Z. Anorg. Allg. Chem.* **474** 113-122.
- P.J. Hewitt, D.A. Jefferson, G.R. Millward and K. Tsuno (1989), "A new high-resolution stage for the JEM-200CX" *Jeol News* **27** 2-9.
- R.J. Hill and I.C. Madsen (1984), "The effect of profile step counting time on the determination of crystal structure parameters by X-ray Rietveld analysis" *J. Appl. Cryst.* **17** 297-306.
- R.J. Hill and I.C. Madsen (1986), "The effect of profile step width on the determination of crystal structure parameters and estimated standard deviations by X-ray Rietveld analysis" *J. Appl. Cryst.* **19** 10-18.
- R.J. Hill and I.C. Madsen (1987), "Data collection strategies for constant wavelength Rietveld analysis" *Powder Diffraction* **2** 146-162.
- H. Holzapfel and J. Sieler (1966), "Zur Darstellung und Struktur der Seltenen Erd-titanate und des Europium(II)-zirkonats" *Z. Anorg. Allg. Chem.* **343** 174-180.
- S. Horiuchi, T. Kikuchi and M. Goto (1977), "Structure determination of a mixed-layer bismuth titanate, $\text{Bi}_7\text{Ti}_4\text{NbO}_{21}$, by super-high-resolution electron microscopy" *Acta Cryst.* **A33** 701-703.
- S.A. Howard, J.K. Yau and H.U. Anderson (1989), "Structural characteristics of $\text{Sr}_{1-x}\text{La}_x\text{TiO}_{3+\delta}$ as a function of oxygen partial pressure at 1400°C " *J. Appl. Phys.* **65** 1492-1498.
- J.L. Hutchison, J.S. Anderson and C.N.R. Rao (1977), "Electron microscopy of ferroelectric bismuth oxides containing perovskite layers" *Proc. Roy. Soc. Lond.* **A355** 301-312.
- J.L. Hutchison and A.J. Jacobson (1977), "Electron microscopy of the perovskite-related phases $4H \text{Ba}_{0.1}\text{Sr}_{0.9}\text{MnO}_{2.96}$, $5H \text{Ba}_5\text{Nb}_4\text{O}_{15}$ and $6H \text{BaFeO}_{2.79}$ " *J. Solid State Chem.* **20** 417-422.
- E. Iguchi and R.J.D. Tilley (1977), "The elastic strain energy of crystallographic shear planes in reduced tungsten trioxide" *Philos. Trans. Roy. Soc. Lond., Ser. A* **286** 55-85.
- M. Itoh, M. Shikano, R. Liang, H. Kawiji and T. Nakamura (1990), "Synthesis and properties of a new layered compound $\text{Sr}_4\text{V}_3\text{O}_{9.8}$ with layered structure" *J. Solid State Chem.* **88** 597-600.
- D.A. Jefferson, J.M. Thomas, M.K. Uppal and R.K. Grasselli (1983), "Discovery of a new type of layered structure by high resolution electron microscopy and electron-induced X-ray microanalysis" *J. Chem. Soc., Chem. Comm.* 594-595.

- D.A. Jefferson, M.K. Uppal, C.N.R. Rao and D.J. Smith (1984), "Elastic strain at the solid-solid interface in intergrowth structures: a novel example of partial structural refinement by HREM" *Mat. Res. Bull* **19** 1403-1409.
- D.A. Jefferson, J.M. Thomas, G.R. Millward, K. Tsuno, A. Harriman and R.D. Brydson (1986), "Atomic structure of ultrafine catalyst particles resolved with a 200 keV transmission electron microscope" *Nature* **323** 428-431.
- R. Jones and W.R. McKinnon (1990), "A new series of cubic perovskites" *Solid State Comm.* **76** 397-400.
- L. Katz and R. Ward (1964), "Structure relations in mixed metal oxides" *Inorg. Chem.* **3** 205-211.
- M. Kestigan and R. Ward (1955), "The lanthanum-titanium-oxygen system" *J. Am. Ceram. Soc.* **77** 6199-6200.
- M. Kestigan, J.G. Dickinson and R. Ward (1957), "Ion deficient phases in titanium and vanadium compounds of the perovskite type" *J. Am. Chem. Soc.* **79** 5598-5601.
- T. Kikuchi (1976), "Synthesis of new, layered bismuth titanates $\text{Bi}_7\text{Ti}_4\text{NbO}_{21}$ and $\text{Bi}_6\text{Ti}_3\text{WO}_{18}$ " *J. Less Common Met.* **48** 319-323.
- T. Kikuchi (1977), "Synthesis of a new, layered bismuth titanate $\text{SrBi}_8\text{Ti}_7\text{O}_{27}$ " *J. Less Common Met.* **52** 163-165.
- T. Kikuchi (1979), "Stability of layered bismuth compounds in relation to the structural mismatch" *Mat. Res. Bull* **14** 1562-1569.
- T. Kikuchi, A. Watanabe and K. Uchida (1977), "A family of mixed-layer type bismuth compounds" *Mat. Res. Bull* **12** 299-304.
- C. Kittel (1978), "On infinitely adaptive crystal structures" *Solid State Comm.* **25** 519-520.
- J.J. Lander (1951), "The crystal structures of $\text{NiO}\cdot 3\text{BaO}$, $\text{NiO}\cdot\text{BaO}$, BaNiO_3 , and intermediate phases near $\text{Ba}_2\text{Ni}_2\text{O}_5$; with a note on NiO " *Acta Cryst.* **4** 148-156.
- A.C. Larson and R.B. Von Dreele (1987), Los Alamos National Laboratory Report No. LA-UR-86-748.
- Y. Le Page and P. Strobel (1982a), "Structural chemistry of Magnéli phases $\text{Ti}_n\text{O}_{2n-1}$ ($4 \leq n \leq 9$). I. Cell and structure comparisons" *J. Solid State Chem.* **43** 314-319.
- Y. Le Page and P. Strobel (1982b), "Structural chemistry of Magnéli phases $\text{Ti}_n\text{O}_{2n-1}$ ($4 \leq n \leq 9$). II. Refinement and structural discussion" *J. Solid State Chem.* **44** 273-281.
- L.M. Longo and P.M. Raccach (1973), "Structure of dilanthanum copper tetroxide (La_2CuO_4) and lanthanum strontium vanadium tetroxide (LaSrVO_4)" *J. Solid State Chem.* **6** 526-531.
- K. Lukaszewicz (1958), "Die kristallstruktur einiger strontium- und barium titanate" *Angew. Chem.* **70** 320.

- K. Lukaszewicz (1959), "The crystal structure of strontium titanates α - $2\text{SrO}\cdot\text{TiO}_2$ and $3\text{SrO}\cdot 2\text{TiO}_2$ " *Roczniki. Chem.* **23** 239-242. [cited in *Structure Reports* (1960) **24** 440-441.]
- G.J. M^cCarthy, W.B. White and R. Roy (1969a), "Phase equilibria in the 1375°C isotherm of the system Sr-Ti-O" *J. Am. Ceram. Soc.* **52** 463-467.
- G.J. M^cCarthy, W.B. White and R. Roy (1969b), "The system Eu-Ti-O: phase relations in a portion of the 1400°C isotherm" *J. Inorg. Nucl. Chem.* **31** 329-339.
- J.B. MacChesney, H.J. Williams, J.F. Potter and R.C. Sherwood (1967), "Magnetic study of the manganate phases CaMnO_3 , $\text{Ca}_4\text{Mn}_3\text{O}_{10}$, $\text{Ca}_3\text{Mn}_2\text{O}_7$, Ca_2MnO_4 " *Phys. Rev.* **164** 779-785.
- A. Magnéli (1953), "Structures of the ReO_3 type with recurrent dislocations of atoms: 'Homologous series' of molybdenum and tungsten oxides" *Acta Cryst.* **6** 495-500.
- H. Maletta, M.W. Shafer, T. Penney, B.L. Olsen, A.M. Torresse and R.L. Greene (1987), "Antiferromagnetic correlations and superconductivity in the La_2CuO_4 class of compounds" *Physica B* **148** 233-236.
- M. Marezio, D.B. M^cWhan, P.D. Dernier and J.P. Remeika (1973), "Structural aspects of the metal-insulator transitions in titanium oxide (Ti_4O_7)" *J. Solid State Chem.* **6** 213-221.
- M. Marezio, D. Tranqui, S. Lakkis and C. Schlenker (1977), "Phase transitions in Ti_5O_9 single crystals: electrical conductivity, magnetic susceptibility, specific heat, electron paramagnetic resonance, and structural aspects" *Phys. Rev.* **B16** 2811-2821.
- H.D. Megaw (1946), "Crystal structure of double oxides of the perovskite type" *Proc. Phys. Soc.* **58** 133-152.
- C. Michel and B. Raveau (1984), "Oxygen intercalation in mixed-valence copper oxides related to the perovskites" *Rev. Chem. Min.* **21** 407-425.
- M. Minkova and S. Aslanyan (1989), "Isomorphic substitutions in the cerium oxide-lanthanum sesquioxide system at 850°C" *Cryst. Res. Technol.* **24** 351-354.
- M. Nanot, F. Queyroux and J.C. Gilles (1973), "Étude du système $\text{La}_2\text{Ti}_2\text{O}_7$ - CaTiO_3 . Mis en évidence d'une série nouvelle de composés de formule $\text{A}_n\text{B}_n\text{O}_{3n+2}$ " *C.R. Acad. Sci. Paris, Serie C* **277** 505-506.
- N. Nguyen, L. Er-Rakho, C. Michel, J. Choisnet and B. Raveau (1981), "Intercroissance de feuillets 'perovskite lacunaires' et de feuillets type chlorure de sodium: les oxydes $\text{La}_{2-x}\text{A}_{1+x}\text{Cu}_2\text{O}_{6-1/2x}$ (A=Ca,Sr)" *Mat. Res. Bull* **15** 891-897.
- S. Nomura (1978), "Crystallographic and magnetic properties of perovskite and perovskite-related compounds" in *Landolt-Börnstein new series* (K.-H. Hellwege and A.M. Hellwege, eds.) Springer-Verlag **12a** 368-520.
- A. Nozaki, H. Yohiskawa, T. Wada, H. Yamauchi and S. Takana (1991), "Layered perovskite compounds $\text{Sr}_{n+1}\text{V}_n\text{O}_{3n+1}$ ($n=1,2,3$ and ∞)" *Phys. Rev.* **B43** 181-185.
- B. Odekirk, U. Balachandran, N.G. Eror and S.S. Blakemore (1982), "Electronic conduction in quenched ceramic samples of highly reduced lanthanum doped SrTiO_3 " *Mat. Res. Bull* **17** 199-208.

- B. Okai (1989), "High pressure synthesis of $\text{Ca}_{1-x}\text{Sr}_x\text{CuO}_2$ " *Jpn. J. Appl. Phys. Pt II* **28** L2251-L2252.
- M. O'Keefe and B.G. Hyde (1977), "Some structures topologically related to cubic perovskite ($E2_1$), ReO_3 (DO_9) and Cu_3Au (LI_2)" *Acta Cryst.* **B33** 3802-3813.
- M.R. Palacín, A. Fuertes N. Casañ-Pastor and P. Gómez-Romero (1994), "Induction of bidimensionality in mixed Cu-Ti perovskites" *Advanced Materials* **6** 54-57.
- N. Ramadass, J. Golapakrishnan and M.V.C. Sastri (1977), "Preparation and characterisation of La_2TiMO_6 ($M=\text{Co}, \text{Ni}, \text{Cu}$ and Zn) perovskites" *J. Inorg. Nucl. Chem.* **40** 1453-1454.
- A. Reller, J.M. Thomas, D.A. Jefferson and M.K. Uppal (1984), "Superstructures formed by the ordering of vacancies in a selective oxidation catalyst: grossly defective CaMnO_3 " *Proc. Roy. Soc. Lond.* **A394** 223-241.
- H.M. Rietveld (1969), "A profile refinement method for nuclear and magnetic structures" *J. Appl. Cryst.* **2** 65-71.
- M.L. Rojas and J.L.G. Fierro (1990), "Synthesis and characterisation of $\text{LaTi}_{1-x}\text{Cu}_x\text{O}_3$ compounds" *J. Solid State Chem.* **89** 299-307.
- R.S. Roth, C.J. Rawn, J.R. Ritter and B.P. Burton (1989), "Phase equilibria of the system SrO-CaO-CuO " *J. Am. Ceram. Soc.* **72** 1545-1549.
- T. Rouillon, R. Retoux, D. Groult, C. Michel, M. Hervieu, J. Provost and B. Raveau (1989), " $\text{PbBaYSrCu}_3\text{O}_8$: A new member of the intergrowth family $(\text{ACuO}_{3-x})_m(\text{A}'\text{O})_n$ " *J. Solid State Chem.* **78** 322-325.
- S.N. Ruddlesden and P. Popper (1957), "New compounds of the K_2NiF_4 type" *Acta Cryst.* **10** 538-539.
- S.N. Ruddlesden and P. Popper (1958), "The compound $\text{Sr}_3\text{Ti}_2\text{O}_7$ and its structure" *Acta Cryst.* **11** 54-55.
- V.A. Saltykova, O.V. Mel'nikova and N.F. Federov (1989), "Phase formation in the $\text{La}_4\text{Ti}_3\text{O}_{12}\text{-MTiO}_3$ systems ($M=\text{Ca}, \text{Sr}, \text{Ba}$)" *Zh. Neorg. Khim.* **34** 1344-1346.
- A. Santoro, F. Beech and R.J. Cava (1990), "Neutron powder diffraction study of the structures of lanthanum calcium copper oxide ($\text{La}_{1.9}\text{Ca}_{1.1}\text{Cu}_2\text{O}_6$) and lanthanum strontium copper oxide ($\text{La}_{1.9}\text{Sr}_{1.1}\text{Cu}_2\text{O}_{6+\delta}$)" *Mat. Res. Soc. Symp. Proc.* **166** 187-192.
- O. Scherzer (1949), "The theoretical resolution limit of the electron microscope" *J. Appl. Phys.* **20** 20-29.
- J.F. Schooley, W.S. Hosler, E. Ambler, J.H. Becker, M.L. Cohen and C.S. Koonce (1965), "Dependence of the superconducting transition temperature on carrier concentration in semiconducting SrTiO_3 " *Phys. Rev. Lett.* **14** 305-307.
- K. Sekizawa, Y. Takano, H. Takigami, S. Tasaki and T. Inaba (1987), "Superconductivity in the La-Cu-O system" *Jpn. J. Appl. Phys. Lett.* **26** [Suppl. 26-3] L840-L841.

- R.D. Shannon (1976), "Revised effective ionic radii and systematic study of interatomic distances in halides and chalcogenides" *Acta Cryst.* **A32** 751-767.
- R.D. Shannon and C.T. Prewitt (1969), "Effective ionic radii in oxides and fluorides" *Acta Cryst.* **B25** 925-946.
- O.V. Sidorova, N.V. Porotnikov and K.I. Petrov (1982), "Physicochemical investigation of compounds in La_2O_3 - SrO - TiO_2 systems" *Zh. Neorg. Khim.* **27** 1959-1962.
- T. Siegrist, S.M. Zahurak, D.W. Murphy and R.S. Roth (1988a), "The parent structure of the layered high temperature superconductors" *Nature* **334** 231-232.
- T. Siegrist, L.F. Schneemeyer, S.A. Sunshine and J.V. Waszczak (1988b), "A new layered cuprate structure-type $(\text{A}_{1-x}\text{A}')_{14}\text{Cu}_{24}\text{O}_{41}$ " *Mat. Res. Bull.* **23** 1429-1438.
- J.M.S. Skakle and W.R. West (1994), "Subsolidus relations in the La_2O_3 - CuO - CaO phase diagram and the La_2O_3 - CuO binary join" *J. Am. Ceram. Soc.* **77** 2199-2202.
- J.C.H. Spence (1988), "Experimental high-resolution electron microscopy" (2nd edition) Oxford University Press, New York.
- A.M. Stoneham (1971), "Theory of regular arrays of defects. Void lattice" *J. Phys.* **F1** 778-784.
- A.M. Stoneham and P.J. Durham (1973), "The ordering of crystallographic shear planes: theory of regular arrays" *J. Phys. Chem. Solids* **43** 2127-2135.
- E.C. Subbarao (1962), "A family of ferroelectric bismuth oxides" *J. Phys. Chem. Solids* **23** 665-676.
- M.A. Subramanian, J.B. Parise, J.C. Calabrese, C.C. Toradi, J. Gopalakrishnan and A.W. Sleight (1988), "Crystal structure of $\text{TlBa}_2\text{Ca}_2\text{Cu}_3\text{O}_8$ " *J. Solid State Chem.* **77** 192-195.
- M. Sundberg (1976), "The crystal and defect structure of $\text{W}_{25}\text{O}_{73}$, a member of the homologous series $\text{W}_n\text{O}_{3n-2}$ " *Acta Cryst.* **B32** 2144-2149.
- N. Suzuki, T. Noritake, N. Yamamoto and T. Hioki (1991a), "Crystal structure and physical properties of the layered perovskite compound $\text{Sr}_3\text{V}_2\text{O}_{7.01}$ " *Mat. Res. Bull.* **26** 1-9.
- N. Suzuki, T. Noritake, N. Yamamoto and T. Hioki (1991b), "Crystal structure and physical properties of a new layered perovskite compound $\text{Sr}_4\text{V}_3\text{O}_{9.60}$ " *Mat. Res. Bull.* **26** 75-83.
- H.E. Swanson, N.T. Gilfrich and G.M. Uginic (1955), "Standard x-ray powder diffraction patterns" *Nat. Bur. Standards Circ.* **5** No. 539.
- Y. Takano, S. Tasaki, H. Takigami and K. Sekizawa (1987), "Superconductivity and magnetism of the (La,Y)-Cu-O system" *Jpn. J. Appl. Phys.* **26** 1067-1068.
- M. Takano, Y. Takeda, H. Okada, M. Miyamoto and T. Kusaka (1989), "ACuO₂ (A: alkaline earth) crystallising in a layered structure" *Physica C* **159** 375-378.
- J.M. Tarascon, W.R. McKinnon, P. Borboux, D.M. Hwang, B.G. Bagley, L.H. Greene, G.W. Hull, Y. Le Page, N. Stoffel and M. Giroud (1988), "Preparation, structure and properties of

- the superconducting compound series $\text{Bi}_2\text{Sr}_2\text{Ca}_{n-1}\text{Cu}_n\text{O}_y$, with $n=1,2$, and 3" *Phys. Rev.* **B38** 8885-8892.
- Chr. L. Teske and Hk. Müller-Buschbaum (1970), "Zur Kenntnis von Ca_2CuO_3 und SrCuO_2 " *Z. Anorg. Allg. Chem.* **379** 234-241.
- T.Y. Tien and F.A. Hummel (1967), "Solid solutions in the system SrTiO_3 - $(\text{La}_2\text{O}_3:3\text{TiO}_2)$ " *Trans. Brit. Ceram. Soc.* **66** 233-245.
- R.J.D. Tilley (1970), "Formation of shear structures in substoichiometric tungsten trioxide" *Mat. Res. Bull* **5** 813-823.
- R.J.D. Tilley (1977a), "An electron microscope study of perovskite-related oxides in the Sr-Ti-O system" *J. Solid State Chem.* **21** 293-301.
- R.J.D. Tilley (1977b), "Correlation between dielectric constant and defect structure of non-stoichiometric solids" *Nature* **277** 229-231.
- R.J.D. Tilley (1978-9), "The crystal chemistry of some tungsten oxides containing crystallographic shear planes" *Chem. Scr.* **14** 147-159.
- G. Tilloca and M. Perez Y Jorba (1964), "Refractory compounds having structures derived from the perovskite structure in the systems ZrO_2 -alkaline earth oxides" *Rev. Hautes Temper. et Refract.* **1** 331-342.
- B.C. Tofield (1978), "Anion deficiency in strontium titanate" *Nature* **272** 713-714.
- B.C. Tofield and W.R. Scott (1974), "Oxidative non-stoichiometry in perovskites, an experimental survey; the defect structure of an oxidised lanthanum manganite by powder neutron diffraction" *J. Solid State Chem.* **10** 183-194.
- A. Tokiwa, T. Oku, M. Nagoshi, M. Kikuchi, H. Hiraga and Y. Syono (1989), "Crystal structure and phase transition of $\text{PbBaSrYCu}_3\text{O}_y$ ($y=7\sim 8.4$)" *Physica C* **161** 459-467.
- C.C. Toradi, M.A. Subramanian, J.C. Calabrese, J. Gopalakrishnan, K.J. Morrissey, T.R. Askew, R.B. Flippen, M. Chowdry and A.W. Sleight (1988), "Crystal structure of $\text{Tl}_2\text{Ba}_2\text{Ca}_2\text{Cu}_3\text{O}_{10}$, a 125K superconductor" *Science* **240** 631-634.
- J.B. Torrance, Y. Tokura and A. Nazzal (1987), "Overview of the phases formed by rare earth alkaline earth copper oxides" *Chemtronics* **2** 120-125.
- K.R. Udayakumar and A.N. Cormack (1988), "Structural aspects of phase equilibria in the strontium-titanium-oxygen system" *J. Am. Ceram. Soc.* **71** C469-C471.
- G. Van Tendeloo, S. Amelinckx, B. Darriet, R. Bontchev, J. Darriet and F. Weill (1994), "Structural considerations and high resolution electron microscopy observations on $\text{La}_n\text{Ti}_{n-\delta}\text{O}_{3n}$ ($n\geq 4\delta$)" *J. Solid State Chem.* **108** 314-335.
- K. Vidyasagar, A. Reller, J. Golapkrishnan and C.N.R. Rao (1985), "Oxygen vacancy ordering in superlattices of the two novel oxides, $\text{La}_2\text{Ni}_2\text{O}_5$ and $\text{La}_2\text{Co}_2\text{O}_5$ prepared by low temperature reduction of the parent perovskites" *J. Chem. Soc., Chem. Commun.* 7-8.

- A. D. Wadsley (1955), "The crystal chemistry of non-stoichiometric compounds" *Rev. Pure Appl. Chem.* **5** 165-193.
- W.B. White and V.G. Keramidas (1972), "Application of infrared and Raman spectroscopy to the characterisation of order-disorder in high temperature oxides" *N.B.S. Special Publ.* **364** ("Solid State Chemistry") 113-126.
- D.B. Wiles and R.A. Young (1981), "A new computer program for Rietveld analysis of X-ray powder diffraction patterns" *J. Appl. Cryst.* **14** 149-151.
- T. Williams, H. Schmalle, A. Reller, F. Lichtenberg, D. Widmer and G. Bednorz (1991a), "On the crystal structures of $\text{La}_2\text{Ti}_2\text{O}_7$ and $\text{La}_5\text{Ti}_5\text{O}_{17}$: high-resolution electron microscopy" *J. Solid State Chem.* **93** 534-548.
- T. Williams, F. Lichtenberg, A. Reller and G. Bednorz (1991b), "New layered perovskites in the Sr-Ru-O system: a T.E.M. study" *Mat. Res. Bull.* **26** 763-770.
- T. Williams, F. Lichtenberg, D. Widmer, J.G. Bednorz and A. Reller (1993), "Layered perovskitic structures in pure and doped $\text{LaTiO}_{3.5-x}$ and $\text{SrNbO}_{3.5-x}$ " *J. Solid State Chem.* **103** 375-386.